New insights into the mechanical behaviour of rubber bearings

PhD Thesis

Alessandra Orfeo

Department of Civil and Environmental Engineering

University of Strathclyde, Glasgow

April, 2023

Contents

Abstract

This Thesis investigates the mechanical behaviour of elastomeric bearings with a low shape factor (LSF) through the development of advanced and simplified modelling strategies. Such bearings can offer an effective solution for three-dimensional seismic isolation of structures, that is, isolation in vertical as well as horizontal directions. They could also be employed for developing low-cost isolation systems due to their reduced weight and manufacturing cost. The proposed modelling strategies are validated against the results of the experimental tests carried out at Tun Abdul Razak Research Centre (TARRC) on rubber blocks and elastomeric bearings, and at University of Naples Federico II on a prototype building isolated with LSF bearings.

The first part of the Thesis investigates the behaviour of rubber blocks bonded between two plates under combined compression and shear loading, using experimental and numerical analyses, and also approximate analytical theories. Numerical simulations are carried out with three-dimensional finite element (FE) models, allowing insight to be gained into the stress and strain fields within the blocks. Existing analytical theories for blocks under compression and combined compressive and shear loading are then reviewed, and their accuracy is evaluated against test and numerical results. The study shows that those theories accounting for the effect of the axial shortening of the blocks provide a better description of the combined compression and shear behaviour, compared to theories, developed for laminated structural bearings with many thin rubber layers, that ignore this effect. An improved theory is also proposed, which better describes the effects of the bulging of the compressed blocks on their shear and flexural parameters and provides a better fit to experimental and numerical results.

The second part of the Thesis describes tests carried out on low-damping natural rubber (NR) double-shear test pieces, LSF bearings and shaking table tests. The material tests are used to inform the development of a FE model of the bearings, which is validated against the bearing test results. It is shown that the proposed FE model can be used to describe accurately the global non-linear horizontal force-displacement behaviour of the compressed bearings, while providing an insight into the local distribution of stresses and strains. It can also be used to investigate the bearing response under boundary conditions that differ from the one considered in the tests. It has been observed that axial loads have a significant influence on the mechanical behavior of the LSF bearings. Most of existing theories and mechanical models for laminated bearings cannot be employed for LSF bearings because they disregard the important effects of axial shortening and bulging of the rubber layers on the horizontal bearing stiffness. Therefore, a simplified model originally developed for slender rubber blocks is also employed for describing the mechanical behavior of LSF bearings and then used for simulating the seismic response of a structural prototype mounted on LSF bearings. In order to further

evaluate the effect of axial compliance of the bearings on the dynamic properties of the isolation system and to analyse the effect of variation of axial loads during the motion on the response of the bearing, a FE model of the isolated structure has also been developed. Useful insights are provided into the effect of the vertical bearing flexibility on the response and the attainment of critical conditions of zero tangent horizontal stiffness under horizontal displacements.

Elastomeric bearings are widely used also in bridges to support the superstructure, to transfer loads to substructures, and to accommodate movements induced by e.g. temperature changes. Bearing mechanical properties affect the bridge's performance, and its response to permanent and variable loadings (e.g. traffic). The third part of the Thesis describes the research carried out at Strathclyde towards the development of smart natural rubber bearings that can be used as a low-cost sensing technology for bridge and/or weigh-in-motion monitoring. An experimental campaign was performed, under laboratory conditions, on various natural rubber specimens enhanced with different conductive fillers. Each specimen was characterized under loading conditions that replicated in-situ bearings to determine their mechanical and piezoresistive properties. Relatively simple models can be used to describe the relationship between rubber bearing resistivity and deformation changes. Gauge factors (GFs) in the range between 2 and 11 are obtained, depending on the compound and the applied loading. Experiments were also carried out to show that the developed model can be used to predict the state of deformation of the bearings under random loadings of different amplitudes that are characteristic of the passage of traffic over a bridge.

Acknowledgment

Thanks are due for support given by Prof. Giorgio Serino, Dr. Fabrizia Cilento and Alan H. Muhr who provided data from the experimental campaigns carried out at the laboratories of TARRC and Department of Structures for Engineering and Architecture of University of Naples Federico II. The authors are also grateful to Giovanni Cuomo and Robert Picken who assisted with the bearing manufacturing and shaking table tests.

List of Figures

List of Tables

Symbols

Latin letters

A	Deformed cross sectional area
A_0	Initial cross sectional area
A_B	Material constant network B of BB model
A_s	Plan area of bearing effective in shear
B	Tilting stiffness for unit height
c	Dependency of creep strain to effective creep strain rate, BB model
c_d	Wave speed of the material
C_{ij}, C_{10}, C_{01}, C_{20}, C_{30}	Material constants
C_s, C_φ	Material parameters
D	Compressibility factor
d_0	Specimen diameter
d_{max}	Peak displacement in the hysteresis loop
E	Young's modulus
E_C	Compression modulus
$E_{c,0}$	Secant compression modulus at zero deformation
$E_{c,bend}$	Incremental Young's modulus
$E_{c,sec}$	Secant compression modulus
f	Nominal stress
f_{c1}, f_{c2}	Gent and Meinecke numerical factors
F_h	Shear force
F_{max}	Peak force in the hysteresis loop
f_r	Bending stiffness factor
G	Shear modulus

G^*	Complex modulus
G'	Storage modulus
G''	Loss modulus
H,D	Height and width of the superstructure in the simplified model
h_0, a_0, b_0,	Undeformed rubber height, minimum width, maximum width
h_t	Combined height of rubber and steel layers
I	Influence vector
I	Second moment of area of the cross section in the deformed state
I_0	Second moment of area of the cross section in the undeformed state
I_1, I_2, I_3	Strain Invariants
I_b , I_{top}	Moment of inertia of mass m_b and m_{top}
I_{el}	Current amplitude
J	Ratio of the current to original volume
K	Modulus of bulk compression
k	Volumetric deformation factor
k_B	Boltzmann constant
K_h	Horizontal stiffness
K_{h0}	Horizontal stiffness for zero compression
K_{is}	Total stiffness of isolated structure
k_s	Secant or tangent shear stiffness
K_v	Vertical stiffness
k_x, k_θ	Horizontal and rotational stiffness of the bearing in the simplified numerical model
$k_{x,\theta}$, $k_{\theta,x}$	Coupling terms of the bearing in the simplified numerical model
k_z	Vertical stiffness variation with the increase of horizontal displacement
L	Langrangian

l	Specimen stretched length
l_0	Specimen length
L_{min}	Smallest element dimension in the mesh
m	Effective stress dependence of the effective creep strain rate, BB model
M, **C**, **K**	Mass, Damping and Stiffness matrices
m_b	Mass of the support rigid base in the simplified model
m_{top} , k_s	Mass and stiffness of the superstructure in the simplified model
M_{top}	Bending moment at the top of the bearing
M_{tot}	Total mass of prototype superstructure
N_c	Number of the network chains
NE12	Nominal shear strain in the shear plane XY from FEA analysis
NE22	Nominal compressive strain along Y direction from FEA analysis
P	Compressive load
p	Hydrostatic pressure
Pcr	Critical load
q^2	$P(R-P)/(BR)$
R	Shear stiffness for unit height
R_{el}	Resistance
S	Shape factor
T	Temperature
t	Time
$\tan\delta$	Measure of energy loss
T_{fs}	Equivalent period of full-scale structure
T_{is}	Vibration period of isolated structure
t_r	Total rubber height

T_s	Vibration period of the fixed base structure
$u_{x,i}$	Horizontal displacement of the i-th node in the FE model of the isolated structure
$u_{y,i}$	Vertical displacement of the i-th node in the FE model of the isolated structure
v	Displacement vector
V_0	Original volume of a block
$v_{b,top}$	Translation at the top of the bearing
$v_{b,x}$	Horizontal displacement of the base in the simplified model
$v_{b,z}$	Vertical displacement of the base in the simplified model
V_{el}	Voltage
$v_{g,x}$	Response induced by the earthquake ground motion
$v_{s,x}$	Horizontal displacement of the superstructure relative to isolation system
v_{top}	Horizontal displacement at the top of the bearing
V_{top}	Shear force at the top of the bearing
v_v	Vertical displacement
W	Strain energy per unit unstrained volume

Greek letters

θ	Rotation of the base in the simplified model
λ	Axial extension/compression ratio
$\lambda_1, \lambda_2, \lambda_3$	Principal extension ratio
Ψ	Correction factor
ΔS	Change in entropy
Δ_s	Shear deflection
Δt	Time increment
ΔV	Change in volume

$\Delta\%$	Percentage error
β	$R/(R+P)$
ε	Compressive/Tensile strain
γ	Shear deformation
γ_0	Shear deformation amplitude
φ, s	Rotation and shear displacement in the Koh and Kelly's model
κ	Ratio a_0/b_0
μ_p, α_p	Material constants from Ogden material model
ν	Poisson's ratio
ν^*	Fitting parameter akin to Poisson's ratio
$\theta_{b,top}$	Rotation at the top of the bearing
ρ_m	Density of the material
ρ	Resistivity
ρ_0	Resistivity at zero stretch
σ	Compressive/Tensile stress
σ_B	Effective stress network B of BB model
σ_i	True stress
σ_T	True stress in tension or compression
σ_ε	Sensing precision
τ	Shear stress
τ_r	Relaxation time
τ_0	Shear stress amplitude
ω	Angular frequency
ξ, η, ζ	Displacement components in the x,y and z direction

ξ_b, ξ_s	Damping ratio of the base isolation system and of superstructure
ξ_{eq}	Equivalent damping ratio
$\sigma_{\Delta\rho/\rho_0}$	Standard deviation of the residuals
Ω	Shear parameter of Timoshenko theory
η_e	Newtonian viscosity coefficient
$\ddot{v}_g(t)$	Earthquake-induced ground motion
$\dot{\varepsilon}_B$	Effective creep strain rate network B of Bergstrom Boyce (BB) model
$\dot{\gamma}$	Shear strain rate
$\dot{\boldsymbol{\lambda}}$	Strain rate

Abbreviations

3D	Three-Dimensional
CBS	Cyclohezyl benzothiazxy sulphenamide
DBS	Double Bonded Shear
EERC	Earthquake Engineering Research Centre
FDD	Frequency Domain Decomposition
FE	Finite Element
FEA	Finite Element Analysis
HAF	High Abrasion Furnace
HDNR	High Damping Natural Rubber
HPPD	Hexyl phenyl phenylenediamine
LSF	Low Shape Factor
MAC	Modal Assurance Criterion
Mw	Moment Magnitude
NR	Natural Rubber
PGA	Peak Ground Acceleration
PGD	Peak Ground Displacement
PGV	Peak Ground Velocity
PHR	Part per Hundred of Rubber
SMR	Standard Malaysian Rubber
SMR	Standard Malaysian Rubber
SSI	Stochastic Subspace Identification
TARRC	Tun Abdul Razak Research Centre
TBBS	Tertiary butyl benzothiazole sulfenamide

1 Introduction

Rubber has been widely employed for more than a century to manufacture components acting in structures or machines as flexible springs and/or energy dissipation devices. The main reason behind the success of rubber is in the possibility of tailoring the compound, mechanical properties and shape of rubber devices to achieve the required performance under service conditions.

The most important applications in the civil engineering context are bridge bearings and joints, vibration isolation bearings, seismic isolation bearings, and elastomeric dampers (Gent, 2012).

Seismic isolation bearings are designed to safeguard buildings from the destructive impact of earthquakes. These natural disasters are triggered by the abrupt discharge of energy accumulated in the Earth's surface, which leads to severe vibrations of the soil. Earthquakes can cause significant destruction and pose a risk to the population living in seismic areas. In order to design structures that can withstand earthquakes, it is necessary to have a lateral force-resisting system in place that is able to absorb and dissipate energy in a stable manner over a large number of cycles. The traditional approach to seismic design involves creating ductile plastic regions where energy is dissipated and damage is concentrated to the main frame. However, this damage cannot be repaired. This approach is generally effective in preventing structural collapse and ensuring life safety (Constantinou, et al., 1998). However, it cannot avoid structural damage. When a building needs to maintain its functionality even after a powerful earthquake, like in crucial structures such as hospitals, nuclear power plants, this approach is not sufficient. To overcome this challenge, engineers have been developing earthquake protection systems for more than a century (Warn, et al., 2012), and laminated bearings have emerged as the most effective solution. These bearings are made of multiple layers of vulcanized elastomer and steel shims that are bonded together. The rubber layers offer low horizontal stiffness and high deformation capabilities, while the steel shims provide vertical rigidity and keep the rubber in place. Laminated rubber bearings can support gravity loads while providing horizontal flexibility, which is needed to limit the forces transmitted to the superstructure. The bearings can also provide energy dissipation, if high-damping compounds containing carbon black or other material fillers are used in the manufacturing process.

The current practice for designing laminated rubber seismic isolation bearings is based on thin rubber layers with closely spaced intermediate steel shim plates, corresponding to high values of the shape factor (Warn and Vu, 2012), which is defined as the ratio of the area of the loaded surface to the area free to bulge. This type of design has been well accepted and widely used for over thirty years (Kelly and Lee, 2018) to achieve horizontal seismic isolation and minimise rocking motion. However, it may be not effective in guaranteeing a good performance under the vertical seismic input. In fact, a high

vertical stiffness of the bearings leads to low vibration periods of the isolated structure in the vertical direction. This can potentially cause a substantial increase in the vertical seismic input due to resonance, which could pose a significant risk for important infrastructure such as nuclear power plants or hospitals containing delicate equipment that needs protection against the vertical component of earthquake inputs.

The concept of low-shape factor (LSF) elastomeric bearings made of thick rubber layers has been investigated for many years as a solution for achieving three-dimensional seismic isolation and/or providing vibration isolation together with seismic isolation (Aiken et al.1989). The mechanical behaviour of LSF bearings and the seismic performance of structures equipped with them have been studied extensively for few decades, without reaching any definite conclusion on their effectiveness. The main concerns regard the fact that LSF bearings encourage rocking and they may be subjected to excessive vertical deflections, leading to cavitation or instability. Moreover, the behaviour of LSF bearings is very complex, and there is no validated model for describing their mechanical behaviour.

This Thesis aims to address these above issues by developing and validating advanced and simplified modelling strategies that describe the mechanical behaviour of LSF bearings and the dynamic and seismic performance of structures equipped with them, specifically using natural rubber. The proposed modelling strategies are validated against the results of experimental tests conducted at Tun Abdul Razak Research Centre (TARRC) on rubber blocks and elastomeric bearings, and at the University of Naples Federico II on a prototype isolated with LSF bearings, using natural rubber. The study results provide novel and useful insight into the complex mechanical behaviour of LSF bearings and of structures isolated with them.

This Thesis also aims to provide useful insight into another aspect of the behaviour of rubber bearings, which is related to piezo-resistive behaviour of rubber. Natural rubber is a material that has insulating properties. However, the rubber commonly used in bearing construction is a filled rubber, reinforced with other materials (fillers), and it has been found to have good conductive properties (Busfield, Thomas and Yamaguchi, 2005). This is only the case when the volume fraction of the filler is above a certain value known as the "percolation threshold" (Stauffer, 1979). The piezo-resistive behaviour of rubber means that changes in strain in rubber lead to electrical resistivity changes. This feature of the coupled electrical-mechanical behaviour of rubber paves the way for the development of smart rubber devices, allowing to obtain indirect information on the stress/strain state of the bearings by monitoring the changes in electrical resistivity. This Thesis illustrates the results of an extensive experimental campaign, carried out at University of Strathclyde, to explore the feasibility of exploiting the piezo-resistive properties of various filled rubber compounds to develop smart rubber bearings.

1.1 Objectives

The principal objectives of the Thesis are:

- To characterise the mechanical behaviour of LSF rubber blocks and bearings under vertical loading and combined vertical and horizontal loading.
- To develop an advanced numerical modelling strategy for the analysis of LSF blocks and bearings and validate it against experimental tests.
- To evaluate the accuracy of various analytical formulations for describing the mechanical behaviour of blocks and bearings, using experimental and numerical results from advanced models.
- To investigate the dynamic behaviour and seismic performance of structures isolated with LSF bearings.
- To explore and characterise the piezoresistive behaviour of rubber pieces made with different compounds under various loading conditions.

To achieve the objectives outlined above, the following studies are undertaken:

- A review of the main features of the behaviour of rubber and rubber-based devices, and of constitutive and device models. State of the art of current analytical and experimental studies on the behaviour of LSF rubber blocks and bearings.
- Development of an advanced finite element (FE) modelling strategy for investigating numerically the behaviour of rubber blocks and bearings under compressive and shear loading and validation against experimental results.
- Improvement of existing analytical models to predict the behaviour of LSF blocks under compressive and shear loading, providing a better fit to available experimental and numerical results.
- Development of a simplified modelling strategy for describing the dynamic behaviour and seismic response of structural prototypes mounted on LSF bearings, validated against experimental shaking-table tests. Parametric study investigating the effect of the bearing shape factor on the dynamic and seismic response.
- Experimental investigation of the coupled mechanical-electrical behaviour of rubber pieces under different loading conditions and development of models for relating changes in resistivity to changes in strain.

In summary, the study provides a novel and original contribution towards 1) the characterisation of the complex behaviour of LSF bearings for seismic isolation applications and 2) the exploitation of the piezo-resistive behaviour of rubber for the development of smart bearings.

1.2 Outline

Figure 1.1 presents a graphical representation of the organization of the thesis, which is composed of eight chapters. This introductory chapter provides a general overview of the motivations and objectives of the research. Chapter 2 and 3 present the foundational knowledge necessary to comprehend the key characteristics of natural rubber material behaviour and the models available to describe them. In these chapters, the mathematical and numerical models for elastomeric bearings made of natural rubber are also examined. Chapter 4 and Chapter 5 investigate the coupled horizontal-vertical behaviour of LSF rubber blocks and bearings through an advanced FE modelling strategy. Chapter 6 describes simplified models for LSF bearings and structures isolated with LSF bearings. These models are then applied to investigate the influence of the bearing shape factor on the structural performance. Chapter 7 investigates the piezo-resistive properties of rubber pieces made with different filled natural rubber compounds, with the aim of paving the way to the development of smart rubber bearings with self-sensing capabilities. Chapter 8 discusses the conclusions of this Thesis.

1.3 List of Publications

The following is the full list of peer reviewed journal publications or papers under review that resulted and/or are related with the content of this thesis.

1 Orfeo A., Tubaldi, E., Muhr, A. Mechanical behaviour of rubber blocks. International Journal of Solid and Structures. 2023,112259,ISSN,0020-7683. https://doi.org/10.1016/j.ijsolstr.2023.112259. Chapter 4 is based on this article.

2 Orfeo A., Tubaldi E., Muhr, A., Losanno D. Mechanical behaviour of rubber bearings with low shape factor, Engineering Structures, 2022,114532,ISSN 0141-0296,https://doi.org/10.1016/j.engstruct.2022.114532. Chapter 5 is based on this article.

3 Orfeo A., Tubaldi E., Muhr, A., Losanno D. Dynamic behaviour and seismic response of structures isolated with low shape factor bearings. *Submitted for publication to Earthquake Engineering and Structural Dynamics. Currently under review.* Chapter 6 is based on this article.

4 Orfeo A, Tubaldi E, McAlorum J, Perry M, Ahmadi H, McDonald H. Self-Sensing Rubber for Bridge Bearing Monitoring. *Sensors*. 2023; 23(6):3150. https://doi.org/10.3390/s23063150. Chapter 7 is based on this article.

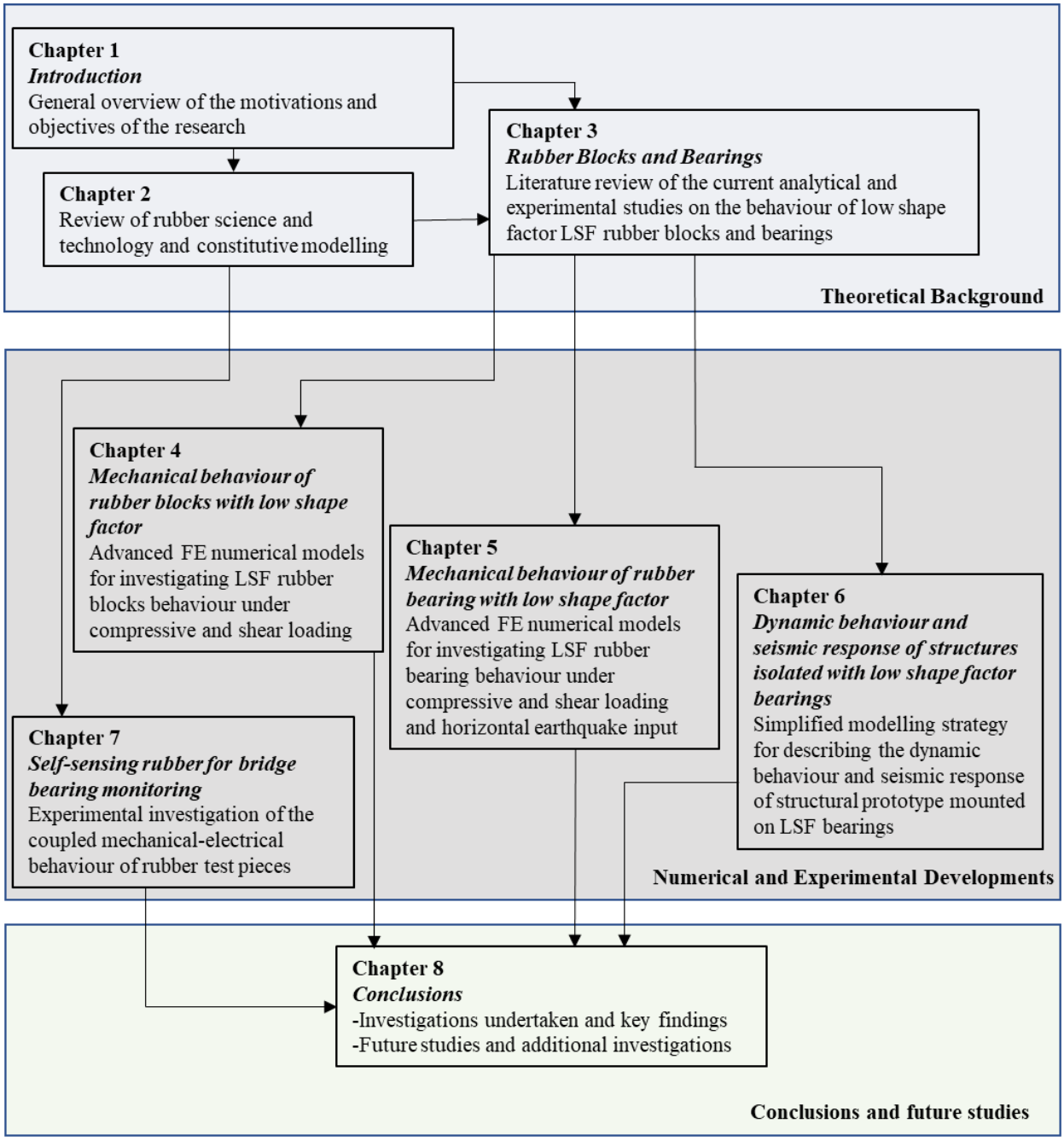

Figure 1.1 Organisation of thesis chapters

2 Review of rubber science and technology and constitutive modelling

Rubber, also known as an elastomer, is a type of amorphous polymer that has been found to be very versatile and more durable than other traditional construction materials such as steel and concrete when used in civil engineering applications (Derham and Thomas, 1980). To give rubber specific desired properties, various chemical ingredients are added during a process called compounding or formulation. These ingredients can include crosslinking agents, reinforcing fillers, and specialty additives. The choice of curatives and fillers is important for the performance of the rubber.

As an engineered product, rubber is subjected to deformations and the resulting stresses can be described by a mathematical relationship called the constitutive law. The next subsections describe typical rubber compounds and provide an overview of the main features of rubber-based devices for civil engineering applications, and the most important features of the mechanical behaviour of rubber and constitutive modelling.

2.1 Rubber compounding

Natural rubber is a flexible material composed of long chains of repeating units. These chains are flexible at room temperature and have the ability to return to their original shape after being deformed, particularly when chemically crosslinked.

The raw material used to make natural rubber is called latex, which is a liquid that is produced by various plants. Rubber compounding, also known as formulation, involves adding various chemicals to raw rubber to give it desired properties. Elastomers have molecules that are intertwined but can easily come apart under stress, resulting in a fluid-like behaviour. Vulcanization is the process of chemically bonding these molecules together to form a network, which transforms the material from a fluid-like state to a tough and elastic solid (Gent, 2012). This process increases the strength and modulus of the material while decreasing hysteresis.

Sulphur is the most commonly used agent for vulcanization, a process that strengthens rubber by creating crosslinks between the polymer chains. The mechanical properties of an elastomer are heavily influenced by the density of these crosslinks. As the density increases, the material becomes more rigid, with a higher modulus and hardness, but also more elastic, meaning it is less hysteretic. However, the tear and tensile strength of the elastomer may reach a peak at a certain level of crosslinking before decreasing. When a rubber-like material is exposed to an external force, a portion of the energy is absorbed by its molecular chains, which can enhance the material's ability to resist breaking apart. The

excess energy that is not stored in the chains during deformation is typically converted into heat through molecular movement, which makes it unavailable to cause breaks in the chains. At high levels of crosslinking, the movement of the chains is restricted, leading to a "tight" network that is unable to effectively dissipate energy. This can result in low elongation and brittle failure. Elastomers have an optimal range of crosslink density for practical use, where the level of crosslinking must be sufficient to prevent failure due to viscous flow, but not so high as to cause brittle failure. It's important to consider both the level and type of crosslinking. Figure 2.1 illustrates the formation of a crosslinked molecular network after the vulcanization process.:

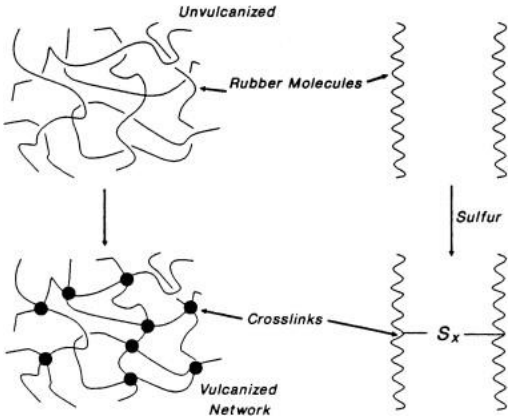

Figure 2.1 Network formation (Coran, 2005)

Incorporating particulate fillers, like carbon black and silica, into an amorphous rubber can enhance its strength. These fillers are especially effective at reinforcing rubber and can enhance the material's mechanical and physical properties. Figure 2.2 shows a diagram of the network structure in a carbon black filled elastomer.

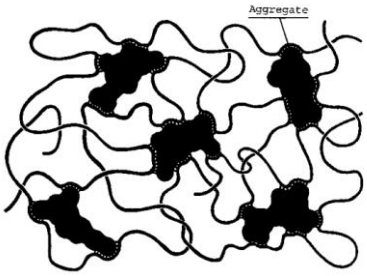

Figure 2.2 Physical network structure in a carbon black filled elastomers (Litvinov, et al., 1999)

The properties of fillers, specifically their structure and surface chemistry, have a significant impact on their ability to enhance the strength of rubber. The structure of a filler pertains to the irregularity in shape of its aggregates, which is formed by the degree of primary particles. Fillers that possess a high level of structure have a considerable void volume within their aggregates, which allows rubber molecules to become trapped, or occluded, within the spaces. The resulting combination of occluded

rubber and filler functions as a reinforcing agent, thereby raising the effective volume fraction of the filler. In general, the effectiveness of reinforcing a material is increased when the filler has a high degree of structure and a strong bond with the rubber. One common example is the use of carbon black, which is often grouped together in clusters, called agglomerates, before being mixed with rubber. For optimal reinforcement, it is crucial to reduce the size of carbon black agglomerates into smaller aggregates and evenly distribute them throughout the rubber. This can be achieved through mixing at high shear, which also facilitates chemical bonding between the rubber and carbon black. It is essential to guarantee that the rubber's viscosity is not too low, otherwise the shear forces could be insufficient in breaking apart the filler agglomerates, thereby reducing the reinforcing effect (Gent, 2012). In addition to increasing strength, carbon black can also improve the processability of the rubber by reducing its melt elasticity. This allows for shaping operations to be carried out with less shrinkage and distortion of the melt.

2.2 Elastic behaviour of rubber

Before the crosslinking process, rubber is a highly viscous and elastic liquid. Crosslinking transforms rubber into a soft and highly elastic solid. Isotropic materials that have similar properties in all directions can be identified using two basic elastic constants (Gent, 2012). The first, known as the modulus of bulk compression, or *K*, measures the material's resistance to compression under hydrostatic pressure and it is illustrated in Figure 2.3a.

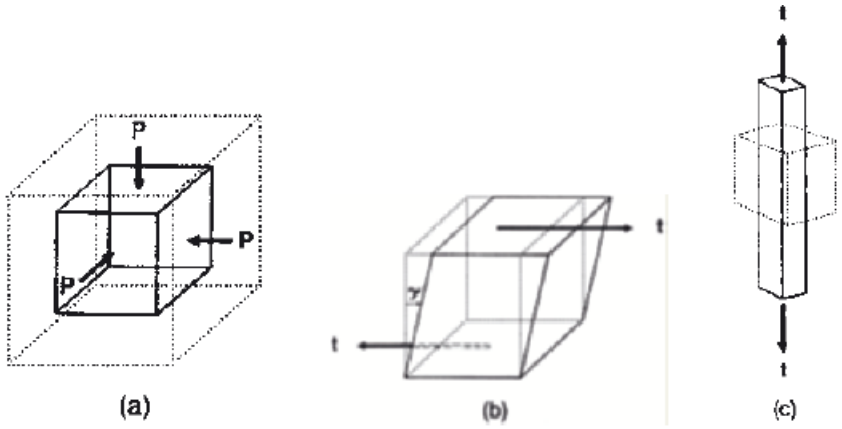

Figure 2.3 (a) bulk compression, (b) simple shear, (c) simple extension (Gent, 2012)

The modulus of bulk compression, *K*, is a measure of the elasticity of a material and describes the linear relationship between the applied pressure *P* and the change in volume $-\Delta V$ normalised by the original volume V_o of a block. This relationship can be represented by the Equation 2.1:

$$P = K\left(\frac{-\Delta V}{V_0}\right) \tag{2.1}$$

The second constant is the shear modulus *G*, and it is represented by the Equation 2.2:

$$G = \tau / \gamma \tag{2.2}$$

where τ is the shear stress and γ is the amount of shear deformation, defined for a block as the ratio of the horizontal displacement to the height of the block (see Figure 2.3b).

Another commonly used elastic constant is the Young's modulus, also known as tensile modulus, or *E*. It is defined by the relationship between the tensile stress σ and the corresponding fractional tensile elongation ε. It can be calculated using the following Equation:

$$E = \frac{\sigma}{\varepsilon} = \frac{9KG}{3K + G} \tag{2.3}$$

This elastic constant is useful for characterizing the material's response to tensile forces and is often used to predict the behaviour of a material under various loading conditions.

Poisson's ratio, represented by the symbol ν, is another widely used elastic constant. It can be mathematically expressed as (Gent, 2012):

$$\nu = \frac{(1/2)(3K - 2G)}{(3K + G)} \tag{2.4}$$

Rubbery solids typically have a high value of the bulk compression modulus, which is similar to that of simple liquids and is in the range of 1.5-2 GPa (Gent, 2012).. In contrast to their high bulk compression modulus, rubbery solids typically have a much lower shear modulus, denoted as *G*. This value is typically in the range of 0.5 to 3 MPa. This difference in the values of *G* and *K* results in a Poisson's ratio, ν, that is close to 0.5. Additionally, the tensile modulus of elasticity, *E*, for these materials is almost equal to 3*G*. This means that the ratio of Young's modulus to the shear modulus is 3, which is a distinct feature of these materials. When rubber is assumed to be incompressible in bulk, ν is equal to 0.5. This means that the rubber block bulges laterally, and the volume of the rubber remains nearly constant under compression. In this case, the elastic behaviour at small strain can be described by a single elastic constant, *G*. However, it is important to note that when the pressure is high, the volume of the rubber block can decrease significantly, and the assumption of incompressibility may not be valid anymore.

2.2.1 Statistical theory and Phenomenological theory

As discussed in section 2.2, network fibres are formed by a combination of two mechanisms: crosslinking and molecular entanglement. Entanglement refers to the network structure formed by the

crosslinking points within or between polymer chains, which restrict the movement of the chains and alter the nature of the polymer. The degree of crosslinking influences the elastic modulus of the material, with a higher degree of crosslinking resulting in a higher elastic modulus. The number of elastic elements (portions of molecules between crosslinks) plays a crucial role in determining the elastic modulus of a material. With an increase in the number of crosslinks, the number of elastic elements also increases proportionally. This relationship is illustrated in Figure 2.4, which shows a schematic representation of an elastomer at the molecular level, highlighting the crosslinks and entanglements between the polymer chains.

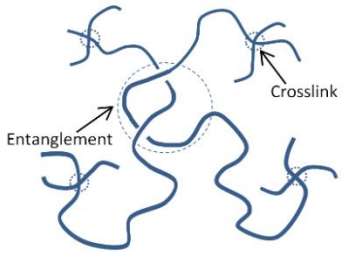

Figure 2.4 Sketch of a molecular entanglement

Natural rubber and synthetic elastomers are unique engineering materials that are capable of deforming to very large extents under relatively low stresses and returning to their original shape when the external stress is removed. This property is known as hyperelasticity. The study of the elasticity of rubber can be approached in two different ways: the statistical theory and the phenomenological theory. The statistical theory is based on the statistical behaviour of polymer chains, while the phenomenological theory is based on the macroscopic behaviour of the material as a whole. Both approaches are useful for understanding the behaviour of rubber and describing how it responds to various loading conditions.

The statistical theory of polymer chains is a theoretical framework that describes the statistical behaviour of polymer chains based on their molecular properties. It is based on the principles of statistical mechanics and provides a detailed understanding of the behaviour of polymers in various environments. The theory considers the polymer chain as a collection of interacting subunits and characterizes the properties of the chain through statistical analysis of these subunits. It provides a statistical description of the conformational changes of the polymer chain and the thermodynamics of these changes (Treloar, 1975). The entropy of each chain is dependent on the number of possible configurations. The elastic behaviour of this structure is predicted using statistical physics, which is a branch of physics that uses statistical methods to understand the behaviour of systems composed of many particles. The statistical theory of rubber elasticity, proposed by Treloar in 1949 (Treloar, 1949) and further developed in 1975, posits that the chain segments between crosslinks in rubber can be represented by Gaussian statistic chains. The three principal extension ratios (the ratios of stretched to

unstretched length) along three mutually perpendicular axes are represented by λ_1, λ_2 and λ_3. The change in entropy ΔS of the network under deformation λ_1, λ_2, λ_3 can be defined as (Treloar, 1975):

$$\Delta S = -\frac{1}{2} N_c k_B \left(\lambda_1^2 + \lambda_2^2 + \lambda_3^2 - 3\right) \tag{2.5}$$

where k_B is the Boltzmann constant and N_c is the number of network chains.

The strain energy per unit unstrained volume, denoted by W, is a measure of the amount of energy stored elastically in a unit volume of material under a specific state of strain represented by λ_1, λ_2, λ_3. This is given by

$$W = \frac{1}{2} G \left(\lambda_1^2 + \lambda_2^2 + \lambda_3^2 - 3\right) \tag{2.6}$$

with G defined as $G = N_C k_B T$, where T is the temperature.

The statistical theory of rubber elasticity is built on two fundamental physical parameters: the rubbery modulus, G, and a chain locking stretch (Treloar, 1975). The chain locking stretch is used to describe the degree of extension of the polymer chains within the network and how it affects the overall properties of the material. It is a measure of the degree of stretching of the chains before they reach a point where they can no longer be stretched any further. Some statistical models may also require additional parameters to fully characterize the behaviour of the material.

Phenomenological models of rubber deformation, on the other hand, aim to obtain expressions for the elastic strain energy of the material that are consistent with the principles of continuum mechanics, which is a branch of mechanics that deals with the behaviour of continuous, isotropic, incompressible, and hyperelastic solids. These models are based on the macroscopic behaviour of the material and do not consider the behaviour of individual polymer chains at the molecular level.

The strain energy density W is also expressed as a function of the three strain invariants I_1, I_2 and I_3:

$$W = W\left(I_1, I_2, I_3\right) \tag{2.7}$$

Rivlin (1971) proposed a model for predicting the stress-strain behaviour of rubber-like solids. The model is based on the assumption that the rubber-like solid's behaviour is isotropic, meaning that the material properties are the same in all directions, and incompressible in bulk, meaning that the material's volume remains constant under a change in pressure. He used symmetry considerations to identify three strain invariants that could be used as measures of strain. These invariants are defined as follows:

$$I_1 = \lambda_1^2 + \lambda_2^2 + \lambda_3^2$$
$$I_2 = \lambda_1^2\lambda_2^2 + \lambda_2^2\lambda_3^2 + \lambda_3^2\lambda_1^2 \quad 2.8$$
$$I_3 = \lambda_1^2\lambda_2^2\lambda_3^2$$

Equation 2.6 can also be written in the form (Treolar, 1949,1975)

$$W = C_{10}\left(I_1 - 3\right) \quad 2.9$$

where C_{10} is a material constant equal to half the shear modulus G.

Equation 2.9, known as the neo-Hookean material model, is a simple extension of Hooke's law to describe the behaviour of hyperelastic materials. Several alternative theories have been developed to describe hyperelastic materials under large deformations (Rivlin, 1948; Mooney, 1940; Ogden, 1976; Yeoh 1993; Arruda and Boyce, 1993; Treloar, 1949). These theories are based on strain energy density functions and can be used to analyse and design elastomer products that are subjected to highly deformed states. In general, these constitutive Equations can be broadly categorized into two groups. The first group includes the polynomial material models, which are a mathematical function that describes the material's response to strain based on the principal strain invariants. If the material is incompressible, the model is typically referred to as a Rivlin material model. Mooney (1940) developed Equation 2.10 to provide a more accurate representation of the behaviour of unfilled rubber in uniaxial tension. The amount of energy stored in a material due to deformation can be described by a polynomial function that depends on the first and second principal strain invariants:

$$W = C_{10}\left(I_1 - 3\right) + C_{01}\left(I_2 - 3\right) \quad 2.10$$

where C_{10} and C_{01} are material constant that can be determined experimentally. Rivlin (1948) built upon Mooney's work by showing that the most general strain energy function for a homogeneous, isotropic, incompressible, and elastic material can be represented as a Taylor series expansion. This means that the strain energy density function can include an infinite number of higher-order terms, allowing for a more accurate prediction of the material's behaviour under various loading conditions. This approach is particularly useful for modelling rubber-like materials, as they exhibit nonlinear behaviour and can be described by a series of polynomials of the principal strains. The Taylor series expansion allows for a more accurate representation of the material's behaviour by taking into account the higher-order terms that are not captured by first-order models. The strain energy function can be written as:

$$W = \sum_{i+j=1}^{n} C_{ij}\left(I_i - 3\right)^i \left(I_2 - 3\right)^j \quad 2.11$$

where C_{ij} are material constants.

The second category of constitutive laws for hyperelastic materials describes the strain energy density as a function of the three principal stretches. An example of this type of model is the Ogden material model, which was developed by Ogden (1976). It is expressed as:

$$W = \sum_{p=1}^{n} \frac{\mu_p}{\alpha_p} \left(\lambda_1^{\alpha_p} + \lambda_2^{\alpha_p} + \lambda_3^{\alpha_p} - 3 \right) \qquad 2.12$$

where μ_p and α_p are material constants.

One method of modelling the response of hyperelastic materials is to define the strain energy density, W, as a function of I_1 only. This approach has been found to be robust and can be used to accurately fit comprehensive stress-strain data with only a minimal loss of precision (Gregory, 1979; Gough et al.; 1999,Yeoh and Fleming, 1997). Yeoh (1990) adopted this approach and proposed a cubic form of Equation 2.11, as follows:

$$W = C_{10} \left(I_1 - 3 \right) + C_{20} \left(I_1 - 3 \right)^2 + C_{30} \left(I_1 - 3 \right)^3 \qquad 2.13$$

The parameters, C_{10}, C_{20} and C_{30} are material constants to be determined from experiment. The values of these parameters are used to describe the behaviour of the material. It is commonly observed that C_{10} and C_{30} are positive and C_{20} is negative. This is because C_{20} represents the effect of change in volume, which is negative for most rubber-like materials.

The material constants for the Rivlin, Ogden, or Yeoh material models can be determined by conducting stress-strain measurements in various modes of deformation. These include stretching a specimen along one axis, applying shear stress to the specimen without any change in its length, and applying equi-biaxial extension to the specimen. Additionally, other techniques such as applying simple shear stress to bonded blocks, or applying a combination of extension, inflation, and torsion to a tubular specimen have also been used for this purpose.

The material constants can be determined from the stress-strain data by using regression analysis. This involves fitting a curve to the data using a mathematical model that describes the behaviour of the material. The material constants are then obtained as the parameters of the curve that best fit the data. It is important to note that these constants are specific to the particular material being studied and may vary depending on the type of rubber, the degree of crosslinking, and other factors.

2.2.2 General expression for stress-strain relationship in tension compression and simple shear

The effectiveness of a specific W-form can be evaluated by comparing its predictions of a material's stress-strain behaviour under specific deformation conditions to experimental measurements. Rivlin

(1948) demonstrated that for an incompressible material, the principal stresses can be calculated using the strain invariants I_1 and I_2 as given by the following Equation:

$$\sigma_i = 2\left(\lambda_i^2 \frac{\partial W}{\partial I_1} - \frac{1}{\lambda_i^2}\frac{\partial W}{\partial I_2}\right) + p \tag{2.14}$$

where p is an arbitrary hydrostatic pressure, σ_i is the true (or Cauchy) stress (Treloar 1975).

Imagine a rubber sheet with its major surface perpendicular to the z-axis and not subjected to any force. According to Equation 2.14, it can be inferred that:

$$\sigma_1 - \sigma_3 = \left[2\left(\lambda_1^2 \frac{\partial W}{\partial I_1} - \frac{1}{\lambda_1^2}\frac{\partial W}{\partial I_2}\right) + p\right] - \left[2\left(\lambda_3^2 \frac{\partial W}{\partial I_1} - \frac{1}{\lambda_3^2}\frac{\partial W}{\partial I_2}\right) + p\right] \tag{2.15}$$

In order to satisfy the condition of incompressibility, which requires that the third principal stress, σ_3, be equal to zero, the third principal stretch, λ_3, must be equal to $1/(\lambda_1\lambda_2)$. With this condition, the stresses in the sheet can be determined as follows:

$$\begin{aligned}\sigma_1 &= 2\left(\lambda_1^2 - \frac{1}{\lambda_1^2\lambda_2^2}\right)\left(\frac{\partial W}{\partial I_1} + \lambda_2^2\frac{\partial W}{\partial I_2}\right)\\ \sigma_3 &= 2\left(\lambda_2^2 - \frac{1}{\lambda_1^2\lambda_2^2}\right)\left(\frac{\partial W}{\partial I_1} + \lambda_1^2\frac{\partial W}{\partial I_2}\right)\end{aligned} \tag{2.16}$$

For uniaxial tension and compression, the second and third principal stretches are equal to $1/\sqrt{\lambda_1}$, and the second and third principal stresses are equal to zero. Substituting these values into Equation 2.16 gives:

$$\sigma_T = 2\left(\lambda^2 - \lambda^{-1}\right)\left(\frac{\partial W}{\partial I_1} + \frac{1}{\lambda}\frac{\partial W}{\partial I_2}\right) \tag{2.17}$$

Where σ_T is the true stress in tension or compression. The nominal stress is given by:

$$f = \frac{\sigma_T}{\lambda} \tag{2.18}$$

and hence:

$$f = 2\left(\lambda - \lambda^{-2}\right)\left(\frac{\partial W}{\partial I_1} + \frac{1}{\lambda}\frac{\partial W}{\partial I_2}\right) \tag{2.19}$$

Simple shear is a type of deformation that is characterized by a homogeneous displacement of points in a body, parallel to a given direction, in proportion to the distance of each point from a fixed plane that is also parallel to that direction. It is not considered as pure deformation.

As an example, take a cube-shaped material that has its edges aligned with the *x*, *y*, and *z* coordinate axes (Figure 2.5). The displacement of each point within the cube, parallel to the x-direction, can be represented by an Equation that is proportional to the distance of each point from the *xz*-plane. The displacement of each point in the body can be described by the following mathematical Equations.:

$$\xi = \gamma y \quad \eta = \zeta = 0 \tag{2.20}$$

where γ is the amount of shear and ξ, η and ζ are the displacement components in the *x*, *y* and *z* direction, respectively. Figure 2.5 illustrates the stress components due to the simple shear deformation.

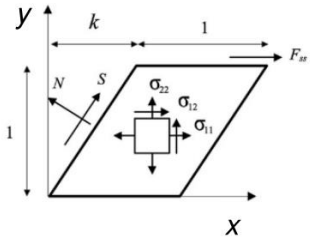

Figure 2.5 Simple shear deformation

The simple shear described by Equation 2.20 is associated with stress components given by:

$$\begin{aligned}
\sigma_{11} &= 2\gamma^2 \frac{\partial W}{\partial I_1} - p' \\
\sigma_{22} &= -2\gamma^2 \frac{\partial W}{\partial I_2} - p' \\
\sigma_{33} &= -p' \\
\tau_{13} &= \tau_{23} = 0 \\
\tau_{12} &= 2\gamma \left(\frac{\partial W}{\partial I_1} + \frac{\partial W}{\partial I_2} \right) \\
-p' &= -p + 2\left(\frac{\partial W}{\partial I_1} + \frac{\partial W}{\partial I_2} \right)
\end{aligned} \tag{2.21}$$

In Equations 2.21, $\partial W / \partial I_1$ and $\partial W / \partial I_2$ are functions of I_1 and I_2, where:

$$I_1 = I_2 = 3 + \gamma^2 \tag{2.22}$$

The stress components in a material subjected to simple shear are indeterminate to the extent of an arbitrary hydrostatic pressure, *p*'. In order to determine this pressure, one of the normal stress components must be specified. One approach is to assume that the third normal stress, σ_3, is equal to zero (which means that no forces are applied to the faces of the cube normal to the z-axis). With this assumption, the hydrostatic pressure is equal to zero, and the stress components can be determined as follows:

$$\begin{aligned}
\sigma_{11} &= 2\gamma^2 \frac{\partial W}{\partial I_1} \\
\sigma_{22} &= -2\gamma^2 \frac{\partial W}{\partial I_2} \\
\sigma_{33} &= 0 \\
\tau_{13} &= \tau_{23} = 0 \\
\tau_{12} &= 2\gamma \left(\frac{\partial W}{\partial I_1} + \frac{\partial W}{\partial I_2} \right)
\end{aligned} \qquad 2.23$$

Another approach to determining the hydrostatic pressure in a material subjected to simple shear is to assume that the normal component of the traction on the inclined face is equal to zero, $N = 0$ (Gent et al. 2007 and Horgan and Murphy, 2010). Under this assumption, the hydrostatic pressure can be defined as:

$$p = -\frac{2\gamma^2}{1+\gamma^2}\left(3+\gamma^2\right)\left(\frac{\partial W}{\partial I_1} + \frac{\partial W}{\partial I_2} \right) \qquad 2.24$$

Thus, substituting Equation 2.24 into Equation 2.21:

$$\begin{aligned}
\sigma_{11} &= 2\gamma^2 \frac{\partial W}{\partial I_1} + \left(2 + \frac{2\gamma^2}{1+\gamma^2}\left(3+\gamma^2\right) \right)\left(\frac{\partial W}{\partial I_1} + \frac{\partial W}{\partial I_2} \right) \\
\sigma_{22} &= -2\gamma^2 \frac{\partial W}{\partial I_2} + \left(2 + \frac{2\gamma^2}{1+\gamma^2}\left(3+\gamma^2\right) \right)\left(\frac{\partial W}{\partial I_1} + \frac{\partial W}{\partial I_2} \right) \\
\sigma_{33} &= \left(2 + \frac{2\gamma^2}{1+\gamma^2}\left(3+\gamma^2\right) \right)\left(\frac{\partial W}{\partial I_1} + \frac{\partial W}{\partial I_2} \right) \\
\tau_{13} &= \tau_{23} = 0 \\
\tau_{12} &= 2\gamma \left(\frac{\partial W}{\partial I_1} + \frac{\partial W}{\partial I_2} \right) \\
-p' &= \left(2 + \frac{2\gamma^2}{1+\gamma^2}\left(3+\gamma^2\right) \right)\left(\frac{\partial W}{\partial I_1} + \frac{\partial W}{\partial I_2} \right)
\end{aligned} \qquad 2.25$$

The relation between principal stretches and amount of shear, considering a plate strain state, i.e. $\lambda_2 = 1$, may be given by Ogden (1976):

$$\lambda_1 - \lambda_1^{-1} = \gamma;\ \lambda_1 = \sqrt{1 + \frac{\gamma^2}{2} + \gamma\sqrt{1+\frac{\gamma^2}{4}}};\ \lambda_3 = \sqrt{1 + \frac{\gamma^2}{2} - \gamma\sqrt{1+\frac{\gamma^2}{4}}} \qquad 2.26$$

2.3 Inelastic Behaviour of rubber

Rubber exhibits hysteresis, meaning that it behaves differently during the loading and unloading phases of a stress cycle. When a rubber material is subjected to a stress cycle (meaning it is subjected to alternating stress and then relieved of that stress), its stress-strain curve takes the form of a hysteresis loop instead of a reversible curve. This is because energy is dissipated during the stretching and relaxing of the rubber. As a result, the rubber appears to be softer when it is unloaded compared to when it is loaded. The energy loss or hysteresis that occurs during the stress cycle of a rubber material can be calculated as the area enclosed within the force-deformation plot. Research by Harwood and Schallamach (1967) found that the amount of energy lost during this process is related to the energy input, with a larger proportion of energy being lost in filled rubber compared to unfilled rubber. The reason for this has been explained as the disintegration of the arrangement of carbon black particles in rubber that has been reinforced, which aids in the distribution of energy and thus results in a higher energy dissipation during the process of being stressed (Payne, 1962). For the first stress cycle, the hysteresis is typically large. However, as the rubber undergoes more stress cycles, the hysteresis tends to decrease and the stress-strain curve becomes more stable. This phenomenon is known as "stress softening". Figure 2.6 shows the behaviour of a high-damping natural rubber specimen under cyclic simple shear input. It can be noted that the stress-softening characterizing the shear response under repeated cycling is significant and that after certain number of cycles the stress-softening is stabilized.

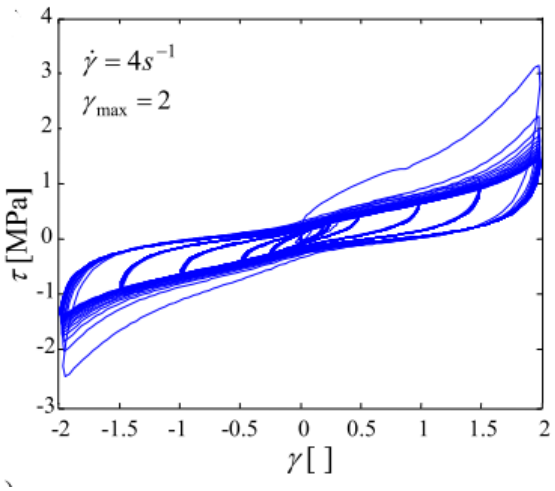

Figure 2.6 Uniaxial shear tests results for a high damping natural rubber test piece (Ragni et al., 2018)

The next subsections discuss various features of the mechanical behaviour of rubber that cannot be explained using hyperelastic models.

2.3.1 Mullins' effect/stress-softening

The Mullins' effect Mullins (1948) refers to the stress-softening phenomenon in which rubber becomes progressively softer with each loading cycle. When a sample of virgin rubber is subjected to repeated strains, it will soften, particularly after the first cycle. The Mullins' effect is observed for strains that are smaller than the maximum strain that the rubber has previously experienced. Eventually, a steady-state is reached after a certain number of cycles, at which point the softening effect of subsequent cycles is negligible. The Mullins effect is a recoverable phenomenon, as discussed e.g. in Tubaldi et al. (2017) and Ragni et al. (2018). It has been demonstrated experimentally that rubber can regain some of its original stress-strain characteristics over time (Kingston and Muhr, 2011; Kulak et al., 1998; Constantinou et al., 1998; Thompson et al., 2000). This recovery process tends to be quick at the beginning but slows down over time. Factor such as the type of elastomeric material, the manufacturing method and the temperature can affect the recovery rate. For seismic reliability evaluation of structures isolated with rubber bearings it is crucial to consider the recovery of the rubber properties as an earthquake can occur after a long period of inactivity and the bearings could have fully regained their original state at the time of the event. Kikuchi and Aiken, (1997), Grant et al., (2004), and Kikuchi et al. (2010) proposed a model to incorporate the stress-softening of rubber during cycling loadings. Tubaldi et al. (2017) carried out an extensive experimental campaign on High Damping Natural Rubber (HDNR) double shear specimens and validated a model that can be used to evaluate the influence of stress softening on the seismic response of isolated structures under design condition. This model was extended by Ragni et al. (2018) to describe the behaviour of laminated bearings under biaxial loading.

2.3.2 Payne effect

In addition to the Mullins' effect, another interesting phenomenon that characterises the behaviour of filled rubber is the Payne effect, which describes the dependency of the rubber stiffness on the strain amplitude, as also evident in Figure 2.6. The Payne effect was studied by Fletcher and Gent (1954) and Payne (1962), who looked at how the dynamic modulus (the proportion of stress to strain in the material) of various natural rubber compounds with fillers changed when they were subjected to a sinusoidal deformation (Figure 2.7). The primary characteristics of the "Payne effect" are:

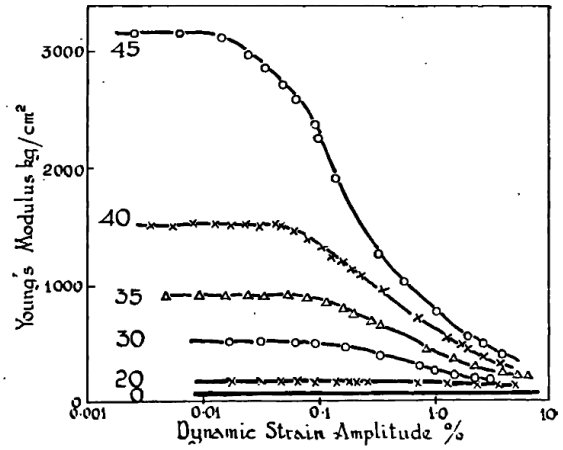

Figure 2.7 Relationship between Young's modulus and strain amplitude for natural rubber vulcanizates containing different amounts of carbon black (Payne, 1962) (Gough, 200)

1. At extremely small strain amplitudes (below 0.01%), the modulus is not influenced by the strain amplitude but is strongly influenced by the amount of filler present. The Payne effect is therefore more pronounced in filled rubber than in unfilled rubber.
2. The dynamic modulus of a filled rubber compound decreases as the strain amplitude increases beyond 0.1%. This reduction is most pronounced in rubber compounds with a high filler content and is not present in unfilled rubber. This shows that the ability of the filler to make the rubber stiffer is greatly reduced when the rubber subjected to large strains.
3. The flexibility of rubber that contains filler decreases as the temperature increases, in contrast to unfilled rubber, which becomes more flexible when the temperature increases according to statistical theory (as described in Equation 2.6). Furthermore, the use of filler material amplifies the increase in modulus as the rate of deformation increases.
4. The following deformations typically result in a lower dynamic modulus compared to the first deformation. In fact, if the rubber is allowed to relax for a period of time, the Payne effect may dissipate, causing the dynamic modulus to return to its original value.

2.3.3 Strain-Crystallization

Some elastomers can undergo a phase change from a rubbery, amorphous state to a crystalline state when subjected to large strains. This process, called crystallization, results in a significant increase in stress for a small increase in strain. When the strain is reduced, the elastomer reverts to its original, flexible state. This phenomenon has been observed and described by Rivlin and Thomas (1953), Lake and Lindley (1965), and Choi and Roland (1997). Figure 2.8 shows the crystalline molecular structure of natural rubber before and after deformation. Short chains are represented by thick lines whereas filled circles represent crosslinks. When crystallization stiffening begins, the rubber stiffens because of reorientation of its molecular structure.

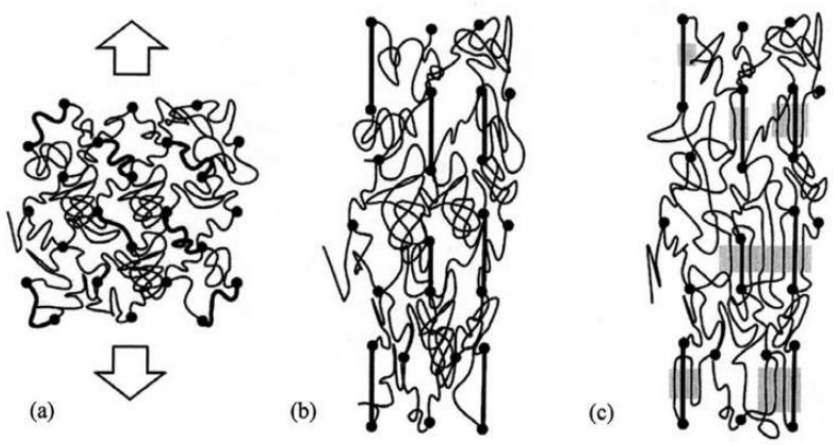

Figure 2.8 Molecular structure of natural rubber (a) before deformation, (b) after deformation before crystallization (c) fully stretched chains acting as crystallites (shaded part) (Tosaka et al., 2004)

Fillers, such as carbon black, can inhibit crystallization as they act as a physical barrier to the alignment of polymer chains, whereas large filler particles, such as clay and talc, can promote strain crystallization by creating more defects and more nucleation sites by hindering the alignment of polymer chains (Candau et al., 2014). Mistry and Govindjee (2014) and Loos et al. (2021) developed phenomenological continuum models to describe the macroscopic behaviour of strain crystallizing natural rubber.

2.3.4 Time-dependent behaviour

2.3.4.1 Stress relaxation and creep

Stress relaxation is a process that occurs in vulcanized rubber when it is subjected to constant strain and the stress level gradually decreases. On the other hand, creep occurs when a rubber testpiece is subjected to a constant stress and its length gradually changes. Gent (1962a) developed an Equation to describe the relationship between these two processes and found that, in the case of unfilled natural rubber, the rates of stress relaxation and creep are similar, taking into account the effect of non-linear geometry (such as the change in shape of a test piece when it is stretched along one axis). He also found that the degree of stress relaxation is generally proportional to the logarithm of time, with a typical increase of 2% for every thousand-fold increase in time, with the exception of very long intervals when chemical processes start to dominate over physical ones. It is important to note that, according to Gent (1962a), the rate at which the stress in the material decreases is not affected by how much the material has been stretched up to strains of around 200%.

In general, the rates of stress relaxation and creep in filled natural rubber are higher than those of unfilled vulcanized rubber. Gent (1962b) found that the rates of stress relaxation and creep in a natural rubber compound containing 54 parts carbon black were generally between 5-10% per tenfold increase in time due to "Strain amplification" (Mullins and Tobin, 1965). Strain amplification refers to the phenomenon

where the internal strains within the rubber molecules are higher than the macroscopic strain, due to the inability of the filler material to stretch (Gough, 2000). As a result, at very high levels of strain, the rate of stress relaxation is expected to be similar to that observed in unfilled rubber.

Both static and cyclic stress relaxation and creep involve applying and removing a load or deformation to a test piece. In static stress relaxation and creep, the test piece undergoes one loading and unloading cycle, while in cyclic stress relaxation and creep, the test piece undergoes multiple cycles of loading and unloading. Derham and Thomas (1977) found that the amount of creep in a material is linearly related to the logarithm of the number of loading and unloading cycles, in a similar way to how the amount of static creep is linearly related to the logarithm of the time. However, according to Hillmer and Scheele (1970), cyclic tests typically result in greater creep than static tests. Their study on unfilled rubbers under low strain loading and unloading cycles found that cyclic creep rates were lower than static rates. Similarly, McKenna and Zapas (1983) found that cyclic stress relaxation rates for a filled polybutadiene had a less pronounced effect compared to the results observed Derham and Thomas (1977).

2.3.4.2 Viscoelastic behaviour of rubbers

The theory of viscoelasticity is important in understanding materials like filled rubber, which exhibit time-dependent stress-strain behaviour. The loading and unloading curves differ due to the loss of mechanical energy that occurs during internal processes, such as the flow of a viscous substance or the breaking of bonds within the material due to stress. Elastomers are materials that have the ability to return to their original shape after being deformed. They exhibit some level of viscous behaviour, meaning they are able to flow or deform under stress. It is expected that linear viscoelastic behaviour can be described by a constitutive Equation that combines elastic behaviour, i.e, stress is directly proportional to strain, and viscous behaviour, i.e. stress is proportional to rate at which strain changes over time. One example of such an Equation is the one of the Kelvin model (spring and damper arranged in parallel) also illustrated in Figure 2.9:

$$\sigma = E\varepsilon + \eta_e\left(\frac{d\varepsilon}{dt}\right) \qquad 2.27$$

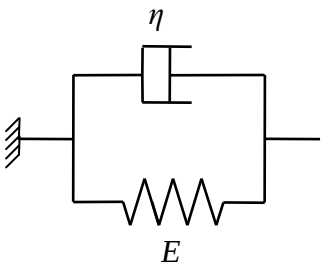

Figure 2.9 Kelvin model

where σ is tensile stress, ε is tensile strain, E is the elastic tensile modulus and η_e is the Newtonian viscosity coefficient in tension. This Equation relates the stress experienced by a material to its strain and the rate of change of strain with time.

However, the viscoelastic response of a rubber material can be described as a combination of spring and damper elements arranged in various ways. One such model is the Maxwell model, which consists of a spring and a dashpot connected in series (Figure 2.10).

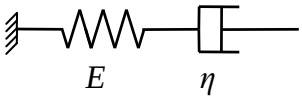

Figure 2.10 Maxwell model

The constitutive Equation of the Maxwell model is:

$$\frac{d\varepsilon}{dt} = \frac{1}{E}\frac{d\sigma}{dt} + \frac{\sigma}{\eta_e} \qquad 2.28$$

The generalised Maxwell model (Figure 2.11) is a general approach that can be used to analyse linear viscoelastic behaviour. It is defined by the distribution of elastic moduli $E(\tau)$ in relation to the relaxation time $\tau_r = \eta/E$ of multiple Maxwell elements that are connected in parallel.

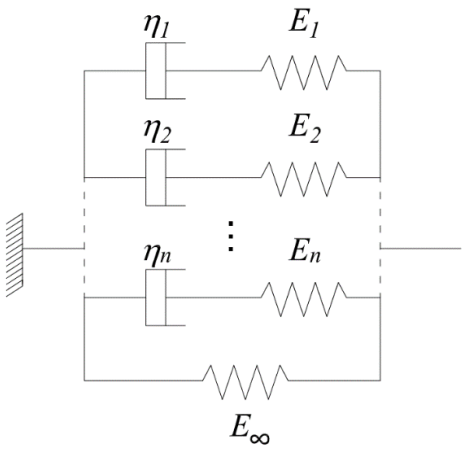

Figure 2.11 Generalised Maxwell model

Linear viscoelasticity refers to the behaviour of materials that follows the linear superposition principle. This principle states that the deformation caused by multiple forces is equivalent to the sum of the individual deformations caused by each force. This principle holds true for small deformations and is identified by a relaxation rate that is directly proportional to the current stress. Linear viscoelastic materials follow the Boltzmann superposition principle, which asserts that the deformation caused by multiple forces is equivalent to the sum of the individual deformations caused by each force. This behaviour is characterized by a relaxation rate that is proportional to the current stress.

Linear viscoelastic behaviour in simple shear is described by the following Equation 2.29 (Ferry, 1970) which states that the shear stress τ at time *t* is proportional to the integral of the relaxation modulus *G(t-t')* multiplied by the shear strain rate $\dot{\gamma}$ over all past times:

$$\tau(t) = \int_{-\infty}^{t} G(t-t')\dot{\gamma}(t')dt' \qquad 2.29$$

This theory is generally considered to be a good approximation for unfilled rubber materials that experience moderate deformations and exhibit linear stress-strain behaviour under simple shear conditions.

When a material experiences large strain, it may exhibit non-linear viscoelastic behaviour, which can be difficult to model accurately. To simulate this behaviour in computer simulations, modified versions of the Mooney-Rivlin, Ogden, and other polynomial strain energy functions may be used in non-linear finite element analysis codes. These modified versions of the models take into account the non-linear nature of the material's response to strain and can be used to simulate the behaviour of materials like rubber that exhibit non-linear viscoelasticity. The time-dependent behaviour of elastic materials, such as rubber, can be described using a model proposed by Bergström and Boyce (1999). According to this

model, the mechanical response of rubber to applied loads is a result of two different networks within the material's molecular structure as shown in Figure 2.12.

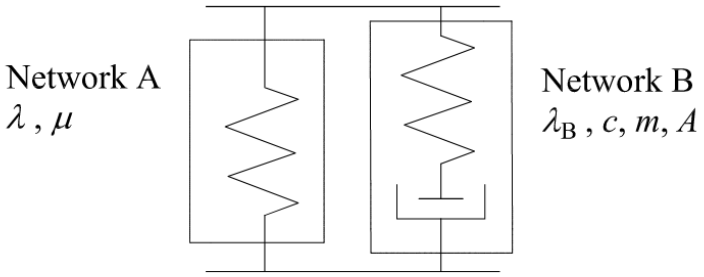

Figure 2.12 Bergstrom Boyce model

The first network (A), referred to as the equilibrium network, describes the time-independent behaviour of rubber. The second network, called B, is accountable for the non-linear and rate-dependent aspect of the mechanical response. The equilibrium network's mechanical behaviour is described by the use of hyperelastic models, while the Equation below represents the strain rate in network B:

$$\dot{\varepsilon}_B = A_B\left[\lambda_B - 1\right]^c \left(\sigma_B\right)^m \qquad 2.30$$

where $\dot{\varepsilon}_B$ is the effective creep strain rate, A_B is a material constant, (λ_B-*1)* is the nominal creep strain, σ_B is the effective stress, *m* is a positive value greater than 1 representing the effective stress dependence of the effective creep strain rate and *c* is a value between -1 and 0 that represents the dependency of creep strain to effective creep strain rate (Ghoreishy et al., 2014). Additionally, a scaling factor *SF* is needed to express the proportion of stress borne by network B compared to the stress carried by network A under immediate loading conditions.

Other constitutive models have been developed over the years to describe the nonlinear viscoelastic effects that the filled rubbers exhibits at different amplitudes. These are described in a recent work by Carleo et al. (2018), where it is discussed that none of these models have a full predictive ability.

2.3.5 Dynamic behaviour

Rubber is frequently utilized in applications that require the reduction of vibrations, so it is important to understand how it behaves when subjected to cyclic deformations. For instance, when a rubber sample is subjected to a sinusoidal shear stress, the resulting shear strain will also be sinusoidal but will be shifted in phase by a constant angle known as, δ. The tangent of δ, $tan\delta$, is a measure of the material's energy loss, hysteresis, or damping. As an example, Dhir et al. (2022) investigated the behaviour of high damping natural rubber under simple shear using quadruple shear tests, showing that the energy dissipated, which is the area enclosed in the shear stress-strain hysteresis loop, can be represented by

an equivalent ellipse, and thus by a viscoelastic model. Figure 2.13 shows the nominal shear stress-strain response of a quadruple specimen subjected to a sinusoidal displacement input.

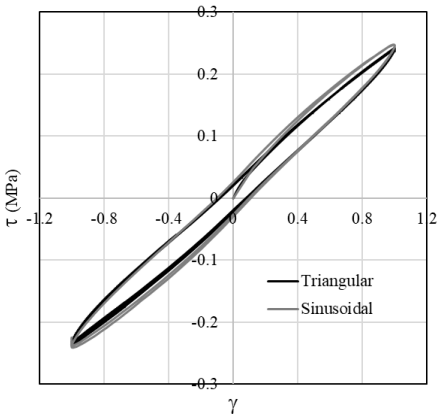

Figure 2.13 Shear response of rubber quadruplet specimen subjected to sinusoidal displacement input (Dhir et al. 2022)

In the case of linear stress-strain behaviour, a sinusoidal strain with amplitude γ_0 and angular frequency ω:

$$\gamma = \gamma_0 \sin(\omega t) \tag{2.31}$$

induces a stress τ which can be described by the following function of time *t*:

$$\tau(t) = \gamma_0 \left(G' \sin \omega t + G'' \cos \omega t\right) \tag{2.32}$$

where *G*' is the storage modulus, and *G*" is the loss modulus. The former is a measure of the elastic behaviour of a material and it is defined as the ratio of the in-phase stress to strain (the stress that is in phase with the strain). The loss modulus is a measure of the energy dissipated by a material due to hysteresis. It is defined as the ratio of the out-of-phase stress to strain (the stress that is out of phase with the strain). Equation 2.32 can also be represented in complex number notation as (Gough, 2000):

$$\tau(t) = \mathrm{Re}\left\{\gamma_0 \left(G' + iG''\right) e^{i\omega t}\right\} \tag{2.33}$$

With the complex modulus, *G**, defines as:

$$G^* = G' + iG'' \tag{2.34}$$

The stress represented by Equation 2.32 varies out of phase and sinusoidally with the strain and it can also be expressed as:

$$\tau(t) = \tau_0 \sin(\omega t + \delta) \tag{2.35}$$

where τ_0 is the stress amplitude and δ the phase angle. Equation 2.35 can also be expressed as follows:

$$\tau(t) = \tau_0 \left(\sin \omega t \cos \delta + \cos \omega t \sin \delta\right) \tag{2.36}$$

Comparison of Equations 2.32 and 2.36 gives:

$$G' = \frac{\tau_0}{\gamma_0}\cos\delta$$
$$G'' = \frac{\tau_0}{\gamma_0}\sin\delta \qquad 2.37$$

And

$$\frac{G''}{G'} = \tan\delta \qquad 2.38$$

The theory of linear viscoelasticity allows for the derivation of relationships between various properties of a rubber material, such as the relaxation modulus, creep compliance, loss modulus, and storage modulus (Ferry, 1970; Tschoegl, 1989). These material properties vary with the frequency and amplitude of the vibration to which the material is exposed. Fletcher and Gent (1954) carried out research on the impact of frequency on the modulus of filled rubbers within a narrow frequency range. Warnaka (1963) studied the effect of frequency on the modulus of a filled polystyrene-butadiene over a frequency range of 50 to 150 Hz and found that the frequency had little impact on the modulus. Payne and Whittaker (1970) also conducted a study on a filled polybutadiene and found similar results. However, (Mullins, 1948) found that dynamic modulus increases as the frequency increases, particularly at low temperatures. Ahmadi and Muhr (1992) conducted more extensive measurements of the frequency dependence of the dynamic shear modulus of various rubber materials over a range of frequencies from 5 to 400 Hz. They found that the dynamic shear modulus of low damping rubbers, like unfilled natural rubber, increased slightly with frequency. Adding filler materials, such as carbon black, to rubber materials can significantly increase the shear modulus, but does not significantly affect its frequency dependence. These results suggest that the frequency dependence of the shear modulus may depend on the specific properties of the rubber material.

It is well-established that rubber materials reinforced with fillers exhibit some non-linear properties, which result in hysteresis loops that are not perfect ellipses and have a significant dependence on amplitude (Fletcher and Gent, 1954).

Despite these non-linearities, linear viscoelasticity models are still commonly used. The belief is that using linear theory, with properly selected parameters, can provide an accurate prediction of the performance of an elastomeric vibration isolator under steady-state conditions. Thus, for a given frequency and amplitude, an elastomeric isolator can be characterized using a Kelvin mode calibrated through the equivalent linearized viscoelastic frequency-domain parameters G' and G'' (or G^* and δ) (Ahmadi and Muhr, 1997; Muhr, 2009).

Progress has been made on developing rate independent non-linear models to describe shear stress-strain behaviour of rubber containing reinforcing filler. Ahmadi and Muhr (1997) developed a model that captures the stiffening effect observed at high strains through two adjustable parameters, enhancing the accuracy of hysteresis loop fitting. However, this model does not account for the impact of rate or Mullins effect. Advanced models combining rate-independent and rate-dependent components can be used to provide a comprehensive description of the behaviour of laminated HDNR, including the stress softening that occurs during cyclic loading (Kikuchi and Aiken, 1997; Grant et al. 2004; Kikuchi et al, 2010). An extensive review of these models has been made in Tubaldi et al. (2017).

2.4 Piezoresistivity

Elastomers, or rubber-like materials, are typically poor electrical conductors. However, when they are filled with a conductive material such as carbon black, they form a composite that has properties that are intermediate between those of the matrix and the filler. The extent of the conductivity depends on various factors, including the amount, shape, and size of the filler, as well as the dispersion of the filler within the matrix. In general, an increase in the surface area to volume ratio of the filler leads to a more conductive material. The amount of filler also plays a significant role in determining the conductivity of the composite. As the amount of carbon black in the matrix increases, the level of conductivity is expected to increase as well. As the level of carbon black in a matrix is increased, the conductivity of the composite also increases. However, the relationship is not linear and there is a point known as the percolation threshold at which any further increase in the filler level leads to a rapid increase in conductivity. This is because at the percolation threshold (Medalia, 1986), significant conduction becomes possible. The relationship between the conductivity of the composite and the filler level is usually depicted schematically using a curve, as shown in Figure 2.14.

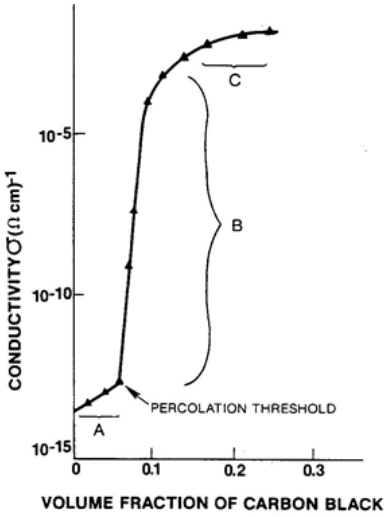

Figure 2.14 Conductivity of NR with carbon black. (Medala, 1986): A, insulating, B, percolation, C, limiting high conductivity

At low levels of filler, the composite behaves as a dielectric medium (region A). As the volume fraction of the filler is increased above the percolation threshold, the conductivity of the composite rapidly increases until it reaches a plateau (region C). At this stage, the composite becomes a conductor. The region between the percolation threshold and region C is known as the percolation region (region B). In this region, the conductivity of the composite is highly sensitive to changes in the filler level.

After the percolation threshold is reached, it is typically easy to measure the resistance of a carbon black-filled elastomer because these materials have Ohmic behaviour, meaning that the current flow through them is directly proportional to the applied voltage. The state of aggregation of the carbon black can affect the percolation threshold of the composite. Carbon blacks that are chain-like in appearance tend to have lower percolation thresholds (Ezquerra et al. 1986), while carbon blacks that consist of isolated clusters have higher percolation thresholds. Porosity is another factor that can contribute to the conductivity of the composite. Highly conductive fillers are often porous (Medalia and Rivin, 1982; Verhelst et al., 1977), and a more porous filler with a similar surface area to a non-porous filler can result in the same level of conductivity at a lower volume fraction of carbon black.

For non-porous carbon blacks, particle size is a major factor that affects resistivity. Boonstra and Dannenberg (1959) compared different carbon blacks of similar structure at the same volume fraction of carbon black and found that resistivity increases with increasing particle size. This behaviour can be explained by considering that smaller particles have a greater number of particles per unit volume, which leads to an increase in the probability of conductive chains being present with smaller gaps between the aggregates. In addition to particle size, the particle size distribution of the filler within the matrix can also affect the conductivity of the composite (Sircar and Lamond, 1978). In general, a wider particle size distribution leads to better conductivity within the matrix. This may be due to the presence of smaller particles that compensate for a fewer number of larger particles. Smaller particles can coalesce to form a larger number of smaller agglomerates, which effectively reduces the gaps between the aggregates and leads to an increase in conductivity.

Carbon black aggregates that have a high structure, meaning they have a high degree of branching and chain-like arrangement, tend to coalesce to form agglomerates. The degree of agglomeration can affect the final properties of a filled elastomer. Carbon black fillers with low surface area, such as HAF N330, have a low tendency to agglomerate, while carbon black fillers with high surface area and shape factor, such as Printex-XE2, have a high tendency to agglomerate. Research by Jha et al. (2010) has shown that the piezo-resistive behaviour of rubbers filled with HAF N330 is very complex and difficult to model. On the other hand, tensile tests carried out on rubber filled with Printex-XE2 have shown a more predictable and virtually reversible with strain, indicating that the filler network is not permanently altered. This reversibility in the electrical resistivity behaviour of rubber filled with Printex-XE2 is significant because it suggests that devices can be made that measure forces and strains based on

changes in electrical resistivity. However, further experimental work is needed to characterise the piezo-resistive properties of rubber filled with Printex-XE2 under various loading conditions.

3 Rubber blocks and bearings

Rubber is a versatile material that has a variety of technical applications, including vibration isolation, bridge bearings, suspension bearings, earthquake protection, flexible joints, energy absorption, and elastomeric dampers and many other areas outside the civil engineering world. Most of the civil engineering applications utilise rubber in shear, compression or a combination of shear and compression.

This section focuses on rubber blocks and bearings, used as seismic protection and vibration isolation systems as well as supports for bridge decks. Rubber blocks are widely employed as springs. In their simplest form they consist of solid blocks of uniform thickness, located between two rigid surfaces to which they adhere or are bonded. Rubber blocks that are bonded to rigid plates have various important uses, such as minimizing movement caused by traffic, providing seismic isolation for buildings and protecting equipment that is sensitive to vibrations (Horton et al. 2002).

Rubber bearings with multiple layers are widely utilized in the fields of civil, mechanical, and automotive engineering due to their ability to combine horizontal flexibility with high vertical stiffness. This is achieved through the use of thin steel plates as reinforcement in rubber blocks. These types of bearings have a diverse range of uses, such as providing earthquake resistance for structures like buildings and bridges, as well as acting as vibration dampeners for equipment and structures. Rubber bridge bearings were developed in the 1950s as a replacement for mechanical devices used to accommodate thermal expansion and contraction of bridge decks. These bearings are designed to be stiff vertically to minimize changes in vertical deflection under varying traffic loads, but soft horizontally to prevent large forces on the supporting piers when the deck length changes. Elastomeric bearings are made by placing uncured natural or synthetic rubber sheets and steel shims in a mold and vulcanizing them under high temperatures and pressures to bond the materials together. These bearings are usually covered to protect the internal layers from the degradation and corrosion (Symans, 2004) as shown in Figure 3.1.

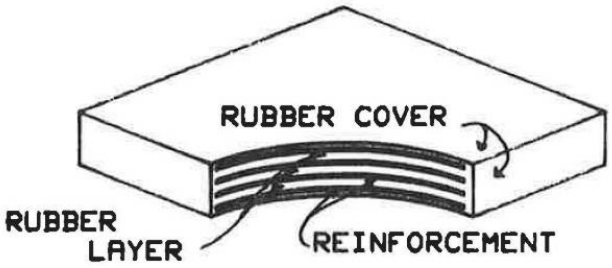

Figure 3.1 Typical steel reinforced elastomeric bearing (Roeder et al.1987)

If a simple rubber pad such as the one in Figure 3.2 (a) is squeezed between two surfaces that are well lubricated, it will deform in the manner depicted in Figure 3.2 (b), resulting in a uniform lateral expansion of the rubber. On the other hand, if the surfaces in contact are rough or the rubber adheres to them, the shape of Figure 3.2 (c) will be produced. Incorporating internal laminates to inhibit this bulging, as shown in Figure 3.2 (d), will significantly enhance the pad's compressive stiffness. However, adding internal reinforcing layers has little effect on the shear stiffness as long as the total rubber thickness remains constant. This allows the horizontal and vertical stiffness to be adjusted independently by choosing the right type of reinforcement.

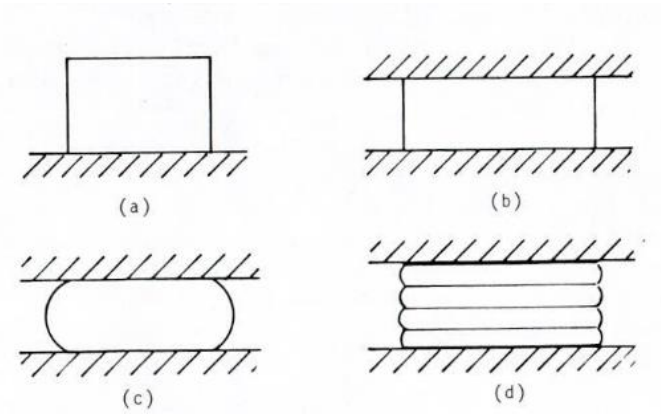

Figure 3.2 Compressive behaviour of bearings (Stanton and Roeder, 1982)

The compression stiffness of a rubber block depends on its aspect ratio, i.e. the ratio of the height to the width for a rectangular or square block, whereas for a circular block it is the ratio of the height to the diameter. This dependency means that the vertical stiffness of a rubber block of a certain size can be significantly increased by adding horizontal metal spacer plates that are firmly bonded to the rubber and divide the block into layers with a higher shape factor.

3.1 Vibration isolation and control

Vibration isolation systems are designed for reducing the transmission of vibration energy in structures and machines. There are several types of isolators, including metal springs, rubber mounts, which can be used in different applications. Anti-vibration mounts are often used to reduce the transmission of vibrations to equipment. Vibration isolation for buildings is a well-established practice in Europe and the United States, and additional information about this technique can be found in the works of Grootenhuis (1982) and Crockett (1982). Furthermore, Talbot and Hunt (2003) provided an extensive review of the practice and theory behind the vibration isolation systems. Rail traffic or construction activities, are common sources of building vibrations, with the frequency of these vibrations varying between 25 and 50 Hz, depending on factors such as the local soil conditions and the specific source of the vibrations (Kelly and Konstantinidis, 2011). Rubber bearings are often used to reduce the

transmission of these vibrations to a level that is below the threshold of perception or that does not disrupt the operation of sensitive equipment, such as electron microscopes. To achieve this, the rubber bearings are designed to provide a vertical natural frequency to the structure approximately one-third of the lowest frequency of the disturbance. One example of this technique was implemented in Albany Court, a London apartment building built in 1966 above the St James' Park Station of the London Underground, which was the first building to utilize natural rubber for vibration isolation. The isolation system installed in this building was tested for performance and durability. TARRC and Aktins Research and Development monitored the system for several years after its construction (Derham and Waller, 1975). Vibration isolation has also been used in concert halls. The Glasgow Royal concerts Hall in Glasgow, Scotland, was completed in 1990 and is situated above two underground railway lines. It has a structural frame made of reinforced concrete supported by 450 natural rubber bearings. In the United States, more recent example of concert halls that have implemented vibration isolation include the Benaroya concerts Hall in Seattle, Washington (Kelly and Konstantinidis, 2011). Rubber bearings were used to isolate noise caused by trains travelling through a tunnel underneath the building. It is worth noting that the Benaroya concerts Hall, which is located in area with high seismic activity, did not incorporate both vibration isolation and seismic isolation in the design. Researchers at the Earthquake Engineering Research Center at the University of California, Berkeley have conducted experiments using a shake table, and have found that it is feasible to develop a rubber bearing system that offers both vibration isolation and seismic protection. However, the vertically located bearings used in the Benaroya and Walt Disney concert halls to prevent lateral movement of the building's support bearings added significant cost that could have been avoided with a more suitable design.

3.2 Energy dissipation and Seismic isolation

Civil structures are traditionally designed to have a combination of strength and ductility in order to withstand lateral loads. When subjected to high seismic loads, they experience non-linear behaviour and damage. This is because the energy from the seismic activity is dissipated through the hysteretic behaviour of the structural components, as well as the non-linear nature of the materials used, leading to permanent deformations and the formation of plastic hinges. Passive energy dissipation devices, such as elastomeric dampers, can improve the seismic performance of structures by reducing the demands on structural elements that provide lateral load resistance, as well as reducing velocity and acceleration demands on non-structural components. An example of dissipation devices is the elastomeric damper realised by TARRC, as shown in Figure 3.3 which consists of a rubber layer bonded between steel plates.

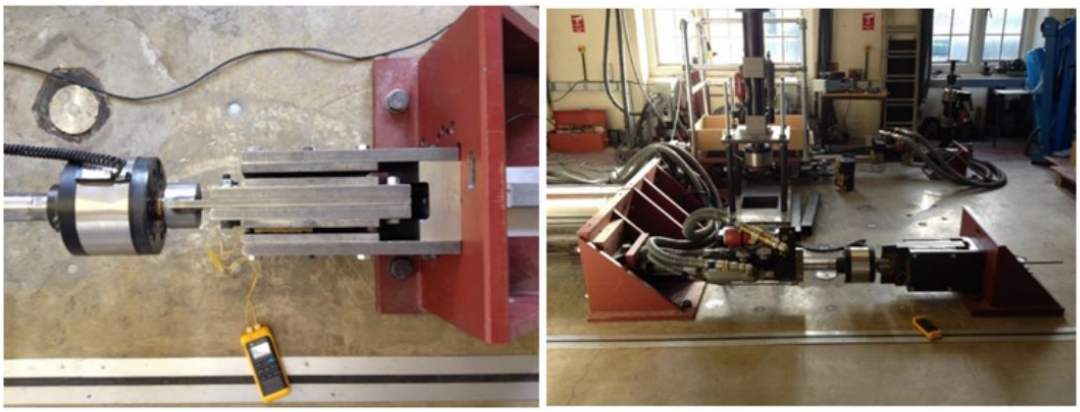

Figure 3.3 Elastomeric dampers and experimental setup (TARRC) (Basagiannis and Williams, 2017)

Seismic isolation is an alternative approach (often used in conjunction with energy dissipation) for improving the performance of structures exposed to earthquakes. This technique involves the use of flexible elements in order to change the period of a structure so that it is different from the predominant period of ground motion. Elastomeric bearings are often used to provide seismic isolation. These bearings can isolate a building or structure from horizontal ground motion due to their low horizontal stiffness. The fundamental frequency of a structure that uses seismic isolation is much lower than both its fixed-base frequency and the predominant frequencies of ground motion. When a structure is isolated, its first dynamic mode of deformation occurs solely in the isolation system, with the structure itself remaining relatively rigid. Higher modes of deformation that affect the structure are orthogonal to the first mode and therefore to the ground motion (Kelly, 1993a). These higher modes do not participate in the motion. If there is a lot of energy in the ground motion at these frequencies, it cannot be transmitted to the structure. Instead of absorbing earthquake energy, an isolation system deflects it through the dynamics of the system. This technique is effective when the system is linear and even when it is undamped, although some damping can be helpful in reducing resonance at the isolation frequency. This damping can be achieved through appropriate compounding of the rubber itself.

Figure 3.4 shows the components of a horizontally seismic isolated structure. The superstructure is separated from its foundation and the isolation system is placed between the building base and the foundation. Adequate space must be incorporated in the design of the isolator system to allow for inspection and replacement of individual isolators.

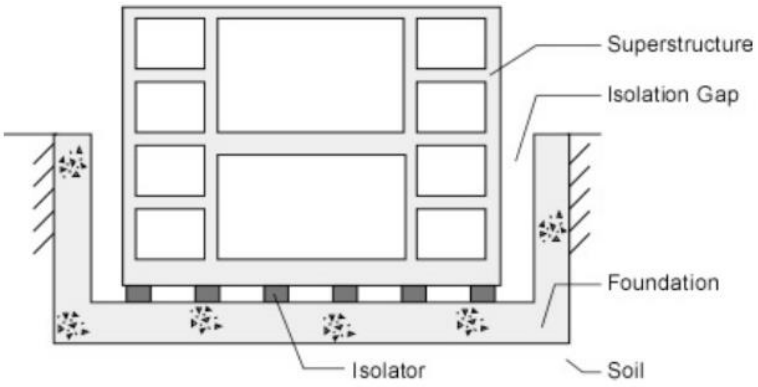

Figure 3.4 Base isolated structure (E. Blanford *et al.*, 2010)

During a seismic event, the superstructure will experience reduced floor acceleration and less movement between floors compared to a traditional, non-isolated structure, which deforms within each story and has amplified accelerations at upper floors, as shown in Figure 3.5.

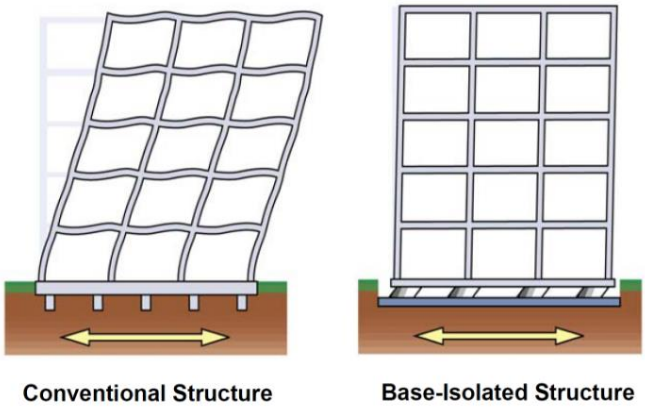

Figure 3.5 Conventional and base isolated structure deformations (Symans, 2099)

By using isolators at the base of a structure, the demands on the superstructure are reduced, allowing it to remain in the elastic or nearly elastic range. This reduces the risk of damage to equipment, non-structural components, and contents that are sensitive to displacement or acceleration. Isolated structures tend to experience deformation primarily at the isolation interface, leading to consistent accelerations throughout the height of the building (Warn and Ryan, 2012).

The vertical frequency of an isolation system is a critical design element for vibration isolation projects, as it is dependent on the vertical stiffness of the system's bearings. The first reaction of a bearing when subjected to a vertical load is often highly nonlinear and is affected by various factors. In general, bearings have a significant period of "run-in" before reaching their maximum vertical stiffness. This run-in period is largely affected by the alignment of reinforcing shims and other elements of the molding

process. While it cannot be accurately predicted through analysis, the run-in period is typically not a significant factor in determining the vertical response of a bearing. One factor that must be taken into account during the design process is the way in which the isolator responds to buckling. Section 3.3 describes the horizontal and vertical behaviour of rubber blocks and bearings and Chapters 5 and 6 include a thorough discussion of the calculations used to determine the horizontal and vertical stiffness of a LSF bearing, with a focus on how horizontal and vertical motion interact and influence one another.

3.2.1 3D seismic isolation

The effectiveness of laminated rubber bearings for horizontal base isolation of structures has been proven by several experimental and numerical studies carried out over the years (Buckle and Liu, 1994; Kelly and Naeim, 1999 ;Warn et al., 2007). However, in many situations it may be preferable and/or required to isolate structures also against the vertical component of the seismic excitation. For example, nuclear reactors are structures that may be vulnerable to vertical seismic excitations and ground borne vibrations (Aiken and Kelly, 1990; Kelly, 1988; Kelly and Lee, 2018).

Some studies in the literature, such as the work of Kelly and Lee (2018), Kelly (1988) and Tajirian (1990) have investigated the use of elastomeric bearings for 3D seismic isolation of structures. The vertical stiffness of laminated elastomeric bearings is controlled by the shape factor, which is defined as the ratio of the area of the loaded surface to the area free to bulge. The shape factor does not significantly affect the horizontal stiffness. Thus, in principle bearings with low shape factor can be used to achieve low horizontal stiffness as well as low vertical stiffness. However, particular care must be taken in the choice of the appropriate values of the shape factor, by avoiding excessively low critical buckling loads, which can increase the importance of stability under lateral deformation. In addition, attention has to be paid to the fact that the rocking effects may become more significant for low values of the bearing vertical stiffness. Kelly and Lee (2018) analysed the existing literature about 3D seismic isolation and explored theoretically the dynamics of 3D isolation systems and the presence of rocking modes.

An experimental investigation of a base-isolated building mounted on low-stiffness-factor (LSF) bearings was conducted by Kajima Corporation Technical Research Institute (Kelly, 1988). Another experimental research program on low shape factor was carried out at the Earthquake Simulator Laboratory of University of California, Berkeley Earthquake Engineering Research Centre (EERC) (Kelly, 1993). A very extensive test program on full size and scaled bearing was carried out on liquid metal reactor isolated with low shape factor bearings designed by (Aiken et al. 1989). Both the Kajima project and EERC test program showed potential for using elastomeric bearings for 3D isolation, but other methods like steel springs and combined systems were also explored. The combined systems, which include complex components such as air springs developed by the Japanese nuclear industry, are found to be too complicated and expensive. Thus a more practical and affordable solution is still being

sought (Kelly and Lee, 2018). A few studies (Kelly and Lee 2018, Warn and Vu, 2012) have also numerically investigated the dynamic behaviour of structures mounted on LSF bearings. To fill existing gaps of knowledge, a comprehensive analysis of the behaviour of LSF bearings using advanced finite element modelling has been performed and discussed in depth in Chapter 5 and 6.

3.3 Mechanical behaviour of rubber blocks and bearings

Rubber blocks can be analysed based on three different modes of deflection: compression/extension, in which one bonded surface moves closer to or farther away from the other; bending, in which one bonded surface rotates around an axis of symmetry within its own plane; and apparent shear, in which one bonded surface moves in a parallel direction to the other within its own plane. Studies have indicated that the stiffness of rubber blocks bonded to end plates under compression is influenced by the shape factor *S*, a non-dimensional parameter that is a good indicator of the compressive stiffness of the layer (Keys, 1937 and Kimmich, 1940). It is defined by:

$$S = \frac{\text{Area of one loaded surface}}{\text{Area free to bulge}} \tag{3.1}$$

$$S = \frac{ab}{(a+b)t} \qquad S = \frac{D}{4t} \tag{3.2}$$

Notation for dimensions is shown in Figure 3.6.

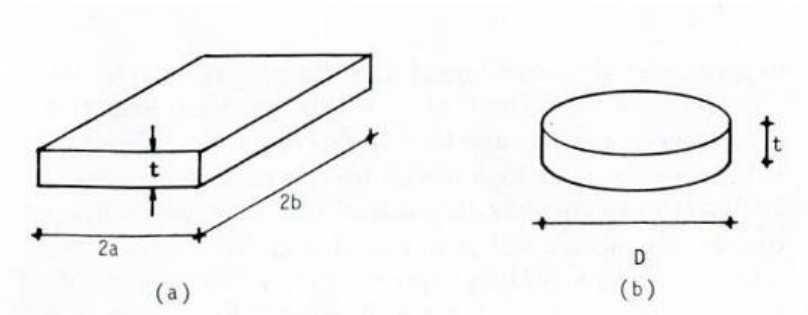

Figure 3.6 Notation for dimensions (Stanton and Roeder 1982)

3.3.1 Vertical Behaviour

Gent and Lindley (1959) and Gent and Meinecken (1970) developed closed-form solutions for analysing the behaviour of bonded rubber blocks based on the following assumptions: 1) Rubber is an incompressible, linear elastic material; 2) The stress within the rubber in the vertical direction remain constant; 3) when the rubber is deformed, the shape of the free side becomes parabolic; 4) Planes parallel to the end plates remain flat before and after deformation. It is assumed that the overall

deformation of the rubber block is a combination of two simple deformations: a uniform, homogeneous deformation and a separate deformation that returns the block to its original position in the plane.

Several formulations are proposed for the compression modulus of the rubber blocks, E_C. Gent and Lindley (1959) proposed a relationship for circular bonded rubber as follows:

$$E_C = E\left(1+2kS^2\right) \tag{3.3}$$

The constant k represents the volumetric deformation effect and is dependent on the hardness of the elastomer. It tends to approach unity for soft rubber, and is typically around 0.7 for engineering rubbers with moderate amounts of carbon black filler (Derham et al. 1969). However, this approximate theory is not precise, as it does not take into account the effect of shape on the behaviour of rubber blocks or the nonlinear behaviour of elastomers. Rubber blocks and bearings often experience large deflections under service loads, with important deformations including reductions in height and increases in plan area due to bulging under compressive load. Lindley (1966), Stanton et al. (1990), Goodchild et al. (2018) and Muhr (2017), provided an extension of the classic theory of rubber blocks to include axial shortening and these theories are deeply discussed in Chapter 4 and compared with experimental and numerical predictions.

The vertical stiffness of a laminated rubber bearing made of multiple layers of rubber and steel plates can be evaluated as follows:

$$K_v = \frac{P}{v_v} = \frac{E_C A_0}{t_r} \tag{3.4}$$

where P is the vertical load, v_v is the vertical displacement, A_0 is the area of the bonded rubber and t_r is the total rubber height. In order to predict the compression stiffness, Haringx (1948, 1949) developed load-compression relationships for the case of bonded rubber blocks. Gent confirmed that the evaluation formula can be applied to elastomeric bearings (Gent, 1965). Gent and Lindley (1959) carried out experimental tests on rubber blocks subjected to compression between rigid adhering plates and developed approximate load-deformation relations for infinitely long rectangular blocks and circular disks. For the latter case, they proposed Equation 3.3. Lindley (1966) observed that Equation 3.3 also applies to rectangular blocks with comparable maximum and minimum plan dimensions, and is valid only under small strains.

Gent and Meinecke (1970) extended the theory of Gent and Lindley (1959) to the case of bonded rubber blocks of any cross-section under small compression. The compressive load P can be related linearly to the axial strain ε through the following expression:

$$P = A_0 E_C \varepsilon = 3GA_0\left(f_{c1} + f_{c2}\right)\left(1-\lambda\right) \tag{3.5}$$

Where λ is the axial extension or compression ratio, f_{c1} and f_{c2} are numerical factors describing the effect of the bonded surfaces (Gent and Meinecke, 1970).

The theories mentioned before are based on three main assumptions: that horizontal planes remain flat, vertical lines become parabolic when subjected to force, and the normal stress in all directions is constant and equal to the average pressure. Koh and Kelly (1989) developed a solution for calculating the compression modulus of bonded rubber layers that does not rely on the assumption of stress. Tsai and Lee (1998) calculated the compressive modulus for bonded layers of infinite strips, circles, and squares. Koh and Lim (2001) estimated the compressive modulus for rectangular pads using an analytical solution that builds upon the work of Koh and Kelly (1989).

Kelly and Konstantinidis (2011) adapted previous theories to the case of laminated bearings with shape factors greater than 5. They derived closed-form Equations for calculating the compression modulus of infinite strips, circular pads, and rectangular pads. These Equations can be written in the same form as Gent and Meinecke's expression, with the numerical factor f_{c1} considered negligible.

Goodchild et al. (2018) used the Mooney-Rivlin constitutive material model to describe the relationship between axial load and stretch for rubber strips (very slender rubber blocks) under a uniform strain field that is not affected by the end plates. Muhr (2017) modified this formulation for use with rubber blocks that have bonded end plates.

Stanton et al. (1990) also developed a theory that expands upon the classic theory of rubber blocks to include axial shortening and the increase in the planar area due to the bulging of a bearing under compressive load. They use a nominal Poisson ratio (rather than 0.5) that is chosen based on empirical observations to account for the non-uniform increase in area along the height due to the influence of the end plates. The theory assumes small deformations and a linear elastic material, and it was applied to the case of discreetly layered bearings. The proposed model features a homogenous and flexible column with varying compressive, shear, and bending stiffness that are dependent on the strain and are approximated by assuming that the planar dimensions of each elastomeric layer increase proportionally to $(1 + \nu)$). The compressive force is:

$$P = 3GA_0\left(f_{c1} + f_{c2}\right)\frac{\left(1+\nu\left(1-\lambda\right)\right)^3 - 1}{3\nu\left(1-\lambda\right)}\left(1-\lambda\right) \qquad 3.6$$

3.3.2 Horizontal Behaviour

Shear deformation is a crucial aspect of the performance of elastomeric bridge bearings. It enables the accommodation of the thermal expansion and contraction of the bridge superstructure and the creep and shrinkage of concrete beams. Researchers such as Stanton and Roeder (1982) have argued that testing the shear stiffness of a completed bearing is the most effective way to evaluate the quality of the

elastomer used. Thus, a thorough understanding of shear behaviour is essential for the design of bearings. Many factors can influence the shear stiffness and overall shear behaviour of elastomeric bearings. The force-deflection relationship typically appears to be nearly linear, and can be approximated by the following Equation:

$$F_h = \frac{GA_s}{t_r}\Delta_s \qquad 3.7$$

Where G is the apparent shear modulus (that can be amplitude dependent), A_s is the plan area of bearing effective in shear, Δ_s is the shear deflection, F_h is the shear force. Performing pure shear or even simple shear tests on bearings may not always be feasible as it requires a significant amount of compressive load to create the friction needed to prevent slipping under shear loading. This compression causes the bearing to bulge, which can make it difficult to determine the loaded area used in the Equation 3.7. Additionally, the inclusion of a compressive load can result in instability and buckling which can significantly change the apparent shear stiffness of the elastomeric material. According to Porter and Meinecke (1980), there is a geometric effect associated with shear deformation and they included horizontal component of the compression load when analysing the experimental results of bearings with a shape factor of 0.6. Additionally, it has been proposed that the shape and shape factor of the bearing may also have an impact on its shear behaviour. The horizontal stiffness of a bearing made up of multiple rubber/metal laminates is not accurately described by the Equation GAs/t_r. This is because under the combined action of compressive and shear forces, some bending of the bearing occurs, involving the tilting of one face of an element relative to the other. Haringx developed a theory accounting for both the shear and bending modes of deformation, which was later applied to laminated rubber bearings by Gent.

In the late 40s, Haringx published a series of six papers (1948, 1949) on the use of highly compressible helical springs and rubber rods for vibration-free mountings. In his research on laminated rubber bearings, Haringx initially approached the bearing as a column with a constant cross-sectional area, composed of a homogenous and isotropic material, and an equivalent height that incorporated both the rubber layers and steel shims. He examined a scenario where an elastic column of length l was subjected to a compressive load P. The base of the column was fixed in place and prevented from rotating at the top, allowing for the occurrence of a reaction moment. The upper end was free to move horizontally, and a horizontal force could be applied. The system is illustrated in Figure 3.7:

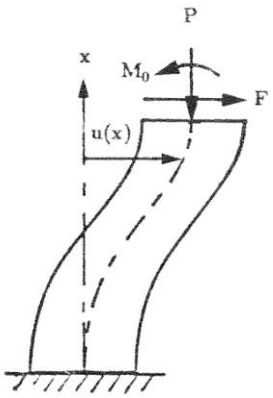

Figure 3.7 Haringx column in deformed configuration

Haringx analysed the deformations of a column equivalent to the bearing using two independent variables: the displacement of the central axis and the rotation of a face that was initially perpendicular to the undeformed axis. Haringx's methodology was applied to investigate the influence of the P-Δ curve on the horizontal stiffness of bearings when subjected to axial compressive loading. The theory showed good agreement with experimental results for moderate levels of shear strain (as reported in Gent, 1964 and Derham and Thomas, 1980). Gent and Lindley (1959) evaluated the horizontal stiffness by analysing a single rubber layer that was bonded to steel shims. Gent (1964) acknowledged that Haringx (1949) was the first researcher to address the issue of instability in elastomeric bearings, showing that Haring'x theory is able to predict buckling loads, vertical and horizontal stiffness. Gent and Meinecke (1970) further expanded upon this approach to include the compression and bending state. Lindley (1981) conducted additional research on the stiffness of rubber bearings and proposed a new method for calculating it. Derham and Thomas (1980) built upon Haringx's theory in their own research. Additionally, Haringx's theory was used to investigate stability issues. Stanton et al., (1990) and Roeder et al. (1987) both examined the stability of laminated elastomeric bearings through a combination of experimental and theoretical methods, taking into account the effect of axial shortening. Buckle and Kelly (1986) also studied the stability of elastomeric bearings by utilizing a model bridge deck that was tested on a shaking table. Koh and Kelly (1986, 1988, 1989) developed a mechanical model that considers the impact of axial load on the horizontal stiffness of elastomeric bearings. Schapery and Skala (1976) and Schapery (2018) developed a theory based on linear elasticity that takes into account the nonlinear effect of axial loads on stiffness and strains and stresses within the rubber. This theory was used to derive bearing properties for various geometries (spherical, flat, and cylindrical), loads, and deformation modes. It was also used to predict stiffnesses for low shape factor values and compare them with finite element solutions. More recently, Muhr (2017) proposed a promising approach for describing the behaviour of low shape factor bearings.

In 1993, Kelly introduced the idea of "effective properties" to take into account the presence of reinforcing shims in rubber bearings. As a result, the area and the second moment of area of the bonded rubber must be adjusted by multiplying them by a factor of h_t/t_r, where h_t is the combined height of the rubber layers and shims, and t_r is the total height of the rubber. To sum up, the effective properties are defined as follows:

$$EI_{eff} = EI_0 \frac{h_t}{t_r}$$
$$GA_{eff} = GA_0 \frac{h_t}{t_r} \qquad 3.8$$

where I_0 is the second moment of area of the cross section of the bearing.

The stability of rubber bearings is often evaluated by using Haringx's theory, which is based on the assumptions of linearity and small displacements. However, elastomeric bearings experience large displacements. Nagarajaiah et al. (1999), developed a non-linear analytical model based on the linear model proposed by Koh and Kelly (1986) with the goal of more accurately predicting the critical load and horizontal stiffness.

According to the studies conducted by Yamamoto et al. (2008) and Han and Warn (2015), it has been proposed to utilize a sequence of nonlinear axial springs in place of traditional rotational springs in order to accurately depict the relationship between axial and moment behaviour. The research done by Yamamoto et al. (2008) was further advanced for three-dimensional analysis by Kikuchi et al. (2010), who incorporated the use of multi-oriented shear springs at the mid-height and a two-dimensional distribution of axial springs at the top and bottom of the bearing. Despite the inclusion of a rotational mechanism to account for instability in all of these studies, the models assume that the end plates of the bearing maintain parallel alignment. This assumption is reasonable in situations where the bearings are fixed in place by rigid diaphragms on top and bottom. However, in certain unique settings, such as when bearings are placed on top of columns or connected to flexible diaphragms or in tall buildings, the end plates may not remain parallel. Imbimbo and Kelly (1997) investigated the effect of end-plate rotation on the undisturbed stability of elastomeric bearings by adjusting the boundary conditions used in Haringx's solution. A significant number of theoretical studies of laminated rubber bearings have been built upon Haringx's model of an equivalent column. However, this model does not take into account the specific mechanical behaviour between the layers of rubber, and cannot account for variations in thickness, material properties, cross-sectional area, or boundary conditions between the layers. In order to accurately model isolation bearings with varying properties between layers, Chang (2002) created a stiffness matrix for individual rubber layers. This formulation allows for the consideration of both displacement and rotation degrees of freedom for each rubber layer, resulting in a comprehensive

stiffness matrix that can describe the bearing in detail. Chang's research found that when the top plate is allowed to rotate while maintaining a constant load, the lateral stiffness decreases. Crowder and Becker (2017) proposed a model that uses a stiffness matrix to investigate the impact of partially restrained boundary conditions on elastomeric isolation bearings. This model has been used and implemented in Chapter 6 for describing the change of the horizontal stiffness with the horizontal displacement accounting for not only large displacement but also the coupled rotational-translation behaviour of the bearings. The evaluation of mechanical models for LSF blocks and LSF bearings are deeply discussed in Chapters 4 and 5, with particular attention on the dynamic behaviour and seismic response of structures isolated with LSF bearing using simplified modelling approaches.

According to the theory of Harnigx and Gent, the horizontal stiffness is given by

$$K_h = \frac{P^2}{Ph_t - 2qB\tan\left(\frac{qh_t}{2}\right)} \tag{3.9}$$

where h_t is the overall height including thickness of the rubber and steel layers,

$$q^2 = \frac{P}{B}\left(\frac{P}{R}+1\right) \tag{3.10}$$

B and R are the titling and shear stiffness for unit height.

Typically, bearings are deformed in shear under a constant vertical load. Under these conditions it has been observed that the height of the bearings decreases with increasing shear deformation. Sufficient clearance must therefore be allowed for this, and these features will be discussed in more detail in Chapter 4 and 5.

In the context of designing and analysing an efficient elastomeric bearing-based seismic isolation system for a specific building, it is crucial to take into account the following features of the behaviour of the bearings:

- The horizontal stiffness of the bearing, which determines its resistance to horizontal deformation and is typically characterized by a specific horizontal natural frequency.
- The vertical stiffness of the bearing, which determines its resistance to vertical deformation and is described by a dominant vertical frequency.
- The stability of the bearing under combined vertical load and lateral displacement, which determines its ability to withstand both types of deformation simultaneously.

These properties are crucial in ensuring the performance and safety of the seismic isolation system. In order to better understand the vertical response and stability of LSF elastomeric bearings, Chapter 4 examines the theoretical foundation of the existing mathematical models for these components.

3.4 Finite element modelling of rubber bearings

Finite Element Analysis (FEA) is a computational method used in engineering to model and analyse the behaviour of complex structures. It involves dividing the structure into smaller elements and solving a set of Equations to determine how the structure will behave under certain conditions. There are three main types of non-linearities that FEA can model: geometric non-linearity, which occurs when a structure deforms significantly or experiences snap-through buckling; material non-linearity, which occurs when a material undergoes large strains, plastic deformation, creep, or viscoelastic behaviour; and boundary non-linearity, which occurs when there are gaps or contact surfaces that open or close, or when follower forces are present.

Non-linear behaviour can also occur in combination with other forms of non-linearity, such as permanent deformations and significant changes in geometry, cracking, crippling, buckling, and material stress-strain values that exceed the elastic limit. Specifying non-linear material properties for elastomers can be difficult. To overcome this challenge, various constitutive theories for large elastic deformations have been formulated, based on strain energy density functions, for the purpose of describing hyperelastic materials. (Mooney, 1940; Rivlin, 1948; Ogden, 1976; M. Arruda and C. Boyce, 1993; Yeoh, 1993). These theories, combined with FEA, can be used to effectively analyse and design elastomeric products that operate under highly deformed states. More advanced nonlinear models (Simo, 1987; Bergstrom, 1998) have also been developed and used to analyse rubber components with the aid of finite element models. Kalfas et al. (2017) also performed finite element studies on the cyclic response of high damping steel-laminated elastomeric bearings to investigate their behaviour under combined axial and shear loads and to analyse the distributions of local stresses and strains within the bearings.

FEA has been applied to investigate the behaviour of elastomeric rubber bearings. In the following, few relevant studies are discussed. Zhou et al. (2022) conducted experiments to examine the impact of lateral displacement on the vertical stiffness of thick rubber bearings. They used tests at both the material and isolator levels to calibrate a finite element model and conduct parametric finite element studies. The results revealed a non-monotonic behaviour of the vertical stiffness in relation to the lateral displacement, which was attributed to a combination of two mechanisms: geometric nonlinearity, which can decrease stiffness, and material nonlinearity, which tends to increase the tangent stiffness of the material. Yang et al. (2017)'s work involved finite element investigation of rubber bearings with four section shapes (circular, annular, square and rectangular), in order to describe the vertical stiffness

degradation. It was observed that the finite element models were able to simulate the bearing response by comparing with typical experimental results. Moghadam and Konstantinidis (2021) performed experimental studies and developed a 3D finite element model in order to investigate the effect of non-zero rotations of the top and bottom supports of the bearings subjected to vertical load and horizontal displacement. It was observed that the hysteresis loops are not symmetric when the bearing is subjected to rotation and therefore the loops shift up and the difference between the maximum and minimum force is evident in comparison with the zero-rotation case. Warn and Weisman (2011) established through the use of the finite element method that there is a correlation between the critical load and the bearing geometry. Imbimbo and De Luca (1998) used finite element analysis to study the stress distribution in laminated elastomeric bearings under vertical loads, focusing on the stress concentration at the edge of the rubber bearing. Several researchers Zhang et al. (2019) and Kalfas et al. (2017) have built finite element models of elastomeric bearings to analyse the non-uniform stress distribution over the cross-section and steel plate deformation when the bearings are subjected to combined vertical and horizontal displacement. It has been observed that despite the bearing was subjected to global shearing and axial compression, local tensile stresses were observed within the bearing.

Chapters 4 and 5 provide an extensive numerical investigation of rubber blocks and elastomeric bearing behaviour using FEA. The analyses are aimed to understand the internal distribution of stresses and strains within bearings due to the application of external boundary conditions, and to determine the effect of the models used to describe the rubber's constitutive behaviour on the horizontal force-displacement behaviour of compressed blocks. The accuracy of different analytical theories for evaluating the horizontal stiffness and critical load of bonded LSF blocks is also assessed.

3.5 Conclusions

In conclusion, this work presents a comprehensive analysis of the behaviour of LSF bearings, focusing on their horizontal and vertical stiffness and the interaction between these properties. Through numerical investigation using advanced finite element modelling, Chapters 5 and 6 provide a thorough discussion of the calculations used to determine the stiffness of LSF bearings and the impact of partially restrained boundary conditions on their behaviour. The analysis also examines the effect of the models used to describe the rubber's constitutive behaviour on the horizontal force-displacement behaviour of compressed blocks.

Furthermore, this study evaluates the mechanical models for LSF blocks and bearings and their accuracy in predicting the horizontal stiffness and critical load of bonded LSF blocks. The height decrease of the bearings with increasing shear deformation is also discussed in detail in Chapters 4 and 5. The stability of the bearings under combined vertical load and lateral displacement is another crucial property for the performance and safety of seismic isolation systems, which is examined in this study.

To better understand the vertical response and stability of LSF elastomeric bearings, Chapter 4 examines the theoretical foundation of the existing mathematical models for these components. Overall, this study provides valuable insights into the behaviour of LSF bearings and their role in seismic isolation systems, which can inform the design and optimization of such systems in the future.

4 Mechanical behaviour of rubber blocks with low shape factor

4.1 Introduction

Rubber pads or blocks have been widely employed for more than a century in numerous applications, e.g. as springs, elastic joints or isolators in structures or mechanical systems, as frictional liners in contact with substrates, and for energy dissipation. The shapes, mechanical properties and chemical composition of the blocks are designed to achieve the performance required by the particular service condition. Usually, the rubber is faced at the mounting surfaces with bonded metal plates; rough contact surfaces such as concrete may also suppress lateral spreading of the rubber when compressed. When lateral spread at the contact surfaces is suppressed, we may define the (primary) shape factor S of a rubber pad or block as the ratio of the loaded area at one end face to the unloaded area of the sides, these being free to bulge when the pad is compressed.

For some applications, a high shape factor is desirable, and may be achieved by laminating the rubber with an appropriately large number of reinforcing steel plates, so that each rubber layer has a high shape factor, resulting in high axial stiffness (i.e. in the direction normal to the steel plates). In other applications the use of lower shape factors may be preferred (Orfeo et al. 2022). For example, bridge bearings with relatively low shape factor can better accommodate rotations compared to high shape factor bearings. Low shape factor blocks have been used as vibration isolation mounts for equipment, combined shear and compression mounts for car engines and transmissions, and as suspension springs for rail vehicles and heavy goods road vehicles, typically as multilayer laminates with a shape factor of each layer of the order of 1 (e.g. (Hirst, 1961)).

Low shape factor (LSF) blocks have interesting characteristics for seismic isolation of structures. The first building to be isolated on rubber bearings, the Pestalozzi school in Skopje, Macedonia, was mounted on unreinforced elastomeric LSF blocks (S = 0.5), a design stemming from prior experience of mounting systems for imparting blast resistance to military structures ((Siegenthaler, 1970)). More usually, LSF rubber bearings consist of a few rubber layers of moderate thickness sandwiched between, and bonded to, steel plates to increase the stiffness in the direction normal to the plates (Aiken et al. 1989). Thus, they might constitute a cost-effective solution for providing isolation for ground-borne vibration or three-dimensional seismic isolation of structures. The process needed to produce rubber bearings requires many steps from initial conception (assembling, vulcanization) to final installation, and assembling fewer steel and rubber layers to form LSF bearings can save time and costs, lower the

risk of defects during the production process, and also reduce the weight of the bearings, making them easier to manhandle.

Many experimental and analytical studies since the early 1960s have focused on the characterization of the behaviour of rubber blocks and laminated bearings under compressive loading and under combined vertical and horizontal loading. A theory was developed by Haringx (1948, 1949) considering a shear-flexible column, and applied to rubber rods with no reinforcing plates. Gent (1965) adapted this model to study the elastic stability of multilayer laminated rubber bearings and the reduction of their horizontal stiffness for increasing axial loads. Experimental tests on the behaviour of cylindrical rubber blocks under combined vertical and horizontal loading were also carried out by Payne (1962), who provided a validation of the theory of Haringx in the case of low shape factors, between 0.08 and 2.2. The dynamic shear experiments of Howgate (1979) were the first to highlight an interesting aspect of the mechanical behaviour of rubber blocks, which exhibit an increase in hysteresis and non-linearity under horizontal forces when compressed by increasing axial loads approaching the critical load for stability. The behaviour of laminated rubber bearings continued to be the subject of many experimental and analytical studies in the subsequent decades up to date (see e.g. Warn (2014) for a review of the most important ones, including the Koh and Kelly model (1988), widely used for seismic isolation bearings).

Although these theories and models stemming from the original formulations of Gent (1965), Thomas (1982) and Koh and Kelly (1988) can be used to describe the behaviour of multilayer laminated bearings with moderately high shape factors, they are not suitable for the case of LSFs, whether laminated or as single rubber blocks. Indeed, apart from the initial application of the theory by Haringx (1949) to rubber rods, the focus was on high shape factors ($1<<2S^2$), and on the correction for a finite bulk modulus K which becomes significant if the assumption that $6GS^2 << K$, is not justifiable, corresponding to $S > \sim 10$ (eg Chalhoub & Kelly, 1990, and some papers reviewed by Roeder et al (1987)). In contrast, for LSF bearings, we cannot disregard important effects such as the reduction in height and the increase in plan area due to bulging of the elastomer under compressive load (Stanton et al., 1990; Muhr, 2017; Schapery, 2018). Few experimental studies have focused specifically on LSF rubber blocks. Fan et al. (1992) carried out experimental tests on quadruple shear assemblies made with blocks with S values below 1.5. The assemblies were tested by varying the horizontal displacements at each of several fixed vertical compressions. Cilento et al. (2017) conducted further experiments on LSF rectangular and cylindrical blocks. Experimental tests on multilayer laminated bearings are numerous (e.g. Aiken et al. 1989, Yabana and Matsuda, 2000, Cardone and Perrone, 2012), though mainly focused on S values higher than 5.

Some analytical formulations were specifically developed for LSF rubber blocks and bearings. Among these, Roeder et al. (1987) and Stanton et al. (1990), proposed to take into account the effect of axial shortening due to compression on the shear and bending stiffnesses. Their theory was also validated by

experimental tests demonstrating that bearings with a height-to-width ratio below a certain limit do not become laterally unstable under any axial load. Lanzo (2004) took into account the axial stiffness of rubber bearings, considering both a linear elastic and a hyperelastic constitutive model for the rubber. Muhr (2017) also developed a theory for the lateral stiffness of single layer blocks of rubber with bonded endplates under finite axial deformation, based on the work of Goodchild et al. (2018) on the lateral stiffness and damping of stretched rubber beams. A comparison of these theories and an in-depth assessment of their accuracy has never been carried out to date.

This chapter investigates, with theoretical and numerical tools, the behaviour of low-damping LSF rubber blocks under combined vertical and horizontal loading. In particular, the blocks tested experimentally by Fan et al. (1992) are considered. Different numerical models, developed in Abaqus (2018) considering various constitutive laws, are employed to simulate these tests. They are also used to gain an insight into the internal distribution of stress and strain within the bearings due to the application of the external boundary conditions, and to evaluate the influence of the models used to describe the rubber constitutive behaviour on the horizontal force-displacement behaviour of the compressed blocks. The accuracy of various analytical theories for the evaluation of the horizontal stiffness and the critical load of bonded LSF blocks is assessed. An extended theory, accounting for the non-uniform bulging along the compressed rubber block, is also proposed.

Section 4.2 of the chapter describes the experimental campaign at TARRC carried out by Fan et al. (1992). In Section 4.3, the numerical simulations of the tests are illustrated, whereas in Section 4.4 the accuracy of the various analytical models considered is evaluated. The chapter ends with a conclusion section, where future studies are also discussed.

4.2 Experimental campaign

The tests considered in this study are those described in Fan et al. (1992) and were performed at the Tun Abdul Razak Research Centre (TARRC) on rectangular rubber blocks. An unfilled natural rubber mix was employed to make the samples and the compound recipe is SMR5, 100; ZnO, 5; stearic acid, 2; sulphur 2.5; CBS, 0.6; Santoflex 13, 2; where the numbers are parts by weight. Both ends of each block were bonded to metal plates using the Chemlok 205/220 system. The dimensions and shape factors of the rubber blocks are given in Table 4.1 where h_0, a_0 and b_0 are the undeformed rubber height, minimum width and maximum width respectively. The top and bottom metal plates share the rubber width dimension (e.g. see Block B in Figure 4.1a), except for Block X, which has oversized plates, i.e. 50mm, as shown in Figure 4.1b.

Table 4.1 Rubber blocks geometry

Block	h_0	a_0	b_0	$S = \frac{a_0 b_0}{(2a_0 + 2b_0)h_0}$
	mm	mm	mm	-
B	10	54	66.5	1.49
C	20	53.5	66.5	0.74
D	30	53.5	66	0.49
X	77.5	34	64	0.14

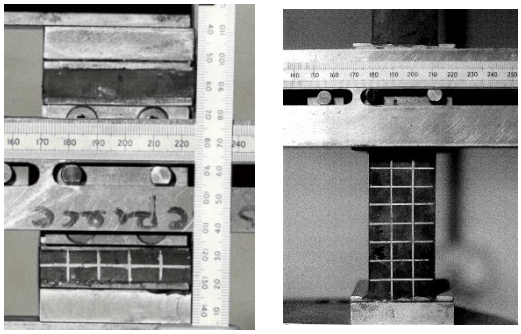

(a) (b)

Figure 4.1 Details of two blocks used during for the experimental tests (a) Block B (b) Block X. (pictures courtesy of A. Muhr)

A quadruple shear apparatus was used for the force-deformation experiments, as shown in Figure 4.2a. The rectangular blocks were sheared in the direction normal to side b_0, their longest plan dimension, this being the direction of lowest stability. A 100kN Instron universal test machine (model 1115) was used to achieve the desired compression, and then shear deflections were achieved by hand adjustment of a lead screw (D in Figure 4.2a), threaded through the steel block separating the righthand pair of bonded rubber blocks, and able to control the relative separation of the two stacks at their midheight for either sign of lateral force, measured by the load cell B. It was initially assumed that the shear deflections would remain equal and opposite for the two stacks of blocks, so that the turns on the lead screw could be used to determine the lateral deflection at the mid height of each stack. However, the mid-height plane of the apparatus is free to toggle to any position where the lateral force applied between the stacks is in balance, and at high loads their deflections are not necessarily equal and opposite. To determine the lateral deflection of each individual bearing, a dial gauge attached to the Instron crosshead was introduced. The two lateral deflections could then be calculated from the dial gauge reading plus the differential deflection determined from the lead screw. A shear force-deflection curve with little hysteresis was found when the block was subjected to shear deflection while keeping the compressive deflection constant and small, as shown in Figure 2b for a compression of 5.4mm.

However, for a compressive deflection exceeding instability there was a large spontaneous shear deflection, although this was observed to take place over several seconds, suggestive of a viscoelastic relaxation process. The shear force-deflection curve shown in Figure 4.2b for a compression of 9.4mm reveals a large hysteresis. As the compound chosen for the testpieces is a low-damping one, this observation may seem puzzling, but is a consequence of the very high strain energy throughout the rubber, and the low magnitude of lateral elastic stiffness under this deformation, making the viscous part of its viscoelastic nature more evident. Reference can be made to Orfeo et al. (2022) for further insight into this phenomenon. A mean curve for the pair of blocks (the dashed line in Figure 2b) showing the large excursion in shear was constructed and taken as the experimental shear force-deflection curve.

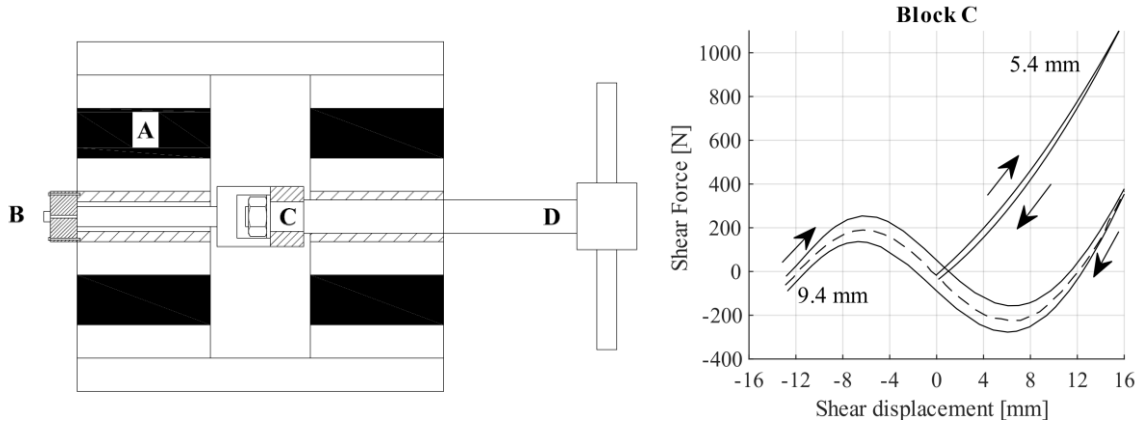

a) b)

Figure 4.2 (a) Quadruple shear apparatus (b) Typical shear-deflection plots (source: block C at vertical deflections of 5.4mm and 9.4mm, (Fan *et al.*, 1992))

4.3 Numerical modelling and comparison with experimental results

4.3.1 FE models

This section describes the three-dimensional FE models developed in Abaqus (2018) to simulate the tests on the LSF blocks. Only half of each block is modelled, thanks to symmetry. Figure 3 shows the blocks meshed using solid C3D8R elements, which are 8-node linear elements with reduced integration. Geometric non-linearities are taken into account in the analysis. Blocks B, C and D have a mesh finer toward the free rubber surface, where the strain gradients are highest. Block X has all elements with the same approximate global size. Moreover, the model of Block X includes the steel end plates meshed using C3D8R elements and connected to the rubber block using tie constraints. Refining further the meshes does not affect the global force-displacement response of the bearings, nor the strains and stresses far from critical locations at the boundaries, where singularities are expected.

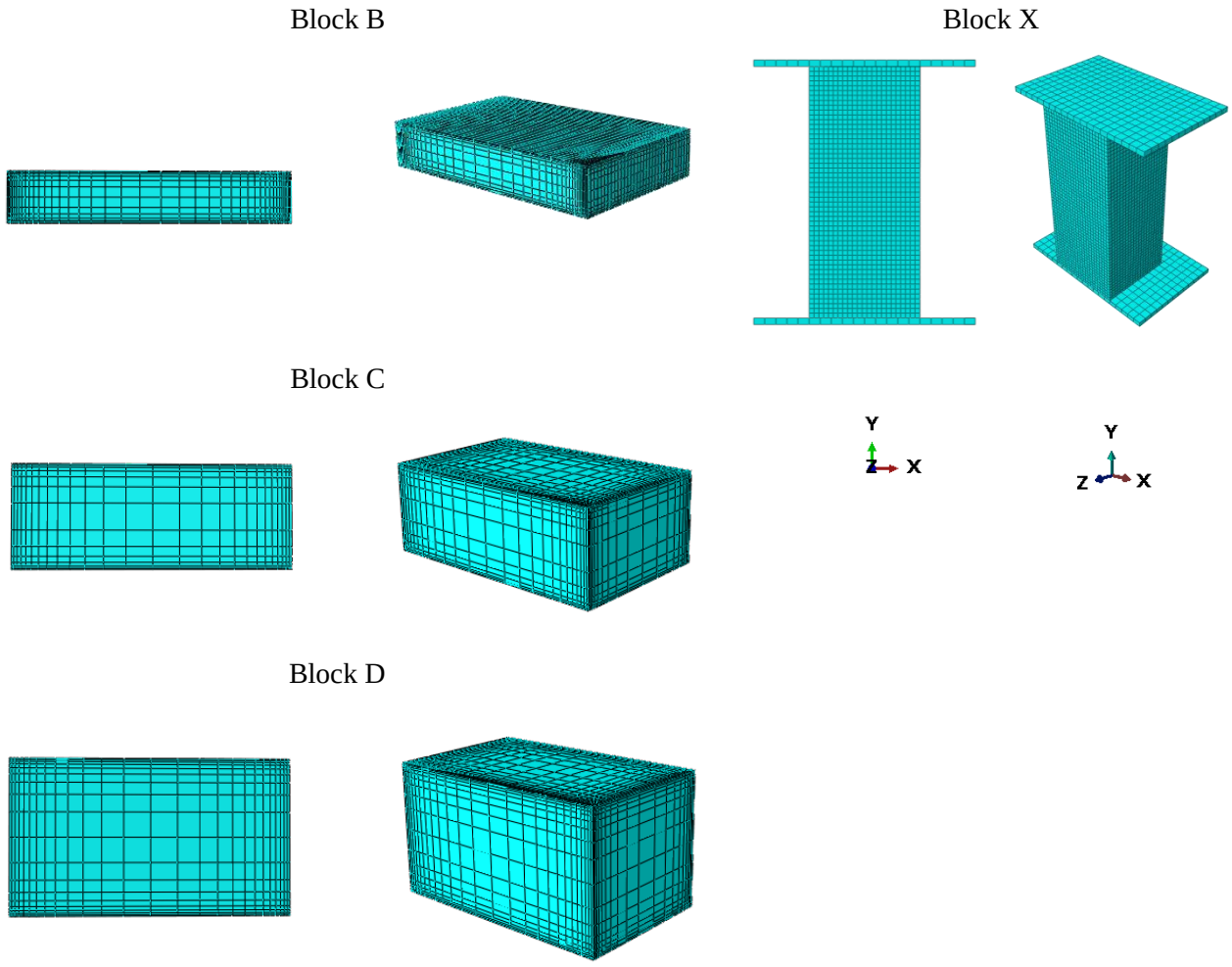

Figure 4.3 Finite element model of the rubber blocks: Front and 3D view

In Abaqus (2018), the following strain energy function is used for modelling rubber materials:

$$W = \sum_{i=1}^{N} \frac{2\mu_i}{\alpha_i}\left[\lambda_1^{\alpha_i} + \lambda_2^{\alpha_i} + \lambda_3^{\alpha_i} - 3\right] + \sum_{i=1}^{N} \frac{1}{D_i}\left(J-1\right)^{2i} \qquad 4.1$$

where W is the strain energy per unit of reference volume, λ_i are principal stretches, J is the ratio of current to original volume, the parameters μ_i and α_i control the deviatoric behaviour of the material, while the constant D_i characterize the volumetric behaviour (compressibility).

Two different constitutive models are considered in the FE analyses, with the aim of investigating the influence of the rubber constitutive model on the simulation of the behaviour of the blocks. The first one is an Ogden model, with N=1, μ_1 = 0.478 MPa, α_1=2.3, D_1= 0.0001 $N^{-1}mm^2$ (corresponding to a bulk modulus of K = 2000MPa). The values of μ_1 and α_1 for this model have been chosen to provide the best fit to all the experimental tests carried out on the blocks. The second model considered is a

simpler, neo-Hookean constitutive model, corresponding to N=1, μ=0.5MPa, α=2 and D_1= 0.0001 $N^{-1}mm^2$.

The behaviour of the constitutive rubber models in uniaxial compression and tension is shown in Figure 4.4a-b in terms of nominal stresses, i.e. ratio of force to unloaded area, versus λ_1,. Figure 4.4c shows the rubber behaviour in simple shear configuration in terms of shear stresses - shear strain γ. Figure 4.4d shows the variation with λ_1 of the strain energy density function of the Ogden and neo-Hookean constitutive models in both uniaxial tension and simple shear configurations. The two material models exhibit a similar behaviour under the various deformation modes only at small strains, while at large strain the Ogden model is stiffer in shear and tension, and slightly softer in compression. It is noteworthy that under vertical and horizontal loading, the rubber blocks are subjected to a complex state of deformation, involving compressive, shear and even tensile strains.

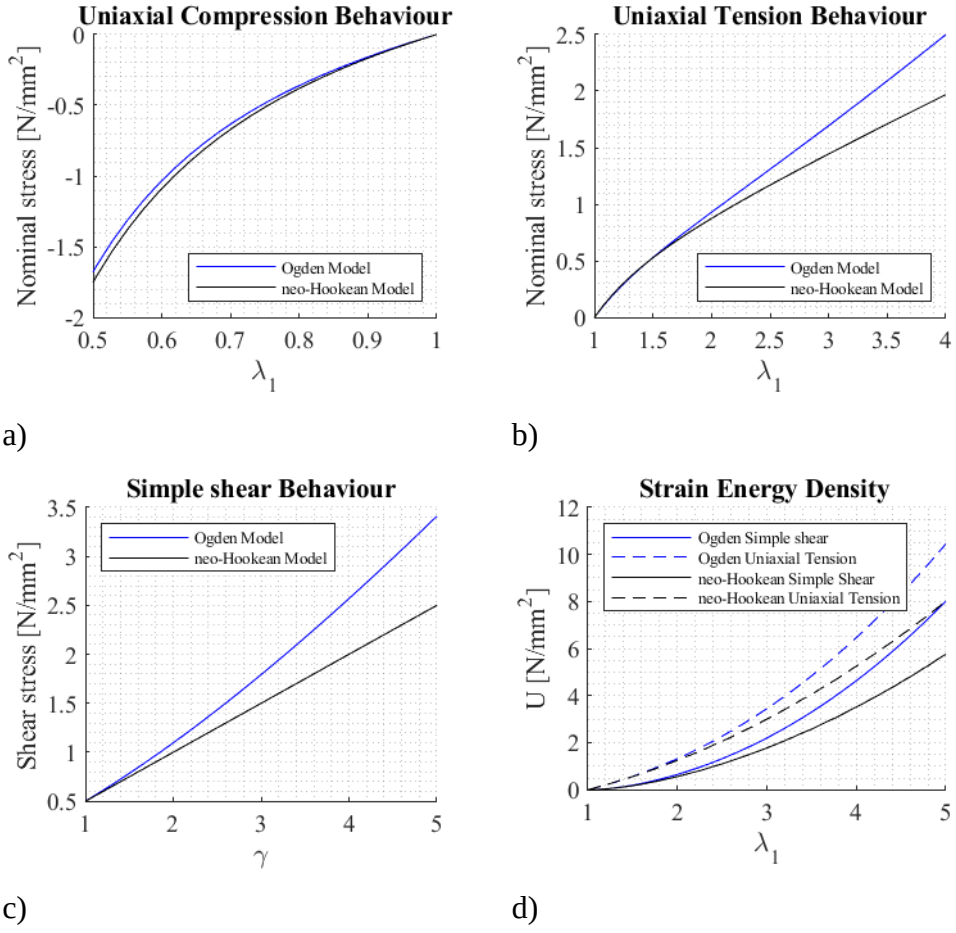

Figure 4.4 Comparison of Ogden and neo-Hookean constitutive models under (a) uniaxial compression, (b) uniaxial tension $\lambda_2=\lambda_3$ and (c) simple shear $\lambda_2 = 1$. (d) Strain Energy Density function in uniaxial tension and simple shear configuration

The numerical simulations of the quasi-static tests on the rubber blocks are carried out using a dynamic explicit solution algorithm, in order to overcome some difficulties in achieving convergence in the analyses of highly compressed and sheared blocks. The choice of the time step size Δt is very critical

in this type of explicit analysis, since small-time increments need to be used to achieve stable and accurate results. An approximate estimate of the limit value $\Delta t_{\max}$ of the time increment ensuring stability is given by the smallest transit time of a dilation wave across any of the element in the mesh (2018):

$$\Delta t_{\max} = \frac{L_{\min}}{c_d} \tag{4.2}$$

where $L_{\min}$ is the smallest element dimension in the mesh and c_d is the wave speed of the material, which in the case of a linear elastic material can be expressed as follows:

$$c_d = \sqrt{\frac{E}{\rho_m}} \approx \sqrt{\frac{1.5MPa}{967kg/m^3}} \approx 39ms^{-1} \tag{4.3}$$

where E is the Young's modulus and ρ_m the density. Applying Equations 4.2 and 4.3 to the problem at hand, very small values of $\Delta t_{\max}$ are obtained. Thus, a mass scaling factor of 10^{-5} was used to increase the time step size and reduce the computational burden of the analyses. At the end of each analysis, a check was made that the value of the ratio of the kinetic energy to the total energy in the system was less than 4%. It is noteworthy that using an implicit solution algorithm the analyses would not converge in many cases.

With regards to the boundary condition of the blocks, the displacements and rotations along the *x*-, *y*- and *z*- directions of the bottom surface were constrained for all the tests. The out of plane displacement along *z* and rotation about *x* and *y* of the nodes lying on the *z*=0 plane are restrained to account for symmetry. Finally, only displacement along *x*- and *y*- are allowed on the top surface. In the experiments, vertical displacements were first imposed on the top surface of the blocks. Subsequently horizontal differential displacements were applied, while preventing vertical motion and rotation of the top surface.

4.3.2 FE analysis results

Table 4.2 reports the experimental values of vertical and horizontal displacements applied for each block, which were also used as the FEA inputs. Table 4.2 also reports, for each block, the values of the nominal axial and shear strains, obtained by dividing respectively the maximum vertical and horizontal displacement by the rubber block height. The vertical and horizontal experimental reaction forces obtained at the end of the application of the maximum vertical and horizontal displacements are also reported, together with the corresponding nominal stresses, obtained by dividing these forces by the initial area A_0 of the transverse section of each rubber block. These values are considered as references to understand the extent of local variations in the stress and strain contours. The "nominal true stresses"

given in Table 4.2 are calculated in a similar way to the "nominal stresses", except that they are based on the deformed area, defined as:

$$A = A_0 / \lambda \tag{4.4}$$

where λ is the axial compression of the block.

Table 4.2 Experimental data reported by Fan et al. (1992)

	Block B	**Block C**	**Block D**	**Block X**
***S* [-]**	1.49	0.74	0.49	0.14
***h_0* [mm]**	10	20	30	77.5
Vertical displacements [mm]	0, 3.2, 3.8, 4	0, 5.3, 6.8, 8.2, 9.4	0, 8, 12, 15	0, 5.99, 8.97, 11.94, 13.42, 14.89
Maximum horizontal displacement [mm]	7	17	25	36
Nominal axial strain at max compression [-]	0.4	0.47	0.5	0.19
Nominal shear strain at max. shear [-]	0.7	0.85	0.83	0.47
Vertical reaction force at max compression and zero shear[N]	30130	13191	8852	944
Horiz. reaction force at max shear and max compr force [N]	275	505	351	33
Nominal axial stress at max. compression [N/mm^2]	8.39	3.71	2.51	0.43
Nominal true axial stress at max. compression [N/mm^2]	5.03	1.97	1.25	0.35
Nominal shear stress at max shear and max compr. force [N/mm^2]	0.08	0.14	0.10	0.015
Nominal true shear stress at max shear and max compr. force [N/mm^2]	0.046	0.075	0.050	0.012

Figure 4.5 and Figure 4.6 give contour plots of local compressive and shear strains respectively for each block subjected to the highest displacements applied. These plots were evaluated considering the Ogden constitutive model for the rubber. It is noteworthy that using a different mesh could lead to significant changes in the local strain and stresses close to the border of the block. This issue is not investigated in this chapter . Under compression, in Block X, it can be noted that there is a significant variation of the axial deformations along the rubber height but not along the rubber width, apart from the corners. In blocks B, C and D the bulging is more evident than in Block X, and the maximum compressive and shear strain values are concentrated along the corners. Under shear loading, tensile strains are developed

at the top right and bottom left areas of the blocks and there is concentration of compressive strains along a diagonal band, corresponding to the formation of a compression strut. Kalfas et al. (2017) found a similar behaviour in the case of a laminated bearing with the upper plate restrained against rotation. In addition, bending deformation is predominant in block X, as witnessed by the increasing tilt, from the ends towards the midheight cross-section, of the originally horizontal mesh lines, whereas in block B, characterized by the highest shape factor, shear deformation predominates in the core of the block, the originally horizontal mesh lines remaining horizontal, accompanied by bulging on the side. A combination of shear and bending deformation can be observed in C and D. It is also worth noting that the transverse sections stay horizontal in the middle of blocks B, C and D, whereas in the central part of the Block X they are almost perpendicular to the deformed axial centreline, again demonstrating the high contribution of bending deformations.

Block B

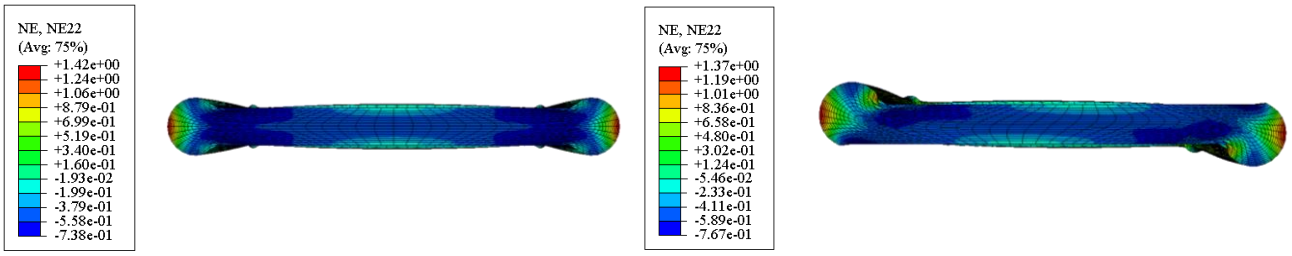

Block C

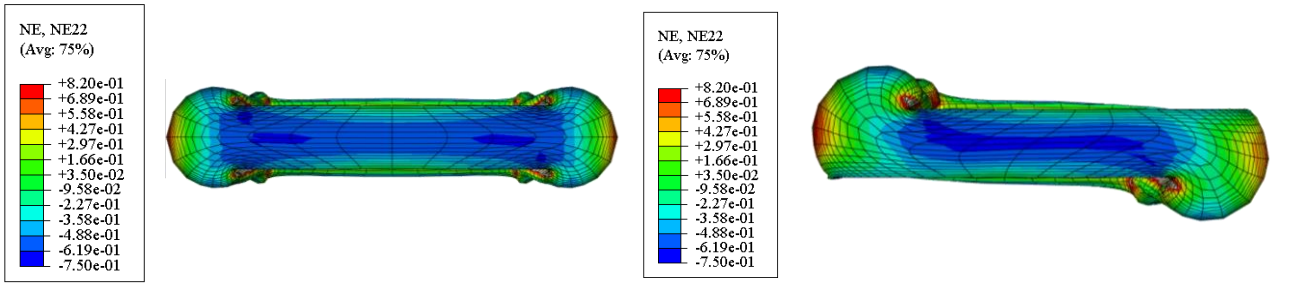

Block D

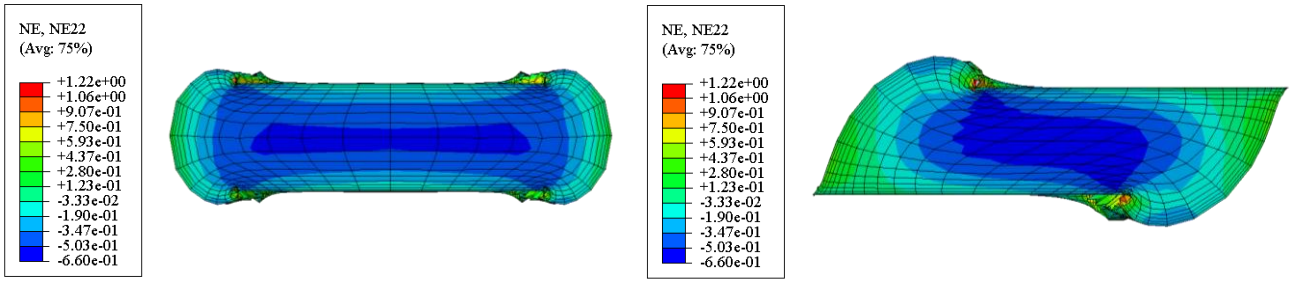

Block X

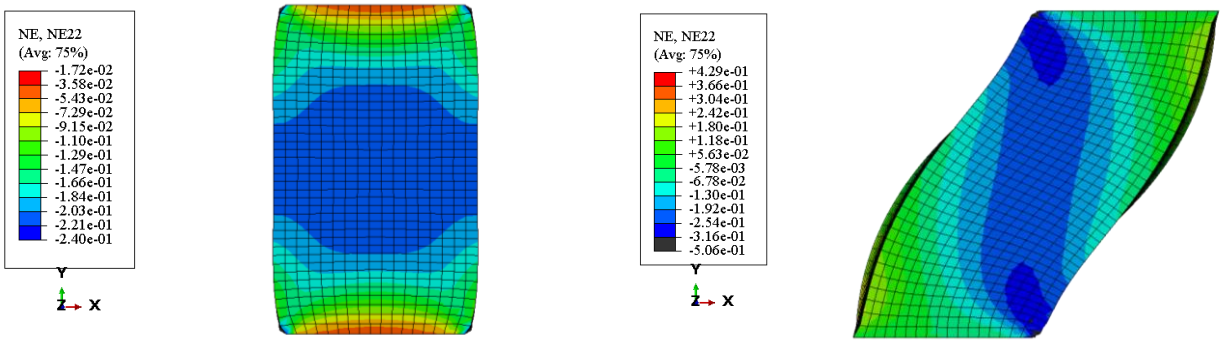

a) b)

Figure 4.5 Contour plot of NE22, i.e. nominal (i.e. engineering) compressive strains along Y direction, for half blocks subjected to (a) maximum compressive displacement alone and (b) maximum compressive displacement in combination with horizontal displacement.

Block B

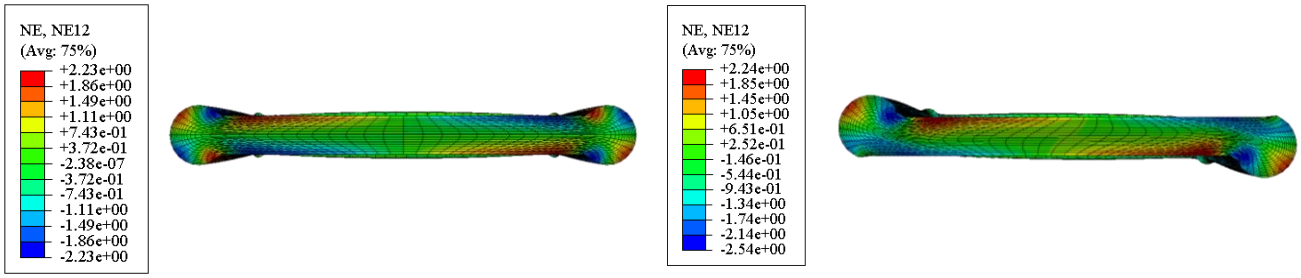

Block C

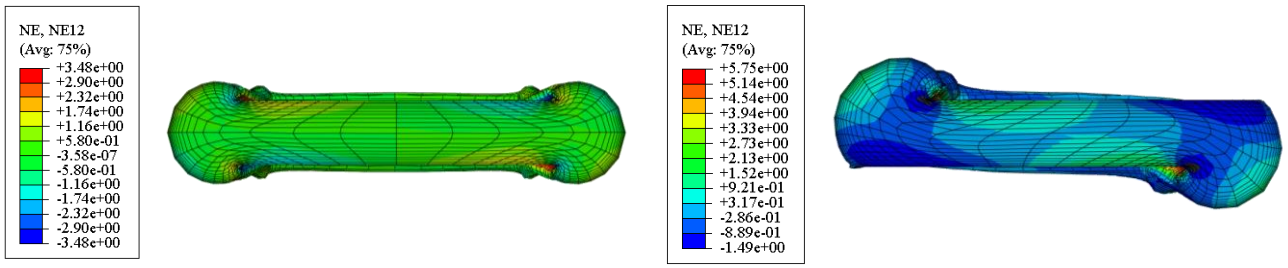

Block D

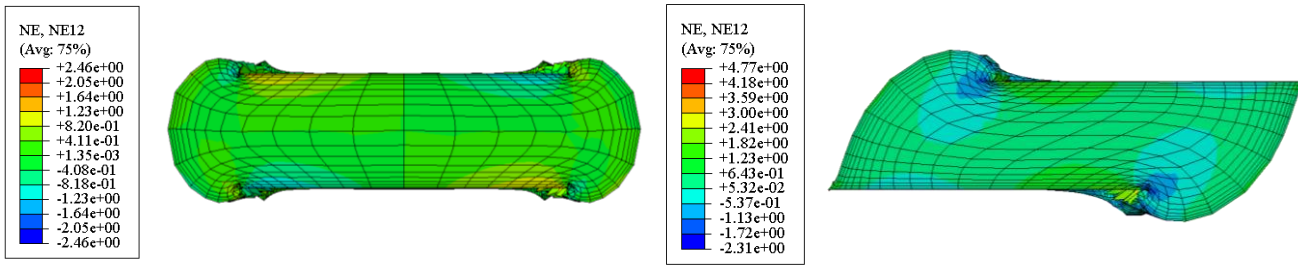

Block X

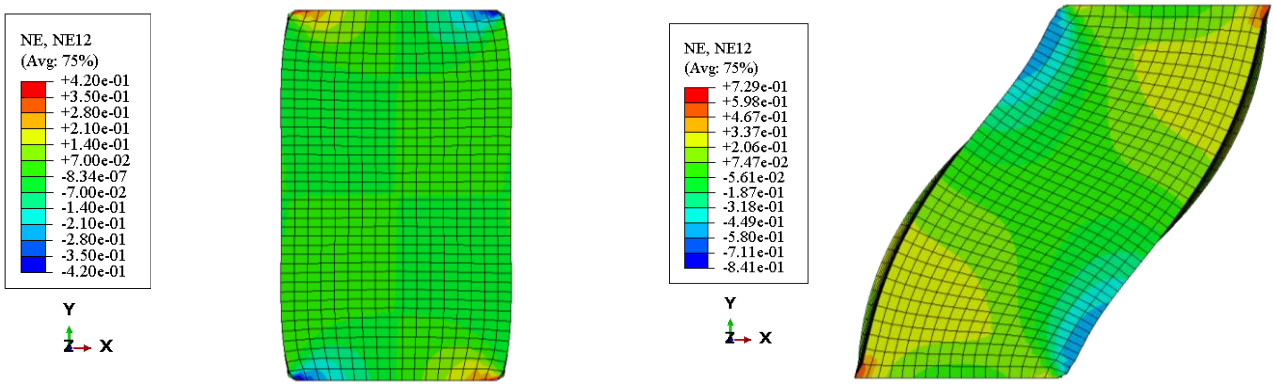

a) b)

Figure 4.6 Contour plot of NE12, i.e. nominal (i.e. engineering) shear strain distribution in the shear plane XY for half blocks subjected to (a) maximum compressive displacement alone and (b) maximum compressive displacement in combination with horizontal displacement.

The local distribution of Cauchy compressive and shear stress within the blocks is similar to that of the strains, and thus is not reported due to space constraints.

Figure 4.7 illustrates the contour plot of the total strain energy densities of the elements of each block subjected to the highest vertical compression and horizontal displacement applied in each test. It can be observed that the local strain energy densities increase with increase of the shape factor and thus they are the highest in Block B.

It is noted that the stress and strain concentrations occur at the edges of the plates bonded to the rubber; this is a well-known issue to designers of rubber components, and is mitigated by introducing filets in these regions. The detailing of such designs can be guided by FEA, as discussed by Gough & Muhr (2005).

Block B

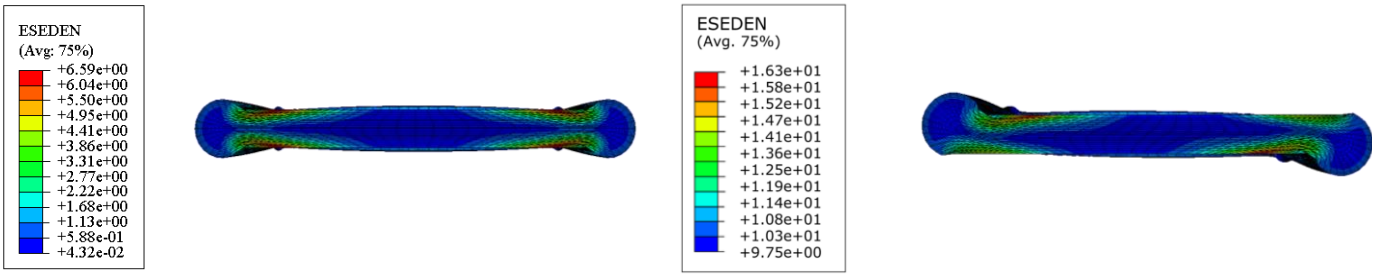

Block C

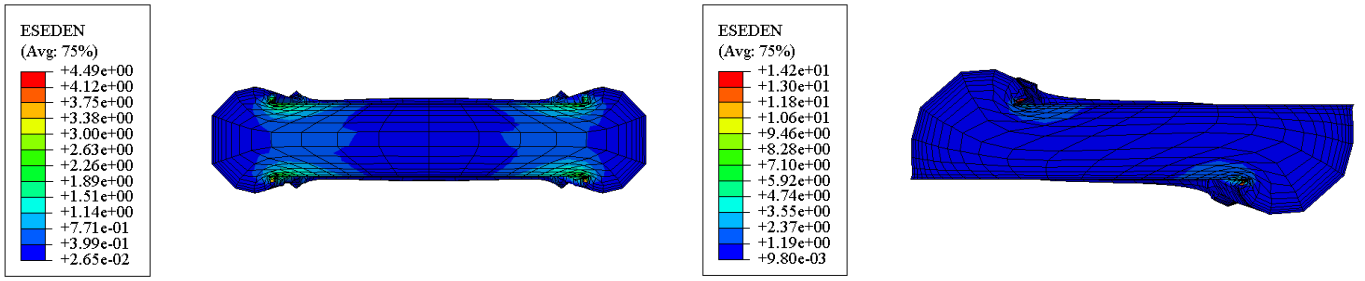

Block D

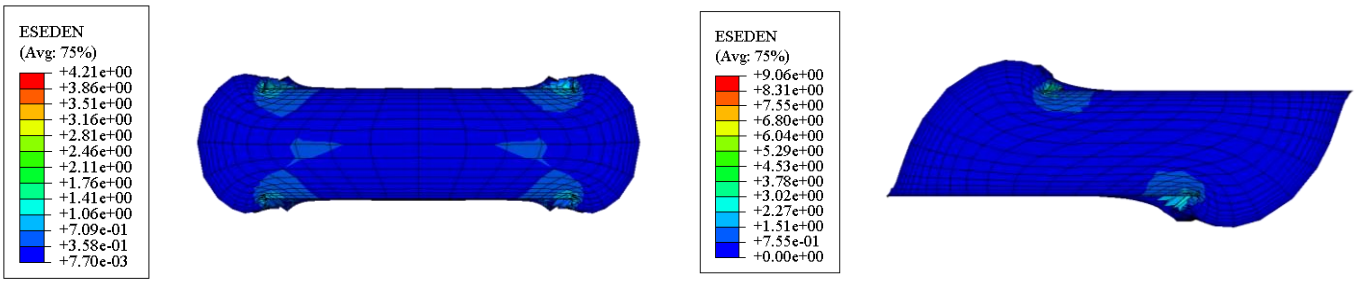

Block X

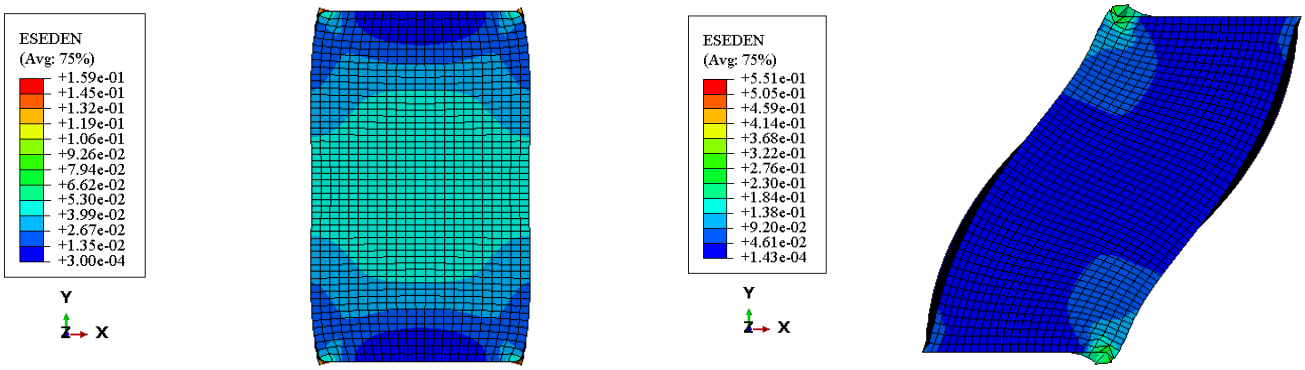

a) b)

Figure 4.7 Distribution of Total Strain Energy Density in N/mm^2 for half block subjected to (a) maximum compressive displacement alone and (b) maximum compressive displacement in combination with horizontal displacement.

4.3.3 Comparison of numerical and experimental results

Figure 4.8 shows the variation of the vertical force during compression of the blocks against the vertical deflection according to the experimental results and the FE analyses for the two rubber models. The trend of increase of the compressive forces with the increase of vertical displacement has a rising rate, due to the nonlinear hyperelastic behaviour of the rubber (Figure 4.4b), the increase of rubber area due to the bulging of the block, and the approach towards a limiting compression equal to the height of the block, when the tangent stiffness would be infinite. Overall, the compressive behaviour can be adequately characterized by both material models, with a comparable level of accuracy between them.

Further refinement of the models may be necessary to fully capture the complexity of the compressive behaviour, but the current results suggest that either model can be a viable option for modelling and simulation purposes. The response for the neo-Hookean model is stiffer than that of the Odgen model in the case of Block X, as is also the case in homogeneous compression (Figure 4.4a). On the other hand, Blocks B, C and D are characterized by high local shear strains due to the bulging, even under compression, and thus the shear behaviour significantly affects the response. Figure 4.4c shows that the behaviour of the neo-Hookean model in simple shear is softer than that of the Ogden model, which is consistent with the softening behaviour particularly evident in Block B for the neo-Hookean material model. Because the forces are much higher for block B, and its initial height is low, accurate displacement measurements during tests on it were more challenging, and in particular the compliance of the test machine might have resulted in the deflection being overestimated. Similarly, the very high stresses and strains may also impair the accuracy of the FEA.

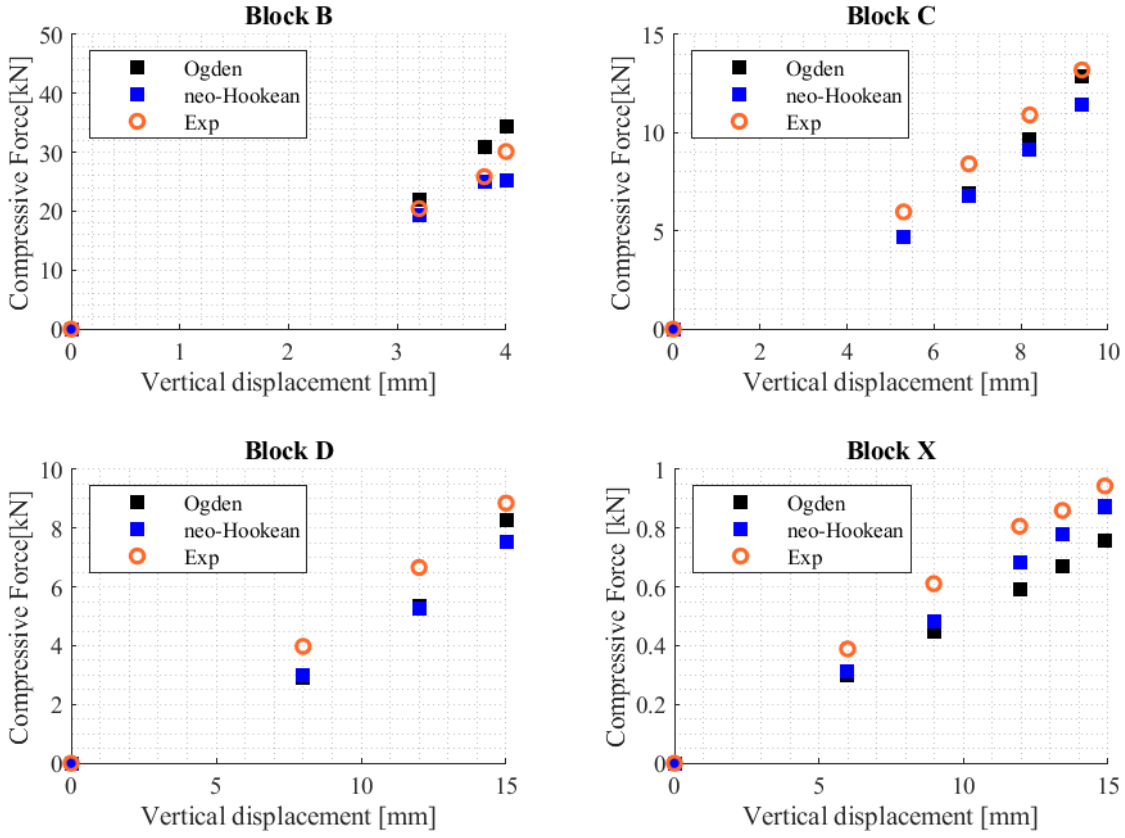

Figure 4.8 FEA predictions of compressive load vs vertical displacement and comparison with experimental results

Figure 4.9 shows the variation of the compressive force for increasing values of the shear displacement according to the experiments and the FE models. In general, it can be observed that the compressive force reduces with shear deflection. This is related to the well known observation that shear displacement under constant vertical load is accompanied by a decrease in height of rubber bearings.

Since this drop in height is prevented by the vertical restraint, the compressive loads decrease with increase in shear.

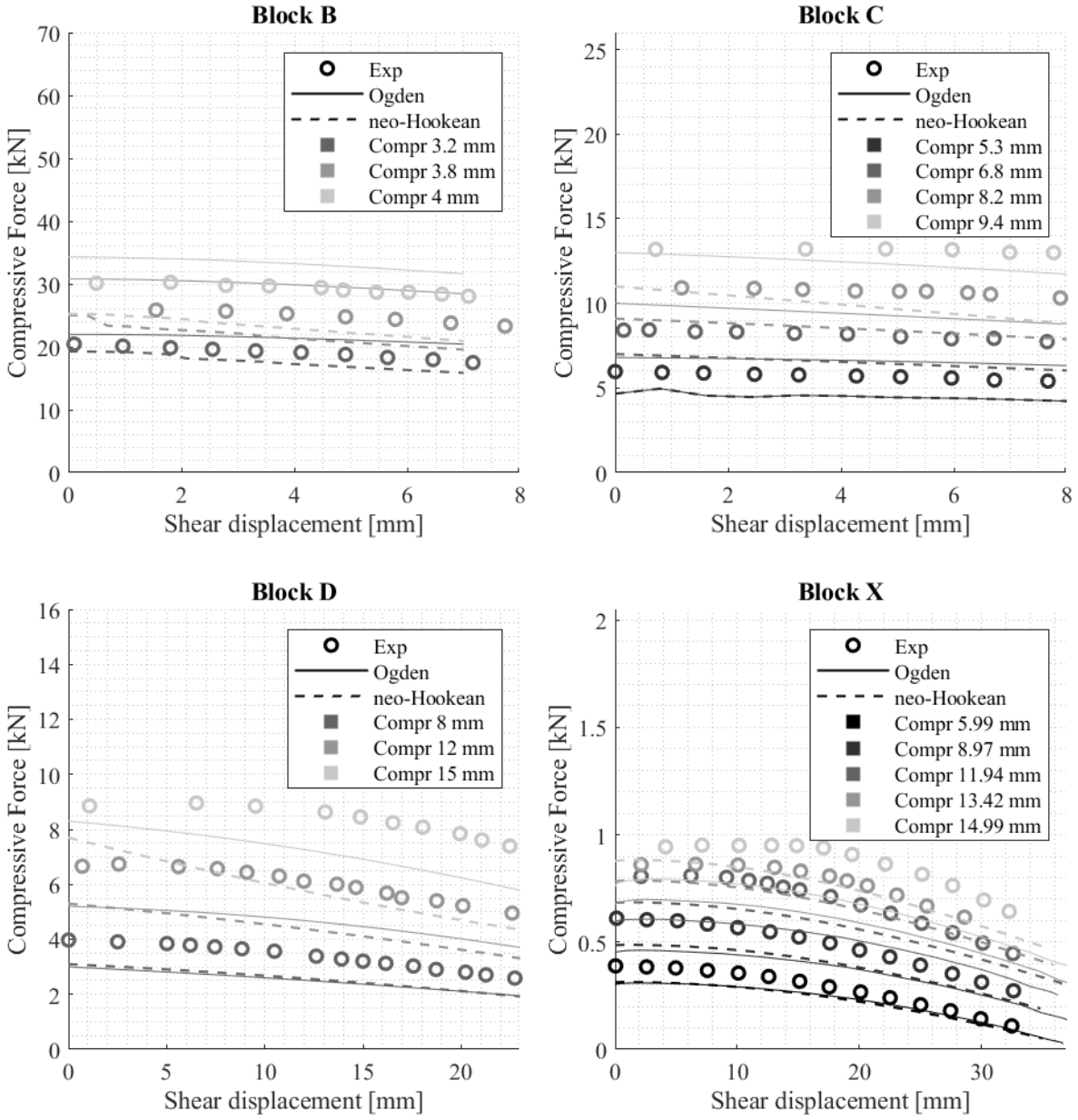

Figure 4.9 FEA predictions of compressive force vs shear displacement of each block and comparison with experimental results (different colours refer to different values of the vertical compression)

For sufficiently low vertical displacement values, both FEA models describe well the compressive and coupled compressive-shear behaviour of blocks. With the increasing of vertical displacement (i.e. from 11.94 mm for Block X, from 3.8 mm for Block B, from 6.8 mm for block C and from 12 mm for block D), a less good agreement is observed between the FEA results and the experimental results. Using the Ogden material model for the rubber, better results are obtained compared to those obtained using the neo-Hookean model. It is worth noting that the Ogden material model gives higher compressive forces

than the neo-Hookean model for all shear displacement values and for all blocks, except for Block X. This can be explained by the fact that in Block X the state of deformation is closer to homogenous compression, under which the Ogden model is softer than the neo-Hookean model (Figure 4.4a).

Figure 4.10 shows the shear load-deflection curves obtained for different fixed vertical compressions of the blocks. In general, by increasing the vertical displacement, the horizontal stiffness reduces, in line with other studies on the coupled compression-shear behaviour of rubber bearings (Thomas, 1982; Koh and Kelly, 1988). A horizontal tangent marks the condition of instability for the blocks for zero shear displacements.

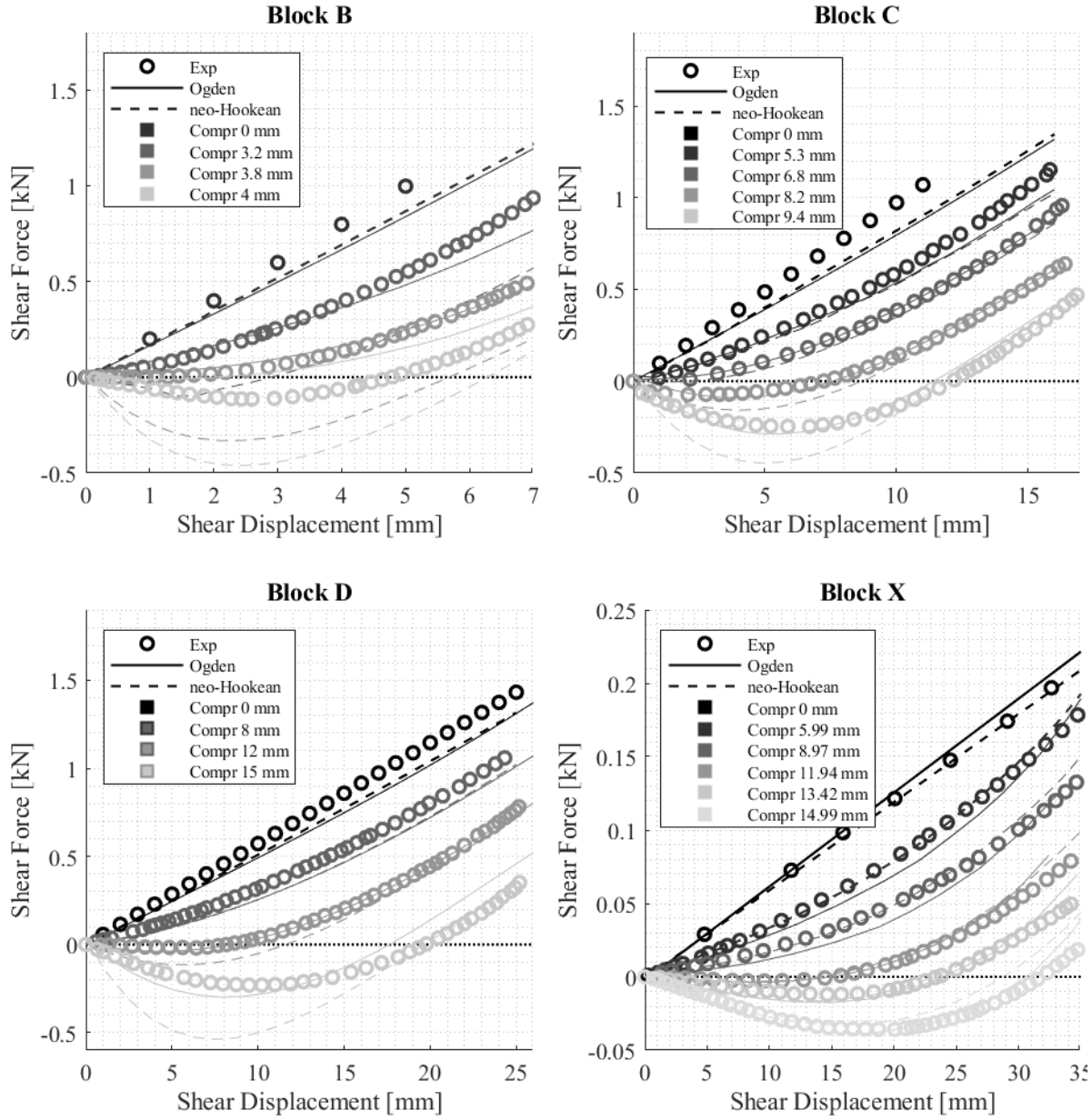

Figure 4.10 FEA predictions of shear force vs shear displacement of each block and comparison with experimental results

In the case of small compressions, the shear forces exhibit an almost linear trend of increase for increasing shear displacement, whereas under large compression the shear behaviour is highly nonlinear. The FEA model predictions are in good overall agreement with the experiments, with the Ogden model providing the best fit to the test results. The differences between the results obtained with the two different constitutive models are higher for higher compression levels and shear deflections, and the accuracy of the neo-Hookean model reduces significantly for very high values of the compressive displacement. It is also interesting to note that only in the case of shear of the shorter blocks (B,C,D) is there much difference between the FEA models. This can be explained by observing in Figure 4.5 and Figure 4.6, that local strains and stresses are higher for these blocks than for Block X when the maximum compressive displacement is considered, and that the two hyperelastic constitutive models are very different only at high shear strains (see Figure 4.4). It is also interesting to observe that in the case of blocks B, C and D, the response obtained with the neo-Hookean model is stiffer than that obtained with the Ogden model for low compression levels, and more flexible for high compression levels. The opposite trend is observed for Block X.

In order to shed further light into the influence of the compression of the blocks on the shear behaviour, the values of the tangent shear stiffness at zero shear strain according to the FE model and experimental results are calculated and plotted in Figure 4.11 vs. the values of the applied vertical deflection.

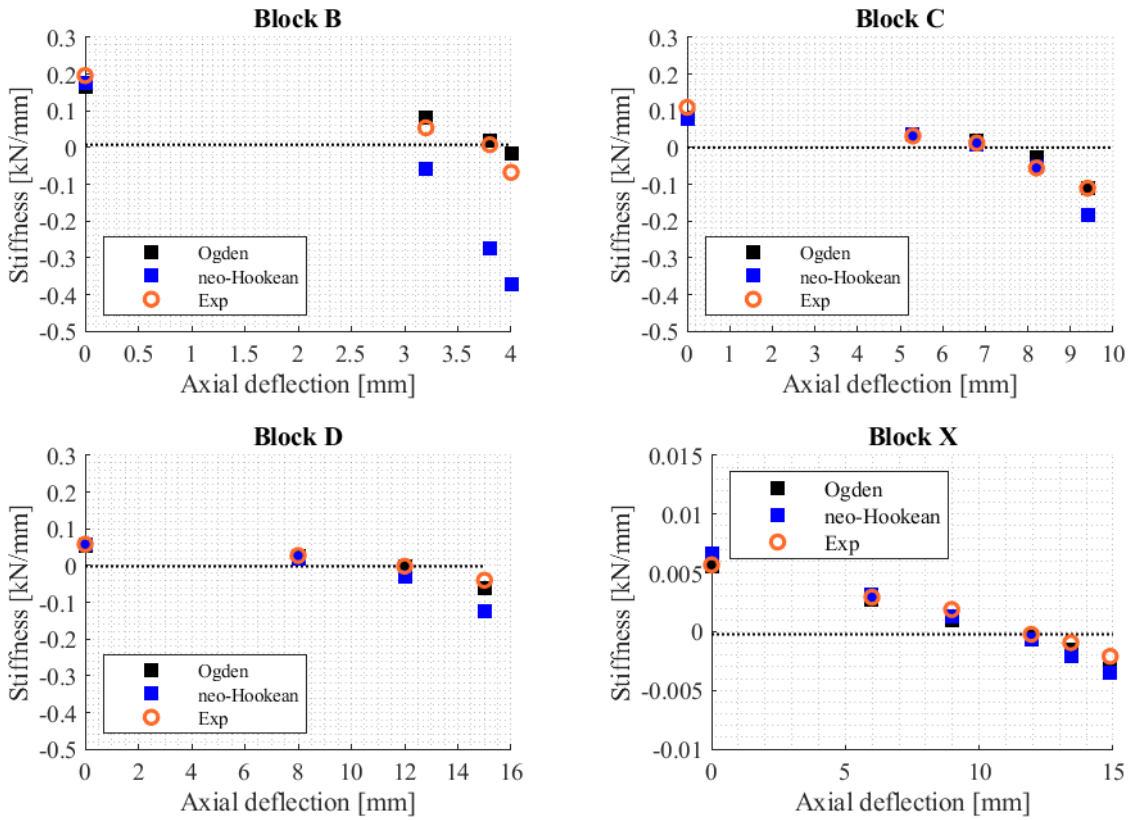

Figure 4.11 Tangent horizontal stiffness (at zero shear deflection) vs. axial deflection: comparison between FEA and experimental results

A progressive reduction of the tangent stiffness is observed with increase of the vertical displacement. The results of FEAs show that both material models can reproduce the response of the blocks in terms of shear stiffness versus the axial deflection, and thus also the critical load, to a fair approximation, except for Block B for which the neo-Hookean material model provides very inaccurate estimates when there is significant compression. This can be explained by the fact that the Ogden model is stiffer than the neo-Hookean model under simple shear at very high strains (see Figure 4.4).

4.4 Analytical modelling and comparison with experimental and numerical results

In this section, the theories proposed over the years for describing the compressive behaviour of rubber blocks of any aspect ratio are tested against the experimental and numerical results presented in the previous section. An extended theory, informed by the FE analyses results, is also proposed to take into account the non-uniform bulging along the compressed rubber block in the evaluation of the horizontal response of compressed blocks. Finally, analytical and numerical predictions of critical loads are compared with the experimental results.

4.4.1 Compression behaviour

Haringx (1948,1949) developed load-compression relationships for the case of bonded rubber blocks using Kosten (1942) boundary condition at the rubber ends: 1) unrestrained shear behaviour up to the bonded surface and 2) a fraction of the total rubber height equal to 1/8 of the shortest side of a rectangular block is assumed rigid to compression and (presumably) tilt. The compression load-displacement of the remainder of the block was taken as proportionality between true axial stress and strain, giving:

$$P = 3G\frac{A_0}{\lambda^{*2}}\left(1-\lambda^{*}\right) \tag{4.5}$$

Where

$$\lambda^{*} = \frac{\lambda h_0 - \frac{1}{8}a_0}{h_0 - \frac{1}{8}a_0} \tag{4.6}$$

G is the shear modulus, A_0 is the initial cross-sectional area of the rubber block, and λ is the axial extension/compression ratio of the block, which is related to the strain through $\varepsilon = \left(1-\lambda\right)$. Since in this chapter we are only discussing compression behaviour, we have chosen a sign convention such that the compression load P and deflection $\lambda(h_0\text{-}h)$ are both positive in compression, so that plots of

load versus deflection appear in the positive quadrant. Indeed, if the Haringx beam-column theory is used for both tensile and compressive behaviour, it is convenient to use two positive symbols for the load: P if it is compressive and $N = -P$ if it is tensile, each expressible using real numbers in terms of trigonometric functions for P and hyperbolic functions for N (eg Goodchild et al, 2018).

Gent and Lindley (1959) carried out experimental tests on rubber blocks subjected to compression between rigid adhering plates and developed approximate load-deformation relations for circular disks and for infinitely long rectangular blocks. For the former case, they proposed the following expression of the effective compression modulus E_C

$$E_c = E\left(1+2kS^2\right) \tag{4.7}$$

where E is the Young's modulus of rubber, equal to $3G$ in the case of incompressible rubber, S is the shape factor, and $k \approx 1$ for unfilled rubber, but is an empirically determined factor less than unity used to take into account, albeit crudely, the strain-softening and imperfectly elastic stress-strain behaviour of filled rubber in simple shear. Lindley (1966) observed that Equation 4.7 also applies to rectangular blocks with comparable maximum and minimum plan dimensions, and is valid only under small strains.

Gent and Meinecke (1970) extended the theory of Gent and Lindley (1959) to the case of bonded rubber blocks of any cross-section under small compression. The vertical load P can be related linearly to the axial strain ε through the following expression:

$$P = A_0 E_c \varepsilon = 3GA_0\left(f_{c1} + f_{c2}\right)\left(1-\lambda\right) \tag{4.8}$$

where f_{c1} and f_{c2} are numerical factors describing the effect of the bonded surfaces. For a rectangular cross section with sides $2a$ and $2b$, these factors can be expressed as:

$$\begin{aligned} f_{c1} &= \frac{4}{3} - \frac{2\left(a_0 b_0 + {h_0}^2\right)}{3\left({a_0}^2 + {b_0}^2 + 2{h_0}^2\right)} \\ f_{c2} &= \frac{4}{3} {S_1}^2 \left(1+\kappa\right)^2 \left[1 - \frac{192}{\pi^5}\kappa \sum_{n=1,3,5} \frac{1}{n^5} \tan\left(\frac{n\pi}{2\kappa}\right)\right] \end{aligned} \tag{4.9}$$

where $\kappa = a_0/b_0$.

For other sections, reference can be made to the original paper of Gent and Meinecke (1970).

The theories discussed above are derived by making three main assumptions: horizontal plane sections remain plane, vertical lines become parabolic after loading and the normal stress components in all three directions are the same, and equal to the mean pressure. Koh and Kelly (1989) proposed a solution of the compression modulus of bonded square rubber layers eliminating the stress assumption, whereas Tsai and Lee (1998) derived the compressive modulus of a bonded layer of infinite-strip, circular or

square shape. Koh and Lim (2001) estimated the compressive modulus for the case of rectangular pads, providing an analytical solution as an extended version of the Koh and Kelly (1989) approach.

Kelly and Konstantinidis (2011) adapted the theories discussed above to the case of laminated bearings with values of shape factor S>5. They provided closed-form relations of the compression modulus for infinite strips and circular and rectangular pads. These expressions can be cast in the same form as Gent and Meinecke's expression (Equation 4.8), with the numerical factor f_{c1} considered negligible and f_{c2} defined as in Equation 4.9.

Yeoh (1985) developed an expression for the compressive stiffness of tall cylinders of solid circular cross-section bonded at both ends to rigid plates, based on an improved description of the lateral constraining effect of the plates. However, he did not consider the case of rectangular blocks and assumed a linear behaviour and small strains.

Lindley (1966) provided an expression accounting for the non-linear relationship between force P and strain for a block of circular cross-section. He assumed the Young's modulus E to be independent of the state of strain and considered the increase of shape factor due to the decreasing thickness of the rubber block by a factor of $1/\lambda$, which coincides with the increase of loaded area of rubber:

$$P = 3GA_0\left[-\ln\lambda + S^2\left(\frac{1}{\lambda^2}-1\right)\right] \tag{4.10}$$

Equation 4.10 can be generalised to blocks of any cross-section by using the correction factors provided by Gent and Meinecke as follows ((Fabrizia Cilento *et al.*, 2017)):

$$P = 3GA_0\left[-f_{c1}\ln\lambda + \left(\frac{1}{\lambda^2}-1\right)\frac{f_{c2}}{2}\right] \tag{4.11}$$

Goodchild et al. (2018) used the Mooney-Rivlin constitutive material, instead of a linear elastic one, to express the axial load–stretch relation for rubber strips (very slender rubber blocks) under a homogeneous strain field not perturbed by the end plates, corresponding to the following relationship:

$$P = 2A_0\left(\frac{1}{\lambda^2}-\lambda\right)\left(C_{10}+\frac{C_{20}}{\lambda}\right) \tag{4.12}$$

where C_{10} and C_{20} are material constants such that $G=2(C_{10}+C_{20})$ for a Mooney-Rivlin material model (at zero shear deformation).

Muhr (2017) revised this formulation for application to the case of rubber blocks with bonded end-plates, obtaining the following expression, devised to reduce to Equation 4.10 for significant shape factors and to Equation 4.12 for a negligible shape factor:

$$P = GA_0\left[\left(\frac{1}{\lambda^2}-\lambda\right)+3S^2\left(\frac{1}{\lambda^2}-1\right)\right] \tag{4.13}$$

Stanton et al. (1990) also provided an extension of the classic theory of rubber blocks to include axial shortening and the increase in plan area due to bulging of an elastomer under compressive load. They consider a nominal Poisson ratio $\nu = 0.3$ (rather than 0.5), chosen empirically to account for the non-uniform increase of area along the height due to the effect of the end plates. The theory assumes small deformation and a linear elastic material, and it was applied to the case of discreetly layered bearings. The model consists of a homogeneous shear flexible column, with compressive, shear and bending stiffnesses, which are functions of strain and are approximated by assuming that the plan dimension of each elastomeric layer increases by a factor (1 + ν(1–λ)). The compressive force is:

$$P = 3GA_0\left(f_{c1}+f_{c2}\right)\frac{\left(1+\nu\left(1-\lambda\right)\right)^3-1}{3\nu\left(1-\lambda\right)}\left(1-\lambda\right) \tag{4.14}$$

In order to evaluate the accuracy of the different theories, the values of the axial load *P* are calculated using equations 4.5, 4.8, 4.11, 4.12, 4.13 and 4.14 for different values of the vertical deflection and compared with the experimental and numerical results in Figure 4.12. The value of shear modulus *G* is 0.5 MPa.

The formula proposed by Gent and Meinecke (1970), reported here in Equation 4.8, valid for small compression levels, is not able to describe the nonlinear trend. Also the theory of (Stanton *et al.*, 1990), Equation 4.14, despite considering the increase of transverse area of the rubber due to Poisson's effect, significantly underestimates the compressive stiffness of the blocks. On the other hand, both the models of Lindley (1966), Equation 4.11, and Muhr (2017), Equation 4.13, agree well with the experimental results.

In order to investigate further this issue, the secant compressive modulus $E_{c,\mathrm{sec}}$ at a given deformation level λ is evaluated considering the various formulations as follows:

$$E_{c,\mathrm{sec}} = \frac{P}{A_0\left(1-\lambda\right)} \tag{4.15}$$

The secant modulus is then normalized by dividing it by the value at zero deformation. Muhr (2017) derived the following expression for the normalized compressive secant modulus:

$$\frac{E_{c,\mathrm{sec}}}{E_{c0}} = \frac{\frac{1}{\lambda^2}\left\{\left(\lambda^2+\lambda+1\right)+3S^2\left(\lambda+1\right)\right\}}{3\left(1+2S^2\right)} \tag{4.16}$$

where E_{c0} coincides with $E_{c,\sec}$ for λ =1. In the case of *S*=0 (homogeneous strain field not perturbed by the plates), this relation reduces to the one found by Goodchild et al. (2018).

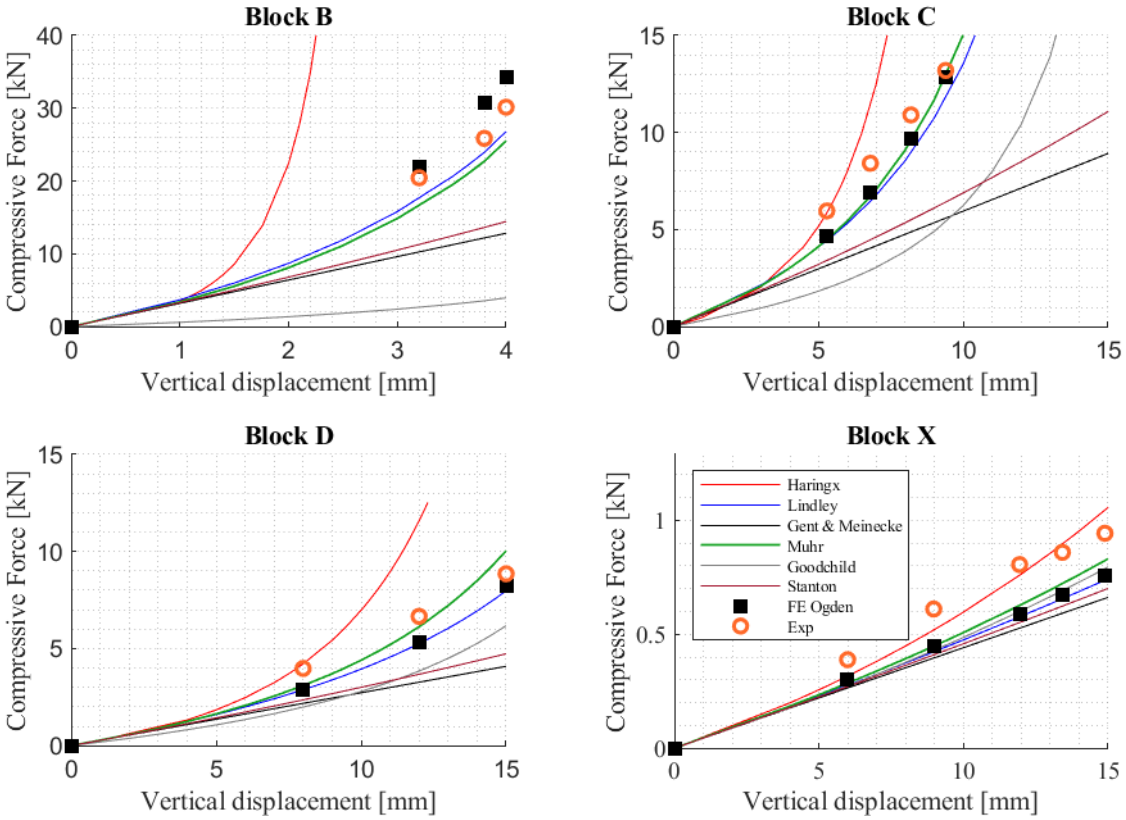

Figure 4.12. Force-displacement behaviour according to equation 4.5 (Haringx's theory) equation 4.8 (Gent and Meinecke's theory), equation 4.11 (Lindley's theory), equation 4.12 (Goodchild's theory), equation 4.13 (Muhr's theory) and equation 4.14 (Stanton's theory) and experiments. FE results (Ogden) from Figure 4.8 are also reported.

The normalized secant compression modulus from Stanton's theory has the following expression:

$$\frac{E_{c,\sec}}{E_{c0}} = \left(1+\nu\left(1-\lambda\right)+\frac{\nu^2\left(1-\lambda\right)^2}{3}\right) \qquad 4.17$$

Figure 4.13 shows the variation with λ of the secant compression modulus defined by the above equations and by the FEA results obtained by using the neo-Hookean material model.

In general, the FE analyses reveal a high sensitivity of the ratio $E_{c,sec}/E_{C0}$ with respect to λ and also with respect to the shape factor *S*. It can be observed that the ratio $E_{c,sec}/E_{C0}$ increases for decreasing λ and increases for increasing shape factor. The secant compression modulus according to Stanton et al.'s model is not very sensitive to λ, and independent of the shape factor. Muhr's theory is capable of accounting for the dependency of the secant compressive modulus on both the axial shortening and the shape factor, although there are discrepancies with the FEA results.

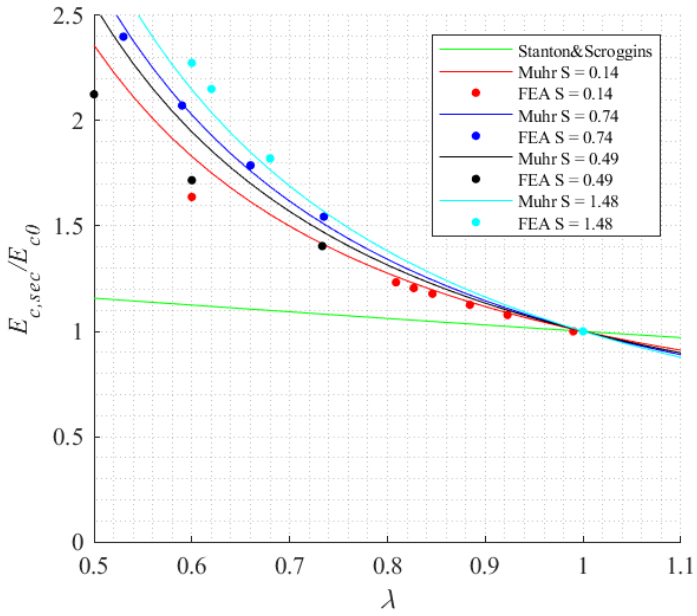

Figure 4.13 Effect of vertical compression on secant compression modulus

4.4.2 Combined compression and shear behaviour

The theory for the behaviour of flexural-shear deformable elastic beams under the combined action of compressive and shear forces was originally developed by Timoshenko (1921). Haringx (1948,1949) derived a similar theory for application to coil springs and rubber cylinders, and Gent adapted this for application to rubber laminated bearings ((Gent, 1965)). The model at the base of these theories is a flexural-shear deformable column of length h_0 subjected to an axial compressive load P; in this chapter we shall assume that the axial direction is vertical and the lateral direction is horizontal. The kinematics can be described by the lateral displacement of the centre line $v(x)$, and the rotation of the cross section, $\psi(x)$. A horizontal force F is applied at the upper end which is free to move horizontally but is restrained from cross section rotation, while the lower end of the column is fixed. In the linear elastic case, the following expression of the horizontal stiffness of the beam is obtained (Thomas, 1982):

$$K_h = \frac{P^2}{Ph - 2qB\tan\left(\frac{qh}{2}\right)} \tag{4.18}$$

Where

$$q^2 = \frac{P(R-P)}{BR} \tag{4.19}$$

In equation 4.19, *B* and *R* are the bending and shear stiffness parameters for unit length of the column, respectively, derivable from constitutive relations for the particular type of beam-column in mind.

From equation 4.18, the lateral stiffness of the block would fall to zero if $(q/2)h \to \pi$. Under this condition, the term $\tan\left((q/2)h/2\right) \to \infty$ and the compressive load *P* attains a critical value P_{cr}, given by

$$\frac{P_{cr}}{B}\left(1+\frac{P_{cr}}{R}\right)=\frac{\pi^2}{h^2} \tag{4.20}$$

This equation can be solved for P_{cr}, to obtain the expression of the critical load:

$$P_{cr}=\frac{R}{2}\left[-1+\sqrt{1+\frac{4\pi^2 B}{Rh^2}}\right] \tag{4.21}$$

Thomas et al. (1982) assumed *B*, *R* and *h* in the undeformed initial configuration. Bending and shear stiffness parameters have been derived by Haringx for the case of a rubber rod in (Haringx, 1949). Gent (1965) provided these parameters for the case of laminated rubber bearings, further refined by Gent and Meinecke (1970) and extended to any cross-section. Goodchild et al. (2018) derived expressions for the bending and shear stiffness of a rubber prism, modelled as a Mooney material, as functions of finite-strain axial elongation. Muhr (2017) investigated the applicability of the expressions of Goodchild et al. (2018) to blocks of rubber with bonded end faces. The bending stiffness $B = E_{C,bend}I$ corresponding to an axial elongation λ was obtained from an incremental Young's modulus, $E_{C,bend}$, referred to the strained state and expressed as a function of the shape factor, and the second moment of area of the cross section in the deformed state, *I*. The expression obtained for $E_{C,bend}$ is:

$$E_{C,bend} \approx G\left(2\lambda^2+\frac{1}{\lambda}\right)\left(1+\frac{2S^2}{3}\right) \tag{4.22}$$

This reduces to the case of Goodchild et al. (2018) for $S = 0$.

The expression of *I* for a deformed rectangular rubber prism normal to its axis was taken to be:

$$I=\frac{a^3 b}{12}=\frac{a_0{}^3 b_0}{12\lambda^2}=\frac{I_0}{\lambda^2} \tag{4.23}$$

where I_0 is the second moment of area of the cross section in the undeformed state.

The shear stiffness parameter according to Goodchild et al. and Muhr's theory is evaluated as follows:

$$R=\frac{A_0}{\lambda}\frac{\tau}{\gamma}=\frac{A_0}{\lambda}\frac{1}{\gamma}\left[2\gamma\lambda^2\left(\frac{\delta U}{\delta I_1}+\frac{1}{\lambda}\frac{\delta U}{\delta I_2}\right)\right]=2A_0\lambda\left[C_{10}+\frac{1}{\lambda}C_{20}\right] \tag{4.24}$$

For $C_{20} = 0$, as assumed by Muhr (2017) and throughout the remainder of this chapter :

$$R = \lambda G A_0 \tag{4.25}$$

Stanton et al. (1990) suggested an expression of the bending stiffness, intended for rubber bearings with multiple laminations rather than a single block, in the form:

$$B = f_r E I_0 \left(1 + \nu^* \left(1 - \lambda\right)\right)^4 \tag{4.26}$$

where ν^* is a fitting parameter akin to Poisson's ratio, but of uncertain magnitude, and f_r is the bending stiffness factor ((Gent and Meinecke, 1970)), taken here as $f_r = 1 + 0.5S^2$.

The shear stiffness parameter according to Stanton's theory is:

$$R = G A_0 \left(1 + \nu^* \left(1 - \lambda\right)\right)^2 \tag{4.27}$$

The global lateral stiffness K_h from Muhr's theory is obtained by substituting Equations 4.22, 4.23 and 4.24 into Equation 4.18 and considering the rubber height in the deformed configuration, evaluated as $h = \lambda h_0$, reducing to Goodchild's expression if the shape factor is zero; Stanton's theory is applied by substituting 4.26 and 4.27 into 4.18.

It is noteworthy that in a conventional Euler column, the reduction in transverse stiffness caused by axial load can be approximated by

$$K_h = K_{h0}\left(1 - \frac{P}{P_{cr}}\right) \tag{4.28}$$

where K_{h0} denotes the horizontal stiffness for zero compression.

In the case of a shear-flexible column such as the one considered in Haringx's theory, under some simplifying assumptions, the following expression can be derived, as also discussed in Roeder et al. (1987):

$$K_h = K_{h0}\left(1 - \left(\frac{P}{P_{cr}}\right)^2\right) \tag{4.29}$$

Figure 4.14 compares the plots of the horizontal stiffness vs. the axial deflection according to these theories and the experimental results. Shown in the same figure are the plots corresponding to Equation 4.29 and to Haringx's theory, i.e. Equation 4.18 with the bending and shear stiffness parameters defined in (Haringx, 1949) for rubber rods, with his end "correction" to allow for the lateral restraint of bonding the rubber to rigid endplates. Goodchild et al.'s theory is appropriate only for the lowest shape factor considered (S = 0.14), whereas for higher shape factors it provides horizontal stiffness values almost

constant as the axial deflection increases. This demonstrates the high importance of the shape factor on the compressive modulus of the rubber in evaluating the behaviour of the rubber blocks. Stanton's theory, instead, captures the trend of decrease of the horizontal stiffness due to the axial deflection. Muhr's theory provides quite good estimates of the horizontal stiffness for Block X and is also able to describe the effect of the compression with quite good accuracy. However, shear stiffness predictions for the other blocks diverge from the experimental results to a progressively greater extent as the compression is increased, and the model fails to predict the observed instabilities at the highest compressions. The next section presents a modified theory to meet these shortcomings.

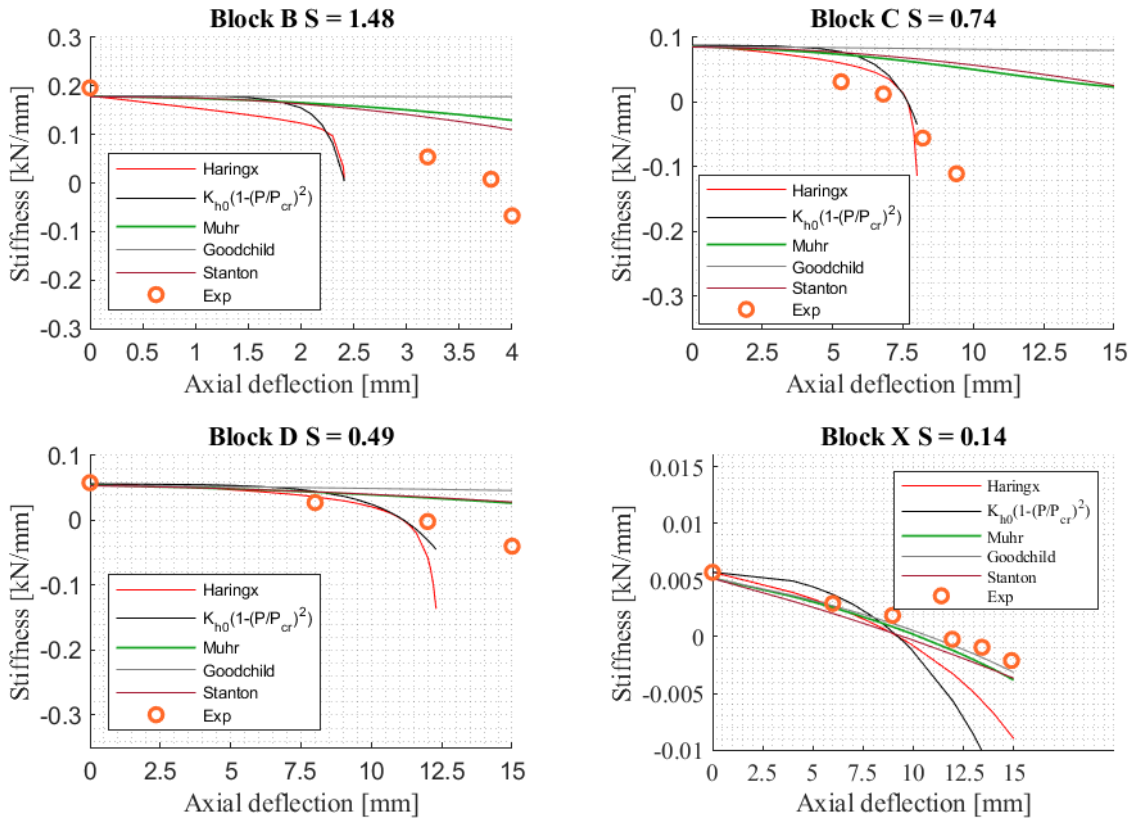

Figure 4.14 Tangent horizontal stiffness (at zero shear deflection) vs axial deflection: comparison between experimental tests and analytical estimates obtained according to equation 4.18, with B and R evaluated using Haringx, Muhr, Goodchild and Stanton theories, and equation 4.29.

4.5 Improved theory for lateral stiffness of compressed rubber blocks

For low and moderate shape factors rubber may be assumed to be incompressible, so that when a rubber block is compressed, each side bulges laterally such that the volume is kept constant. Figure 4.15 shows an example of a square block (W_0 is the initial width of the transverse section) made of an incompressible rubber, which is compressed in the vertical direction by λ. Since the volume is constant, the deformation on the two horizontal directions is $1/\sqrt{\lambda}$. This is true only in the case of an unconfined

rubber block (Figure 4.15a). On the other hand, in the case of a rubber block bonded at each end, the stretch along the horizontal directions is higher than $1/\sqrt{\lambda}$ (Figure 4.15b) in the middle section, and decreases towards unity at the bond edge.

The theory of Stanton et al. (1990) accounts for the bulging in a simplified way by introducing an "equivalent Poisson ratio" ν^* which they chose to be 0.3; if the block is compressed by a strain of $\varepsilon = 1-\lambda$, it will bulge and increase laterally its dimensions by, on average, the factor $\nu^*\varepsilon$ so that the cross sectional area will become $A \approx (1+\nu^*\varepsilon)^2 A_0$ and the second moment of area will become $I \approx (1+\nu^*\varepsilon)^4 I_0$.

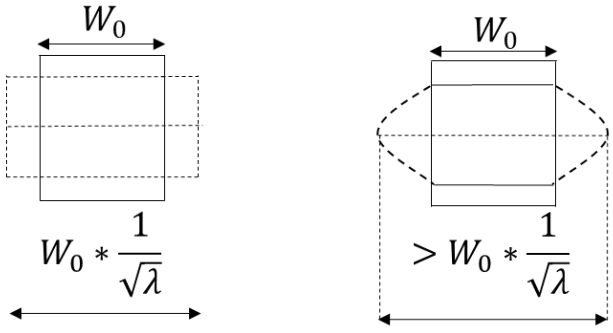

(a) (b)

Figure 4.15 Incompressible rubber block subjected to a vertical compression: (a) unbonded rubber block, (b) bonded rubber block

FE analyses, using the neoHookean material model, have been performed to investigate further the effect of the non-uniform bulging on the shear and tilting stiffness. For this purpose, Block B (Figure 4.16) is considered. This is a very stocky block, for which the response to horizontal deflections is dominated by shear deformation. Subjecting an FE model of Block B to a shear loading without applying any pre-compression results in a horizontal stiffness of 174 kN/m, close to the value of 180 kN/m evaluated for a block under simple shear, GA_0/h_0, where A_0 is cross-sectional area. Another block is considered (Figure 4.17a), with dimensions that correspond to the reduced height and an idealised bulged area of block B of incompressible rubber subjected to the maximum compression load observed experimentally (30kN). The plate dimensions are the same as in the original block, i.e., the extended portion of the block is not confined. When this block is subjected to a shear loading (Figure 4.17b), the unconfined parts of the block tilt without deforming, and thus they do not contribute to the shear stiffness. The shear stiffness evaluated numerically, equal to 270 kN/m, is comparable to that obtained with the simple expression GA_0/h_0 = 300 kN/m, considering A_0 as shear area and h_0 as height 6mm. Therefore, it can be concluded that under horizontal deflections, only the rubber within the area of the reinforcing plates contributes to the shear behaviour. This effect is also evident in shear of pre-compressed blocks, as shown in Figure 6b.

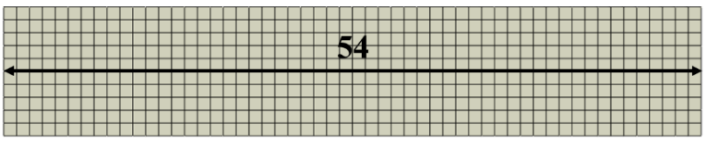

(a)

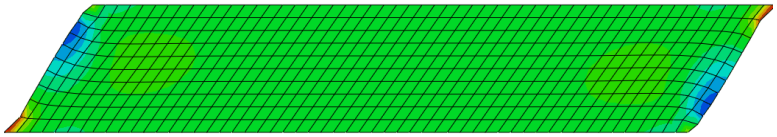

(b)

Figure 4.16 Block B a) Undeformed configuration b) Deformed configuration due to the highest shear load observed experimentally. Modified geometry to simulate the behaviour with the additional area

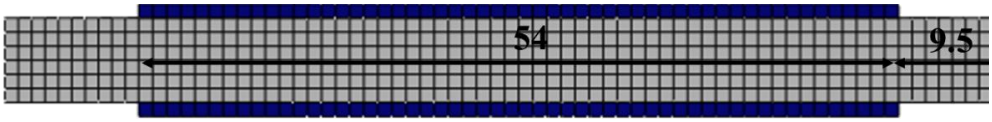

(a)

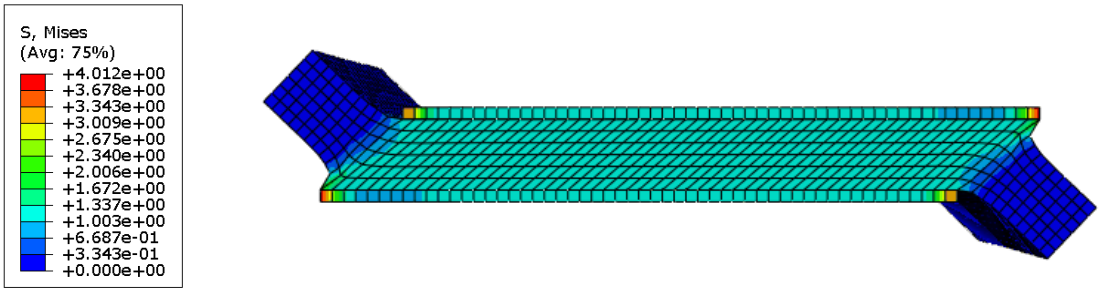

(b)

Figure 4.17 Block B, modified geometry to simulate the shear behaviour of the block of Figure 16 when precompressed a) Unsheared configuration b) Sheared configuration due to the highest shear load observed experimentally.

In the original theory of Goodchild (2018), R was taken to be equal to $\frac{A_0}{\lambda}\frac{\tau}{\gamma}$ (see the Appendix of Goodchild et al. (2018) and Equation 4.24), which neglects the absence of tractions on the lateral free surface of the rubber, and thus the effect shown in Figure 4.17b and evident also in Figure 4.6b. This observation suggests the shear parameter would be reduced by approximately the factor $A_0/A = \lambda$ leading to a revision to the value of R by the same factor, which yields

$$R = GA_0\lambda^2 \qquad 4.30$$

Equation 4.30 gives a stronger softening effect on the shear parameter at a given compression than in Muhr's theory (Equation 4.25).

On the other hand, the bulging is expected to contribute to the bending stiffness of the rubber blocks. This contribution is found to be evident for more slender blocks such as Block X, for which the effect of the confinement of the plates is small, whereas it is expected to be negligible for stocky blocks such as block B, for which the behaviour is dominated by shear compliance.

A novel expression is proposed for the second moment of area I to be considered in evaluating the tilting stiffness. Instead of using Equation 4.23, this is expressed as $I = I_0\Psi^2$, where Ψ is a correction factor describing the effect of the confinement of the plates on the rubber block bulging. The aspect ratio a_0/h_0 (a_0 being in direction of shear loading) is used to define the effect of the bulging. It is noteworthy that in the case of incompressible rubber ($E = 3G$), this factor is equal to:

$$\frac{a_0}{h_0} = 4\sqrt{\frac{EI_0}{h^2{}_0 GA_0}} \tag{4.31}$$

Thus, this geometrical parameter is related to the shear parameter of Timoshenko theory defined as $\Omega = EI_0/GA_0h_0^2$ ((Wang, 1995)) which describes the relative importance of shear compliance over the bending compliance. In fact, GA_0/h_0 is the shear stiffness and EI_0/h_0^3 is the flexural stiffness. When EI_0/h_0^3 is small, i.e. small a_0/h_0, there is a higher contribution of flexure, whereas when GA_0/h_0 is small, i.e. high a_0/h_0, there is a higher contribution of shear deformability. In the case of laminated rubber bearings, the ratio between the rubber layer width and total bearing height is denoted as secondary shape factor (Montuori et al., 2016).

The following semi-empirical expression for Ψ was devised using a trial-and-error analysis to achieve the best fit to the FE analysis results:

$$\psi = \begin{cases} \left(\dfrac{1}{0.125\, a_0/h_0 + \sqrt{\lambda}\left(1 - 0.125\left(a_0/h_0\right)^2\right)} \right)^2 & \left(a_0/h_0\right)^2 < 8 \\ 1 & \left(a_0/h_0\right)^2 \geq 8 \end{cases} \tag{4.32}$$

It can be noted that $\Psi = 1/\lambda$ for $(a_0/h_0)^2 = 0$, as in Muhr's original theory, since the effect of the confinement is not significant in an infinitely slender block, whereas $\Psi = 1$ for $(a_0/h_0)^2 \geq 8$, since in stocky blocks the confinement is very significant.

The value of the bending stiffness parameter, which has been modified using Ψ to take into account the bulging effect, is

$$B = E_{C,bend} I_0 \psi^2 \tag{4.33}$$

Figure 4.18 shows the results obtained using the expression of the shear stiffness of equation 4.30 and of the bending stiffness of equation 4.33 with $E_{C,bend}$ defined from equation 4.22. It also shows the

comparison with Muhr theory, experimental and numerical results. It can be observed that the modified theory provides an excellent fit to the results, both FEA modelling and experimental.

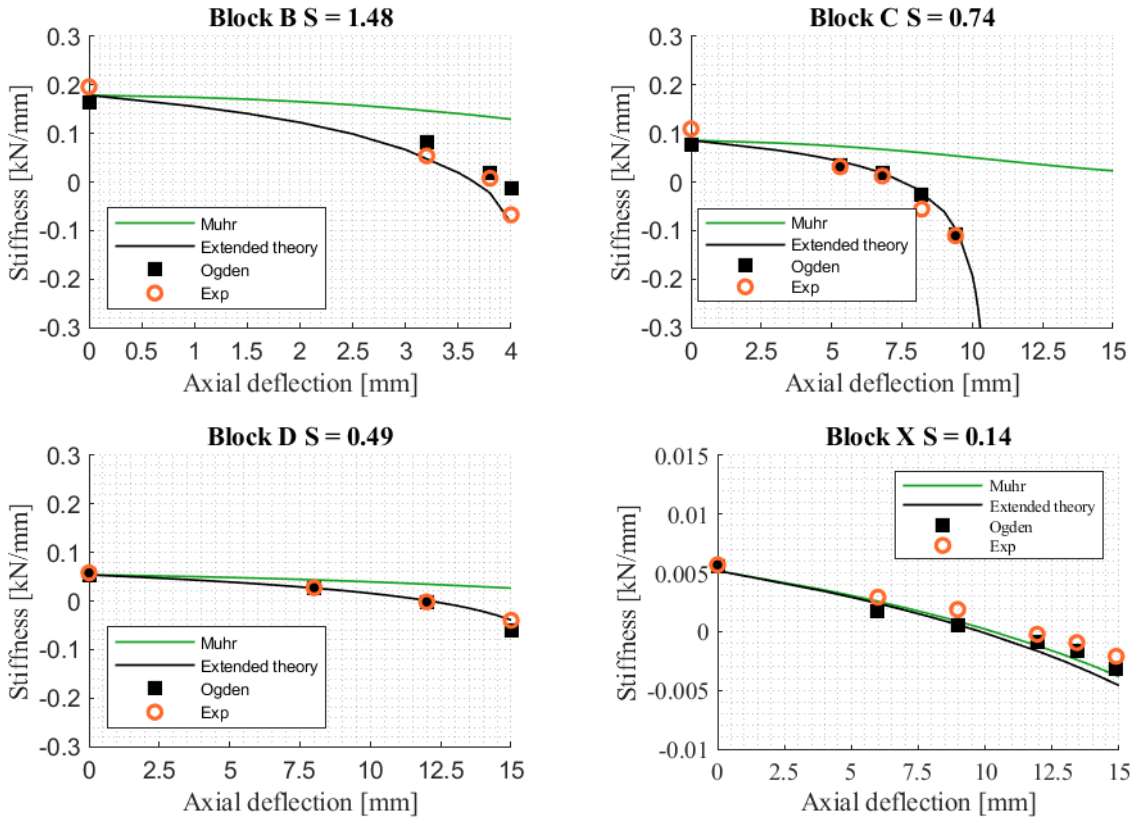

Figure 4.18 Tangent horizontal stiffness (at zero shear deflection) vs axial deflection: comparison between experimental tests and analytical results obtained with Muhr and the proposed extended theory

4.5.1 Critical load

Table 4.3 shows the predicted critical loads from the Haringx theory, equation 4.21; Stanton et al. model, equation 4.21 with bending and shear stiffness expressed as functions of their Poisson ratio parameter and adapted to the case of rubber blocks; extended theory, equation 4.21, with bending and shear stiffness evaluated with equations 4.33 and 4.30, and h is the rubber block height in the deformed configuration due to the compressive load. Table 4.3 also reports the values of the critical load according to Lanzo's theory. Lanzo (2004) provided a closed form of the critical load of multi-layered rubber bearings on the basis of a linear elastic model, derived from the classical beam theory, but enriched with the axial deformability in addition to the shear and flexural deformability, as follows:

$$P_{cr} = \frac{-1+\sqrt{1+\frac{4\pi^2 B}{h_0^{\,2}}\left(\frac{1}{R}-\frac{1}{EA}\right)}}{2\left(\frac{1}{R}-\frac{1}{EA}\right)} \qquad 4.34$$

However, similarly to Haringx's theory, this theory does not account for the dependency of bending and shear stiffnesses on axial shortening and shape factor.

These values are compared against the critical load obtained from experimental and numerical results by means of an average percent error defined as follow:

$$\Delta\% = \frac{\sum_{i=A,B,C,D} \left|\Delta\%_i\right|}{4} \qquad 4.35$$

Where $\Delta\%_i$ denotes the percentage ratio of the analytical estimates to the experimental or numerical estimate for block *i*, with i = A,B,C,D.

Table 4.3 Predicted and experimental critical loads and average percent errors

	Haringx	**Stanton et al. (1990)**	**Lanzo (2004)**	**Extended theory**	**FEA Ogden**	**FEA neo-Hookean**	**Experim.**
	P_{cr} (kN)	P_{cr} (kN)	P_{cr} (kN)	P_{cr}(kN)	P_{cr} (kN)	P_{cr} (kN)	P_{cr} (kN)
Block B	60.4	24.5	17.4	21.0	30.8	25.0	26.0
Block C	17.0	14.0	10.1	8.2	6.9	6.8	8.4
Block D	9.2	8.1	6.3	6.3	5.3	5.3	6.7
Block X	0.50	0.44	0.41	0.50	0.59	0.68	0.81
Δ% to Experim.	70%	35%	27%	17%	21%	15%	0%
Δ% to FEA (Ogden)	80%	25%	34.4%	24.4%	0%	9.5%	24.6%
Δ% to FEA (neo-Hookean)	90%	50%	34.8%	20.7%	10%	0%	18.4%

It is remarkable that the estimates of P_{cr} calculated naively from the Stanton or Lanzo theories show a relatively small deviation of only 25% to 35% from the FEA or experimental results, since these theories are based on a continuum beam-column limit for bearings comprising a sufficiently large number of identical layers laminated in series such that the discreteness of the layers may be smeared into a continuum (see Schapery and Skala, 1976 and Gent, 1965). It can be observed that Haringx's theory overestimates the critical load when compared to both numerical and experimental results for Block B, C and D, whereas for Block X the value is underestimated. Stanton et al.'s theory overestimates the critical load when compared with experimental results, for Block C and D. Lanzo's theory provides higher critical loads with respect to the Gent theory due to contribution of the axial deformability of the rubber block, but it gives the highest average percent error when compared to the numerical results. The extended theory, which attempts to include effects of non-linearity and finite strain, provides overall the best estimates when compared to the numerical results. Finally, it can be observed that both Ogden

and neo-Hookean material models are in good agreement with experiments. It is noteworthy that the Ogden material model provides higher values of the critical load for all blocks expect for Block X. This is consistent with the results shown in Figure 4.9 where it can be observed that the Ogden model is stiffer for the same blocks, presumably because the Ogden model is softer than neo-Hookean only in homogeneous compression (Figure 4.4), which is the predominant mode of deformation only for Block X.

4.6 Conclusions

The behaviour of bonded rectangular blocks with low shape factor subjected to vertical and horizontal loading is investigated in this study by a combination of experimental, numerical, and theoretical studies. When compressed, these blocks are characterised by significant shortening and bulging, two effects that significantly influence their mechanical behaviour under shear loading.

Based on the results of the experimental and numerical investigations, the following conclusions can be drawn:

- The investigated blocks behave very differently under the applied horizontal deflection, with the block of highest shape factor deforming mainly in shear, and the lowest shape factor block deforming mainly under bending.
- The Ogden material model provides more accurate results than the neo-Hookean model, particularly for high vertical compressions.
- The analysis of the local distribution shows high concentration of stresses in the case of the stocky block. The analyses also reveal the formation of a compression strut under shear deflection of a compressed block, and the concentration of tensile stresses and strain at top right and bottom left areas of the blocks when the top is displaced to the right. These could be important for defining limit conditions in the blocks, e.g. related to cavitation or delamination.
- When compressed blocks are sheared, only very modest shear strains are generated in the rubber that has bulged beyond the reinforcing plates

The second part of the chapter investigates the applicability of alternative theories for describing the compressive behaviour first and then the combined compressive and shear behaviour of slender rubber blocks. With regards to the compressive behaviour, it is observed that Muhr and Lindley's theories, which include the influence of the axial shortening and shape factor on compressive load, are found to provide very good approximations of the load-displacement response and of the secant compression modulus. With regard to the description of the horizontal stiffness of the blocks under constant vertical compression, it is concluded that:

- According to Haringx's theory, the horizontal stiffness decreases very rapidly with the increase of vertical compression, with critical values obtained for small axial compression levels.
- Stanton's theory, accounting for the height reduction and increase of plan area due to compression, but within the hypotheses of small deformations and a linear elastic material, provides more accurate results than Haringx's theory, but they are still quite far from the experimental and FE simulations.
- The theory of Muhr, accounting for the height reduction and increase of plan area due to compression with a finite deformation formulation, but disregarding the non-uniform bulging of the compressed blocks, provides good estimates of the horizontal stiffness only for small compressions, or, at large compression, for the case of very slender blocks.
- The proposed extended theory, which starts from the theory of Muhr but provides an improved description of the non-uniform bulging of the compressed blocks on the shear and bending stiffness, is able to accurately describe the horizontal stiffness variation with the axial deflection for all the blocks considered.

In the final part of the chapter , the estimates of the critical load according to the numerical and various theoretical models are computed and compared with the experimental ones. Also in this case, the proposed theory yields the best prediction of the critical load and outperforms the other theories when compared to the experimental and FE results.

It is remarkable that the theories that include the shape factor effect of bonded end plates (Lanzo, Stanton et al., Muhr and the Extended theory) work so well for a single block despite the non-uniform lateral restraint (due to bonded endplates) along the length of the block, and the treatment of it as being a beam column with a uniform constitutive behaviour along its axis. This observation implies that the theories are expected to have similar accuracy, or better, for beam columns consisting of several such units in series.

5 Mechanical behaviour of rubber bearings with low shape factor

5.1 Introduction

Seismic isolation is a technique aimed at protecting structures from earthquakes by shifting their fundamental frequency away from the undesirable frequencies of seismic ground motions. Laminated rubber bearings are widely used in the isolation system. They consist of multiple layers of rubber vulcanized to steel reinforcing layers that produce a vertically stiff but horizontally flexible isolator (Kelly and Konstantinidis, 2011). A non-dimensional parameter usually employed to characterize the geometry of these bearings is the primary shape factor, S. This defines the ratio of the loaded area to the area free to bulge for an individual rubber layer (Constantinou et al. 1992; Montuori et al., 2016). Common values of S for laminated rubber seismic isolators are in the order of 10-20. This is to enhance the critical load capacity of the bearings, and to minimise rocking motion in isolated structures by providing a high vertical stiffness, while maintaining a low horizontal stiffness. Such bearings have been widely deployed and thoroughly studied, and most design criteria in publications and Standards are focussed on bearings of this type. However, high S values, ranging from 10 to 30, result in a large number of steel plates, resulting in significant weight of the bearings, and generally high production and installation costs. At the same time, the high vertical stiffness of the bearings yields high vibration frequencies of the isolated structure in the vertical direction.

Vibration isolation is a technique for protecting structures from ground-borne vibration, for example produced by underground trains. Laminated rubber-steel bearings have been used as structural vibration isolators from the 1960s (Derham et al., 1985; Kelly and Konstantinidis, 2011; Kelly and Van Engelen, 2016). In vibration isolation systems the objective is to provide an approximately isotropic stiffness, vertical and horizontal, with natural frequencies of approximately 5Hz, so as to attenuate ground-borne vibrations in the audible range (>15Hz). The success of such systems was the inspiration for developing seismic isolation systems based on rubber bearings. However, it was quickly realised that designing for an approximately isotropic system would be impractical for seismic isolation, since most damage is associated with a predominant low frequency horizontal content, typically in the range between 1Hz and 10Hz, calling for an isolation frequency of around 0.5Hz (Derham et al. 1985; Kelly and Konstantinidis, 2011). While it proved possible to design laminated bearings giving such a low horizontal natural frequency for typical column loads, for a linear spring with a vertical natural frequency of f = 0.5Hz, the vertical deflection would be of the order of $g/(2\pi f)^2 \approx$ 1m, and thus completely impractical. Fortunately, typical superstructures are far from isotropic in modal frequencies,

only the horizontal structural modes having low enough modal frequencies to be dangerously excited by the seismic motion, and so the standard base isolation system was developed to have a horizontal natural frequency of about 0.5Hz, and to be nearly rigid vertically, to minimise rocking. Such a "two dimensional" isolation system provides good protection to the superstructure, however, it does not provide isolation from significantly higher frequency vertical ground motion, whether seismically or otherwise induced, that might cause undesirable excitation of vertical modes of superstructure or contents. This could be the case for critical facilities such as nuclear power plants or hospitals hosting sensitive equipment, for example. Moreover, the encouragement of some rocking in the first horizontal mode, by lowering vertical stiffness, has also the potential to lower its modal frequency and hence might also significantly improve isolation from the horizontal component of seismic excitation.

It is noteworthy that in the early stages of development of seismic isolation bearings, some researchers investigated the possibility of employing low shape factor (LSF) rubber bearings, ranging from 0.5 to 5, as a way to achieve an economic three-dimensional (3D) isolation of structural systems. The first example of a structure isolated using rubber bearings, the Pestalozzi school built in 1969 in Skopje (Macedonia), was realized using unreinforced rubber blocks, with S=0.5, assuming no lateral slip on the pedestals. These blocks exhibited significant lateral bulging under the weight of the building and were eventually replaced with high shape factor steel-reinforced bearings (Yenidogan, 2021). A base-isolated laboratory building realized in Kajima Corporation Technical Research Institute (Kelly, 1988) was one of the earliest applications of LSF bearings (S=2.5). The two-story reinforced concrete building was supported on eighteen bearings, and auxiliary steel bars provided damping. The aim was to provide 3D seismic isolation from earthquakes as well as ambient ground vibrations and the effectiveness of the system was shown in the laboratory testing. (Aiken et al. 1989) designed a 3D isolation system for a liquid metal reactor building; their study involved the design and testing of bearings with shape factor S=5.4, made from different types of rubber material, and the development of an analytical bearing model. For them, "low shape factor bearings" corresponded to those designed to achieve both vertical and horizontal isolation. However, the dynamic response of the structure supported on such bearings was not investigated in detail, either experimentally or theoretically.

A solution investigated by many researchers to reduce the weight and cost of isolators consists of the replacement of steel plates with fiber reinforcement materials (Kelly, 1999; Thuyet et al. 2018; Losanno et al., 2019, 2020). Fiber-reinforced elastomeric bearings have also been proposed to provide 3D isolation, since they have a lower vertical stiffness in comparison to an equivalent steel-reinforced elastomeric bearing (Kelly and Niel Van Engelen, 2016).

Kelly and Lee (2018) analysed the existing literature about 3D seismic isolation and explored theoretically the dynamics of 3D isolation systems and the presence of rocking modes for low values of the bearing vertical stiffness. Warn and Vu (2012) showed with the aid of numerical simulations that

buildings isolated on LSF bearings could experience minor non-structural damage following a major earthquake event. Yabana and Matsuda (2000) carried out tests to evaluate the mechanical characteristics and the performance of rubber bearings with a shape factor of 4.2, highlighting the effect of decrease of the rubber thickness, caused by the vertical pressure, on the bearing horizontal stiffness, and the high displacement capacity (shear strains>500%), which is similar to that of more conventional bearings. Zhou et al. (2016) and Okamura et al. (2011) both considered the application of LSF bearings to 3D isolation of modern nuclear facilities. Cilento et al. analysed results from an extensive experimental campaign to investigate the effectiveness of isolating a structure with LSF bearings (Cilento et al., 2017).

In the last decades, several studies investigated the mechanical behaviour of elastomeric bearings, and various models were developed for describing their response under horizontal loading or combined vertical and horizontal loading (see e.g, Koh and Kelly, 1989; Kikuchi and Aiken, 1997; Nagarajaiah and Ferrell, 1999; Grant et al. 2004; Kumar et al. 2012; Montuori et al., 2016; Tubaldi et al., 2016, 2017; Kalfas et al., 2017; Kumar and Whittaker, 2018)). These models were successfully employed to evaluate the seismic performance of structures isolated with rubber bearings, see e.g. Cardone et al. (2013); Ragni, Cardone, et al., (2018); Tubaldi et al. (2018). However, most of the bearing models developed thus far have been validated against tests on high shape factor bearings, and they do not account for important effects such as the reduction in height and the increase in plan area due to bulging of the elastomer under compressive load, which affect significantly the response of LSF bearings. Attempts were made by Stanton and Roeder (Stanton et al., 1990; Roeder and Stanton, 1991) Schapery (Schapery, 2018b, 2018c) and Muhr (2017)to include such effects in bearing models, in order to extend their applicability to the LSF case, but more experimental tests are needed to validate these models.

Recently, some works have investigated experimentally and numerically the behaviour of LSF bearings, by mainly focusing on the compressive response. Gu et al. (2021) carried out comprehensive tests on high damping rubber bearings with LSF, evaluating their behaviour in terms of vertical and horizontal stiffness, and equivalent damping ratio. They also proposed a corrected calculation of the vertical stiffness to provide a better agreement with the experimental results. Ren et al. (2020) carried out both experimental and numerical investigations on the compressive behaviour of LSF lead-rubber bearings, demonstrating that differently from the case of high shape factor bearings, the axial load has a non-negligible effect on their compressive stiffness.

The few studies (Warn and Vu, 2012; Kelly and Lee, 2018) that have investigated numerically the dynamic behaviour of structures mounted on LSF bearings are based on oversimplified descriptions of the bearings, e.g. using uncoupled spring elements for the various directions. Thus, an in-depth analysis of the behaviour of LSF bearings and of structures mounted on them, using experimental testing and advanced numerical modelling, is needed.

This chapter aims to further explore the LSF concept in rubber bearings through the development of an advanced finite element (FE) modelling strategy for these isolation devices. The first part of the chapter focuses on the bearing behaviour, using the results of double shear tests on rubber pieces and quasi-static tests on rubber bearings under compression and shear displacements carried out by Tun Abdul Razak Research Centre (TARRC). These tests are simulated in Abaqus (2018) using a 3D modelling approach for the LSF bearings, with alternative constitutive laws for the rubber stress-strain behaviour based on the double shear test results. The advanced numerical modelling approach is used to achieve a deeper understanding of the mechanical behaviour of LSF bearings under combined axial and horizontal loads, and in particular to investigate the resulting local distribution of stress and strain throughout the rubber. It is noteworthy that these quantities are relevant for assessing the likelihood of local failure (e.g. debonding, and splitting in the rubber along the peak of the bulge), and that this is particularly important for LSF bearings, which may exhibit debonding problems due to high shear stresses at the outer edge of the shim-rubber interface.

In the second part of the chapter , the 3D bearing model is used for simulating shaking table tests carried out at the Department of Structures for Engineering and Architecture of University of Naples Federico II on a prototype base-isolated building with LSF bearings under a horizontal seismic input. The tests induced high displacements at the isolation system level, and significant variations of vertical forces. The simulation allows characterization of the complex bearing behaviour under dynamic loadings, involving significant coupling between the horizontal and vertical response.

It is noteworthy that although analysing an entire isolated structure with 3D FE modelling (Ohsaki et al., 2015) is feasible, it is computationally too expensive for routine use. Here, this modelling strategy is used to shed light on the local behaviour of the rubber layers arising due to the application of external loading, for investigating the mechanical behaviour under loadings not considered experimentally but potentially encountered in real applications, and for checking the attainment of limit state conditions during the design stage (Saidou et al., 2021). It can also be used to calibrate and validate simplified modelling approaches for describing the bearing mechanical properties (Stanton et al., 1990; Roeder, 1991; Muhr, 2017; Schapery, 2018b, 2018c).

5.2 Material and bearing tests

This section describes first the tests carried out by Cuomo (2014) and Cilento et al.(2017) at TARRC to characterize the mechanical behaviour of the LSF bearings with low damping rubber. The tests include those on double shear test pieces for the characterization of the material behaviour and those on the compressed bearings under shear loading. Subsequently, these tests are simulated using a 3D finite element analysis approach. Although bearings manufactured with a high damping compound were also tested at TARRC, this study considers only the bearings made with the low

damping rubber compound. This choice is motivated by the fact that low damping rubbers have a relatively simple constitutive behaviour, allowing the focus to be on the effects of finite strains and geometrical nonlinearity, arising from the combination of axial loads and horizontal displacements. The bearings made with the high damping compound would be characterized by a much more complex mechanical behaviour, affected by Payne effect, stress-softening, and potential heating of rubber upon repeated cycling (see e.g. Tubaldi et al., 2017; Ragni et al., 2018).

5.2.1 Experimental Tests

Double-shear cylindrical test pieces made of lightly filled natural rubber compound were subjected at TARRC to harmonic displacement histories. The test pieces consisted of two rubber layers hot-bonded to metal parts as shown in Figure 5.1a. The thickness of each layer was 6mm and the diameter 25mm. Double shear tests were performed under sinusoidal shear displacement histories with a frequency of 0.5 Hz. The samples were preconditioned (i.e. non virgin). Nevertheless, the stress-softening effects (Tubaldi et al., 2017; Ragni et al., 2018) are not significant since the compound is a low damping and essentially unfilled natural rubber, and for the same reason the effect of the temperature rise in the rubber upon repeated cycling is negligible. Figure 5.1b shows the results of the tests in terms of variation of the secant shear modulus G with the maximum nominal shear strain γ_{max}. The nominal shear strain γ is defined as the ratio between the shear displacement and the rubber height of a single layer, whereas the secant shear modulus G is evaluated as the ratio between the maximum nominal shear stress τ_{max} (obtained by dividing the maximum shear force by the cross-sectional area of the rubber sample) and γ_{max}, under the assumption of uniformly distributed shear strains. It can be observed that G assumes values in the range between 0.62 MPa and 0.47 MPa, reducing slightly for increasing values of γ_{max}. Figure 5.1c also shows the variation of the equivalent damping ratio (Chopra, 2013) with the strain amplitude. The damping ratio is generally very low, as expected for this type of rubber compound, and increases slightly for increasing γ_{max} values.

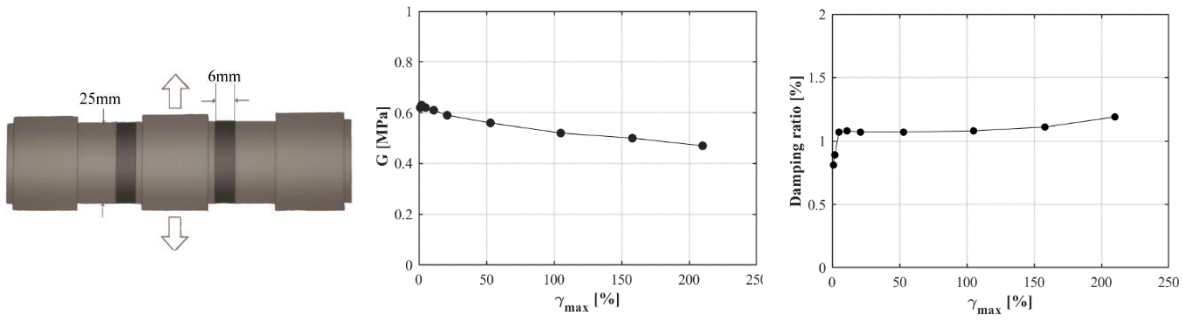

(a) (b) (c)

Figure 5.1 –Results from Cilento et al. (2017): (a) Double shear test piece geometry, (b) Secant shear modulus vs. maximum shear strain, (c) Equivalent damping ratio vs. maximum shear strain.

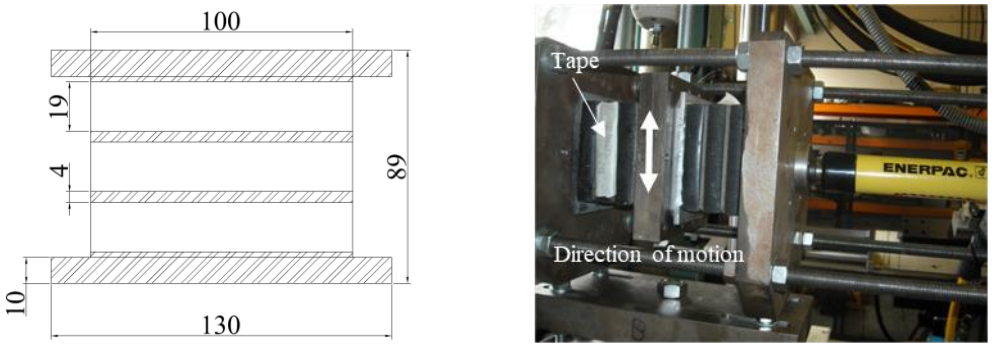

Figure 5.2 – Test set up from Cuomo (2014) and Cilento et al. (2017): (a) Bearing geometry, (b) Double shear test set-up: two identical bearings mounted in the test jig, the external plates are fixed after the application of compression load and the central plate is free to move along the direction perpedicular to the compression load.

Figure 5.2a illustrates the laminated bearing considered in the tests and Figure 5.2b shows the bearings in the test jig. These prototype bearings were designed to achieve target horizontal and vertical natural periods respectively equal to 0.92s and 0.25s for the scaled prototype. They consist of three layers of rubber 19mm thick and sides 100x100 mm, vulcanised and simultaneously hot-bonded (using the Chemosil 211/220 system (Lord Technical Data), as also used for the double shear test piece of Figure 5.1a) to steel plates (nominal thickness 2mm) on their major faces, designed to achieve a shape factor S=1.32. Loctite 638 (Henkel Technical Data, 2022) retaining compound was used to bond the three rubber–steel laminates together, on the two internal steel to steel interfaces. Steel end plates 130mm x100mm, with thickness 10 mm, were bonded to the end steel faces of the 3-layer bearing using Araldite standard epoxy adhesive. Four bearings were built and tested at TARRC; a pair of bearings was subjected simultaneously to static compression and dynamic shear loading in a double shear configuration. A hydraulic jack was used to apply a compression load to the bearings to simulate gravity loads, whereas the shear displacements were imposed by a Dartec uniaxial servohydraulic actuator. The compression load was increased up to the desired level, and subsequently the external plates were locked tightening bolts on both sides (see Figure 5.2b) before applying a shear displacement through the central plate. The testing sequence consisted of two cycles of sinusoidal displacement at increasing shear strain amplitudes (Cuomo, 2014; Cilento et al., 2017). It is worth observing that during both these tests and the shaking table tests described in Section 5.3, no failure in terms of rubber-to-metal bonding was observed, despite the bearings having been subjected to relatively high horizontal displacements. Similarly in other studies on LSF bearings (Yabana and Matsuda, 2000) no debonding was observed, for bearings subjected to higher compression and shear deformations. Nevertheless, some technological solutions may be employed to minimize the debonding risk, e.g. using fillets (Gough and Muhr, 2005). The test setup considered to characterise the shear response of the bearings under different compressive loads is somewhat different from that employed in studies in the literature, where the compressive load rather than the compressive displacement is fixed. Obviously, the approach followed is cheaper and also easier, but care must be paid in interpreting the obtained results and comparing them to those in

the literature. Nevertheless, the obtained results are still useful for model validation and the shear response under small deflections is the same regardless of the boundary condition, as discussed below.

The secant shear stiffness is calculated from the hysteresis loops obtained from the shear tests, and can be defined based on values of peak force F_{max} and peak displacement d_{max} as follows:

$$k_s = F_{\max} / d_{\max} \tag{5.1}$$

Figure 5.3a shows the shear stiffness values of one bearing for increasing nominal shear strains, defined by the ratio between peak displacement and the total rubber thickness, obtained under a compressive displacement corresponding to 19kN (i.e. a pressure of 1.9 MPa) at zero shear deformations. It can be noted that contrary to what was observed in the case of double shear tests under zero compression, the secant shear stiffness first reduces slightly for increasing nominal shear strains, and then it increases. This behaviour is in contrast with the existing literature on elastomeric bearings, showing a reduction of the horizontal stiffness under increasing horizontal displacements (Aiken et al., 1992; Pond and Thomas, 1993). This is due to the fact that the vertical load in the bearings (which was not measured during the experiments) is expected to decrease with increasing lateral displacement. The Payne effect (i.e., the decrease of stiffness for increasing deformation, typical of HDNR compounds (Tubaldi et al., 2016, 2017; Ragn et al., 2018) cannot explain this behaviour since the rubber compound incorporates very little filler. Figure 5.3b illustrates the equivalent damping ratio of the bearing at various shear strains. It is interesting to observe that the equivalent damping ratio of the device (between 2% and 3%) is in general significantly higher than that of the rubber compound (about 1%) and it increases for increasing compression levels. This phenomenon was observed in experiments reported by Thomas (1982) and also acknowledged by Koh and Kelly (1989) and Raithel and Serino (1993), who noted that when viscoelasticity is included in their theory the compression load increases the phase difference between the horizontal force and the horizontal displacement, thus increasing the energy dissipation per cycle. Despite this increase, the damping ratio of the bearings is still quite low and in real applications a higher value may be desirable to control the displacement demand. This could be achieved by using auxiliary damping devices, e.g. viscous dampers or steel bar dampers (Kelly, 1988; IAEA, 2020) or by using more dissipative compounds. The second solution is preferable since it would not reduce the cost benefits of the LSF bearings. It is noteworthy that similar bearings were also made using a high damping NR compound and, due to the augmentation of damping through the high compressive load, were very effective in the shaking table tests in controlling the displacements, albeit at the expense of higher drifts and accelerations in the superstructure (Fig 14, Cilento et al. 2017), though are not further discussed here.

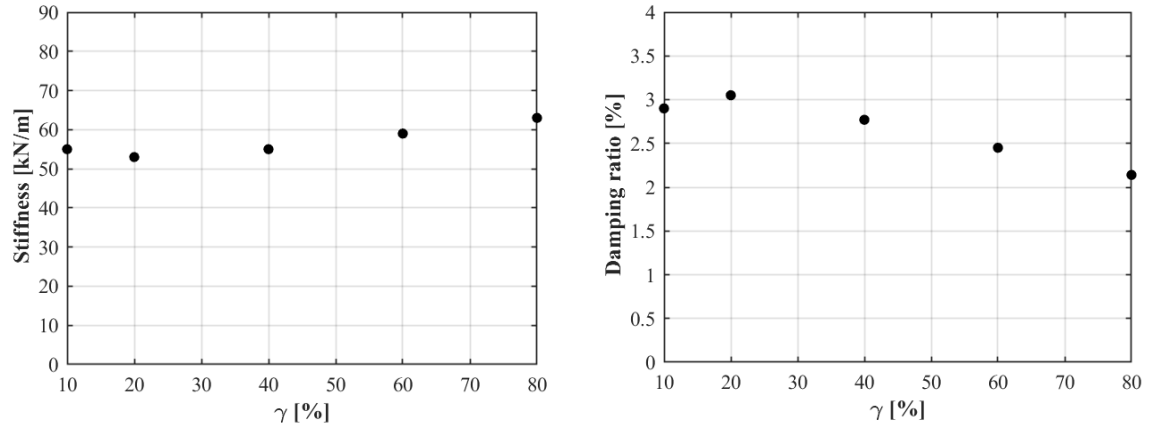

(a) (b)

Figure 5.3 –Test results from Cilento et al. (2017) (a) Bearing horizontal stiffness vs. nominal shear strain, (b) Damping ratio vs nominal shear strain. The compressive strain is held constant during shear, at a value corresponding to 19kN force for zero shear strain.

5.2.2 3D Numerical Model

This subsection describes the 3D numerical models developed in Abaqus (2018) to simulate the tests on the double shear pieces and the elastomeric bearings, to provide an insight into the local stresses and strains throughout the double shear pieces and the elastomeric bearings, to investigate the influence of axial compression on the horizontal response and to estimate the critical load.

5.2.2.1 Constitutive models

In the models, the rubber is described using a hyperelastic constitutive material. Hyperelastic materials are defined by the strain energy potential *W*, the strain energy stored in the material per unit of reference volume as a function of the strain in the material. Three alternative constitutive relationships are used and compared in this study, namely the neo-Hookean, Ogden and Yeoh models (Ogden, 1984).

Assuming an incompressible material, the Ogden strain energy function depends on the three principal stretches λ_1, λ_2, λ_3 and *2N* material constants, i.e. the hyperelastic parameters, μ_i and α_i, according to the following expression:

$$W = \sum_{i=1}^{N} \frac{\mu_i}{\alpha_i} \left(\lambda_1^{\alpha_i} + \lambda_2^{\alpha_i} + \lambda_3^{\alpha_i} - 3 \right) \qquad 5.2$$

where *N* is the number of terms that constitute the strain energy density function, chosen to be 1 in this study.

The Yeoh and neo-Hookean strain energy potentials are derived from the reduced polynomial strain energy potential that is a function of only the deviatoric strain invariant I_1 and has the following expression:

$$W = \sum_{i=1}^{N} C_{i0} \left(I_1 - 3 \right)^i \tag{5.3}$$

where C_{i0} are material parameters. The Yeoh and neo-Hookean form are obtained for a number of terms N equal to 3 and 1, respectively. The values of material parameters μ_i, α_i and C_{i0} in the Equation 5.2 and 5.3 can be obtained from the double shear experiments described in the previous section. These parameters have been calibrated by considering the simple shear secant modulus-strain relation for all three material models, assuming a homogeneous state of simple shear strain within the cylindrical rubber pieces (Figure 5.1a). The relation between principal stretches and amount of shear, is given by Ogden (1984):

$$\lambda_1 = \lambda = \sqrt{1 + \frac{\gamma^2}{2} + \gamma \sqrt{1 + \frac{\gamma^2}{4}}}; \; \lambda_2 = \lambda^{-1}; \; \lambda_3 = 1; \; \lambda - \lambda^{-1} = \gamma \tag{5.4}$$

The principal first invariant as a function of the amount of shear is expressed as follows:

$$I_1 = \gamma^2 + 3 \tag{5.5}$$

As developed by Rivlin (1948), the relation between shear stress and γ is:

$$\tau = 2 \left(\frac{\partial W}{\partial I_1} + \frac{\partial W}{\partial I_2} \right) \gamma \tag{5.6}$$

Assuming the strain energy density depends only on I_1, then Equation 5.6 gives:

$$\tau = \frac{\partial W}{\partial I} 2\gamma \tag{5.7}$$

The stress-stretch relation according to Ogden's model, Yeoh's model and the neo-Hookean model can be expressed respectively as follows:

$$\tau = 2\mu \frac{\lambda}{1 + \lambda^2} \left(\lambda^{\alpha} - \lambda^{-\alpha} \right) \tag{5.8}$$

$$\tau = 2\gamma \left(C_{10} + 2C_{20}\gamma^2 + 3C_{30}\gamma^4 \right) \tag{5.9}$$

$$\tau = 2\gamma C_{10} \tag{5.10}$$

where $2C_{10}$ in Equation 5.10 represents the rubber shear modulus.

The method used to determine the material parameters of the constitutive models is based on a trial and error analysis. The goal is to find the values of the parameters that best fit the experimental double-shear test results. This process involves repeatedly adjusting the values of the parameters until the

model's predicted response closely matches the experimental data. The material parameters of the various constitutive models are shown in Table 5.1

Table 5.1 Material parameters for the three hyperelastic material models

Model parameters	**C10 [MPa]**	**C20 [MPa]**	**C30 [MPa]**	**α [–]**	**μ [MPa]**
Ogden	-	-	-	1.42	0.61
Yeoh	0.3	-0.005	0.000311	-	-
neo-Hookean	0.292	-	-	-	-

The damping property of the rubber material is described in a simplified way by using a Rayleigh damping model, whose coefficients are calculated to provide a damping ratio of 1% in correspondence of the first and second vibration modes of the isolated system described in Section 5.3. The coefficient α for the mass matrix and the coefficient β for the elastic initial stiffness matrix are equal to 0.067926 and 0.00080, respectively.

5.2.2.2 Simulation of material characterisation tests

Figure 5.4 describes the FE model of the double shear test. Since the double shear configuration has a plane of symmetry, only half of a single layer is modelled, in order to reduce the computational cost of the simulation, by imposing appropriate boundary conditions. The rubber layer is modelled using 8-node solid elements (C3D8H) with first-order hybrid formulation, which is recommended for incompressible materials (Abaqus, 2018). The model domain has been meshed employing only hexahedron elements, and avoiding excessive values of their aspect ratio in the central part. In the simulation, a sinusoidal load in the horizontal direction (i.e., *x*) is applied to the top reference point in a displacement control analysis and the bottom of the layer is fixed.

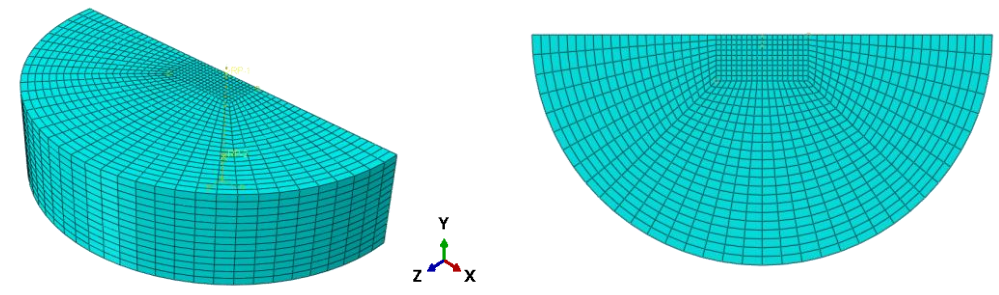

(a) (b)

Figure 5.4 – FE model and meshing of the double shear test (a) 3D Perspective, (b) Top View.

Figure 5.5a shows the distribution of shear stresses and strains in a vertical section along the diameter of the reference cylindrical layer, obtained using the Yeoh model under a shear displacement of 6 mm.

This corresponds to a nominal shear strain of 100%. The local shear strains and stresses within the rubber layer exhibit a nearly uniform distribution, with a common value of approximately 100% strain, which matches the nominal strain value. However, deviations from this uniform distribution occur near the edges of the layer, where both stresses and strains are higher. This confirms that the state of deformation in this test configuration is nearly, but not exactly, "simple shear", as also pointed out by others (Rivlin, 1971; Gregory and Muhr, 1999). Figure 5.5b compares the experimental force-displacement response with the response simulated using the Yeoh model. It is observed that the response is close to linear and that the model provides a good approximation of the experimental results. The value of the shear modulus for the neo-Hookean model that provides the best fit, using the trial-and-error analysis, to the experimental results among various investigated values is 0.584MPa, corresponding to C_{10}=0.292 MPa.

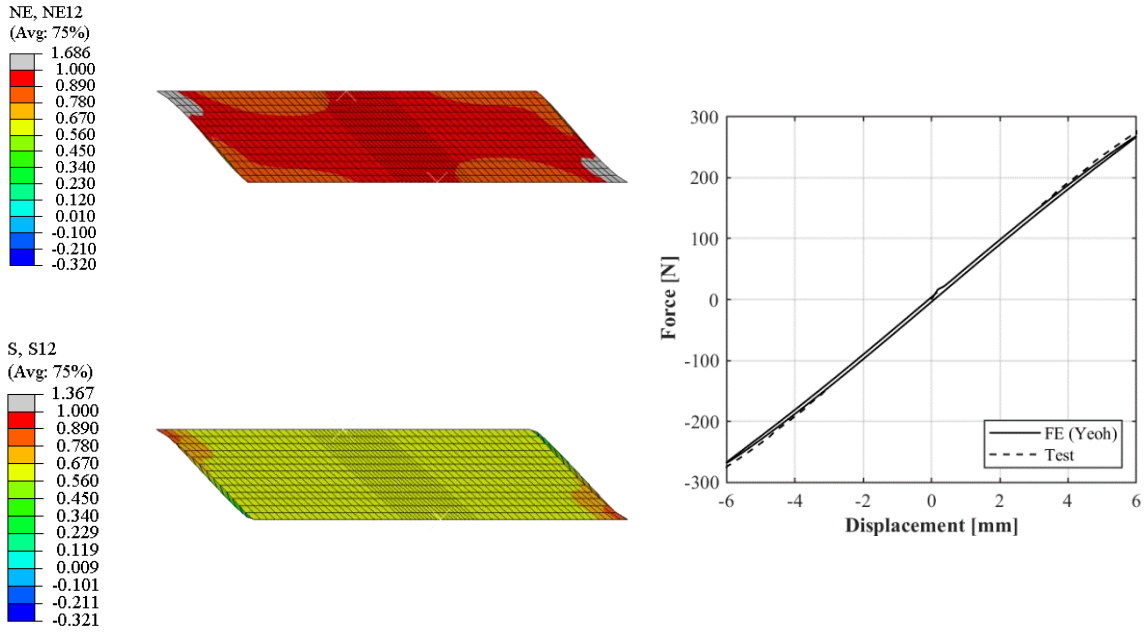

(a) (b)

Figure 5.5 – (a) Contour plot of the shear strain (top) and stress (bottom) component within the rubber shear test piece, (b) Hysteresis loop of each rubber test piece for a nominal maximum shear strain of 100%

Figure 5.6a reports and compares the shear stiffness values from both the experimental tests and the FE analyses results for different maximum shear strains. A good agreement between simulations and the test is found for all the investigated shear deformation amplitudes, apart from low values of shear strains. In general, using the Ogden and Yeoh constitutive relationship for the rubber yields the most accurate results, especially at high levels of shear strains. The neo-Hookean relationship provides a worse fit, because it is characterized by a reduced number of parameters compared to the other models and yields an almost linear response under simple shear strains (the slight departure from linear response

is due to the strain field not being exactly simple shear). The estimates of the equivalent damping ratio of the rubber block obtained with the Yeoh constitutive model combined with Rayleigh damping for different levels of strain amplitude are shown in Figure 5.6b, where they are compared with the corresponding values obtained experimentally.

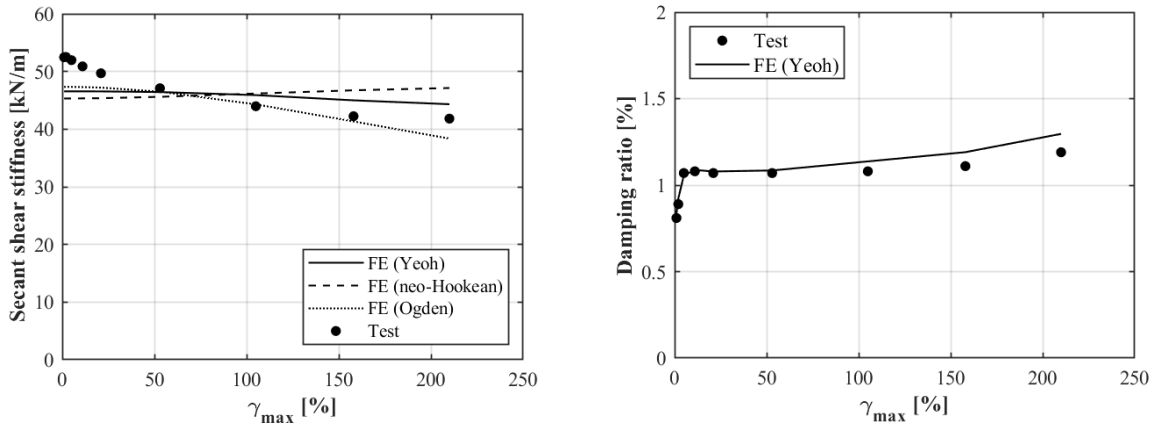

(a) (b)

Figure 5.6 – Experimental results from Cilento et al (2017) and FE models' results of (a) Secant shear stiffness for different maximum shear strains, (b) Equivalent damping ratio for different maximum shear strains.

It is noteworthy that more advanced description of the damping, e.g. using a Prony series approach can also be used to capture the behaviour of low damping natural rubber with a simple fitting procedure described in Ahmadi et al's work (1992). However, in this chapter the Rayleigh damping model has been employed because the agreement with experimental results is already good, considering that a relatively simple description of the damping is used for the rubber material.

5.2.2.3 Simulation of bearing tests

Figure 5.7 illustrates the model of the LSF bearing, which is the same as those employed in the shaking table test, whose results are discussed in the next section. The intermediate steel shim plates and end plates are also modelled using C3D8H elements. The tie contact between steel and rubber layers of the bearing is expressed by contact pair option available in Abaqus. The bottom anchor plate is fixed in all degrees of freedom and the top end plate is fixed against rotation but allowed to translate laterally and vertically. For the rubber layers, the constitutive models described in the previous section are employed, and the results shown are those obtained using the Yeoh constitutive model unless otherwise specified. A vertical downward displacement is first imposed at the top plate, until a compressive load of 19kN is achieved, equal to the mean load per bearing under the gravity loads in the shaking table tests. Subsequently, two cycles of sinusoidal displacements are applied while preventing vertical motion and rotation of the top plate.

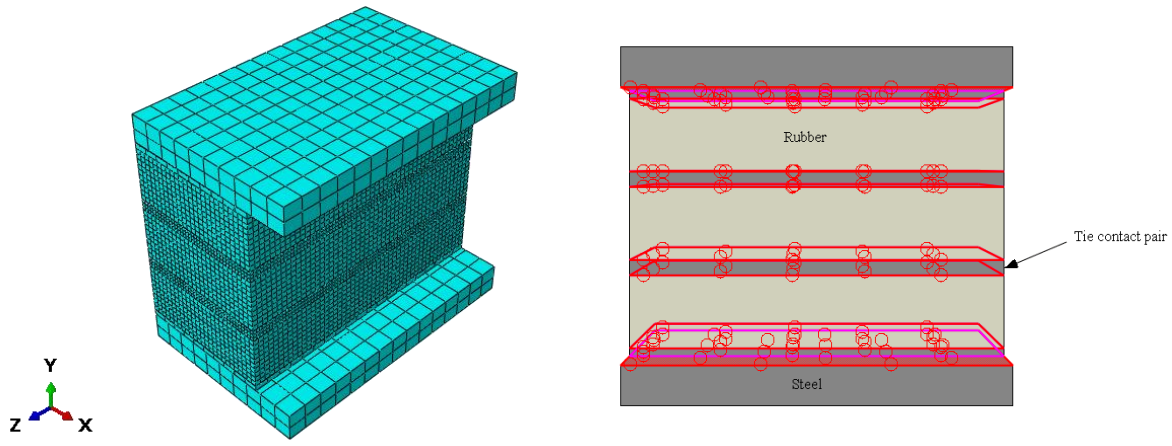

(a) (b)

Figure 5.7 – Elastomeric Bearing: (a) Meshing, (b) Details of connections between various layers.

Figure 5.8a shows the force-displacement curves under the applied compressive load of 19 kN evaluated numerically with Yeoh, neo-Hookean and Ogden material models. Experimental data are not available for this stage of the test, nevertheless a similar behaviour is obtained with the different constitutive models. Figure 5.8b illustrates the compressive load reduction due to the imposed sinusoidal shear displacement, which is due to the fact that the motion of the bearings in the axial direction is restrained. Figure 5.8c shows the shear force-displacement behaviour of the bearing subjected to the applied load in combination with the maximum applied horizontal displacement obtained both numerically and experimentally. It can be observed that a similar shear behaviour is obtained among the different constitutive models. The relative error in terms of energy dissipation (area within the loops) obtained by the three models is only 20% when compared to the experimental result. Figure 5.9 illustrates the deformed bearing during the tests. Figure 5.10a shows the contour plot of true compressive and shear stresses, expressed in MPa, and the engineering compressive and shear strain for the bearing subjected to the compressive load of 19kN. Figure 5.10b illustrates the stress and strain of the compressed bearing subjected to horizontal displacement of 46.48 mm, i.e. a nominal shear strain of about 80%. According to the legend notation, positive values indicate tensile stresses and strains, whereas negative values denote compressive stresses and strains. Although the bearing is globally subjected to axial compression and shearing, it can be observed that local tensile stresses are developed within the bearing due to the bulging of the layers. Under compression, local tensile stresses and strains are concentrated along the bulging area, whereas the shear stress and strain are highest at the four edges, normal to the direction of horizontal deflection, close to the bonded surfaces. These observations are in line with the extensive theoretical investigation of Kelly (1997) showing that high shear stresses appear at the corner of rubber pads, and with previous numerical studies on the response of elastomeric bearings (Kalfas et al. 2017). Under horizontal displacement, compressive stresses and strains are distributed along a diagonal strip

that corresponds to the compression strut, whereas tensile stresses are concentrated at top right and bottom left areas of the bearing (Kalfas et al. 2017). It is also interesting to note that the steel reinforcing plates undergo bending deflections, but without experiencing yielding.

Table 5.2 reports the values of the nominal true axial and shear stresses and nominal strains obtained numerically. The stresses are evaluated by dividing the maximum vertical and horizontal reaction forces by the cross-sectional area of the bearing in the deformed configuration (i.e. the cross sectional area at which the compressive/horizontal displacement is applied), respectively. The strains are obtained by dividing the maximum vertical and horizontal displacements by the rubber bearing height, respectively. These values are compared with the maximum local stress and strain extracted from the contour plots of the numerical investigation, showing that the latter are significantly higher than the nominal values. The amplification percentage Δ% to nominal has been calculated as the difference between the nominal (from hand calculations) and local (from FE analysis) value divided by the nominal value.

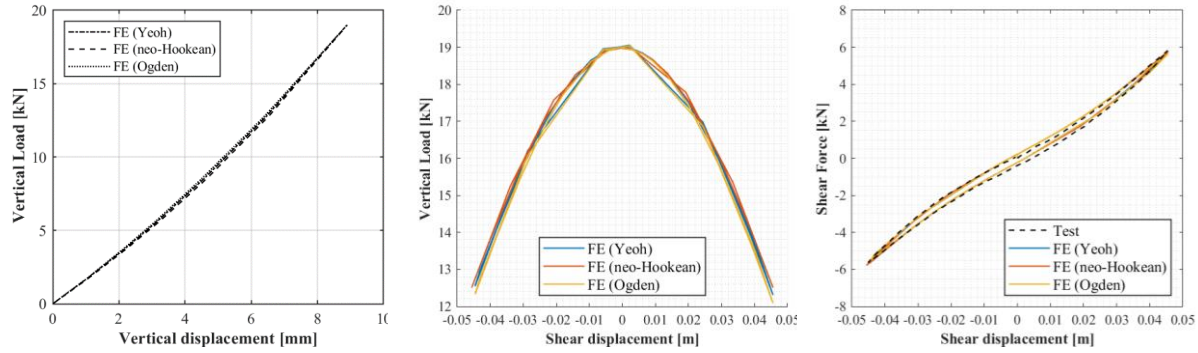

(a) (b) (c)

Figure 5.8 – Force-displacement curves (a) Vertical load-displacement behaviour defined numerically using Yeoh, neo-Hookean and Ogden constitutive material models, (b) Numerical vertical force-shear displacement results (c) Numerical shear force-displacement results compared with the available experimental data.

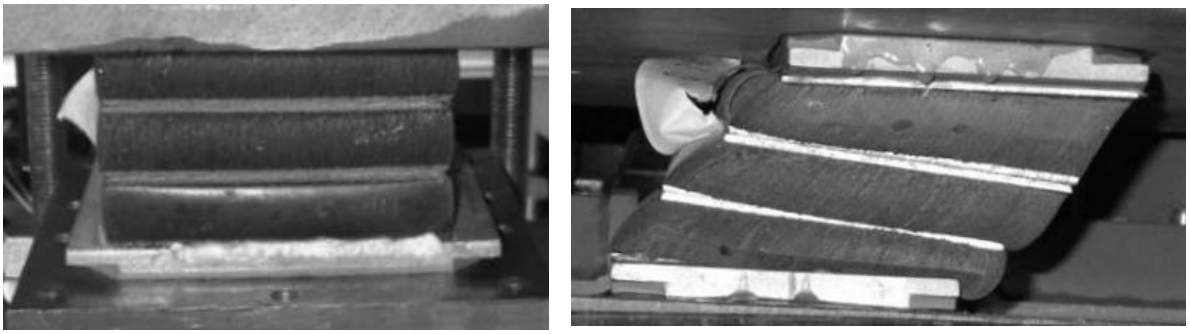

Figure 5.9 – Deformed bearing under a compression load of 19 kN (left) and a combined compression load and shear displacement (right) during the experiment (Cuomo, 2014)

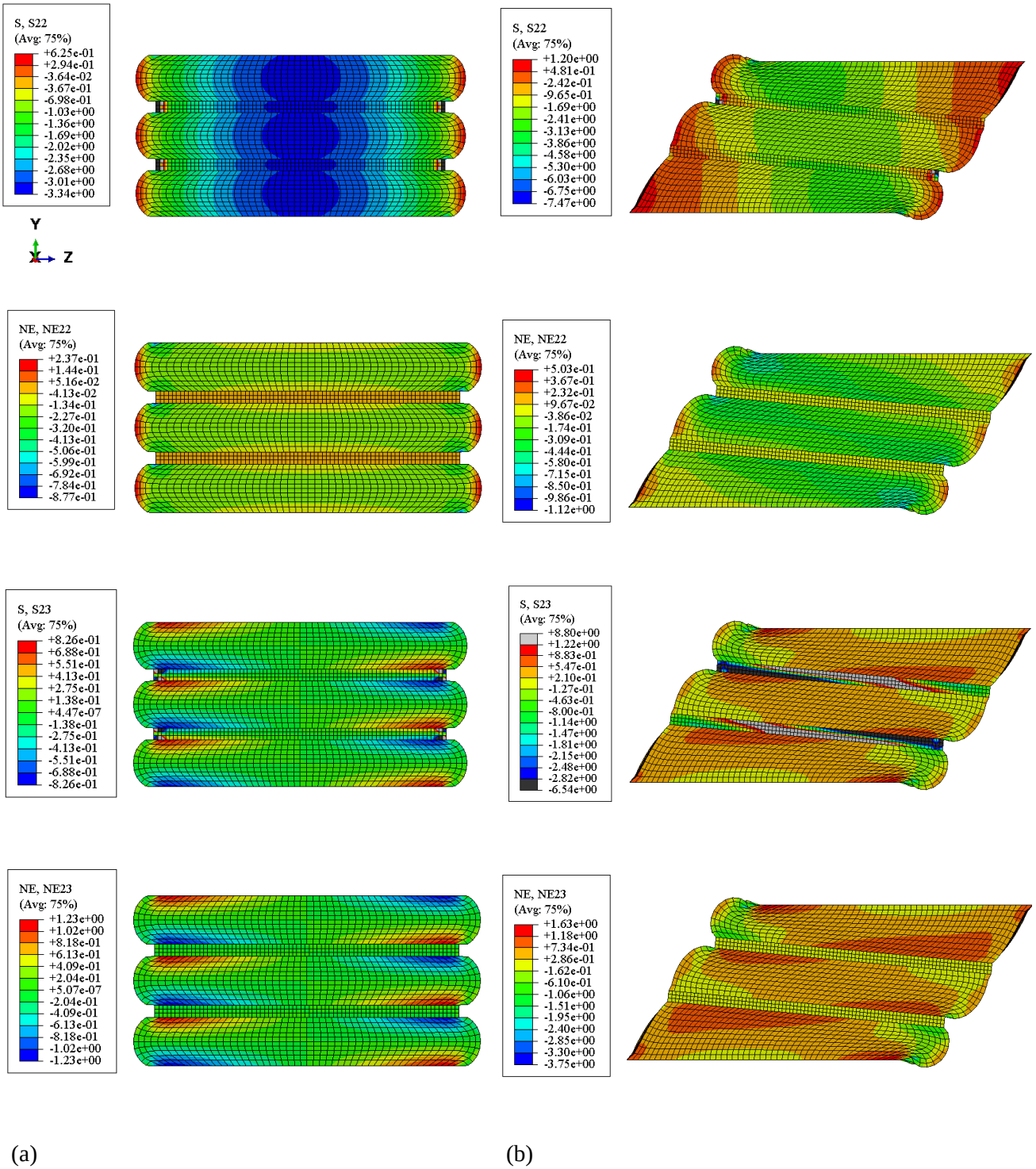

(a) (b)

Figure 5.10 – Contour plot of compressive and shear Cauchy stresses (S) and compressive and shear engineering strain (NE) subjected to (a) Compressive load 19kN, (b) Compressive load 19kN in combination with horizontal displacement.

Table 5.2 Nominal and local stresses and strain values (First three columns related to Figure 5.10a, last two related to Figure 5.10b)

		True axial stress [N/mm^2]	**Axial strain at max compression [-]**	**Shear strain at max compression [-]**	**True shear stress [N/mm^2]**	**Shear strain at max shear [-]**
Nominal		2.25	0.16	0.80	0.68	0.8
Maximum local	neo-Hookean	3.54	0.85	1.20	3.58	3.20
	Yeoh	3.34	0.88	1.24	2.82	3.75
	Ogden	3.35	0.88	1.25	2.83	3.76
Δ% to nominal	neo-Hookean	57	445	50	427	300
	Yeoh	48	463	55	316	369
	Ogden	49	464	57	317	370

Figure 5.11a shows the force-displacement loops obtained numerically using the Yeoh constitutive model and Rayleigh damping to simulate the results of the sinusoidal tests at different shear strain levels under the compressive load of 19kN. For small displacements, up to $\gamma = 40\%$, the bearing has an almost linear behaviour, with low energy dissipation achieved as illustrated both experimentally and numerically in Figure 5.11c. Non-linear force-displacement behaviour is then observed as the displacement amplitude is increased. The horizontal secant stiffness of the bearing, obtained by dividing the base shear force by the maximum displacement at each incremental step, is plotted in Figure 5.11b for each material model considered and compared against the experimental results. The increasing trend in secant stiffness is due to boundary conditions (i.e. reduction of axial force). In general, the experimental and numerical values are very close, except for low shear strains, for which the numerical model is more flexible. The equivalent viscous damping of the bearing is evaluated numerically and compared with the experimental results, as shown in Figure 5.11d. Both experimental and numerical results show that with the increase of shear strains, the damping decreases.

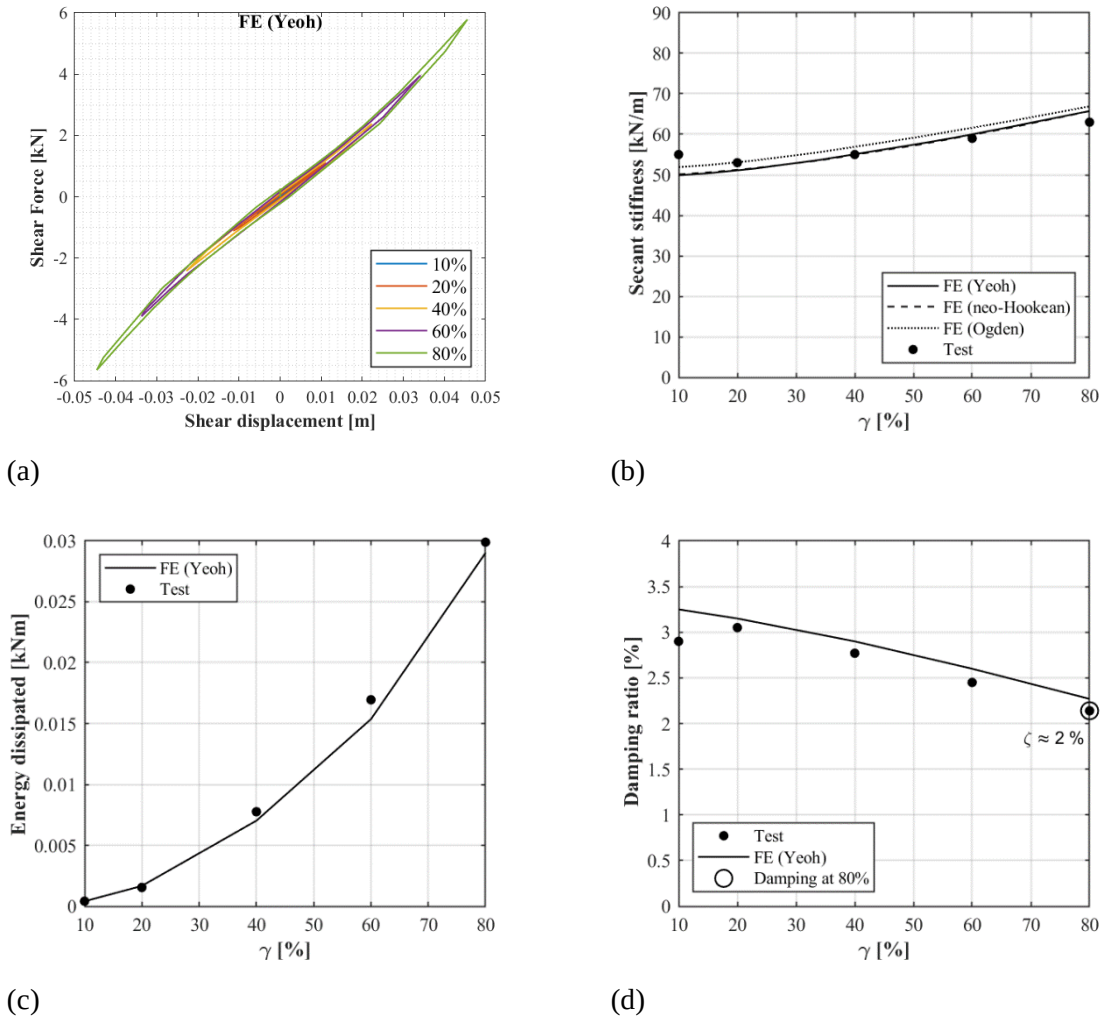

Figure 5.11 –Cyclic behaviour of the bearing under different shear amplitudes with a static vertical displacement equivalent to a load of 19kN; comparison of experiment with hyperelastic FE augmented with Rayleigh damping (a) Hysteretic loops from the sinusoidal tests with amplitudes ranging from 10% up to 80% shear strain; (b) Secant shear stiffness-nominal shear strain relation; (c) Energy dissipated by the bearing, (d) Equivalent damping ratio at different levels of shear strain

5.2.3 Influence of axial compression on horizontal response and critical load estimation

The behaviour of LSF isolation bearings under shear loading is strongly influenced by the applied compression load. In particular, this load induces a significant reduction of the shear stiffness due to nonlinear geometrical effects (i.e., p-delta effects). However, in the case of LSF bearings the bulging of the rubber layers due to compression enhances the bearing stability by strongly increasing the tangent tilting stiffness of the individual bonded sandwiches (Gent, 1965). In the case of bearings with high shape factor, the effect of the bulging on the tilting stiffness is expected to be negligible. The pressure also increases the damping capabilities under horizontal loading (Thomas, 1982; Koh and Kelly, 1989; Goodchild et al. 2018). An analytical model capable of accurately describing all these effects in bearings

for all possible values of shape factors has not been developed, yet. A simple mechanical model was developed in the past by Koh and Kelly (1988, 1989) to describe the coupled vertical-shear response of elastomeric isolation bearings with high shape factor. This model was validated against some experimental results on bearings with values of S in the range 5-10. The dependency of horizontal stiffness on vertical stresses was studied also including large displacements and non-linearity of rubber by other authors (Nagarajaiah et al. 1999; Buckle et al. 2002). However, these theories are accurate only in the case of high shape factors and fail in providing a description of the behaviour of LSF bearings.

The 3D FE modelling strategy described in this study simulates with accuracy such shear-compression behaviour of LSF bearings. Figure 5.12a shows the capability of the FE model to describe the sinusoidal tests performed at different compression levels for an 80% shear strain amplitude. Figure 5.12b-c-d shows the results of the numerical analysis performed at different vertical loads and the comparison with the experimental results.

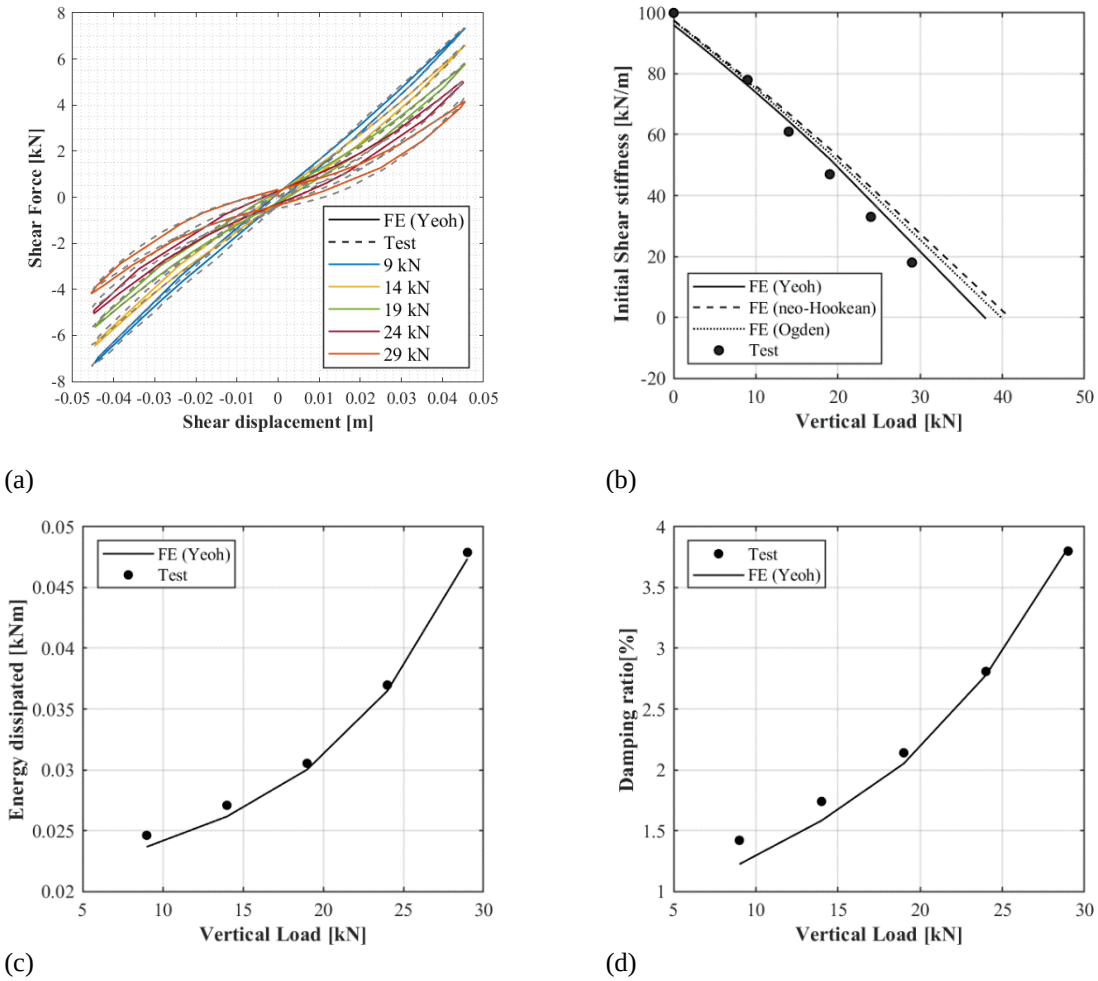

Figure 5.12 – Cyclic behaviour of bearing under different compression levels with 80% shear strain (a) Hysteretic loops from the sinusoidal tests, (b) Shear stiffness vs vertical compression load, (c) Energy dissipated by the bearing, (d) Equivalent damping ratio

Figure 5.12b compares the estimates of the initial shear stiffness at zero shear displacement for increasing values of the applied vertical displacement according to the numerical FE models and the experimental results. In general, the horizontal stiffness reduces for increasing compression levels, attaining the critical condition of zero initial tangent stiffness for compressive loads higher than that considered experimentally. The variation with the compressive load of the energy dissipated (Figure 5.12c) and of the equivalent damping ratio (Figure 5.12d) are both well described by the Yeoh FE model together with Rayleigh damping.

The maximum compressive load considered experimentally is 29kN as shown in Figure 5.12b. However numerical analyses are also performed for higher compression levels to estimate the critical load and the corresponding axial deflection. It can be observed that the vertical deflections are significant, i.e. about 26% of the total rubber height, due to the compliance of the LSF bearing. Table 5.3 illustrates the numerical estimates of the critical load P_{cr} and the axial deflection d_{cr} according to the various constitutive laws considered in the numerical models. Reported in the same table is also the critical load estimated according to the theory of Koh and Kelly (1989), which is only 19% of the values evaluated via the FEAs.

Table 5.3 Critical load estimated by Koh and Kelly and numerical estimates of critical load and corresponding axial deflection

Koh and Kelly	**FEA**					
	Ogden		**Yeoh**		**neo-Hookean**	
P_{cr}(kN)	P_{cr} (kN)	d_{cr} *(mm)*	P_{cr} (kN)	d_{cr} *(mm)*	P_{cr} (kN)	d_{cr} *(mm)*
7.4	40	15.69	39	15.02	41	15.19

In order to investigate the influence of the boundary conditions on the behaviour at large horizontal displacements, two quasi-static numerical analyses are carried out. The first one consists of the application of a constant axial load of 19kN and 39kN to the bearing, followed by a monotonically increasing horizontal displacement. In the second test, the bearing is subjected to a vertical displacement corresponding to a vertical compression of 19kN and 39kN, which is kept constant when the increasing horizontal displacement is applied. Figure 5.13a illustrates how the two responses, in force-controlled and displacement-controlled mode, (and thus the horizontal initial stiffness) are coincident for low values of the horizontal displacement, whereas for increasing horizontal displacements the force-controlled test exhibits a softer response and attains a condition of zero horizontal tangent stiffness (Sanchez et al., 2013) as shown in Figure 5.13b for 19kN axial load. In the case of fixed vertical displacement, the bearing exhibits a hardening behaviour in the horizontal direction, with the horizontal displacement resisted by a tensile load in the bearing. Eventually, the bearing would fail due to either cavitation or debonding between the rubber layer and the steel laminates. These results are very important, since they show that the test setup described in Section 5.2, which is cheaper and simpler

than the one employed in other studies in the literature, is valid not only for model calibration and validation, but also for estimating the initial stiffness and buckling load of the bearings. It is worth observing that regardless the boundary conditions, the buckling load is attained at 39kN, according to the Yeoh numerical model.

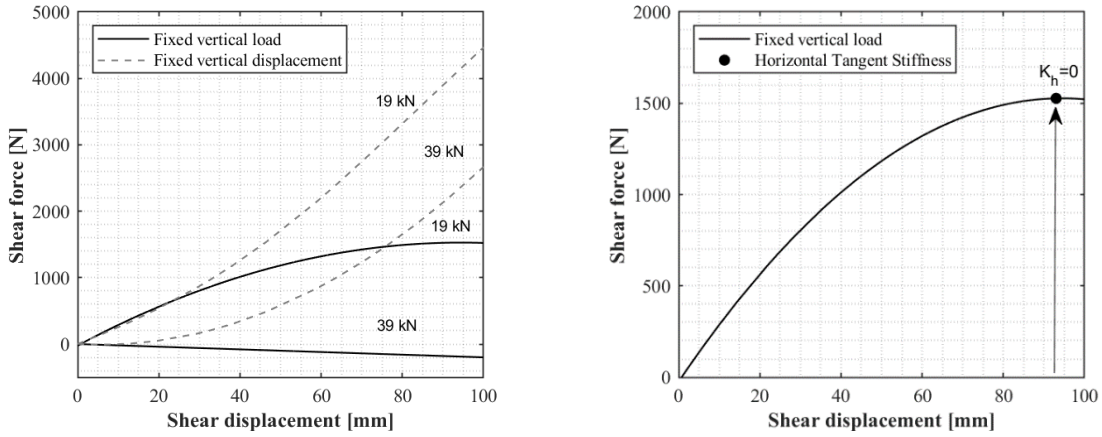

(a) (b)

Figure 5.13 – Shear force-displacement behaviour (a) Force-controlled and displacement-controlled test results at 19kN and 39kN compression levels, (b) Schematic representation for stability limit at 19kN (Sanchez et al., 2013)

5.3 Shaking table tests

5.3.1 Prototype, Tests Description and Dynamic Identification

This subsection describes the shaking table tests carried out by Cilento et al. (2017) at the Department of Structures for Engineering and Architecture of University of Naples Federico II on a prototype base-isolated building with LSF bearings. The superstructure is a one storey steel frame (Figure 5.14) and it has a total height of 2900mm and plan dimensions of 2650x2150mm. The columns are fabricated by full penetration welding of four steel plates, have a box section 150x150x15mm, and they are connected to the base floor by means of a steel plate (610x450mm). The beams of the top floor are pinned to the columns and are hot-formed square hollow sections 120x120x12.5mm. The four perimetric beams at the base of the frame have HEM 160 profile. The bearings are identical to those tested at TARRC. The same mock-up has been recently used for bi-directional tests on recycled rubber and fibre-reinforced unbounded isolators (Losanno et al., 2019; Losanno et al., 2020).

Concrete blocks were added to the two levels to achieve a total mass M_{tot}= 7.7 tonnes. The total base floor mass is equivalent to 3.6 tons and the top floor mass is equal to 4.1 tons. Ground motions were applied along the direction in which the frame span is 2650 mm. The vibration period of the fixed-base structure is T_s=0.24 s. The isolation system of the scaled prototype was designed to achieve a nominal horizontal vibration period T_{is} = 0.92 s, estimated from an assumed value of the rubber shear modulus

of 0.5MPa and considering the superstructure as rigid and the bearings as infinitely stiff in the vertical direction.

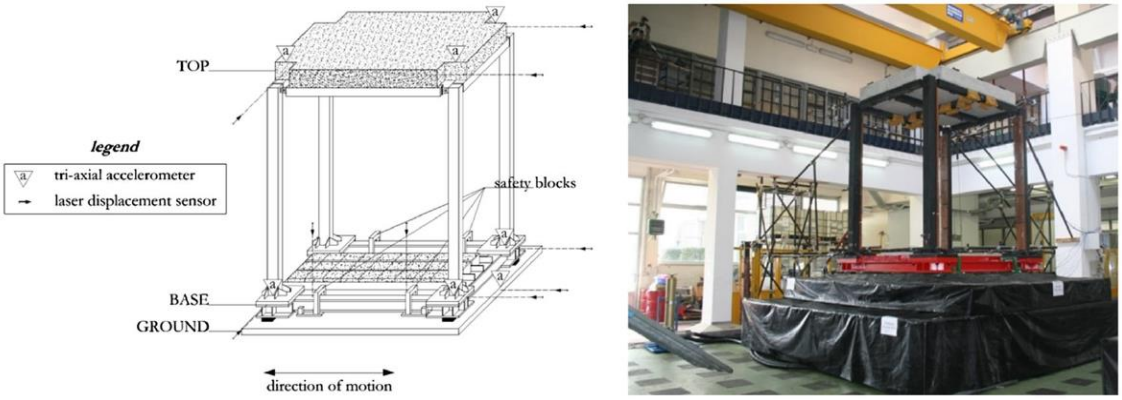

(a) (b)

Figure 5.14 – (a) Cabinet projection of the prototype building and the instrumentation set-up, (b) view of the test frame of the shaking table at the DiST laboratory University of Naples Federico II (Calabrese et al., 2015)

Under these simplifying assumptions, the nominal isolation period can be expressed as $T_{is}=2\pi\sqrt{(M_{tot}/K_{is})}$, where $K_{is} \approx 4GA/nh$ is the total stiffness of the set of four bearings, each of rubber area A and total rubber thickness nh, in the horizontal direction. It is noteworthy that the system was designed considering a geometry scale factor of 1/3 and an elastic modulus scale factor of 1. Therefore, according to the dynamic similitude rule, the equivalent period of the full-scale structure is T_{fs}= 1.59 s, (i.e. $T_{fs}= \sqrt{3}T_{is}$).

Random vibration tests with white noise excitation were performed on the shaking table before seismic excitation tests to characterize dynamically the model structure and evaluate the modal parameters of the isolated system. In particular, the dynamic identification is performed using the recorded acceleration responses at both base and top level from two random input tests (i.e. Test 1, Test 2) that produced a peak horizontal displacement of the bearings of 7.44 mm and 16.33 mm, corresponding respectively to 13% and 29% of shear strain. Two common techniques have been used to calculate the modal parameters, namely the Stochastic Subspace Identification (SSI) (Van Overschee and De Moor, 2008) and Frequency Domain Decomposition (FDD) (Brincker et al. 2001) methods. The difference between the two methods is that the latter calculation uses the output that excites the system, whereas the former also uses the input.

Table 5.4 summarizes the results of the application of these two methods, in terms of modal shapes, frequencies and damping ratios. It can be observed that the fundamental vibration period is higher than the value of 0.92s assumed for the design. This is due to the simplifications made at the design stage, namely the assumptions of a rigid superstructure, of rubber bearings infinitely stiff in the vertical

direction, a shear modulus of rubber of 0.50MPa and neglecting the effect of the compressive load in reducing their shear stiffness. Using the initial bearing stiffness K_{is} evaluated in subsection 5.2.3 under the axial load of 19kN an isolation period $T_{is}=2\pi\sqrt{(M_{tot}/K_{is})}$ =1.21s is obtained, which is close to the experimental values.

Table 5.4 Dynamic identification from white noise tests on the isolated system.

		SSI				**FDD**			
		Mode 1		**Mode 2**		**Mode 1**		**Mode 2**	
		Test 1	**Test 2**	**Test 1**	**Test 2**	**Test 1**	**Test 2**	**Test 1**	**Test 2**
Mode shape	**Base**	0.893	0.898	-1	-1	0.895	0.899	-1	-1
	Top	1	1	0.708	0.746	1	1	0.792	0.782
Frequency [Hz]		0.83	0.81	3.7	3.78	0.78	0.78	3.71	3.71
Natural Period [s]		1.21	1.24	0.27	0.26	1.28	1.28	0.27	0.27
Damping Ratio		0.0752	0.0642	0.0797	0.0425	0.0605	0.0549	0.0605	0.0549

5.3.2 Advanced 3D Seismic Analysis

A FE model of the isolated structure is developed in Abaqus to evaluate the effect of the axial compliance of the bearings on the dynamic properties of the system, to simulate the shaking table tests, and to analyse the effect of variation of axial loads, during the horizontal earthquake input, on the response of the bearings. Figure 5.15a illustrates the developed model, which consists of only half of the total structure, due to symmetry. Beam elements (i.e. "wire elements" in Abaqus) are employed to describe the frame, whereas the same model described in the previous sections is used for the bearings. The global coordinates are defined as shown in Figure 5.15, where the *z* axis is perpendicular to the x-y plane. The steel columns and beams of the frame are assumed to remain elastic, and thus are described by assigning a Young's modulus of 210000MPa, a Poisson's ratio of 0.3, and mass density of 7.8E-09 ton/mm^3. Rigid elements 180mm high are used between the columns and the bearings to simulate the actual height of the beams and slab at the base floor. In the FE-model, the upper surface of the rectangular plate is connected with the bottom node of the rigid element using a "coupling kinematic connection" (see Figure 5.15b). Mass elements are added to describe the bottom and top floor weights. The total mass of the superstructure model including the base beam and the top and bottom floor masses is 3.85 tonnes, which is half of the total superstructure mass and corresponds to a vertical load of 19kN on each rubber bearing. The out-of-plane displacement along *z* and rotation about *x* of nodes on the *x-y* plane are restrained to account for symmetry conditions. Figure 5.15a also illustrates the four nodes and the two degrees of freedom that have been considered for the calculation of the mode shapes: nodes 1-2 represent the isolation system whereas the superstructure is described by nodes 3-4.

Static analysis is first carried out under the self-weight of the system. Subsequently, an eigenvalue analysis is performed. Table 5.5 shows the natural periods and the mode-shapes correspondent to the

horizontal and vertical displacement, denoted as $u_{x,i}$ and $u_{y,i}$, respectively, where *i* is the *i*-th node. The mode shapes and natural periods for the first two vibration modes associated with the horizontal displacement, exhibit a good agreement with the values obtained from system identification of the recorded data (Table 5.4). The fundamental period of the numerical model is higher than the isolation period T_{is}=1.21s obtained by disregarding the compliance of the bearings in the vertical direction and assuming rigidity of the superstructure, as expected. It is also slightly higher than the fundamental isolation period evaluated experimentally using SSI and FDD methods (respectively 1.21s and 1.28s).

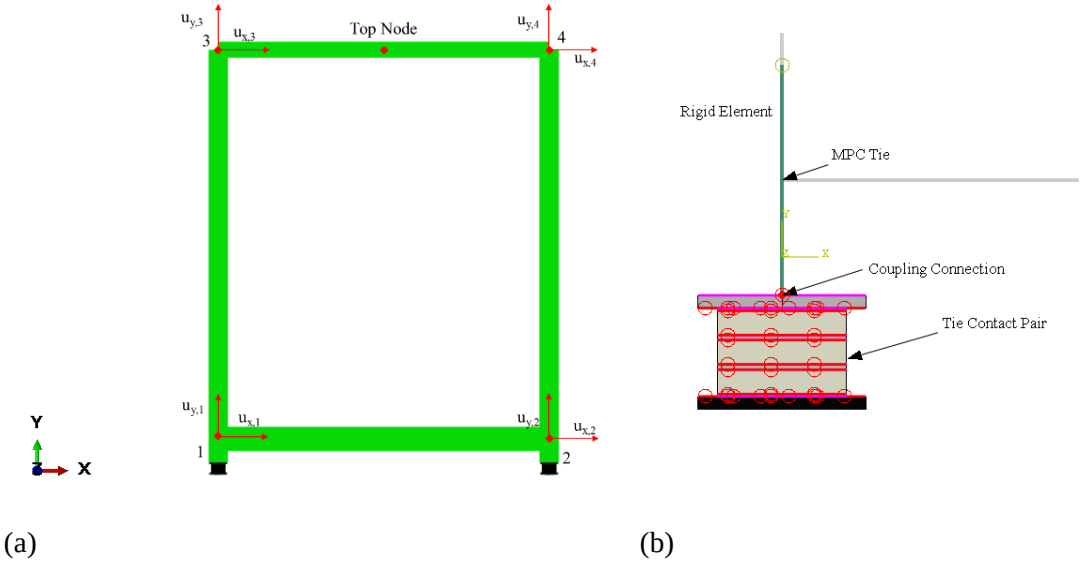

Figure 5.15 – (a) Finite element model of the isolated structure, (b) Contact details

Table 5.5 Abaqus FEA - Natural periods and mode shapes for base-isolated model

Mode			**First (Isolation mode)**	**Second**	**Third**
Natural Periods [s]			1.39	0.27	0.19
Natural Frequency [Hz]			0.72	3.70	5.26
Mode Shape	$u_{x,i}$	1	0.89	1.00	0.0003
		2	0.89	1.00	-0.0003
		3	1.00	-0.63	-0.0016
		4	1.00	-0.63	0.0016
	$u_{y,i}$	1	0.026	-0.379	1.00
		2	-0.026	0.379	1.00
		3	0.026	-0.379	1.00
		4	-0.026	0.379	1.00

Figure 5.16 also illustrates the mode shapes for the first two modes. It is evident that the first dynamic mode of the isolated structure involves mainly a horizontal motion of the isolation system, with a slight in-phase rocking of the building, whereas the second mode involves strong antiphase motion but with significant deformation of the bearings in the vertical direction, with one bearing being compressed and the other extended by the rocking. Thus, some coupling is expected between the horizontal and vertical response of the bearings, even under the application of horizontal component of the earthquake (Kelly and Lee, 2018). It is noteworthy that the vibration periods of the first and second mode obtained by performing the eigenvalue analysis on the system not subjected to the static gravity loadings are equal respectively to 0.97s and 0.30s. Thus, the fundamental period increases by about 40% considering the effect of static loadings, whereas the period of the second mode decreases slightly by about 10%. This is due to the increase of axial stiffness of the bearings, which reduces the rocking component of vibration motion (Figure 5.16b).

After application of the self-weight of the frame, dynamic implicit time-history analysis is carried out to simulate seismic response of the base-isolated frame under Bingol earthquake. Other seismic records were also considered in the experimental tests, but the response under this earthquake is the most interesting one since it is characterized by the largest displacement demands in the bearings among the various records and a condition close to instability.

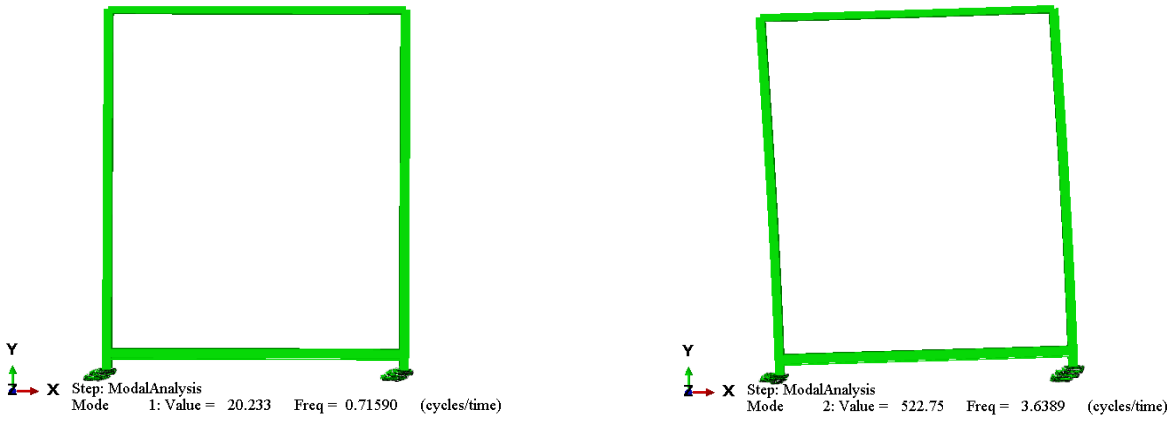

(a) (b)

Figure 5.16 – Mode Shapes corresponding to (a) the first mode, and (b) the second mode.

It is noteworthy that the analyses are computationally very expensive, due to the high number of degrees of freedom, the use of a large displacement formulation and the bearings being in a highly deformed condition, and also approaching instability. Thus, more than 3 days are required on a medium-performance personal computer to run this analysis.

Figure 5.17a shows the earthquake history imposed on the bottom of the bearing in the FE analysis. The initial time step of integration is 0.02 s, which is automatically reduced, if necessary. Figure 5.17b-c-d show and compare the time histories of relative horizontal displacement of the bearing, interstorey drift (calculated as relative top-base displacement over interstorey height) and acceleration of the superstructure according to the experimental test (Cilento et al., 2017) and the FE model.

The relative horizontal displacement of the bearing is the displacement of the top of the bearing with respect to the ground (that is the bottom of the bearing). The agreement between the two bearing responses (Figure 5.17b) is quite good, up to approximately 10 sec, at which point the amplitude of the input ground motion decreases and the differences between the test and model becomes more significant. This may be due to the fact that the bearing model is more flexible than the actual bearing at low nominal shear strains (Figure 5.11b). Moreover, higher discrepancies between the model and test results are observed for the superstructure acceleration and drift responses. This may also be due to the fact that the connection of the steel column to the base has some flexibility, while it is assumed to be rigid in the numerical model. This discrepancy is reflected in the shape of mode 2, with the experimental modal shape characterised by higher superstructure deflections (0.708) compared to the numerical shape (0.63). It is noted that the oscillation period, measured as the distance between two consecutive displacement peaks, is equal to 1.38s (i.e., the value of the fundamental period from eigenvalue analysis) for small displacement amplitudes, and 1.5s for higher displacement amplitudes. This shows that at high amplitudes of deformation the bearing stiffness reduces significantly, as discussed more in detail below. Figure 5.17e shows the rotation experienced by the base slab under seismic load, which is in phase with the bearing deflection and thus is induced by the deformation of the bearings in the vertical direction. Figure 5.17f illustrates the contributions to the displacement response of the top node by the horizontal deflections of the bearings, the superstructure deflection, the rocking contribution of Figure 5.17e and the sum of the three contributions. It can be observed that the displacements are all in phase (suggesting mode 1 of Figure 5.16a predominates) and the top node response (see Figure 5.15a) is dominated by the bearing deflection. This outcome is in agreement with relevant literature on 3D seismic isolation providing a major contribution of the rocking mode in case of vertical frequency lower than 1.0 Hz (i.e. approximately 30% of the second mode frequency in Table 5.5) (Wang and Wang, 2012; Zhou et al. 2016). It can be noted in Figure 5.17f that superstructure and rocking contribution time history are almost overlapping demonstrating that damage to non-structural components can be mainly due to the former component rather the latter, i.e. approximately 50% of total interstorey drift in Figure 5.17c.

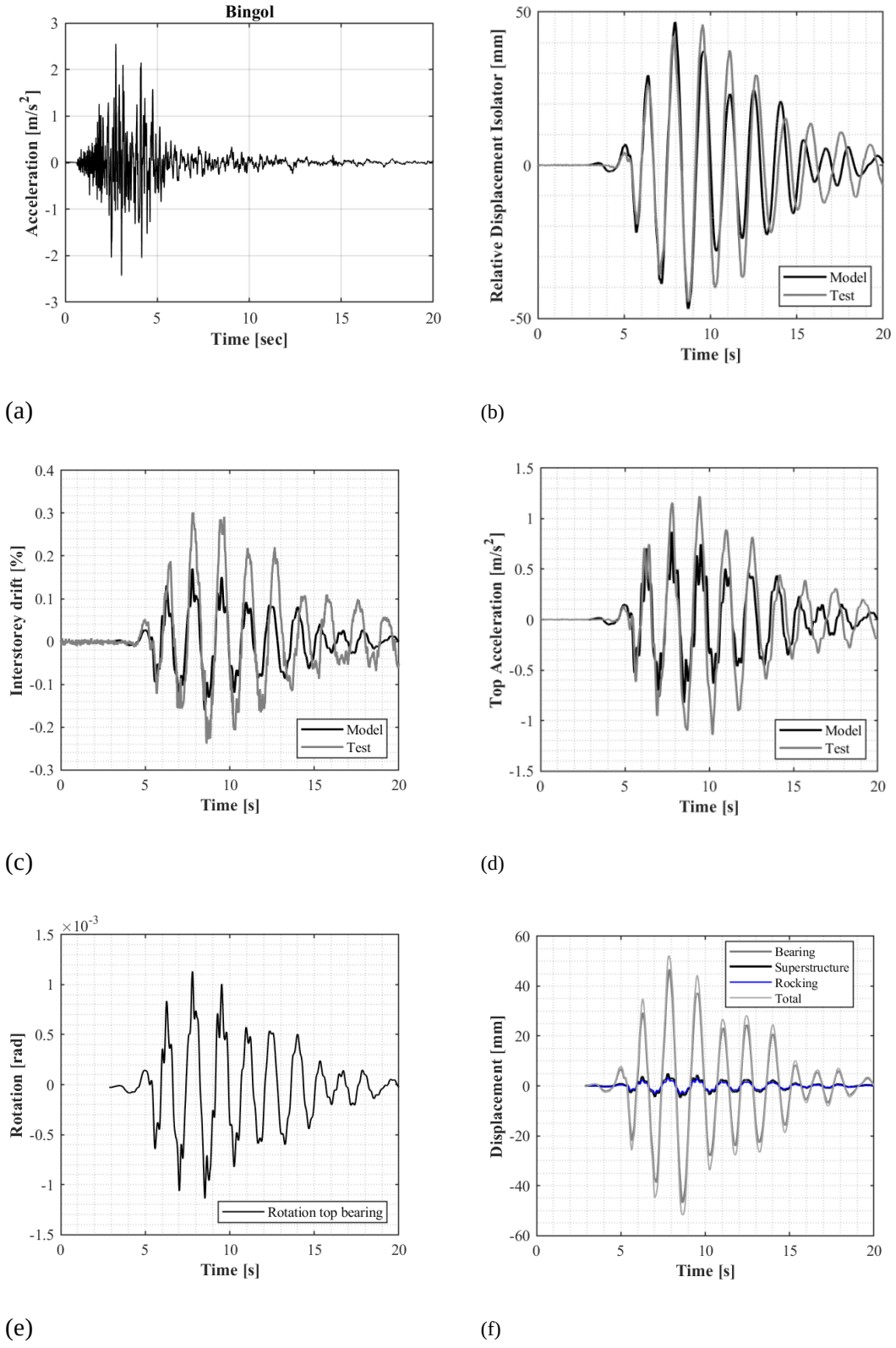

Figure 5.17 – (a) Input ground motion: Bingol acceleration time history, (b) Relative Displacement Isolator time history, (c) Interstorey drift, (d) Acceleration at the top of the superstructure, (e) Rotation time history, (f) Time-history of the various contributions to the top node displacement.

Figure 5.18 shows the bearing deformed shape and the corresponding shear strains and stresses observed at the time when the displacement response is the highest (i.e., 48 mm). It can be observed that the local shear strains vary significantly within the rubber and their values can be very different to the nominal one, which is 80%. Regarding the stresses distribution, local tensile stresses are developed within the bearing due to the bulging of the layers.

The Bingol earthquake involves highly non-linear behaviour in the bearing as well as coupling between the horizontal and vertical responses. In order to shed light into this aspect, Figure 5.19a shows the time history of the vertical reaction for the left and right bearings of the isolated structure and Figure 5.19b shows the variation of the vertical force with the horizontal displacement for the two bearings; the significance of rocking is evident from the inverse correlation between left and right bearings. It can be observed that the vertical forces exhibit a significant excursion, with values varying in the range between 16 kN and 24 kN. It is also interesting to observe that higher modes of vibration significantly affect the bearing responses in the vertical direction.

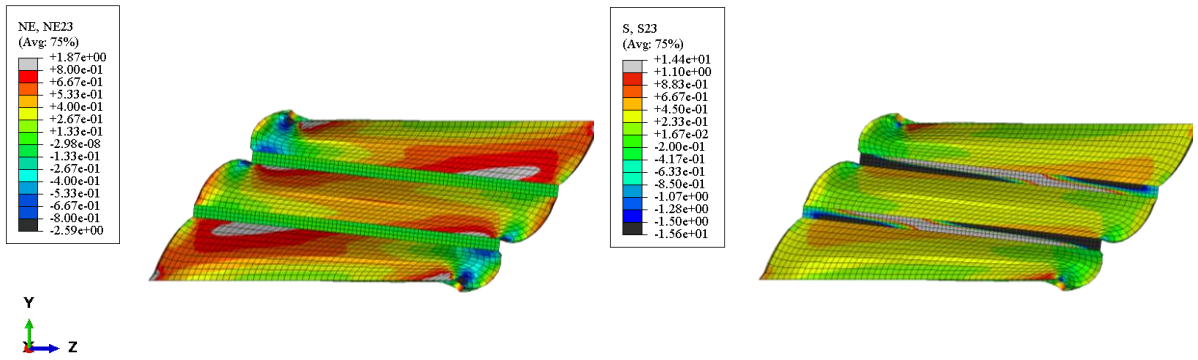

Figure 5.18 – Contour plot of the shear strains (left) and stresses (right) component within the bearing

Figure 5.19c-d illustrate respectively the time history of the horizontal reaction and horizontal force-displacement relationship for the left and right bearings. It can be observed that when the bearings are sheared to the positive horizontal direction, the vertical compression force in the left bearing reduces, while the one in the right bearing increases, while an opposite behaviour is observed in the opposite direction, as expected. When the compressive load increases, the horizontal tangent stiffness decreases, approaching a zero value for a vertical load of about 30kN as shown in Figure 5.12b.

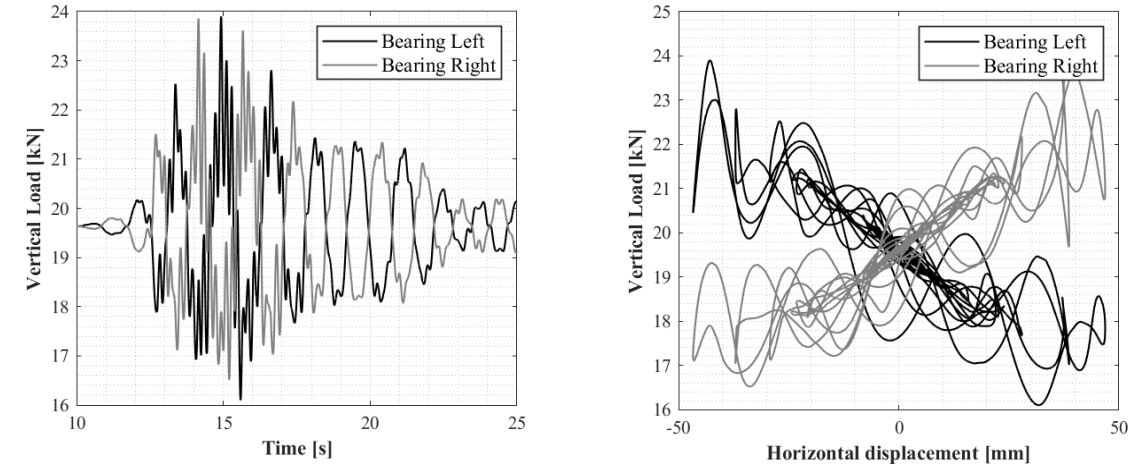

(a) (b)

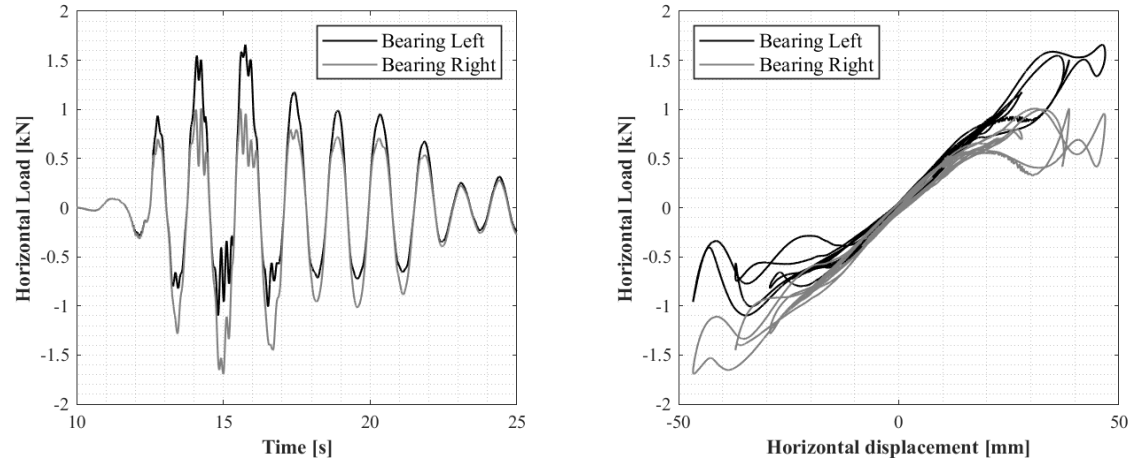

(c) (d)

Figure 5.19 – a) Variation of vertical load with time, (b) Vertical load-horizontal displacement behaviour, (c) Variation of horizontal load with time, (d) Horizontal load vs Horizontal displacement

5.4 Conclusions

This study investigates numerically the mechanical behaviour of elastomeric bearings with low shape factor (LSF) under compressive and shear loading, and the dynamic behaviour of a structure mounted on them. For this purpose, an unconventional test setup has been employed by Cilento et al. (2017) at Tun Abdul Razak Research Centre (TARRC), where LSF rubber bearings with low damping have been subjected first to compression, and then to shear loading under fixed compressive displacements. A three dimensional (3D) numerical model has been developed in Abaqus for simulating the experimental tests. Based on the results of these investigations, the following conclusion can be drawn:

These results are very important, since they show that the test setup described in Section 5.2.1, which is cheaper and simpler than the one employed in other studies in the literature, is valid not only for model calibration and validation, but also for estimating the initial stiffness and buckling load of the bearings.

The 3D numerical model provided useful information in terms of local stress and strain in the rubber bearing due to the application of vertical load of 19kN and of 80% shear strain. Tensile stress and strain are concentrated along the bulging area when the bearing is subjected to the maximum compression load. Under maximum horizontal displacement, the contour plots show the formation of a compression strut, whereas tensile stresses are concentrated along the opposite diagonal.

Hyperelastic material models, calibrated against material double-shear tests, can be used to accurately describe the complex nonlinear shear response of compressed LSF bearings. The neo-Hookean model provides a good fit for the shear rubber response up to nominal shear strains of 100% whereas the Yeoh and Ogden hyperelastic material models are found to also describe properly the rubber material behaviour for larger nominal shear deformations. Moreover, when analyzing the local behaviour, which includes small regions of high strain, significant differences are observed between predictions of the neo-Hookean model and those of the Yeoh and Ogden models, which are larger than the differences observed in the global vertical and horizontal force-deflection responses.

Analytical formulations such as the one developed by Koh and Kelly for simulating the behaviour of isolation bearings with high shape factors cannot be used for the LSF bearings considered in this study and underestimate significantly the critical load and the horizontal stiffness of the compressed bearings. On the other hand, the 3D numerical models provide accurate simulations of the sinusoidal tests performed at different compression levels, with satisfactory predictions of the effect of compression on both the horizontal stiffness and damping.

In the second part of the chapter , shaking table tests carried out on a structure isolated on LSF bearings are simulated using the advanced 3D numerical model of the bearings. Based on the results of these analyses, it can be concluded that:

The simulated modal properties and response of the isolators under a horizontal earthquake input are in very good agreement with the experimental results, whereas the response of the superstructure is slightly underestimated. In particular, the relative errors in terms of maximum absolute value of interstorey drift and acceleration at the top of the structure are of the order of 40% and 30%, respectively.

The displacement response of the system is dominated by the deflection of the bearings, whereas the contribution of the superstructure flexibility and of the rocking of the base due to the vertical compliance of the bearings is significantly smaller despite the bearings are quite flexible vertically.

The horizontal force-displacement relationship of the bearings is linear for shear deformations up to 30%, whereas for higher values a notable and rapid reduction of the tangent stiffness is observed due to the nonlinear geometrical effects.

A future study will investigate the performance and modeling of LSF bearings made with high damping rubber compounds, characterized by a more complex mechanical behaviour, which have been also the object of experimental investigations. Further numerical analyses and parametric studies will be carried out to evaluate the capability of the LSF bearings to provide full three-dimensional isolation, to investigate the coupling between the rocking response and the horizontal response and how the vertical compliance of the bearing influences the rocking behaviour.

Finally, simplified LSF bearing device models will be developed and implemented in nonlinear seismic analysis codes such as OpenSees and SAP2000, allowing to perform more extensive analyses of the seismic response of structure. Specifically, in Chapter 6, simplified models for LSF bearings and structures isolated with LSF bearings will be described, which will be utilized to investigate the dynamic behaviour and seismic response of structure mounted on them and to evaluate the impact of the bearing shape factor on the structural performance.

.

6 Dynamic behaviour and seismic response of structures isolated with low shape factor bearings

6.1 Introduction

Elastomeric laminated bearings are extensively employed to isolate buildings and bridges and protect them from the damaging effect of earthquakes. These devices consist of a number of horizontal rubber layers vulcanized to steel shims (Kelly, 1993b; Kelly and Konstantinidis, 2011). This allows to achieve values of the vertical stiffness that are hundred of times higher than the horizontal stiffness to be achieved, thus ensuring low vertical deflections under permanent loadings together with high flexibility in the horizontal direction. The shape of the rubber layers controls the bearing behaviour in terms of vertical and horizontal stiffness. The primary shape factor S is a non-dimensional parameter used to describe the bearing geometry, and it is defined as the ratio of the loaded area to the area free to bulge (Constantinou et al. 1992; Montuori et al., 2016; Tubaldi et al., 2016). The higher the shape factor, the stiffer the isolator in the vertical direction. Typical values of S are in the range between 15 and 30 (Montuori et al., 2016). With these values, only isolation in the horizontal plane can be achieved. However, in some applications, such as nuclear power plants, isolation in the vertical direction could help to protect sensitive equipment and provide functionality after an earthquake event (see e.g. Zhou et al., 2016). Low-shape factor (LSF) bearings could be used to achieve a three-dimensional seismic isolation (albeit only isotropic in horizontal directions) and/or ensure ground-borne vibration isolation in addition to seismic isolation (Derham et al. 1985; Kelly and Konstantinidis, 2011). Moreover, reducing the number of rubber layers and steel plates can yield some cost savings and result in a reduction of the weight of isolators, thus increasing the uptake of seismic isolation in low-income countries. Along the same line, fiber-reinforced elastomeric isolators have been payed increasing interest by several researchers as a lower cost option to traditional systems (Kelly, 1999; Toopchi-Nezhad et al. 2009; D. Losanno et al., 2020).

LSF bearings have been deployed in many structures and have been the object of numerous investigations over the years. For example, the Pestalozzi school, built in 1969 in Skopje (Macedonia) on unreinforced elastomeric bearings with a shape factor $S = 0.5$, can be thought as a first example of a 3D seismic isolation system (Kelly and Konstantinidis, 2011). In 1986, Kajima Corporation Technical Research Institute (Kelly, 1988) utilized low-shape factor bearings with $S = 2.5$ to support a two-story

reinforced concrete building used as acoustic laboratory, demonstrating the effectiveness of the isolation system against both earthquakes and traffic-induced vibrations. Aiken et al. (1989) designed and tested LSF bearings to provide three dimensional isolation for a liquid metal reactor building. Zhou et al. (2016) and Okamura et al. (2011) both considered the application of LSF bearings to 3D isolation of modern nuclear facilities. Cilento et al. (2017) also carried out an extensive experimental campaign to demonstrate the effectiveness of isolating a structure with LSF bearing, through the same tests that are considered in this chapter . Yabana and Matsuda (2000) carried out static, dynamic and failure tests on rubber bearings with thick rubber layers (S=4.2), to evaluate their mechanical characteristics, showing that they are efficient as 3D base isolation devices. It has been highlighted the influence of the decrease of rubber thickness on the vertical stiffness and the good performance of thick rubber layers subjected to very high shear strains (500%). Warn and Vu (2012) investigated analytically the concept of LSF as a way to achieve 3D isolation showing that building isolated with LSF bearing could experience minor non-structural damage. Kelly and Lee (2018) explored the dynamics of 3D isolation systems and reviewed the existing literature on 3D seismic isolations.

In the last decades, several studies have focused on the evaluation of the mechanical behaviour of rubber isolation bearings, and on the development of simplified mechanical models for describing their response under combined horizontal and vertical loading. However, few studies have considered specifically LSF bearings and the important effects of the reduction in height and the increase in plan area due to bulging of the rubber layers under compression, which significantly affect the horizontal behaviour. In principle, it could be possible to resort to advanced non-linear 3D finite-element modelling of the bearings (Ohsaki et al., 2015; Kalfas et al. 2017) to capture these effects, as also done by the authors of this study (Orfeo et al., 2022). However, this approach is computationally too expensive and not feasible for the analysis of an entire isolated structure with LSF bearings. For this reason, simplified device models are preferable for evaluating the seismic response of LSF base isolated buildings. In this regard, most of the models available for simulating the horizontal response of laminated bearings under axial loads (mainly due to the gravity loadings acting on the superstructure) (e.g. Kikuchi and Aiken, 1997; Nagarajaiah et al. 1999; Grant et al. 2004; Kumar et al. 2012; Cardone et al. 2013; Tubaldi et al., 2016, 2017; Kumar and Whittaker, 2018; Ragni et al., 2018; Tubaldi et al. 2018) are based on the theory of Koh and Kelly (1988, 1989). Thus, they neglect the changes in the geometry of the rubber layers due to the axial loads. A theory based on linear elasticity and accounting for the nonlinear effect of axial loads on stiffness and on strains and stresses within the rubber was developed by Schapery (2018a, 2018b, 2018c). Bearing properties were derived for different geometries (spherical, flat and cylindrical), loads and deformation modes. Prediction of stiffnesses were also made for LSF values and compared with finite element solutions. Stanton et al. (1990) also explored the effect of large deflections on elastomeric bearings taking into account the reduction in height and the increase

in plane area due to bulging of the rubber layer under compressive load. More recently, a promising approach for describing the behaviour of LSF bearings was also proposed by Muhr (2017) for describing the behaviour of rubber blocks with LSF. Further experimental and numerical studies are required to extend the theory and validate it for the case of laminated bearings.

This chapter aims to illustrate and evaluate a mechanical model for LSF bearings and to investigate the dynamic behaviour and seismic response of structures mounted on them by accounting for the coupling between horizontal and vertical response. The first part of the chapter briefly describes the results of the experimental campaign carried out at Tun Abdul Razak Research Center (TARRC), which have been extensively described in section 5.2.1. These results are used to evaluate the suitability of different theories for describing the horizontal response of LSF bearings, including the one of Gent (1965) and Stanton et al., (1990). The results are also used to validate the theory proposed by Muhr (2017) for rubber blocks, extended here to the case of LSF bearings.

The second part of the chapter focuses on the simulation of the shaking table tests described in section 5.3.1. The capabilities of the proposed simplified modelling approach for simulating the behaviour of LSF bearings are investigated by carrying out numerical analyses of the whole isolated system under different earthquake loadings. Further analyses are carried out to compare the performance of the prototype mounted on bearings with different shape factors. The numerical results of the analyses shed light on the possibility of using the simplified model for the preliminary seismic assessment of isolated structures mounted on LSF bearings and on the effect of the bearing shape factor on the seismic performance of structures.

6.2 Material and bearing tests

The first part of this section briefly illustrates the experimental tests carried on LSF bearings described in section 5.2.1 Subsequently, the analytical formulation developed by Muhr (2017) for LSF rubber blocks is illustrated, together with its extension to the case of laminated bearings, and its capability to describe the bearing behaviour is evaluated based on the comparison with experimental test results. A comparison is also made with the theories of Gent (1965) and Stanton et al. (1990), and with some numerical results (Orfeo et al., 2022).

6.2.1 Experimental Tests

Figure 6.1a illustrates the tested laminated LSF bearings. They were subjected to compression displacements and subsequently two cycles of sinusoidal displacement were imposed at each of a series of increasing shear strain amplitudes (Cuomo, 2014; Cilento et al., 2017).

Figure 6.1b illustrates the tangent horizontal stiffness of the bearing under a compressive displacement corresponding to 19kN, in addition to the secant horizontal stiffness already presented in Figure 5.3. It can be observed that the initial shear stiffness decreases for increasing shear strain amplitudes. On the other hand, the secant shear stiffness first decreases and then increases. This behaviour contradicts the existing literature on elastomeric bearing, which shows a decrease in horizontal stiffness with increasing horizontal displacement (Aiken et al., 1992; Nagarajaiah et al. 1999). This is because the vertical load in the bearings decreases as the lateral displacement increases (see Orfeo et al., 2022). However, the reduction observed in such studies may also be due to the Payne effect, which is the decrease of stiffness for increasing deformation, typical of HDNR compounds (Tubaldi et al., 2016, 2017; Ragni et al., 2018). The Payne effect is not significant in low-damping rubber compounds such as that used for the LSF bearings investigated in this study and thus the observed changes of horizontal stiffness are mainly a geometrical effect. Figure 6.1c illustrates the equivalent damping ratio ξ_{eq} of the bearing at various nominal shear strain amplitudes, which have been previously presented in Chapter 5. Specifically, the nominal shear strain amplitudes represent the ratio between the bearing horizontal deflection and the total rubber height. It is worth to note that the values of ξ_{eq} range from 2% to 3%, and are substantially greater than the equivalent damping ratio of the rubber compound (around 1%). This phenomenon, observed experimentally by Thomas (1982) and numerically by Orfeo (2022), was quantified by Koh and Kelly (1989) and Raithel and Serino (1993). They showed, using a viscoelastic analytical model, that the compression load increases the phase difference between the horizontal force and the horizontal displacement, thus increasing the energy dissipation per cycle.

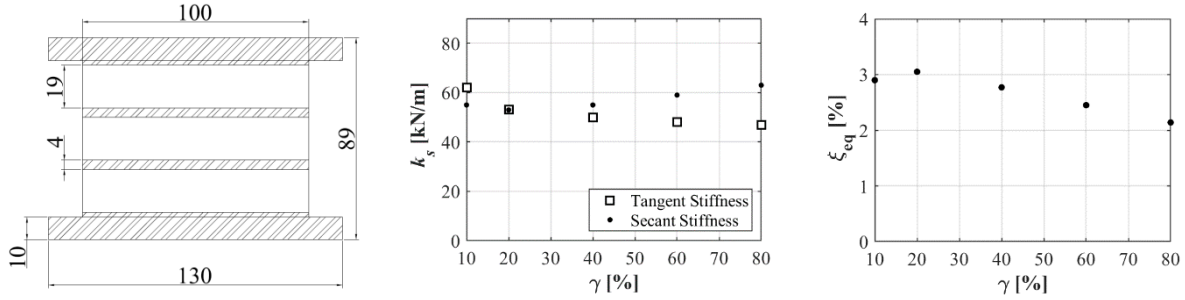

Figure 6.1 – (a) Bearing geometry; initial and secant shear stiffness (b) and equivalent damping ratio (c) at different levels of nominal shear strain, under a static displacement equivalent to a load of 19kN.

In the tests, a vertical downward displacement was first imposed at the top plate, until a compressive load of 19kN was achieved, equal to the mean load per bearing under the gravity loads in the shaking table tests. Subsequently, two cycles of sinusoidal displacements were applied while preventing vertical motion and rotation of the top plate.

It is noteworthy that the level of the applied compressive load is 60% higher than the value of the critical bearing load according to the theory of Gent (1964) and of Koh and Kelly (1989), as also discussed in the subsequent section more in detail. However, no signs of instability were observed in the experiment.

6.2.2 Review of analytical models of LSF bearings

The behaviour of LSF isolation bearings under shear loading is strongly influenced by the applied compression loads. In particular, compressive loads induce a significant reduction of the horizontal stiffness due to nonlinear geometrical effects (P-delta effects), partly mitigated by the increase of the rubber layer area (due to bulging) and reduction of height. The pressure also increases the damping capabilities under horizontal loading (Thomas, 1982; Koh and James M Kelly, 1989; Goodchild, Muhr and Thomas, 2018). An analytical model capable of accurately describing all these effects in bearings for all possible values of shape factors has not been developed, yet. In the following, a brief overview of the theories developed over the years to include axial load effects is provided.

According to the classical theory of rubber blocks, developed under the assumptions of small strains, linear elastic behaviour and incompressibility of the rubber, the vertical load N can be related linearly to the compressive strain ε (i.e. the ratio between the compressive displacement u_v and the undeformed height h_0) through the following expression (defined in section 4.4, Equation 4.8):

$$P = A_0 E_c \varepsilon = 3GA_0 \left(f_{c1} + f_{c2} \right) \varepsilon \tag{6.1}$$

where A_0 is the initial cross-sectional area of the rubber block, G is the shear modulus and f_{c1} and f_{c2} are numerical factors accounting for the confining effect of the steel plates. Their expressions depend on the rubber section shape and can be found in the original paper of Gent and Meinecke (1970).

The transverse stiffness K_h of an axially loaded shear-flexible beam-column that is fixed against rotation at both ends is (Haringx, 1948; Gent, 1965) (Equation 4.18 and 4.19):

$$K_h = \frac{P^2}{Ph - 2qB \tan\left(\frac{qh}{2} \right)} \tag{6.2}$$

where h is the bearing height between the end plates and the term q is:

$$q^2 = \frac{P\left(R - P \right)}{BR} \tag{6.3}$$

where B and R are the bending and shear stiffnesses for unit length of the rubber column, which are given in different expressions by Gent and Meinecke (1970), and P is the applied vertical load, maintained constant under the horizontal deflection.

The bending and the shear stiffness parameters according to Gent and Meinecke (1970) are defined as follows:

$$B = f_r E I_0 \qquad R = G A_0 \tag{6.4}$$

where f_r is a factor that similarly to f_{c1} and f_{c2} accounts for the confinement by the end plates.

The expressions above can be extended to the case of laminated bearings by assuming that the steel layers are rigid, thus increasing the values of B and R according to a factor equal to h/t_r, where t_r is the total rubber layer height (Koh and Kelly, 1989; Roeder et al., 1991; Kelly and Konstantinidis, 2011; Muhr, 2013).

It is noteworthy that based on the work of Haringx (1948) and of Gent (1964), Koh and Kelly (1988,1989) developed a mechanical model to describe the shear response of elastomeric isolation bearings including the effect of axial loads, and validated it against some experimental results on bearings with values of S in the range 5-10. The dependency of horizontal stiffness on vertical stresses was studied also including large displacements and non-linearity of rubber by other authors (Nagarajaiah et al. 1999; Buckle et al. 2002). These theories assume that the rubber layer shape is fixed and independent of the applied vertical load, which is an accurate assumption only for high shape factors. Thus, they do not account for the reduction of height and bulging (i.e. increase of plan area) of the rubber layers due to compression, which is very significant and cannot be neglected in the case of LSFs.

Stanton et al. (1990) derived relations for the compressive, shear and bending stiffnesses of LSF bearings by including the axial shortening and increase in plan area, with the layers' bulging expressed as a function of the Poisson ratio. In the following, reference is made to the "Poisson model", which consists of a homogeneous shear flexible column, made of a linear elastic material and undergoing small deformations. The compressive, shear and bending stiffnesses change with the compressive strain. They are approximated by assuming that the plan dimension of each elastomeric layer increases by a factor $(1 + \nu^* \varepsilon_v)$, where $\nu^* = 0.3$ (rather than 0.5) is a nominal Poisson ratio chosen empirically to account for the non-uniform increase of area along the height due to the effect of the end plates.

The expression of the relationship between the axial force P and the nominal axial deformation ε according to Stanton et al.'s theory (1990) is (defined in section 4.4, Equation 4.14):

$$P = 3GA_0 \left(f_{c1} + f_{c2} \right) \frac{\left(1+\nu\varepsilon\right)^3 - 1}{3\nu\varepsilon} \varepsilon \tag{6.5}$$

Stanton et al. (1990) provided the following expression of the bending and shear stiffness parameters:

$$B = f_r EI_0 \left(1+\nu^*\varepsilon\right)^4$$
$$R = GA_0 \left(1+\nu^*\varepsilon\right)^2 \quad 6.6$$

These expression of B and R can be used within Equation 6.2 and assuming $h=h_0$ to evaluate the horizontal stiffness of the compressed bearing.

Muhr (2017) adopted the work of Goodchild et al. (2018) on the lateral stiffness and damping of stretched rubber beams and developed a theory for the compressive and lateral stiffness of single layer blocks of rubber with bonded endplates under finite axial deformation, accounting for the changes in geometry of the block as functions of the axial shortening and shape factor. The theory of Muhr was developed considering a Mooney-Rivlin strain energy model for the rubber compound, and a simplified deformation field consisting of small shear strains superimposed to finite axial strain.

The expression developed by Muhr (2017) (defined in section 4.4, Equation 4.13), for relating the axial compression to the applied compressive load P considering a block made of a Neo-Hookean rubber material is:

$$P = GA_0\left[\left(\frac{1}{\lambda^2}-\lambda\right)+3S^2\left(1-\frac{1}{\lambda^2}\right)\right] \quad 6.7$$

where $\lambda = 1-\varepsilon$ is the axial stretch ratio (< 1 in the case of compression).

The expressions of B and R according to Muhr are:

$$B = G\left(2\lambda^2+\frac{1}{\lambda}\right)\left(1+\frac{2S^2}{3}\right)\frac{I_0}{\lambda^2} \quad 6.8$$

$$R = \lambda GA_0 \quad 6.9$$

The expressions of B and R according to Muhr's theory can also be used within Equation 6.2 to evaluate the horizontal bearing stiffness, by using the deformed length h instead of h_0.

Figure 6.2a shows and compares the relationship between applied vertical load and vertical displacement according to the Equations 6.1, 6.5 and 6.7. In the same figure, the curve obtained numerically by Orfeo et al. (2022) is shown for comparison (the axial load was not monitored during the experiments). It can be observed that Muhr's theory better captures the nonlinear trend of increase of stiffness with the compressive displacement.

Figure 6.2b compares the estimates of the initial shear stiffness at zero shear displacement for increasing values of the applied vertical displacement according to Muhr's theory, Stanton's theory, Gent (1964), and the experimental results. Since the theories provide estimates of the tangent shear stiffness at zero horizontal displacement, the shear modulus of the rubber material at 0% shear strain is considered,

corresponding to G = 0.63MPa (Figure 6.1b). In general, the horizontal stiffness reduces for increasing vertical load, and the condition of instability is attained when it becomes zero. Muhr's model provide an overall good estimate of the shear stiffness for increasing compression levels. It is also interesting to observe that the ratio between the initial horizontal and vertical stiffness is about 43, which is significantly lower than the values typical of high shape factor bearings (several hundred times as discussed in Kelly, 1993a, e.g. about 800 for S=12 in Tubaldi et al., 2018, which deals with isolation bearings for bridges).

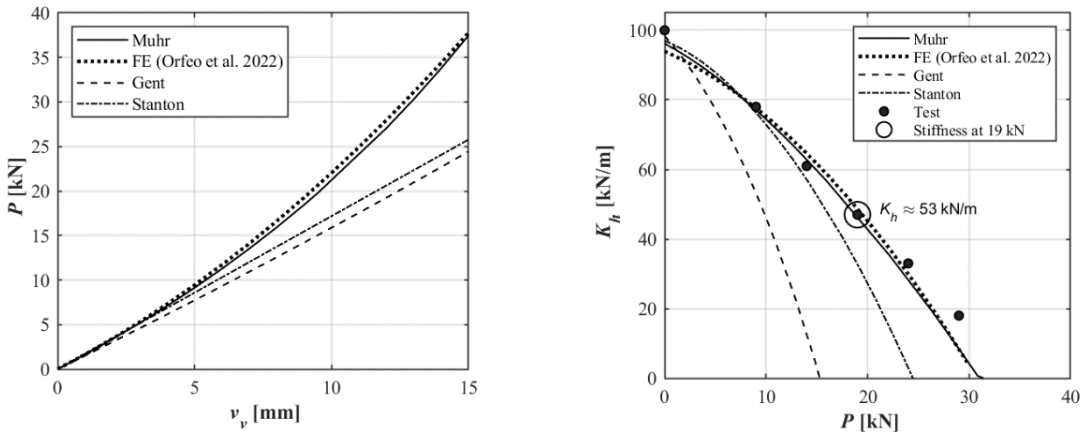

(a) (b)

Figure 6.2– Comparison between the theories (a) Compressive load vs vertical displacement (b) Initial Shear stiffness vs vertical displacement for the bearing of Figure 5.3a. Experimental values taken from (Cuomo, 2014).

While the maximum compressive load considered experimentally is 29kN, analytical formulations are also used for higher compression levels to estimate the buckling load. Table 5.3 illustrates the estimates of the buckling load according to Muhr, Stanton and Gent models. It can be observed that all the theories underestimate the buckling load of the bearing which is likely to achieve the buckling condition for a compressive load equal to 34 kN (obtained by extrapolation of the experimental results). However, Muhr's model provides a better estimate of the buckling load with an error of only 12%. Table 6.1also illustrates the buckling load according to the numerical results provided by Orfeo et al. (2022) which is equal to 39 kN. It is worth observing, from the same table, that the critical load according to the theory of Gent (1964) is only 40% of the value extrapolated from the experiment.

Table 6.1 Buckling load according to various theories and FE analysis (Orfeo et al.; 2022).

Experimental	**Muhr**	**FE (Orfeo et al. 2022)**	**Gent**	**Stanton**
34 kN	30 kN	39 kN	14 kN	26 kN

In general, the bearings are expected to experience some rotation at the top and therefore a formulation is needed to describe their behaviour under rotation, as well as the coupled rotational-translation

behaviour. For this purpose, similarly to Crowder et al. (2017), it is possible to refer to the work of Chang (2002). Denoting with $v_{b,top}$ and $\theta_{b,top}$ respectively the translation and rotation at the top of the bearing, the following relationship can be used to relate these quantities to the shear force and bending moment applied at the top of the bearing (V_{top} and M_{top}):

$$\begin{bmatrix} V_{top} \\ M_{top} \end{bmatrix} = \begin{bmatrix} k_x & k_{x,\theta} \\ k_{\theta,x} & k_\theta \end{bmatrix} \begin{bmatrix} v_{b,top} \\ \theta_{b,top} \end{bmatrix} = \frac{P}{q\beta h - 2\tan\left(\frac{qh}{2}\right)} \begin{bmatrix} q\beta & -\tan\left(\frac{qh}{2}\right) \\ -\tan\left(\frac{qh}{2}\right) & \frac{1}{q\beta} - \frac{h}{\sin(q\beta)} \end{bmatrix} \begin{bmatrix} v_{b,top} \\ \theta_{b,top} \end{bmatrix} \tag{6.10}$$

Where $\beta=R/(R+P)$, k_x is the horizontal stiffness (coincident with K_h of Equation 6.2 for zero horizontal deflections), k_θ is the rotational stiffness and $k_{x,\theta}$ a coupling term.

Under strong earthquake inputs, elastomeric bearings undergo large lateral displacements, and the rubber is subjected to high shear strains. In order to capture these effects, reference can be made to Nagarajaiah et al.'s (Nagarajaiah et al. 1999) extension of Koh and Kelly's mechanical model, which considers large displacements, large rotations, and nonlinearity of rubber. The change of the horizontal stiffness k_x with the horizontal displacement v_{top} is evaluated solving numerically the following system of equations:

$$\begin{cases} \dfrac{R}{h}\left(1 - C_s\left(\dfrac{s}{t_r}\right)\right)s = F\cos\varphi + P\sin\varphi + \dfrac{\pi^2 B}{h}\dfrac{C_\theta \varphi^2}{2} \\ \dfrac{\pi^2 B}{h}\left(1 - C_\varphi\left(\dfrac{s}{t_r}\right)\right)\varphi = P\left(h\sin\varphi + s\cos\varphi\right) + F\left(h\cos\varphi - s\sin\varphi\right) \\ v_{top} = h\sin\varphi + s\cos\varphi \end{cases} \tag{6.11}$$

where F and P are the horizontal and vertical force, the expressions of R,B, and h are evaluated according to the considered theory, C_s and C_φ are material parameters that describe their evolution for increasing nominal shear strain levels, and φ and s are the rotation and the shear displacement in the Koh and Kelly's mechanical model, respectively. The system of equations is solved by finding the values of s, φ and F for increasing values of v_{top}, and the horizontal secant stiffness k_x, corresponds to the ratio between F and v_{top}. For small value of s and φ, C_s =0 and C_φ =0, the system of equations reduces to the expression derived by Koh and Kelly (1988).

For describing the reduction of the vertical stiffness with the increase of the horizontal displacement, Warn et al's model has been adopted (Warn et al. 2007). This model accounts for the drop in height of

the bearing due to the horizontal displacement, whereas the change of the stiffness with the increase of the axial load is assumed negligible. The following expression taken from Warn et al. (2007) can be used:

$$k_z = k_{z0} \frac{1}{\left[1 + \frac{3A_0}{I}\frac{v_{top}^2}{\pi^2}\right]} \tag{6.12}$$

where $k_{z0} = \partial N/\partial v_v$ is the vertical stiffness evaluated in correspondence of the bearing's deformed configuration under the applied compressive force P (coincident with K_v of Equation 3.4) and I is the second moment of area of the bearing cross section.

To summarise, the analytical model of the LSF bearings used in the next section for the simulation of the dynamic response of the prototype uses the expression of the horizontal secant stiffness k_x resulting from the solution of Equation (12), the expressions of the rotational stiffness k_ϕ and of the coupling between horizontal displacements and rotations $k_{x,\phi}$ reported in Equation 6.10, the expression of the vertical stiffness k_z from Equation 6.12, with k_{z0} derived by differentiation of Equation 6.7.

6.3 Shaking table tests

6.3.1 Prototype, Tests Description and Dynamic Identification

This subsection briefly illustrates the shaking table tests described in section 5.3.1. Table 6.2 summarizes the experimental frequencies, periods, and damping ratios of the system. These have been obtained by applying the Stochastic Subspace Identification (SSI) method (Van Overschee and De Moor, 2008), using the recorded acceleration responses at the base and top level under two random input tests (i.e. Test 1, Test 2), with ground motions applied in the direction of the widest frame span. The tests induced a peak horizontal displacement of the bearings of 7.44 mm and 16.33 mm respectively, corresponding to average shear strain of 13% and 29%.

The identified value of the fundamental vibration period is 1.21s, corresponding to an equivalent period of the full-scale structure of 2.1s (the prototype has a geometry scale factor of 1/3 and thus the period of the full scale structure is √3 times the period of the prototype). It is noteworthy that taking the superstructure as rigid and the bearings as infinitely stiff in the vertical direction, and using the initial bearing stiffness K_h = 53 kN/m evaluated in subsection 6.2.2 under the axial load of 19kN, an isolation period $T_{is} = 2\pi\sqrt{M_{tot}/4k_{is}}$ = 1.21s is obtained, which coincides with the experimental one.

Table 6.2 Identified dynamic properties of the isolated system.

	Mode 1		**Mode 2**		**Mode 3**	
	Test 1	**Test 2**	**Test 1**	**Test 2**	**Test 1**	**Test 2**
Vibration period [s]	1.21	1.24	0.27	0.26	0.08	0.08
Damping Ratio [-]	0.08	0.06	0.08	0.04	0.06	0.06

After performing the random vibration tests, further tests were carried out under seven earthquake ground motions selected from the European strong-motion database, whose main characteristics are described in Table 6.3. The next subsection describes the development and validation of a numerical model for simulating the dynamic and seismic response of the isolated structure with LSF bearings.

Table 6.3 Ground motion characteristics (Mw=Magnitude, PGA=Peak ground acceleration, PGV= Peak ground velocity, PGD= Peak ground displacement)

Waveform ID	**Earthquake Name**	**Earthquake Country**	**Mw**	**PGA (m/s^2)**	**PGV (cm/s)**	**PGD (cm)**
7142	Bingol	Turkey	6.3	2.55	18.29	3.25
55	Friuli	Italy	6.5	2.55	15.25	9.29
200	Montenegro	Montenegro	6.9	2.55	12.87	9.60
428	Etolia	Greece	5.3	2.55	12.46	6.06
372	Lazio Abruzzo	Italy	5.9	2.55	15.02	6.80
290	Campano Lucano	Italy	6.9	2.55	44.10	16.20
287	Campano Lucano	Italy	6.9	2.55	43.90	14.00

6.3.2 Simplified model

Since the shaking table test configuration has a plane of symmetry, only half of the building is modelled. Figure 6.3 illustrates the model representing the isolated frame building and the generalised coordinates that are considered for deriving the equations of motion of the system through the Lagrange's equations. The superstructure is simplified as a rigid block with mass m_{top} and stiffness k_s, with the mass located at a distance H from the supporting rigid base of mass m_b. The base, of width $2D$, is supported by two

springs with horizontal, vertical and rotational stiffness denoted as k_x, k_z, $k_{x,\theta}$ respectively. The generalised coordinates are: the rotation θ of the base (coincident with the rotation of the bearing top $\theta_{b,top}$), the vertical displacement of the base $v_{b,z}$ (coincident with the vertical displacement of the bearings), the horizontal displacement of the base $v_{b,x}$ (coincident with the bearings' top displacement $v_{b,top}$), and the horizontal displacement of the superstructure relative to isolation system $v_{s,x}$.

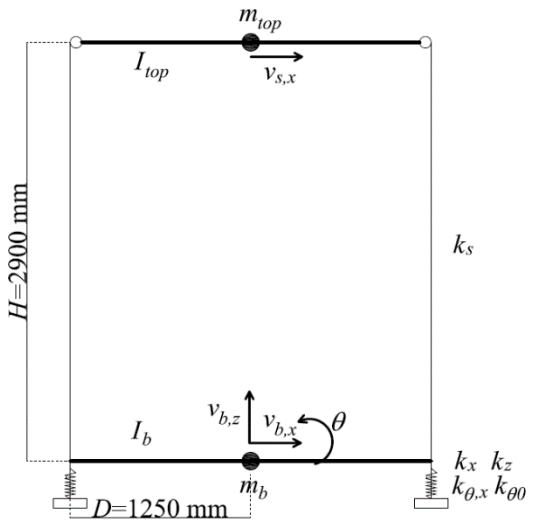

Figure 6.3 Model of the base isolated structure

The kinetic energy and the potential energy of the system are defined as follows:

$$T = \frac{1}{2}m_b\left(\dot{v}_{b,x}+\dot{v}_{g,x}\right)^2+\frac{1}{2}m_{top}\left(\dot{v}_{b,x}+\dot{v}_{g,x}+H\dot{\theta}+\dot{v}_{s,x}\right)^2+\frac{1}{2}m_{tot}\left(\dot{v}_{b,z}\right)^2+\frac{1}{2}I_b\dot{\theta}^2+\frac{1}{2}I_{top}\dot{\theta}^2$$
$$V = 2\left(\frac{1}{2}k_x\left(v_{b,x}\right)^2+\frac{1}{2}k_z\left(v_{b,z}\right)^2+\frac{1}{2}k_z\left(\theta D\right)^2+\frac{1}{2}k_{\theta 0}\theta^2+\frac{1}{2}k_s{v_{s,x}}^2+k_{\theta,x}v_{b,x}\theta+\frac{1}{2}k_{\theta,x}{v_{b,x}}^2\right)$$

6.13

where $v_{g,x}$ denotes the response induced by the earthquake ground motion I_b and I_{top} are the moment of inertia of mass m_b and m_{top} respectively.

The terms $k_{\theta,x}$, denotes the coupling between the horizontal displacement and the rotation.

The Lagrangian is therefore:

$$L = T - V = \frac{1}{2}m_b\left(\dot{v}_{b,x}+\dot{v}_{g,x}\right)^2+\frac{1}{2}m_{top}\left(\dot{v}_{b,x}+\dot{v}_{g,x}+H\dot{\theta}+\dot{v}_{s,x}\right)^2+\frac{1}{2}m_{tot}\left(\dot{v}_{b,z}\right)^2+$$
$$+\frac{1}{2}I_b\dot{\theta}^2+\frac{1}{2}I_{top}\dot{\theta}^2-k_x{v_{b,x}}^2-k_z{v_{b,z}}^2-k_z\left(\theta D\right)^2-k_{\theta 0}\theta^2-k_s v_{s,x}^2-2k_{\theta,x}v_{b,x}\theta-k_{\theta,x}{v_{b,x}}^2 \qquad 6.14$$

The corresponding Euler-Lagrange equations of motion are obtained by the following derivatives of the Lagrangian:

$$\begin{aligned}
&\frac{\partial}{\partial t}\left(\frac{\partial L}{\partial \dot{v}_{b,x}}\right)-\frac{\partial L}{\partial v_{b,x}}=0\\
&\frac{\partial}{\partial t}\left(\frac{\partial L}{\partial \dot{\theta}}\right)-\frac{\partial L}{\partial \theta}=0\\
&\frac{\partial}{\partial t}\left(\frac{\partial L}{\partial \dot{v}_{s,x}}\right)-\frac{\partial L}{\partial v_{s,x}}=0\\
&\frac{\partial}{\partial t}\left(\frac{\partial L}{\partial \dot{v}_{b,z}}\right)-\frac{\partial L}{\partial v_{b,z}}=0
\end{aligned} \qquad 6.15$$

which gives:

$$\begin{cases}
m_b\left(\ddot{v}_{b,x}+\ddot{v}_{g,x}\right)+m_{top}\left(\ddot{v}_{b,x}+\ddot{v}_{g,x}+H\ddot{\theta}+\ddot{v}_{s,x}\right)+2k_x v_{b,x}+2k_{\theta,x}v_{b,x}+2k_{\theta,x}\theta=0\\
m_{top}H\left(\ddot{v}_{b,x}+\ddot{v}_{g,x}+H\ddot{\theta}+\ddot{v}_{s,x}\right)+I_b\ddot{\theta}+I_{top}\ddot{\theta}+2k_z D^2\theta+2k_{\theta 0}\theta+2k_{\theta,x}v_{b,x}=0\\
m_{top}\left(\ddot{v}_{b,x}+\ddot{v}_{g,x}+H\ddot{\theta}+\ddot{v}_{s,x}\right)+2k_s\left(v_{s,x}\right)=0\\
m_{tot}\ddot{v}_{b,z}+2k_z\left(v_{b,z}\right)=0
\end{cases} \qquad 6.16$$

The response of the structure to earthquake-induced ground motion $\ddot{v}_g(t)$, when also damping is included, can be described by the differential equation in matrix form:

$$\mathbf{M}\ddot{\mathbf{v}}+\mathbf{C}\dot{\mathbf{v}}+\mathbf{K}\mathbf{v}=\mathbf{-MI}\ddot{v}_g \qquad 6.17$$

where **I** is the influence vector and the matrices are defined as follows:

$$\mathbf{I}=\begin{bmatrix}1\\0\\0\\0\end{bmatrix} \qquad 6.18$$

$$\mathbf{v}=\begin{bmatrix}v_{b,x}\\\theta\\v_{s,x}\\v_{b,z}\end{bmatrix} \qquad 6.19$$

$$\mathbf{M}=\begin{bmatrix}m_b+m_{top} & m_{top}H & m_{top} & 0\\ m_{top}H & m_{top}H^2+I_b+I_{top} & m_{top}H & 0\\ m_{top} & m_{top}H & m_{top} & 0\\ 0 & 0 & 0 & m_b+m_{top}\end{bmatrix} \qquad 6.20$$

$$\mathbf{K}=\begin{bmatrix}2k_x & 2k_{\theta,x} & 0 & 0\\ 2k_{\theta,x} & 2k_zD^2+2k_{\theta 0} & 0 & 0\\ 0 & 0 & 2k_s & 0\\ 0 & 0 & 0 & 2k_z\end{bmatrix} \qquad 6.21$$

The damping matrix **C** can be constructed in a simplified way by assuming a value for the damping ratio of the base isolation system and of superstructure ξ_b and ξ_s as follows:

$$\mathbf{C}(1,1) = c_b = 2\xi_b \frac{\mathbf{K}(1,1)}{\omega_{is}}$$
$$\mathbf{C}(3,3) = c_s = 2\xi_s \frac{\mathbf{K}(3,3)}{\omega_{is}} \qquad 6.22$$

The adopted value of ξ_b refers to the equivalent damping ratio of the bearing corresponding to a nominal shear strain of 80% (Figure 5.3c). This is the ratio between the maximum horizontal displacement experienced by the bearing due to the Bingol earthquake and the total rubber layers' height. The damping ratio of the superstructure ξ_s is assumed equal to 0.65% (Magliulo et al., 2014). The natural frequency ω_{is} is known from the eigenvalue analysis. Table 6.4 shows the values of the masses and moments of inertia considered in this study along with the values of the initial stiffness and damping of the bearing. The vertical and horizontal stiffness are determined by considering Muhr's theory (2017) for the bearing compressed by a vertical load of 19 kN. In particular, k_{x0} is obtained from Equation 6.2 , and k_{z0} by differentiation of the expression of P in Equation 6.7. The expression of the rotational stiffness $k_{\theta 0}$ and of the coupling term $k_{x\theta}$ can be found in Equation 6.10 and are assumed constant.

Table 6.4 Base isolated system parameters

I_b	I_{top}	m_b	m_{top}	k_{z0}	k_{x0}	$k_{\theta 0}$	$k_{x\theta}$	c_b
[tonnesm^2]	[tonnesm^2]	[tonnes]	[tonnes]	[kN/m]	[kN/m]	[kNm]	[kNm]	[Ns/m]
1.22	1.98	1.26	2.05	1939	53	0.0032	0.5	2.88

The horizontal stiffness variation with horizontal displacement is defined by solving Equation 6.11 as discussed in the previous section, with B and R from the theory of Muhr (2017) and C_s and C_φ calibrated against the experimental double-shear test results and assumed equal to 0.14. The vertical stiffness reduction is evaluated using Equation 6.12. The coupling term is assumed not to change with the horizontal displacement.

Figure 6.4 shows the variation of the horizontal and vertical stiffnesses with the horizontal displacement up to 45mm (i.e. the maximum deflection experienced by the bearing during Bingol earthquake) according to Equations 6.11 and 6.12 for an axial load of 19kN.

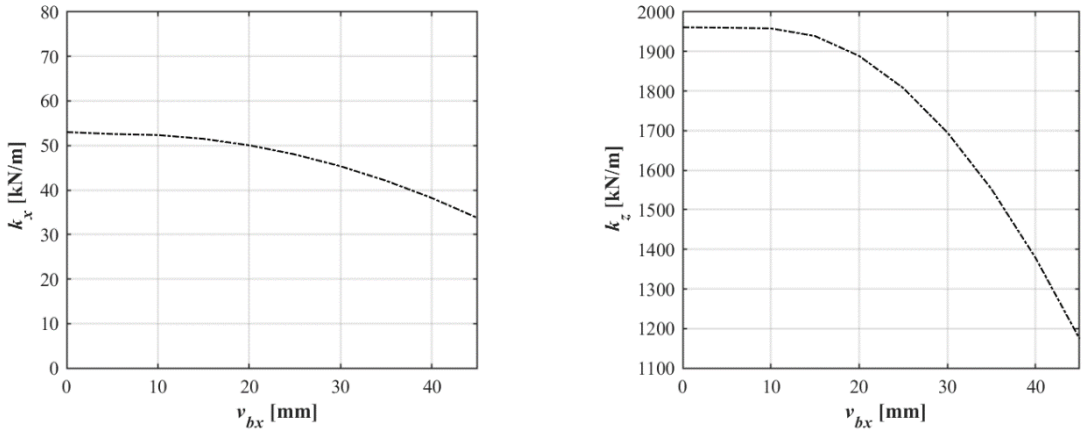

(a) (b)

Figure 6.4 Variation with the horizontal displacement of the secant horizontal stiffness (a) and of the vertical stiffness (b).

The undamped modal properties of the system can be found by solving the eigenvalue problem:

$$\det\left[\mathbf{K}-\omega_n^2\mathbf{M}\right]=0 \tag{6.23}$$

Figure 6.5 illustrates the modal shapes of the horizontal vibration modes of the model, by showing the values of the displacements $v_{b,x}$, $v_{s,x}$ and θH, normalised by the maximum horizontal displacement for each mode. It can be observed that there is a small amount of rocking in the first mode, whereas there is a higher contribution in the second and third mode. Table 6.5 shows the natural periods evaluated at each mode showing a good agreement with those estimated via the dynamic identification (Table 6.2). Furthermore, the Modal Assurance Criterion (MAC) (Magliulo et al., 2014) has been used to compare the mode shapes derived from the analytical model with those obtained experimentally. The obtained MAC values, shown in Table 6.5, indicate that mode shapes 1 and 2 are almost identical with the experiment ones (MAC higher than 0.9) whereas a slight difference (MAC between 0.8 and 0.9) can be found for mode 3.

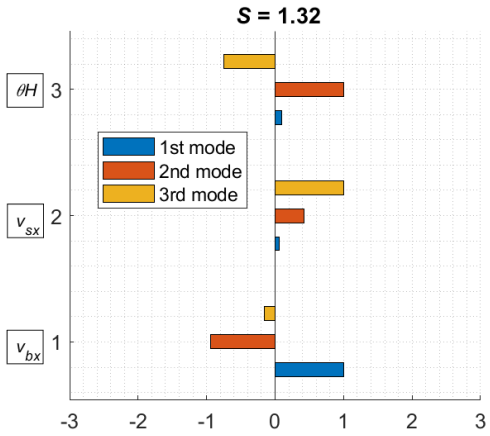

Figure 6.5 Modal shapes of the first three modes of vibration

Figure 6.6 presents the deflection shapes corresponding to the first three horizontal modes. The first mode is primarily dominated by the horizontal deflections of the bearing, with the superstructure moving almost rigidly. The second mode involves significant deflections of the bearings, as well as base rotation and superstructure deflections. The third modal shape is controlled mainly by the rotation of the base and by the deflection of the columns.

Table 6.5 Periods of vibration, mode shapes and MAC values

Mode	**First**	**Second**	**Third**
Natural Periods [s]	1.25	0.28	0.08
MAC	0.99	0.96	0.86

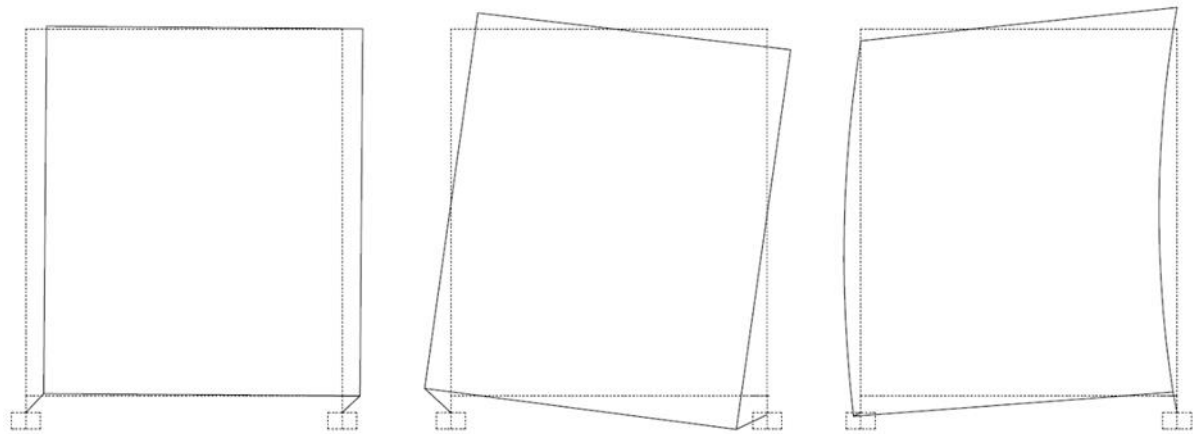

(a) (b) (c)

Figure 6.6 Mode shapes of the Base isolated structure (a) First mode, (b) Second mode, (c) Third mode

A fourth-order Runge Kutta algorithm (ode45 in Matlab; 2021) is used to numerically evaluate the response of the system to the seismic inputs, using the secant values of the horizontal and vertical stiffness corresponding to the maximum bearing displacement during the seismic motion. The changes in axial force in the bearings are not considered for evaluating the secant stiffness. Figure 6.7a-b-c compare the experimental and numerical response under Friuli record, in terms of horizontal bearing displacement (Figure 6.7a), superstructure interstorey drift (Figure 6.7b) and acceleration at the top of the superstructure (Figure 6.7) . In general, a good agreement is observed between the experimental and the numerical response. Figure 6.7c illustrates the contribution to the displacement response of the top node by the horizontal deflections of the bearings, the superstructure deflection, and the rocking contribution. The rocking contribution is the rotation experienced by the base isolation system under seismic load multiplied by the height of the superstructure *H*. It can be observed that the displacements are all in phase, suggesting mode 1 predominates the response, and the superstructure response is dominated by the bearing deflection. The rocking of the bearings contributes to less than 16% of the

peak top displacement of the structure, despite the relatively high vertical flexibility of the LSF bearings, compared to bearings with high shape factors. This outcome is in line with previous findings demonstrating that a vertical frequency higher than 1 to 3 Hz provides negligible rocking motion and results into a fundamental horizontal deflection mode of the structure (Wang and Wang, 2012; Kalfas et al. 2017). Recently Losanno et al. (2022) found that even in the case of fiber-reinforced elastomeric isolators a limited axial-to-horizontal stiffness ratio would not affect the effectiveness of base isolation under seismic motion.

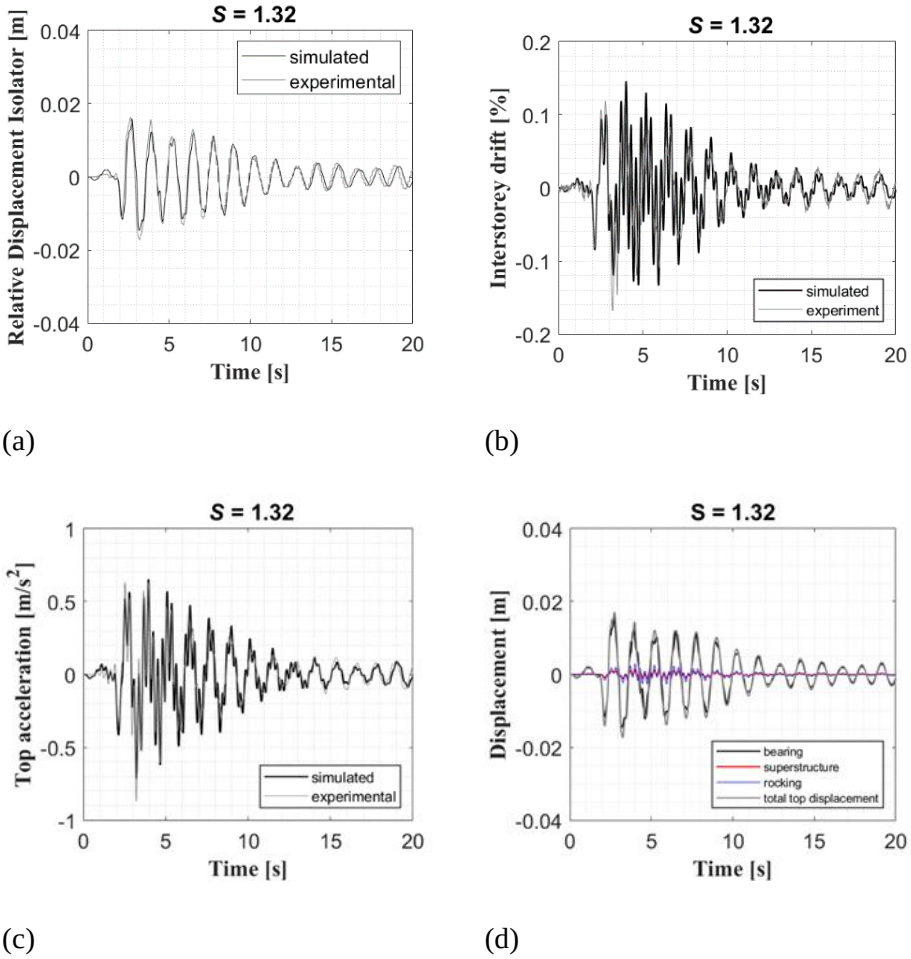

Figure 6.7– Response to Friuli Earthquake (a) Relative Displacement Isolator time history, (b) Interstorey drift (c) Acceleration at the top node (d) Time history of the bearing, superstructure and rocking contributions to the top node displacement

Figure 6.8a-b-c shows the results obtained for the Bingol earthquake, which induces higher deflections of the bearings compared to the other records. The agreement between the experimental and analytical results is very satisfactory for both the relative displacement of the isolator and the interstorey drift. It is noteworthy that to properly simulate the response to Bingol earthquake input and the period elongation that characterises the response under the large amplitudes of vibrations, it is necessary to

consider the horizontal and vertical stiffness reduction for increasing horizontal displacements, as shown in Figure 6.4a and b.

Figure 6.8d illustrates the three contributions to the top displacement response, showing again that these contributions are all in phase and that the rocking of base has a negligible effect on the response.

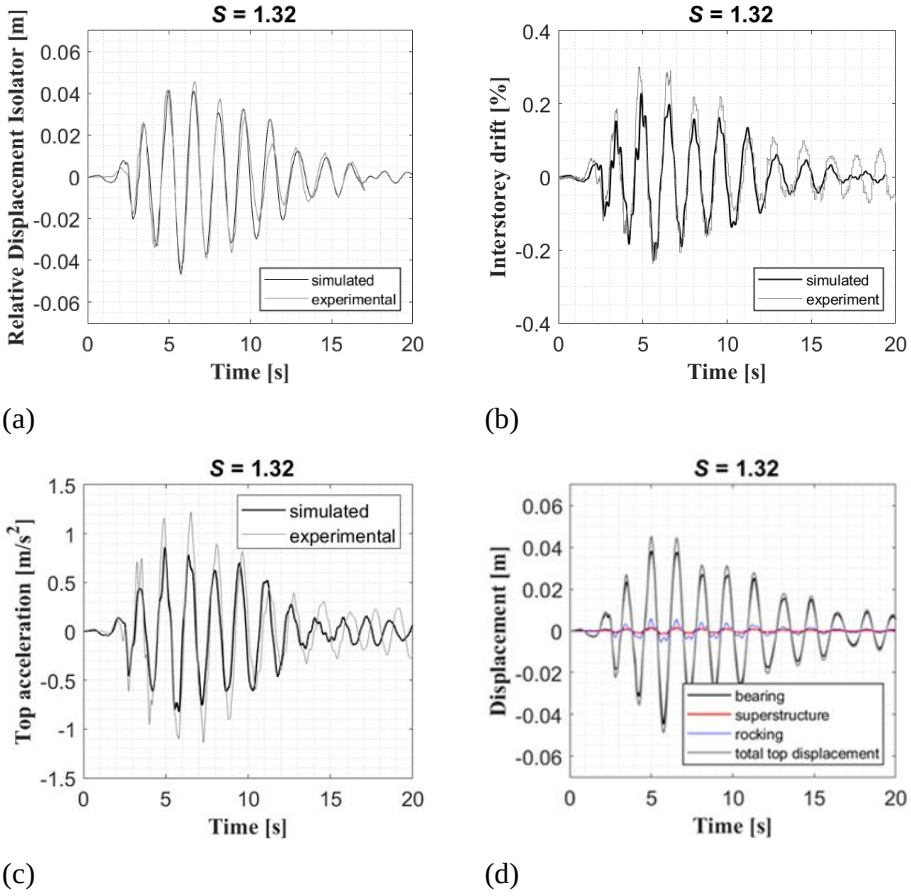

Figure 6.8– Response to Bingol Earthquake (a) Relative Displacement Isolator time history, (b) Interstorey drift, (c) Acceleration at top node and (d) Time history of the bearing, superstructure and rocking contributions to the top node displacement

Table 6.6 compares the experimental and numerical maximum absolute values of the isolator deflection, interstorey drift and acceleration at top for all the records. It can be observed that the numerical model describes accurately the response of the isolator with only 10% of relative error with respect to the experimental results (minimum error of 1.6% under Bingol record corresponding to largest isolator displacement), whereas a slightly higher relative error (24%) can be observed for the prediction of maximum interstorey drift of the superstructure. In terms of top acceleration, the numerical model describes the Bingol response with 28% of relative error, which is due to the assumption of a secant horizontal stiffness (i.e. equivalent linear model) of the superstructure, whereas lower relative errors can be observed under the other records.

Table 6.6 Maximum absolute values of various response parameters according to experimental test and numerical model.

Earthquake Name	**Max Displacement Isolator [mm]**			**Max Drift Structure [%]**			**Max Top Acceleration [m/s^2]**		
	Exp	Numerical model	Relative error %	Exp	Numerical model	Relative error %	Exp	Numerical model	Relative error %
Bingol	45.9	46.6	1.6	0.3	0.23	-24.5	1.2	0.86	-28
Friuli	17.2	15.8	-9.4	0.17	0.13	-24.1	0.9	0.71	-20
Montenegro	17.3	18.8	8.8	0.17	0.14	-19.7	0.9	0.77	-11.4
Etolia	17.4	19.0	9.0	0.17	0.14	-17.4	0.9	0.77	-11.0
Lazio/Abruzzo	17.6	19.0	8.3	0.16	0.14	-13.2	0.9	0.78	-10.3
ID 290	17.6	19.0	8.1	0.16	0.14	-15.8	0.9	0.78	-9.9
ID 287	17.3	18.9	9.2	0.17	0.14	-19.2	0.9	0.78	-10.0

6.4 Parametric study

This section investigates the seismic response of a set of models that are obtained from the model investigated in the previous section by varying the shape factor of the bearings. Table 6.7 describes the geometric and mechanical properties of the bearings, which have been designed in order to obtain the same horizontal stiffness exhibited under the permanent load of 19kN. The initial horizontal and vertical stiffness have been estimated using Muhr's theory.

Table 6.7 – Horizontal and vertical stiffness of the bearings

Shape factor *S*	**Initial horizontal Stiffness k_{x0} [kN/m]**	**Initial vertical Stiffness k_{z0} [kN/m]**	k_{z0}/k_{x0}	**Horizontal Period [s]**	**Vertical Period [s]**
0.90	53	1310	25	1.25	0.24
1.32	53	1913	37	1.25	0.20
9.24	53	31745	608	1.24	0.05
19	53	127120	2434	1.24	0.02

It can be noted that the vertical period reduces significantly with the increase of the shape factor, whereas the first isolation period is not affected, since it is mainly controlled by the horizontal stiffness of the bearings. Figure 6.9 illustrates the variation of the initial horizontal and vertical stiffness of the different bearings for increasing values of the vertical load.

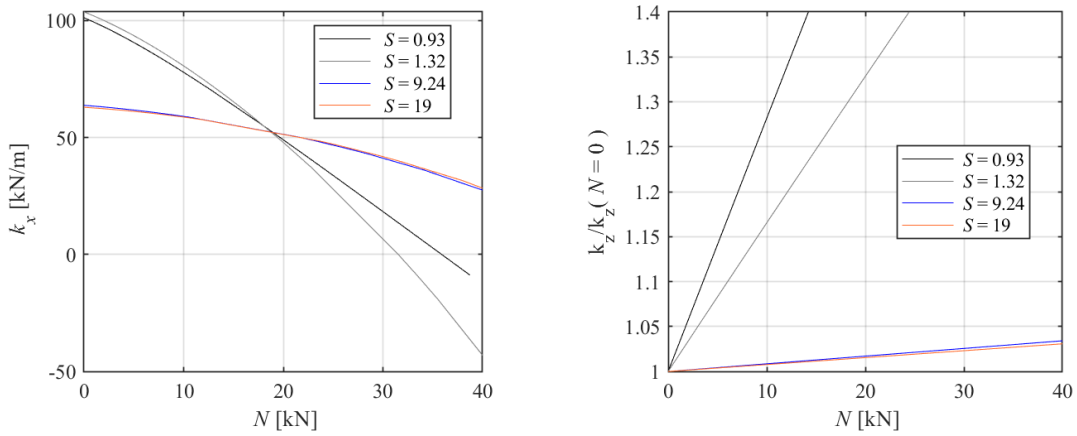

(a) (b)

Figure 6.9– Effect of the vertical load on (a) Horizontal stiffness and (b) Vertical stiffness, for different shape factors

Figure 6.10 describes the contributions of the various Lagrangian parameters to the shapes of the first three modes, for the various values of *S* considered. The system with *S* = 0.9 exhibits modal shapes very similar to those of the system with S=1.32. With the increase of *S*, the contribution of the rotational component in mode 1 and 2 reduces and disappears for *S*=9.24. This is due to the fact that with the increase of shape factor, the ratio k_z/k_x increases as shown in Table 6.7 and this limits the rotation of the base slab.

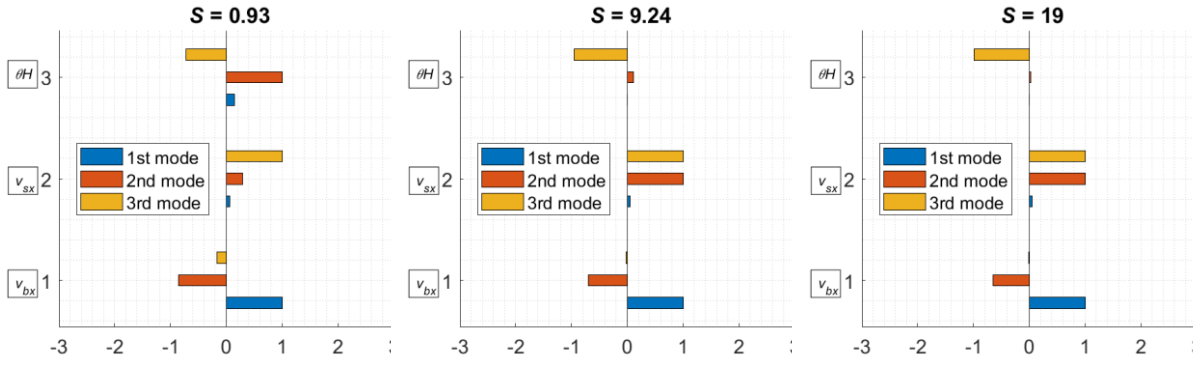

(a) (b) (c)

Figure 6.10 – Mode shapes of the first three modes of vibration for the three designed bearing: (a) *S* = 0.93, (b) *S* = 9.56 and (c) *S* = 10

The second part of the parametric study investigates the seismic response of the isolated systems models corresponding to bearings with different *S* values. Figure 6.11a-c shows the time history of the top displacement responses for the case of Friuli earthquake input. Plotted in the same figures are the contributions to the displacement response of the top node by the bearings, the superstructure, and the rocking base. Figure 6.12a-b-c shows the response in terms of top acceleration under Friuli earthquake. Table 6.8 shows the maximum isolator displacement, the maximum displacement at the top of the superstructure, the rocking contribution due to the Friuli earthquake input and the maximum top

acceleration. The total displacement demand and the maximum top acceleration increase slightly for increasing values of *S*, whereas the rocking contribution follows an opposite trend. In any case, the contribution of rocking to the top displacement response is about 16 % for low shape factors and reduces to 0.15 % for the highest shape factor considered in this study.

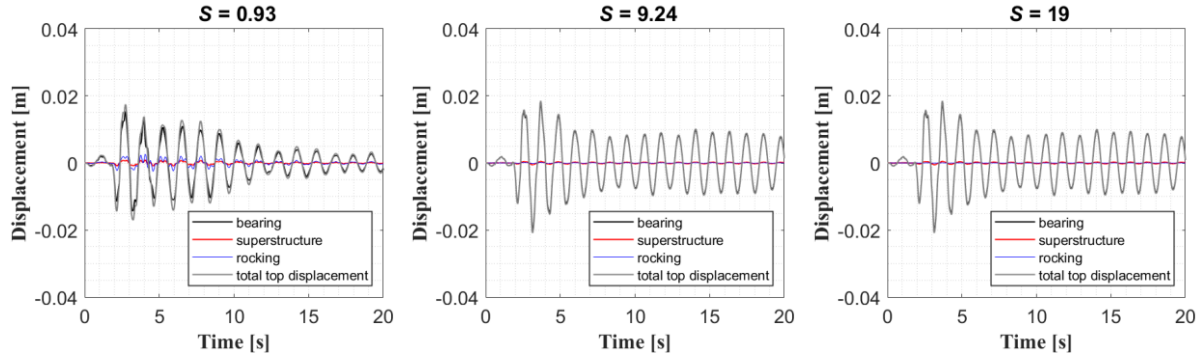

(a) (b) (c)

Figure 6.11 – Response of Friuli earthquake: Time history of the bearing, superstructure and rocking contributions to the top node displacement: (a) *S* = 0.93, (b) *S* = 9.56, (c) *S* = 19

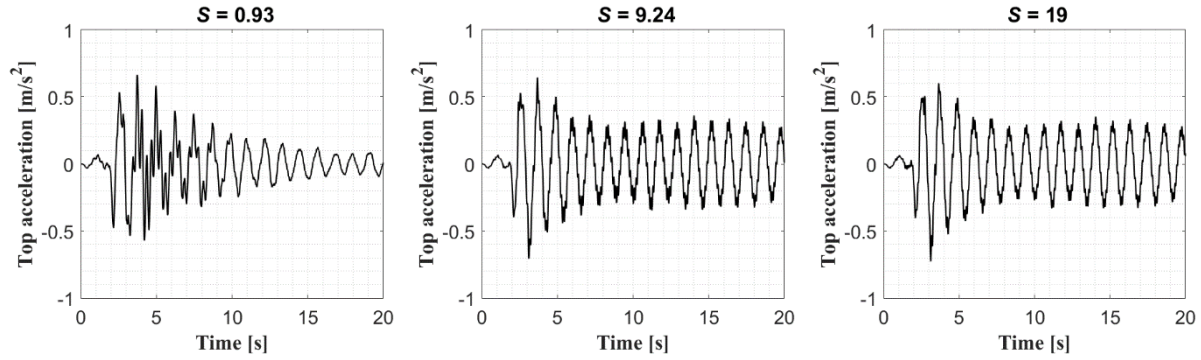

(a) (b) (c)

Figure 6.12 – Response of Friuli earthquake in terms of top acceleration: (a) *S* = 0.93, (b) *S* = 9.56, (c) *S* = 19.

Table 6.8 Response of Friuli earthquake: Maximum isolator displacement, maximum total displacement at the top and rocking contribution

Shape factor *S* [-]	**Max Isolator displacement [mm]**	**Max total top displacement [mm]**	**Rocking contribution [mm]**	**Rocking / Max Total Top displ [%]**	**Max Top Acceleration [m/s²]**
0.93	15.5	17.9	2.9	16.0	0.66
1.32	15.8	18.0	2.8	15.7	0.71
9.56	19.0	20.2	0.1	0.5	0.72
19	19.3	20.3	0.03	0.15	0.73

Figure 6.11a-b-c compares the responses obtained for the different S values of the bearings in the case of Bingol earthquake input. Also in this case, it can be observed that the total displacement demand increases slightly for increasing values of *S*, whereas the rocking contribution follows an opposite trend. In any case, the contribution of rocking to the top displacement response is very low, and the bearing deflections dominate the response also in the case of very low values of S. Figure 6.14a-b-c compares the response in term of top accelerations for the various shape factor of the bearing under Bingol earthquake. Table 6.9 shows the maximum isolator displacement, the maximum displacement at the top of the superstructure, the rocking contribution due to the Bingol earthquake input and the maximum top acceleration. In this case, the contribution of rocking to the top displacement is of the order of 6 % , 4.9 %, 0.62 % and 0.13% for *S* = 0.93, 1.32, 9.56 and 19, respectively. It is worth mentioning that, although the rocking contribution is negligible for the case of high shape factors, it is also not very significant for the case of low shape factors.

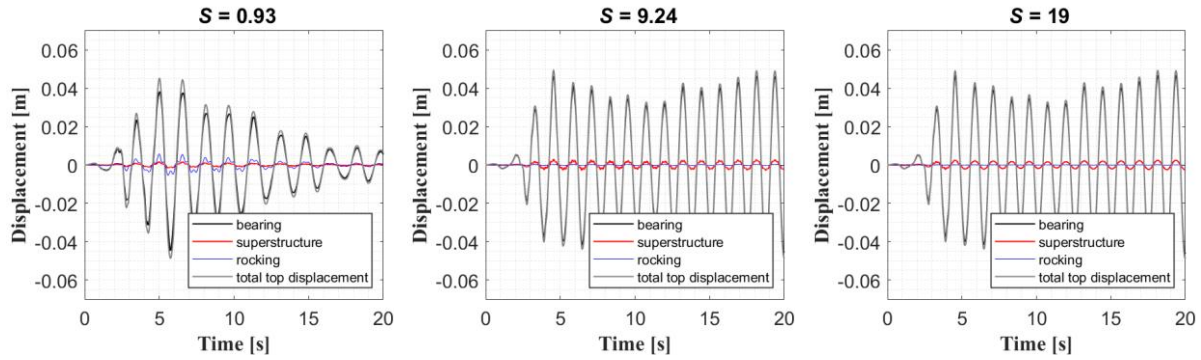

(a) (b) (c)

Figure 6.13– Response to Bingol earthquake: Time history of the bearing, superstructure and rocking contributions to the top node displacement: (a) *S* = 0.93, (b) *S* = 9.56, (c) *S* = 19

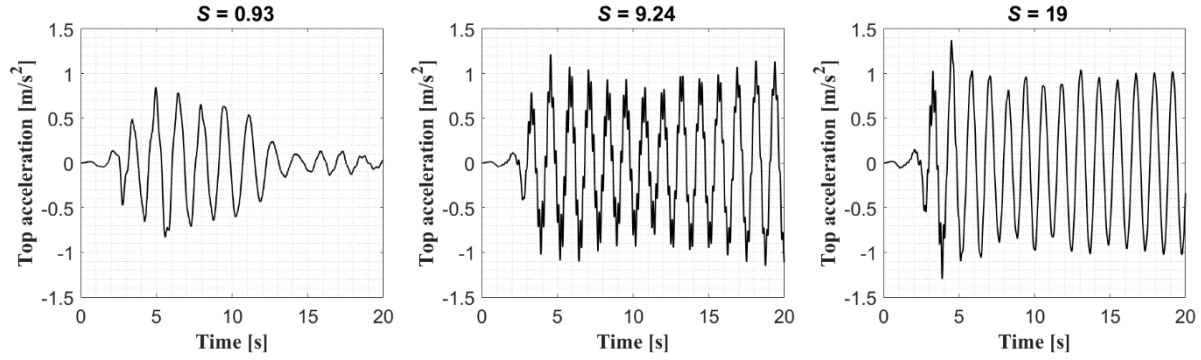

(a) (b) (c)

Figure 6.14– Response to Bingol earthquake in terms of top acceleration: (a) *S* = 0.93, (b) *S* = 9.56, (c) *S* = 19

Table 6.9 Response to Bingol earthquake: Maximum isolator displacement, maximum total displacement at the top and rocking contribution

Shape factor *S* [-]	**Max Isolator displacement [mm]**	**Max total top displacement [mm]**	**Rocking contribution [mm]**	**Rocking / Max Total Top displ [%]**	**Max Top Acceleration [m/s^2]**
0.93	44.7	48.8	3.0	6.0	0.84
1.32	46.6	49.0	2.4	4.9	0.86
9.56	46.6	49.7	0.3	0.6	1.21
19	47.2	49.8	0.067	0.13	1.37

Table 6.10 reports the total displacement of the top of the superstructure and the rocking contribution resulting from the analyses carried out considering the various earthquake inputs. The rocking contribution exhibits the same decreasing trend for increasing values of the shape factor for the various earthquake inputs. A maximum ratio of the rocking to the maximum total displacement of 16% is obtained for the lowest shape factor, whereas a minimum ratio of 0.13% is observed for S = 19. The order of magnitude of the rocking contribution observed in the worst-case scenario is overall quite low. The maximum displacement at the top increases by 2% and 11% for Bingol and Friuli earthquake and by 8% for the remaining earthquakes for values of S increasing from 0.9 to 19.

Table 6.10 Response of all earthquake inputs: maximum total displacement at the top and rocking contribution

Shape factor *S*	**0.9**		**1.32**		**9.56**		**19**	
Earthquake Name	**Max total top displ. [mm]**	**Rocking / max top displ [%]**	**Max total top displ. [mm]**	**Rocking / max top displ [%]**	**Max total top displ. [mm]**	**Rocking / max top displ [%]**	**Max total top displ. [mm]**	**Rocking / max top displ [%]**
Bingol	48.8	6.0	49.0	4.9	49.7	0.6	49.8	0.13
Friuli	17.9	16.0	18.0	15.7	20.3	0.5	20.3	0.15
Montenegro	20.7	15.0	21.6	14.7	23.5	0.6	23.5	0.15
Etolia	20.8	14.9	21.7	14.7	23.6	0.6	23.7	0.14
Lazio/Abruzzo	20.7	15.0	21.7	14.6	23.7	0.6	23.7	0.14
ID 290	20.8	15.0	21.6	14.8	23.6	0.6	23.7	0.14
ID 287	20.7	15.0	21.7	14.7	23.5	0.6	23.6	0.14

Finally, Table 6.11 reports the response of all earthquake input in terms of maximum top acceleration. In terms of effectiveness of base isolation, it can be observed that top acceleration increases with the increase of the shape factor. By including rocking component under horizontal excitation demonstrated

in fact that low shape factor bearings enhance seismic performance of the isolation systems in comparison with higher shape factor bearings. This outcome is confirmed by displacement (Figure 6.13) and acceleration trend (Figure 6.14) demonstrating a lower number of peaks with lower magnitude in case of LSF bearings. Even if rocking contribution to top displacement is higher in case of LSF compared to higher shape factors, total top displacement and acceleration tend to reduce achieving a main advantage of base isolation in the former case.

Table 6.11 Response of all earthquake inputs: maximum top acceleration [m/s^2]

Shape factor *S*	**0.9**	**1.32**	**9.56**	**19**
Earthquake Name				
Bingol	0.844	0.863	1.212	1.372
Friuli	0.664	0.714	0.719	0.733
Montenegro	0.756	0.765	0.814	0.791
Etolia	0.749	0.772	0.819	0.786
Lazio/Abruzzo	0.747	0.775	0.817	0.789
ID 290	0.747	0.779	0.816	0.794
ID 287	0.746	0.778	0.824	0.787

6.5 Conclusions

This study investigates experimentally and numerically the mechanical behaviour of laminated elastomeric bearings with a low shape factor (LSF) and the dynamic response of structures mounted on them.

A simplified theory for describing the mechanical behaviour of LSF bearings under compressive and shear loadings is illustrated. The proposed theory is an extension of the theory of Muhr for slender blocks and, similar to the theory of Stanton, accounts for the important effects of axial shortening and rubber layer bulging on the bearing behavior. The experimental tests conducted at Tun Abdul Razak Research Center (TARRC) rubber research centre on LSF rubber bearings with low damping and double shear testpieces are considered for validating the proposed theory and comparisons are also made with the theories of Koh and Kelly and Stanton. Moreover, the shaking table tests carried out at University of Naples Federico II on the bearings manufactured at TARRC are also considered to show the application of the bearing model for the purpose of evaluating the dynamic behavior and seismic response of structures mounted on LSF bearings.

With regards to the theories for describing the mechanical behavior of LSF bearings, the following conclusions can be drawn:

- Linear theories as the one developed by Gent and Koh and Kelly for simulating the behaviour of isolation bearings with high shape factors cannot be used for the LSF considered in this study.
- Stanton's model, which accounts for the increase of plane area of the bearing due to compression, provides more accurate results estimates of the compressive and horizontal behavior than the theories of Gent and Koh and Kelly.
- The formulation recently developed by Muhr, accounting for the change of height and area of the rubber layers under compression and also based on a finite strain formulation, provides the best fit to the experimental responses to compressive and horizontal loading.

The second part of the chapter illustrates the results of the shaking table tests performed at University of Naples Federico II on a structural prototype isolated on the LSF bearings developed at TARRC. These results are complemented by the outcomes of the simulations carried out with a simplified model derived considering few generalized coordinates and based on the bearing model illustrated in the first part of the study.

The conclusions presented below are drawn from the analysis of a simple structure subjected to the horizontal earthquake loading:

- The simplified model based on very few generalized coordinates yields very good estimates of the system modal properties.
- The eigenvalues analysis shows that rocking of the base affects significantly only the second and third mode of vibration of the system.
- The proposed model provides accurate estimates of the seismic response of the isolated structure. The error in the estimation of the maximum bearing deflections is less than 10%, whereas higher errors are associated with the estimates of the superstructure drifts.
- The reduction of horizontal and vertical stiffness of the bearings for increasing horizontal displacements has to be considered to accurately capture the period elongation and the changes in dynamic behaviour of the system under the Bingol record, which induces larger deflections in the bearings compared to the other records.

In the final part of the chapter , a parametric study is carried out to identify the effect of the bearing the shape factor on the dynamic behavior of the isolated system. Based on the results of the analyses, the following conclusion can be drawn:

- To completely suppress the rocking motion, higher shape factor bearings are needed. However, the bearings with low shape factor perform better in terms of deflection of the base isolation system and of the superstructure in conjunction with lower acceleration.

- The contribution of the base rotation to the top displacement of the prototype is low even for the case of the lowest shape factor (16% for the Friuli earthquake and 6% for the Bingol earthquake).

Based on these results, it can be concluded that the proposed LSF bearing model can be used for preliminary assessment and design purposes and that rocking may not be significant even for low values of the shape factor of the isolation bearings. Additional research is needed to confirm the applicability of these findings to more general structures. Furthermore, it is necessary to extend the model developed by Muhr for describing the mechanical behavior of LSF bearings with high damping rubber compounds and to evaluate its suitability under even larger bearing deflections.

7 Self-Sensing rubber for bridge bearing monitoring

7.1 Introduction

Elastomeric bearings (Lee and Lee, 1995; Aria and Akbari, 2013) are one of the most diffused typology of bearings, with many applications in civil engineering, not limited to supporting bridge decks (e.g. (Talbot and Hunt, 2003; Kelly and Konstantinidis, 2011; Tubaldi et al., 2016, 2017). Although elastomeric bearings are durable and require infrequent maintenance, ensuring that they perform as expected is of paramount importance to bridge safety assessment and management (Lee and Lee, 1995; Agarwal, Subramaniam and Pan, 2005; Aria and Akbari, 2013; Freire et al 2015). Current approaches for evaluating the condition of elastomeric bearings rely heavily on visual inspections, but these only provide intermittent, surface-level information. Researchers have therefore proposed alternative monitoring schemes: Soleimani et al. (2022) proposed three-dimensional digital image correlation coupled with finite element analysis to identify internal defects in bearings; whereas Topkaya and Yura (2002) and Akbari and Maalek (2009) proposed non-destructive test methods to determine the shear modulus of steel reinforced elastomeric bearings. Attempts have also been made to develop "smart" elastomeric bearings, i.e., bearings equipped with internal sensing systems, capable of providing continuous information on bearing reactions and displacements. Agrawal et al. (2005) proposed schemes that use combinations of LVDTs, pressure sensors, accelerometers, thermocouples, and fiber optic sensors.Other schemes include Fibre Bragg Grating displacement sensors for bearing condition monitoring (Li et al. 2012), piezoresistive sensors for bearing stress distribution measurement (Liu et al., 2016), and PVDF polymer film-based sensors for vertical reaction measurement (Kim et al., 2002).

Equipping bearings with additional sensors is a promising, but expensive approach. In this article, we explore the feasibility of exploiting the piezo-resistive properties of filled rubber to monitor the condition of elastomeric bearings and of structures supported by them, without any additional sensors. While natural rubber is an insulating polymer, the Carbon filled rubber commonly employed in bearing construction exhibits a good electrical conductivity (Busfield et al. 2004), provided that the volume fraction of the filler is higher than the percolation threshold (Stauffer and Bunde, 1987; Nan et al., 2010). When this is the case, changes in the strain of the rubber result in changes in its resistivity. The idea at the base of this study is that these changes in resistivity can be used to directly establish the strain state of the rubber and, thus turning the bearing into a multifunctional, self-sensing and low-cost weigh-in-motion monitoring system.

The piezoresistivity, which is defined as change of electrical resistance of filled rubber due to applied mechanical stress/strain, has already been investigated in previous studies (Busfield et al., 2004a, 2004b, 2005; Jha et al., 2010). Some of the first studies considered Carbon Black as a filler considering the impacts of the applied strain direction (Busfield et al., 2004a) solvent swelling and temperature changes on electro-mechanical response (Busfield et al. 2004b), and response to cyclic loading (Jha et al., 2010). Giannone et al. (2015) also investigated the possibility to use conductive rubber filled with Carbon Black to develop piezo-resistive bearings, and highlighted the creep behaviour of the electrical resistance. The results of all these studies showed that bearings containing Carbon Black fillers used in rubber for engineering applications do not exhibit a reversible strain-sensing response, i.e., there is not a clear monotonic relationship between change of strain and change of resistivity, with a different path followed upon loading and unloading. However, a reversible behaviour is essential in order to develop rubber-based strain-measuring devices. Subsequent studies have therefore investigated rubber compounds incorporating alternative Carbon Black fillers that provide more reversible behaviour. Jha et al. (2010) showed that rubber filled with Printex XE2, which is usually used for inks in printing industry, has quite good reversible properties under tensile loading, but they did not characterise the piezo-resistive behaviour of the compound under compressive or shear loading.

More research is needed to further explore the piezo-resistive properties of filled rubber under loading conditions that are more representative of those experienced by laminated bearings in bridges. This chapter aims are to fill this gap and illustrates the results of the experimental campaign carried out to characterise the piezo-resistive properties of specimens made with different rubber compounds under shear and compression loadings in addition to tensile loadings. Section 7.2 of the chapter outlines the various filled rubber compounds tested (made using either carbon-black or Printex XE2 as filler) and the experimental setup used to evaluate the piezo-resistive properties of the filled rubber specimens. Sections 7.3 to 7.6 of the chapter describe the results of the electro-mechanical tests carried out on the specimens made with the different compounds.

The work described here could be of great benefit to bridge asset managers, as bridge responses to external loadings such as those induced by the traffic or the external environment are influenced by bearing mechanical properties. Thus, measurements of stresses and strains in bridge bearings can provide useful information not only on the bearing condition, but also on the health of the bridges (Lee and Lee, 1995; Subramaniam, 1995; Nims et al., 1996; Nims and Parvin, 2000). It can also constitute an indirect means for estimating the traffic on bridge superstructures (weigh-in-motion) (Fred, 1979; OBrien, Enright and Getachew, 2010).

7.2 Specimens and experimental setup

This section describesthe investigated rubber compounds,t he various specimens made with them, and the electro-mechanical testing apparatus used to assess their piezo-resistive behaviour.

7.3.1 Compounds

Table 7.1 shows the formulation of the compounds used in the study, which differ mainly for the type of filler used. The first one (denoted to as Carbon Black 70) is a more traditional compound that is used to develop laminated rubber bearings, whereas the other two are more innovative compounds that use Printex XE2 for enhancing the piezo-resistive properties of rubber and achieve a more reversible behaviour (i.e. similar electrical response upon mechanical loading and unloading). The quantity of filler added is directly related to the conductivity of the final material. For a given type of filler, it is possible to identify the "percolation threshold", i.e., the volume fraction of filler which must be exceeded to allow the compound to become an electrical conductor (as shown in Figure 7.1). In the region of the percolation threshold, the sensitivity of the resistivity to mechanical deformation is highest, whereas it decreases for volume fractions of filler higher than the percolation threshold. The percolation threshold for Printex XE2 is much lower than for Carbon Black due to the hollowed out shell-like structure of Printex XE2, which results in a higher surface area and a more dramatic effect in terms of electrical conductivity properties (Jha et al., 2010; Sae-oui et al., 2014).

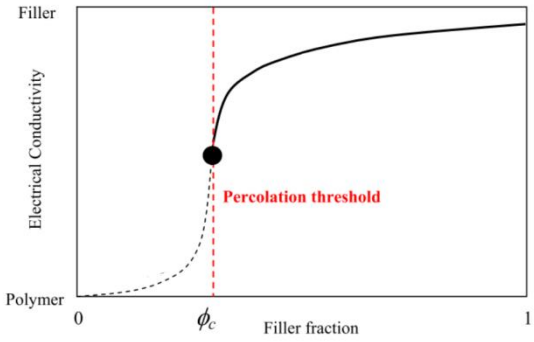

Figure 7.1 Electrical conductivity as a function of filler fraction

The amount of filler in the compound is measured by the parts per hundred of rubber (phr). Jha et al.'s (2010) already investigated the piezoresistive behaviour of Printex XE2 filled rubber tensile specimens, but with a phr of Printex of 10, which is very close to the percolation threshold. The phr values considered in the present study are slightly higher (12 and 15 phr) in order to achieve a more dissipative and stiff behaviour for the compound, as this is typical of laminated bearings used in construction practice.

Table 7.1 Formulation of the filled rubber compound in weight (parts per hundred rubber)

Material	**Abbreviation**		
Standard Malaysian Rubber	SMR		
High abrason furnace	HAF		
Hexyl phenyl phenylenediamine	HPPD		
Cyclohezyl benzothiazxy sulphenamide	CBS		
Tertiary butyl benzothiazole sulfenamide	TBBS		
Ingredients	**Parts per hundred of rubber (phr)**		
	Carbon Black 70 phr	**Printex** XE2 **15 phr**	**Printex** XE2 **12 phr**
NR (SMR CV60)	100	100	100
Carbon Black (N330 HAF)	70	-	-
Printex XE2	-	15	12
Stearic acid	2	2	2
Zinc oxide	10	7	7
Antioxidant (HPPD)	1	-	-
Cobalt naphthenate	3	-	-
Accelerator (CBS)	0.8	-	-
6PPD	-	1.5	1.5
Antilux 654	-	1.5	1.5
Manobond 740 C	-	0.75	0.75
TBBS	-	1.5	1.5
Sulphur	4	1.5	1.5

7.3.2 Testpieces

Three different types of testpiece were manufactured and tested under different loading conditions, namely tensile, compressive and shear, while measuring the changes in electrical resistance. In particular, the changes in resistivity were measured during tensile tests for natural rubber specimens filled with carbon black, and for natural rubber specimens filled with Printex XE2 at 15 phr, and during shear and compression tests for the compound with Printex XE2 at 12 phr. Table 7.2 summarises the compounds and testpieces considered, and the loading conditions they have been subjected to.

Table 7.2 Testpieces and loading conditions.

	Loading				
	Tensile			Shear	Compression
Testpieces	Full cycle	Triangular	Random		
Carbon Black tensile specimen	✓	✓			
Printex 15 phr tensile specimen	✓		✓		

Printex 12 phr Double Bonded Shear (DBS) specimen		✓	
Printex 12 phr compressive disc specimen l_0/d_0 = 0.1			✓
Printex 12 phr compressive disc specimen l_0/d_0 = 0.17			✓

The experimental set up for this test is shown in Figure 7.2. The test specimens considered for the tensile tests are rectangular strip of rubber cross-section, with 80mm × 25 mm sides and a thickness of 1.1 mm. The electical resistivity was measured with a four-point contact method.Figure 7.2

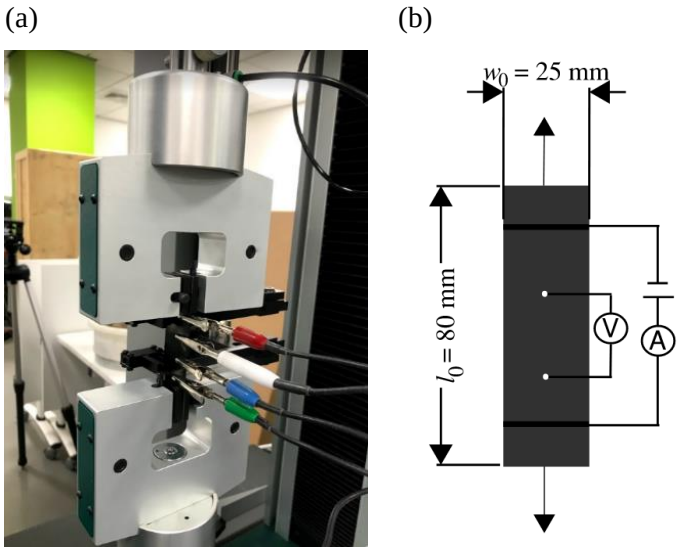

Figure 7.2 (a) Experimental set up for tensile testing and resistance measurement used in this work, (b) scheme of electrical resistance interrogation system (after Yamaguchi et al. 2003).

Double bonded shear (DBS) specimens were used for the double shear tests. They consist of two cylindrical rubber discs moulded between three brass pieces. The thickness of the disc is 6 mm and its diameter d_0 is 25 mm (Figure 7.3a). The compressive specimens consist of one cylindrical rubber disc moulded between two brass pieces and the diameter d_0 of 50 mm (Figure 7.3b). Two compressive specimens filled with Printex 12 phr have been manufactured with two different rubber layer thickness, 5mm and 8.47 mm, corresponding to height over diameter ratio l_0/d_0 =0.1 and l_0/d_0 =0.17, respectively.It is noteworthy that brass was used instead of steel for the end pieces as it could be bonded directly to the rubber without the need for bonding agent which would have affected the resistivity measurements.

(a) (b)

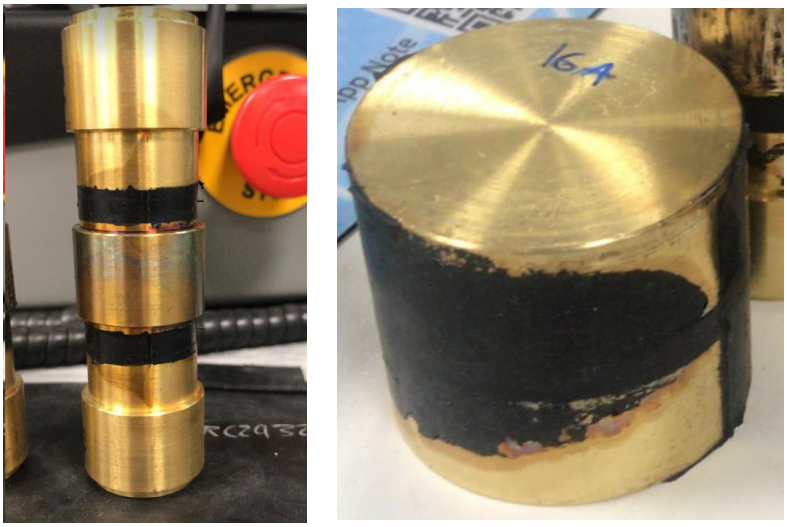

Figure 7.3 (a) DBS specimen, (b) Compressive specimen.

The electical resistivity of the DBS and compressive specimens was measured with a two-point contact method and the experimental set up is shown in Figure 7.4a and b. In this technique, the specimen resistance is measured by two electrodes; a direct current is applied and the drop in the potential between the electrodes is measured. Figure 7.5 illustrates a schematic representation of the experimental resistance measurement of the DBS and compressive rubber specimens.

(a) (b)

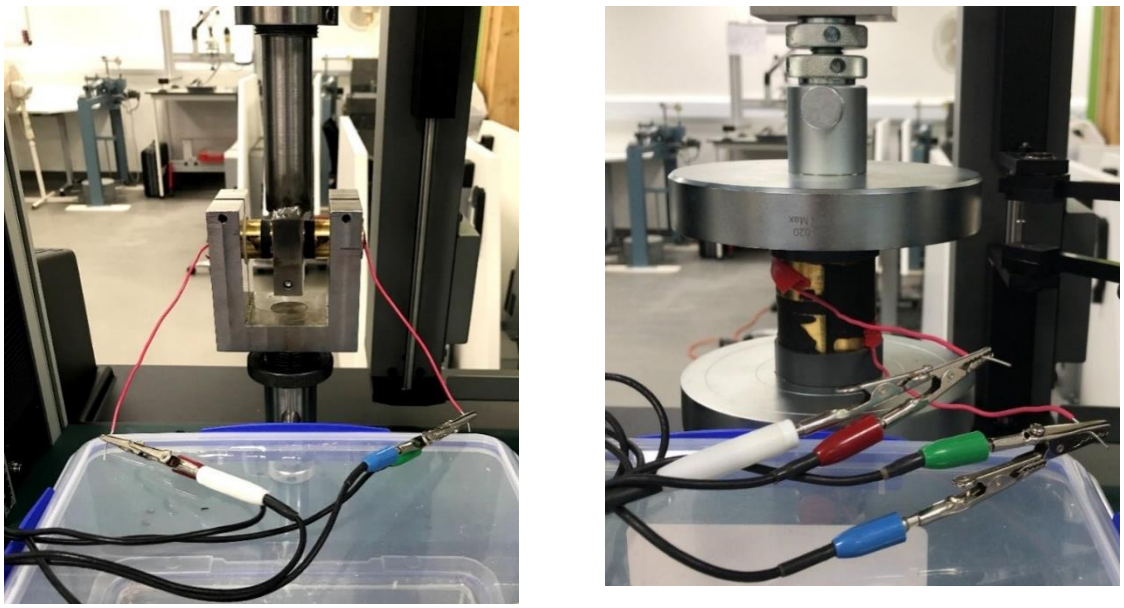

Figure 7.4 Resistance measurement, (a) DBS test equipment, (b) Compressive test equipment.

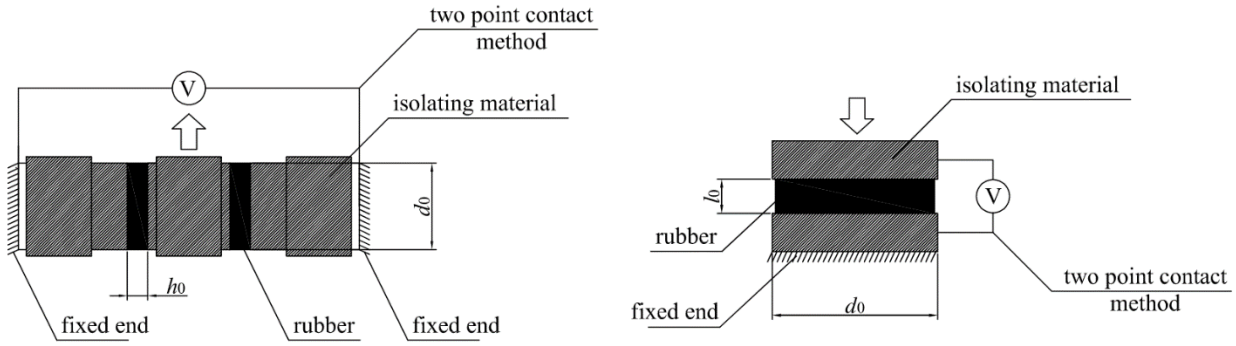

Figure 7.5. A schematic illustrating the two-point probe electrical resistance measurement technique for DBS and compressive specimens

Tensile, double shear and compression experiments were applied in up to five identical cycles to a "virgin" rubber specimen, never tested before. This way, it was possible to evaluate the effect of "stress-softening". This effect takes place within the untested rubber during the first deformation paths, which are generally characterized by a higher stiffness and dissipative capacity (Tubaldi et al., 2017). This effect usually reached equilibrium after a few cycles.

7.3.3 Stress-strain response and resistivity measurement

Mechanical tests were carried out by imposing displacements on the uniaxial testpieces. The mechanical response is described in terms of nominal stress vs. stretch ratio. The nominal stresses are obtained by dividing the axial force in tension (or compression) F_p by the initial cross-sectional area of the uniaxial (or compressive) specimen A_0:

$$\sigma = \frac{F_p}{A_0}. \tag{7.1}$$

The stretch ratio is defined as follows:

$$\lambda = \frac{l}{l_0}, \tag{7.2}$$

where l is the stretched length.

The shear tests were carried out on the DBS specimens by imposing different nominal shear strain amplitudes γ, defined as:

$$\gamma = \frac{\Delta_s}{h_0}, \tag{7.3}$$

where Δ_s is the shear displacement and h_0 is the thickness of a single disc.

The correspondent nominal shear stress is then obtained by dividing the transverse reaction force by two times the initial cross-sectional area of each rubber disk:

$$\tau = \frac{F_h}{2A_0}. \tag{7.4}$$

With regards to the resistivity measurement, direct current (dc) of amplitude I_{el} was imposed during mechanical testing to interrogate the system and the variation of the electrical resistance R_{el} was measured during the test via changes in measured voltage, V_{el}:

$$R_{el} = \frac{V_{el}}{I_{el}} \tag{7.5}$$

Another approach for characterizing the electrical properties of the rubber compounds would be by assessing the electrical impedance, which can be achieved by applying an alternating current (ac) potential and then measuring the phase and amplitude ac voltage response current and carries more information on the system. In particular, the impedance is a combination of the resistance and of the reactance, which measures the opposition of the system to changes in electric current (McAlorum et al., 2021).

The electrical resistivity of the rubber is a material property calculated as follows:

$$\rho = \frac{R_{el} A_r}{t_r}. \tag{7.6}$$

The value of A_r and t_r to be considered depends on the type of loading. For uniaxial tensile and compression loading, A_r is the actual (i.e. deformed) cross-sectional area:

$$A_r = A_0 / \lambda, \tag{7.7}$$

and t_r coincides with the stretched (or compressed) length l.

In the case of double shear tests (two identical resistances arranged in series), the area to be considered in Equation 7.6 is:

$$A_r = A_0 = \pi \frac{d_0^2}{4}. \tag{7.8}$$

where d_0 is the diameter of the rubber layer.

The length t_r corresponds to the total thickness of a rubber discs, i.e., $2h_0$.

7.3 Experimental tests on rubber filled with carbon black

7.3.1 Full cyclic uniaxial tensile tests

Two cyclic uniaxial tensile tests were initially conducted on 80 mm long specimens containing carbon black. In both cycles, the sample was extended in 4 mm steps up to the desired elongation of $\lambda = 2$. A dwell time of 180 s was considered between each further application of stretch. Figure 7.6a shows the stress-extension relation obtained during loading and unloading for both cycles. The stresses are nominal stresses, defined as the load divided by the cross sectional area A_0. The plot exhibits significant hysteresis, as expected for such a type of filled rubber. Moreover, stress-softening behaviour is evident, with the value of the peak stress at the second cycle of about 80% of the peak stress at the first cycle. Following the unloading path, the sample buckled for $\lambda \approx 1.15$, as shown in Figure 7.6b. This instability can be explained with the viscous behaviour of the material: when the sample is unloaded after being stretched, there is some residual set due to viscous deformations and since the sample cannot bear any compressive load, it buckles. It is noteworthy that the initial length of the specimen was recovered after a period of rest of few hours.

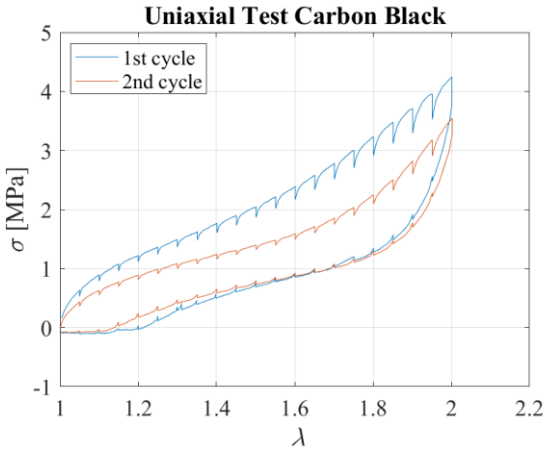

(a) (b)

Figure 7.6 (a) Tensile stress-extension curves for two cycles; (b) Sample immediately after the tensile test

Figure 7.7a and Figure 7.7b show the eletrical resistivity as a function of the extension ratio obtained for the first and second cycle, respectively.

These data show the relationship between the hysteretic mechanical and electrical behaviours of the material. During the 1st cycle, the resistivity starts to rise with the stretching of the untested rubber due to the breakdown of the Carbon Black network into smaller aggregates. This increase is then followed at higher extension by a reduction of the resistivity (Busfield et al. 2004a). During unloading, the electrical resistivity increases to values that are higher than those observed during the initial loading. In the second cycle, the stress-softening effect, related to the breakage of the bonds in the untested rubber, is negligible. After one cycle, the piezo-resistive behaviour of the rubber is more predictable, in the

sense that the resistivity decreases upon loading, and increases upon unloading. This behaviour can be explained by the fact that the Carbon Black aggregates, which are the conductive component of the compound, tend to align when the sample is stretched, thus decreasing the resistivity (Busfield et al. 2004a).

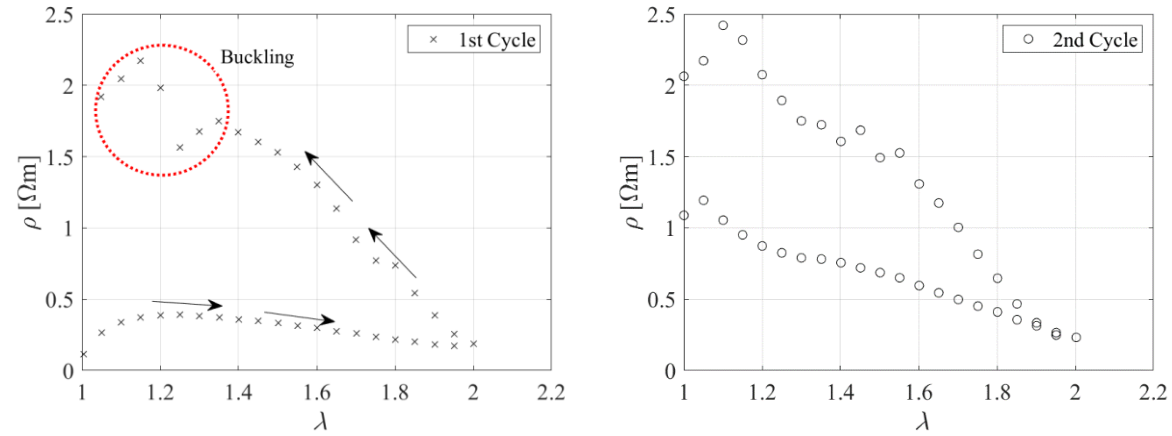

(a) (b)

Figure 7.7 Resistivity as a function of the extension ratio during the (a)1st cycle and (b)2nd cycle

7.3.2 Uniaxial tensile tests: triangular input

Another test was performed on the same carbon-black specimen. This was initially stretched up to λ = 1.2, then the stretch was kept constant for a dwell time of 6 minutes, and finally the stretch pattern shown in Figure 7.8a, consisting of positive and negative triangular inputs, was applied. Figure 7.8b shows the obtained stress-stretch curve. The relaxation behaviour of the rubber for λ = 1.2 is evident, as well as the significant hysteresis.

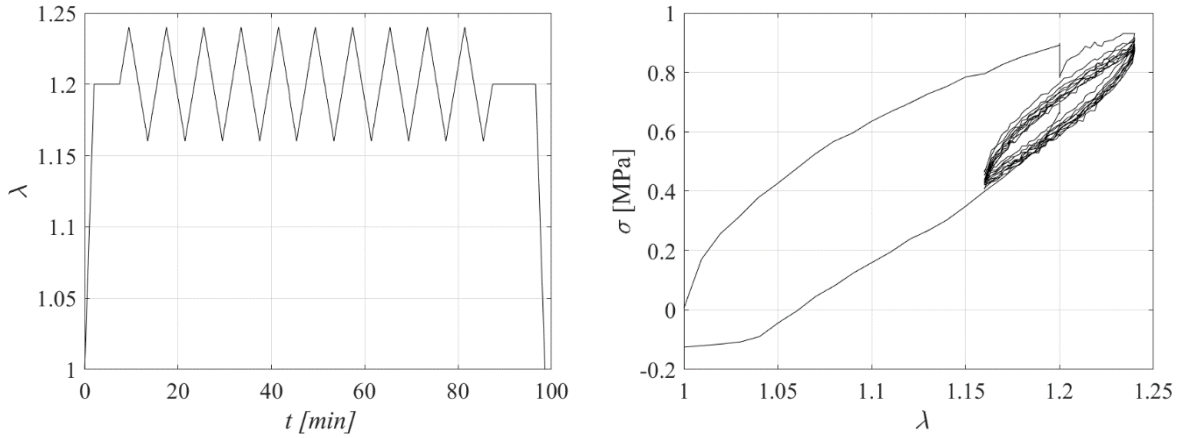

(a) (b)

Figure 7.8 (a) Displacement pattern, (b) Stress-extension curve

Figure 7.9a shows the time histories of the stretch normalised by λ = 1.2, and of the stress and electrical resistivity normalised by their correspondent value at λ =1.2. Following the initial stretch, there is an

overall trend of reduction of stresses with time, due to the relaxation behaviour of the rubber. Then, the stresses respectively increase and decrease for increasing and decreasing stretch levels. There is also a general trend of reduction of resistivity with time, which is more significant than for the stresses. However, it can be observed that the resistivity increases when both an increase of stretch and a decrease of stretch are applied starting from λ = 1.2. The different behaviour of the stresses and of the resistivity is highlighted in Figure 7.9b. It is also noteworthy that the sensitivity of the resistivity, defined as increase of resistivity divided by the change of stretch, is higher when the specimen is shortened, i.e., by passing from λ = 1.2 to λ = 1.16, than when it is stretched further, i.e., by passing from λ = 1.2 to λ = 1.24.

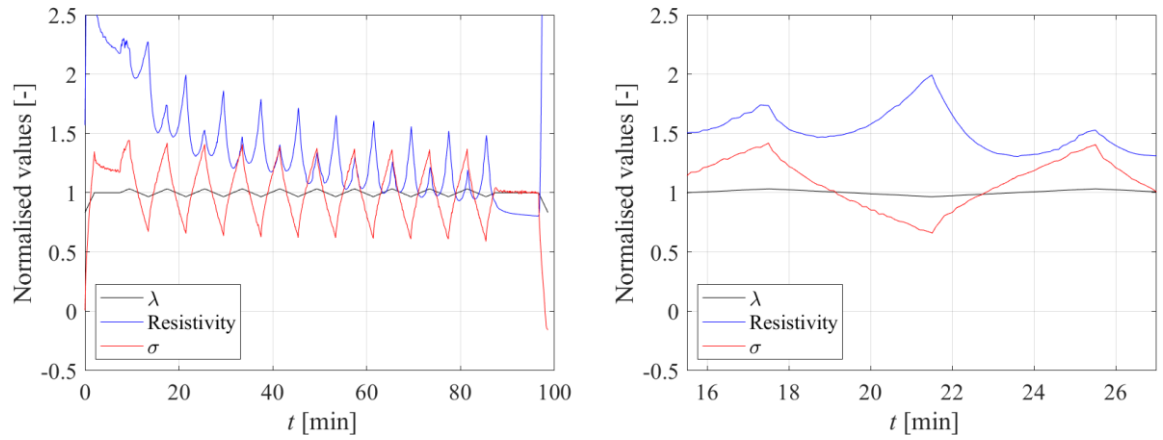

Figure 7.9 Resistivity and stress response due to the applied displacement pattern (a) full time history response (b) single cycle time history response

Another test was performed on a new specimen of the same carbon-black-filled material and geometry. This was stretched up to λ=1.2. The stretch was kept constant for a dwell time until a constant value of the resistance was obtained. Then, the sample was stretched again up to different values of λ (reported in Table 7.3) by imposing a series of positive triangular displacement inputs rather than positive and negative inputs as in Figure 7.8a.Table 7.3 shows the maximum stretch and the strain rate $\dot{\lambda} = \frac{\Delta\lambda}{\Delta t}$ applied in each test.

Table 7.3 Axial elongation and velocity values performed during the tests

	Test 1	**Test 2**	**Test 3**	**Test 4**
λ **[-]**	1.3	1.4	1.6	2
$\dot{\lambda}$ **[s^{-1}]**	0.05	0.1	0.05	0.05

Figure 7.10 shows the stress-stretch curves corresponding to the various tests. For stretch levels higher than 1.6, the strain-crystallisation effect can be observed, resulting in a significant increase of stresses for increasing λ.

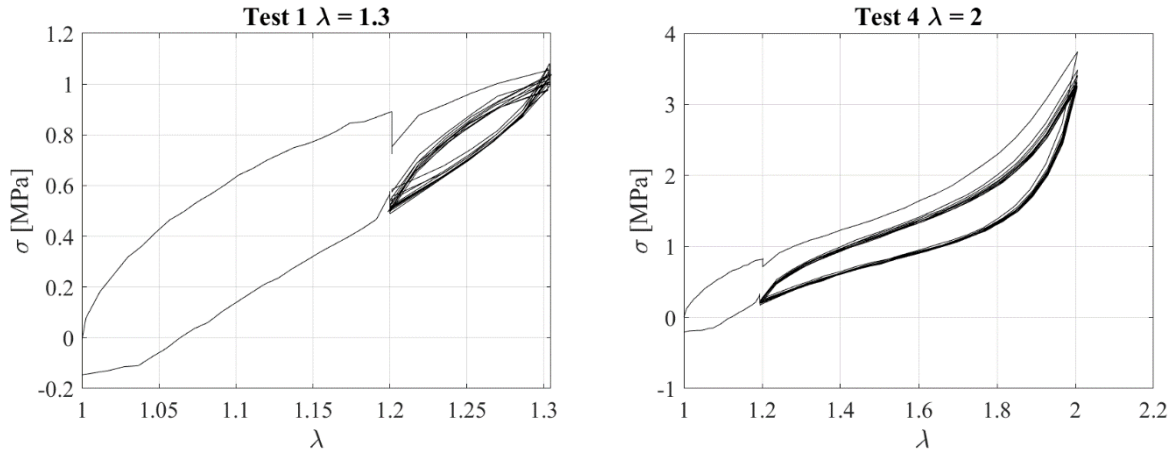

(a) (b)

Figure 7.10 Stress-extension curve for test1 (a) and test 4 (b).

Figure 7.11 illustrates the resistivity against the extension ratio obtained for Test 1 and Test 4. These tests show again that there is not a clear relationship between elongation and change of resistivity. More in general, the results of this first experimental campaign confirmed that typical rubber compounds incorporating carbon-black as filler are characterized by a complex behaviour and phenomena such as stress softening, relaxation, and hysteresis. All these phenomena are somehow also reflected in the piezo-resistive behaviour of the rubber, which is highly nonlinear. Thus, it is not possible to establish a simple univocal relationship between change of stress/strain and change of resistivity and for this reason the first investigated compound is not suitable for the development of smart elastomeric bearings.

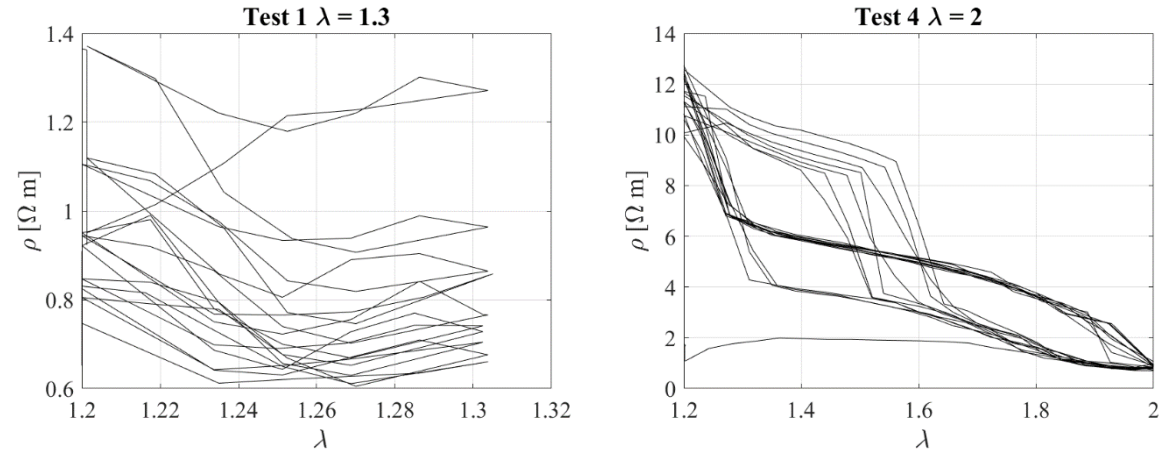

(a) (b)

Figure 7.11 Resistivity versus stretch ratio test 1 (a) and test 4 (b).

7.4 Experimental tests on rubber filled with Printex 15 Phr

7.4.1 Uniaxial tensile tests

Five cyclic uniaxial tensile tests were conducted considering the compound filled with Printex (15 phr). In all the cycles, the specimen was extended by 8 mm steps up to the desired elongation $\lambda = 2$. A dwell time of 60s was considered between each further application of stretch. Figure 7.12 shows the stress-stretch curve obtained during loading and unloading for both cycles. The compound is softer than the one with carbon-black as filler. Nevertheless, it exhibits some hysteretic and stress-softening behaviour, with the peak stress at the third cycle of about 90% of the peak stress at the first cycle.

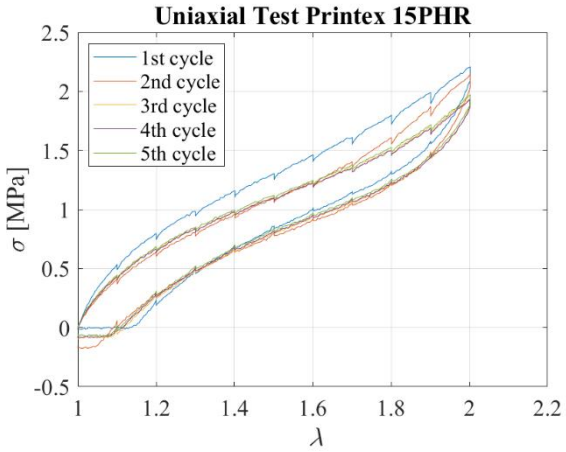

Figure 7.12 Tensile stress-extension curves for 5 cycles: Nominal stress vs extension

Figure 7.13a shows the eletrical resistivity as a function of the extension ratio during the loading and unloading part of the 5th cycle. Resistivity peak data at each extension ratio are also shown in Figure 7.13b for the loading and unloading paths of the 5 subsequent cycles. It can be observed that, apart from the first cycle, all subsequent cycles are almost indistinguishable.

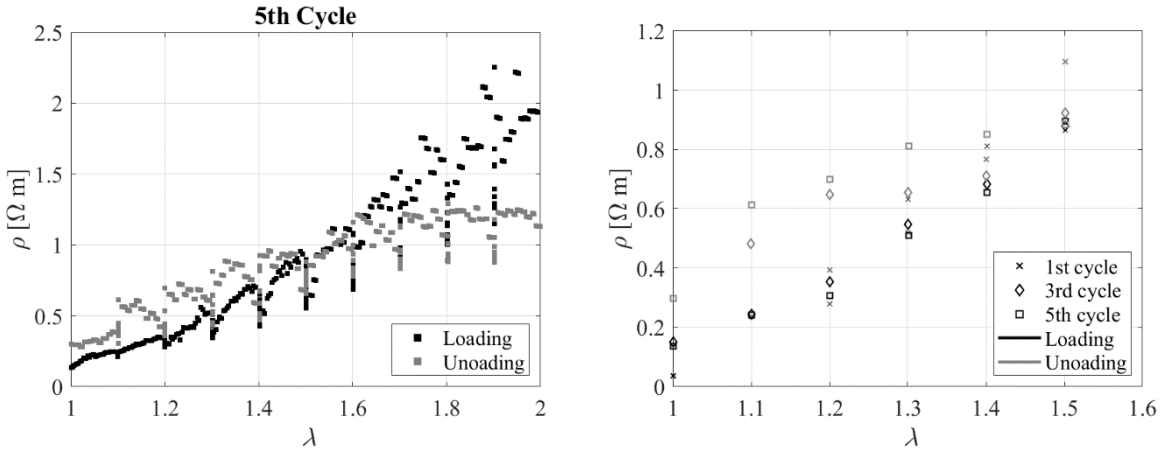

(a) (b)

Figure 7.13(a) Resistivity vs. extension ratio during 5th cycle and (b) Resistivity versus extension ratio during the1st, 3rd and 5th loading cycles.

The electrical resistivity increases with the extension ratio upon loading and reverts to the same initial value along a similar path upon unloading. This confirms the reversibility in the electrical resistivity behaviour of Printex filled compound, as also observed by Jha et al's (2010).

Figure 7.14 shows the variation of the resistivity normalized by the resistivity at zero stretch ρ_0= 0.14 Ωm, i.e. $\Delta\rho/\rho_0$, versus the strain λ. The plotted data refer to the tests of Figure 7.13 a. An interpolating function is fitted to the observed data with the aim of developing a model that relates the changes of resistivity to the changes of stretch. The function has a linear trend of variation:

$$\frac{\Delta\rho}{\rho_0} = 9.27\lambda - 9.27 \tag{7.9}$$

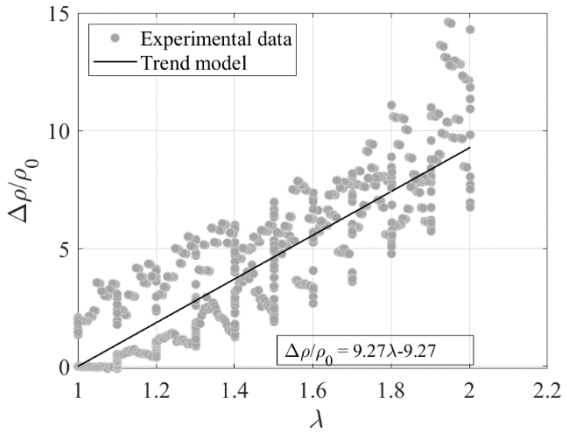

Figure 7.14 Variation of normalised resistivity with stretch ratio.

In order to characterize the sensitivity of the Printex-filled specimen, the gauge factor (GF) is evaluated, which is defined as

$$GF = \frac{\Delta\rho_0 / \rho_0}{\varepsilon} \tag{7.10}$$

where ε = 1 - λ represents the applied strain. The value of the GF according to Figure 7.14 is equal to 9.3.

Furthermore, the sensing precision is evaluated by evaluating the standard deviation of the residuals in terms of $\Delta\rho/\rho_0$,and then dividing it by the GF, as shown in Equation 7.11.

$$\sigma_\varepsilon = \frac{\sigma_{\Delta\rho/\rho_0}}{GF} \tag{7.11}$$

The obtained value of σ_ε is 0.16 and measures the uncertainty in the estimate of ε given the resistivity measurement.

7.4.2 Uniaxial tensile test: random input

A second test was performed on the same Printex-filled specimen by imposing the input shown in Figure 7.15a. This history was designed to be representative of the effect of the traffic passing over a bridge superimposed onto permanent loading. Various stretch ratios are applied to simulate vehicles of different mass. Figure 7.15b shows the stress and electrical resistance behaviour due to the applied displacement pattern. It can be observed that the resistivity change follows the same pattern as the stress and stretch change.

The purpose of this test is to understand whether by measuring the changes in electrical resistivity of the specimen it is possible to reconstruct the strain history it was subjected to, or at least to infer the maximum strain amplitudes it experienced. This is an essential requisite for using the rubber compound to develop smart rubber bearings. Figure 7.15a also compares the imposed stretch history and the corresponding history inferred by measuring the electrical resistivity changes of the specimen and using Equation 7.9 to relate these changes of resistivity to changes of stretch. The predicted changes of deformation are in good agreement with the experimental values, thus confirming the good potential of the compound for the development of self-sensing bearings.

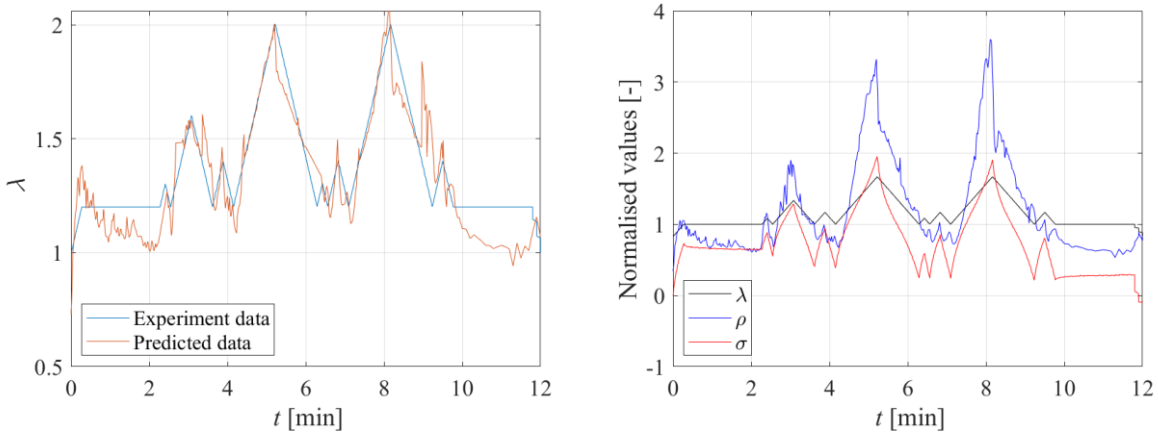

(a) (b)

Figure 7.15(a) Extension ratio versus time: comparison between experiment and predicted data;(b) Time history of normalised displacement, stress, and electrical resistance under the displacement input of Figure 7.15b.

7.5 Experimental tests on rubber filled with Printex 12 Phr

This section describes the tests carried out on double shear and compressive specimens made with Printex with 12 phr. This compound incorporates less fillers than the previous one in order to improve the piezo-resistive behaviour and the sensitivity of the resistivity to the strain. Nevertheless, the fraction of filler is higher than the one considered in Jia et al. (2010), which was found to be higher than the one corresponding to the percolation threshold.

7.5.1 Double bonded shear (DBS) tests

The DBS tests consisted in 6 cycles carried out for increasing levels of the maximum nominal shear strain amplitude γ_{max}, namely 0.05, 0.1, 0.2, 0.5, 0.7, and 1. A dwell time of 180 s was considered between each further application of shear strain to allow the rubber to relax.

After the test with γ_{max}=1, the tests were performed again to evaluate the softening effect (often referred to as scragging as defined in Kingston and Muhr, 2011) of exposing the sample to large shear strain amplitudes on the mechanical behaviour and resistive behaviour at strains below the scragging strain of γ_{max}=1 . Figure 7.16 shows the nominal shear stress-strain relation obtained during loading and unloading for the 6 cycles at different amplitudes, before and after the test at γ_{max}=1. It can be observed that the stress-softening is quite significant at low strain amplitudes (Figure 7.16a), and negligible at higher amplitudes (Figure 7.16b).

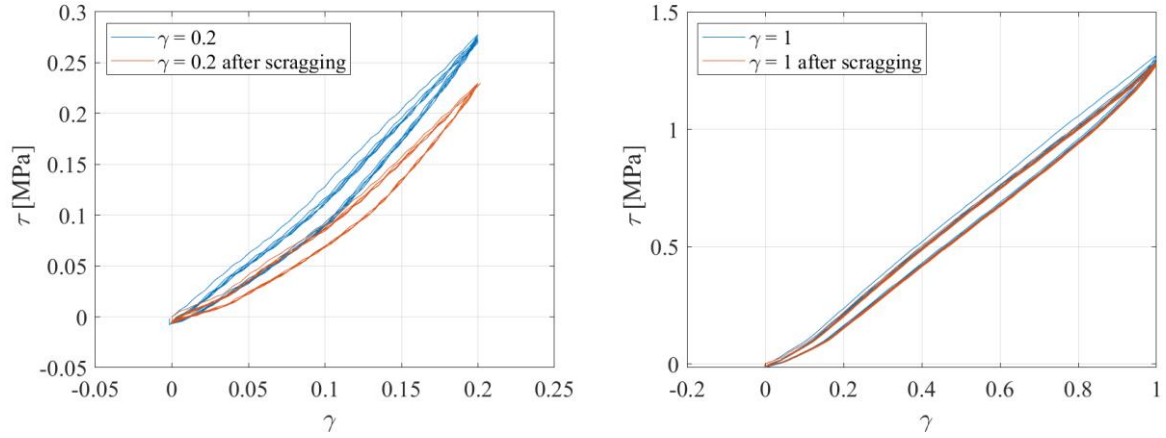

(a) (b)

Figure 7.16 Stress-strain curves for (a) 20% and (b) 100% of nominal shear strain

Figure 7.17 shows the eletrical resistivity as a function of the shear strain during the loading and unloading part of the 6 cycles at γ_{max}=0.2, and γ_{max}=1 applied after pre-scragging the rubber.

In general, the resistivity increases with the shear strain and exhibits an almost reversible behaviour, in agreement with the tests carried out by Jha et al. (2010) on tensile specimens and with the tensile tests carried out on the rubber compound with 15phr of Printex. Only for low strain amplitudes the changes of resistivity are low, which indicates a low sensitivity of the compound (low gauge factor). Nevertheless, such low strain levels are not of interest in bearing applications, since usual values of the maximum design shear strain are of the order of 50% (see e.g. American Association of State Highway Transportation Officials, 2017) while they are usually higher for seismic isolation bearings (Tubaldi et al., 2016).

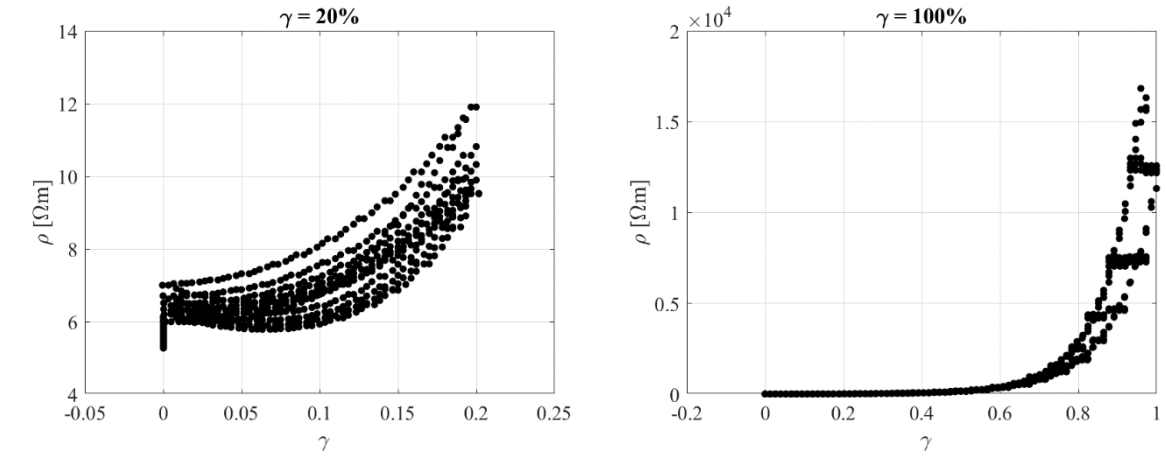

(a) (b)

Figure 7.17 Resistivity as vs. shear strain for different tests (a) γ_{max}=0.2and (b) γ_{max}=1.

Figure 7.18 shows the variation of the resistance normalized by the resistivity at zero strain ρ_0= 7.2 Ωm, i.e. $\Delta\rho/\rho_0$, versus the shear strain γ. The plotted data refer to the test of Figure 7.17b (γ_{max}=1). The data are interpolated using a linear function valid for γ in the range between 0 and 0.7, and a quadratic function for γ in the range between 0.7 and 1, with the aim of developing a model for relating the changes of resistivity to the changes of shear strain.

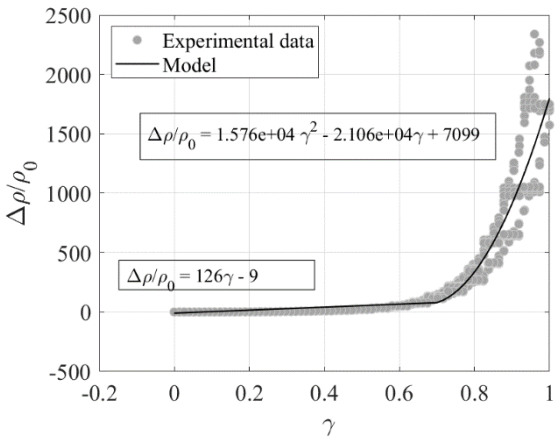

Figure 7.18 Variation of resistivity versus shear strain.

Another test was performed on the same DBS specimen by imposing the input of Figure 7.19a. Figure 7.19b shows the stress and electrical resistance behaviour due to the applied displacement pattern.

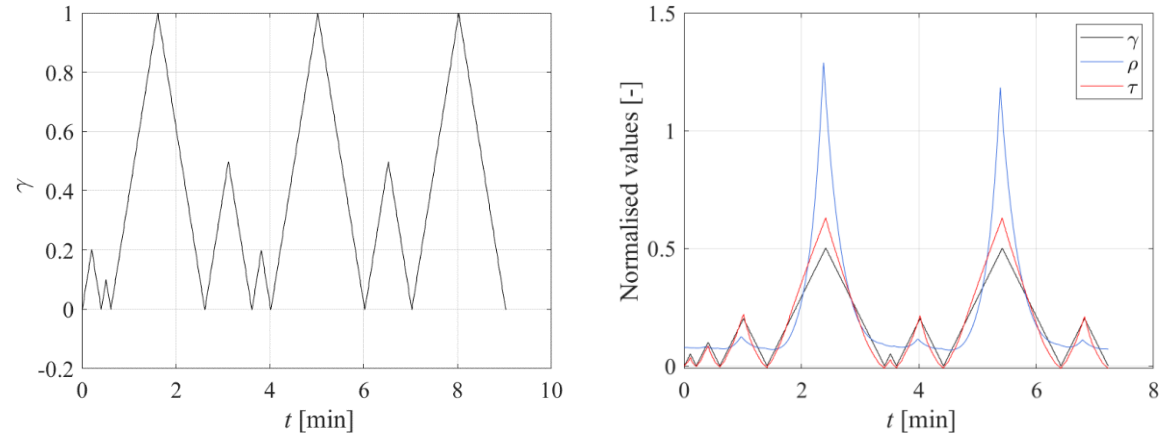

(a) (b)

Figure 7.19 (a) History of input (b) History of normalised input, stress and resistivity

The regression model developed based on the results of the previous tests (shown in Figure 7.18) is used to infer the changes of strain based on the readings of the resistivity. Figure 7.20a shows the measured changes of resistivity vs. the imposed changes of strain. In the same figure, the curve corresponding to the model of Figure 7.18 is shown. Figure 7.20b shows the time history of the experimental and predicted shear strains, which are in reasonable accord with each other. It is noteworthy that the proposed model cannot predict with good accuracy cycles with low deformation amplitudes due to the low sensitivity of $\Delta\rho/\rho_0$ to shear strains for small γ values.

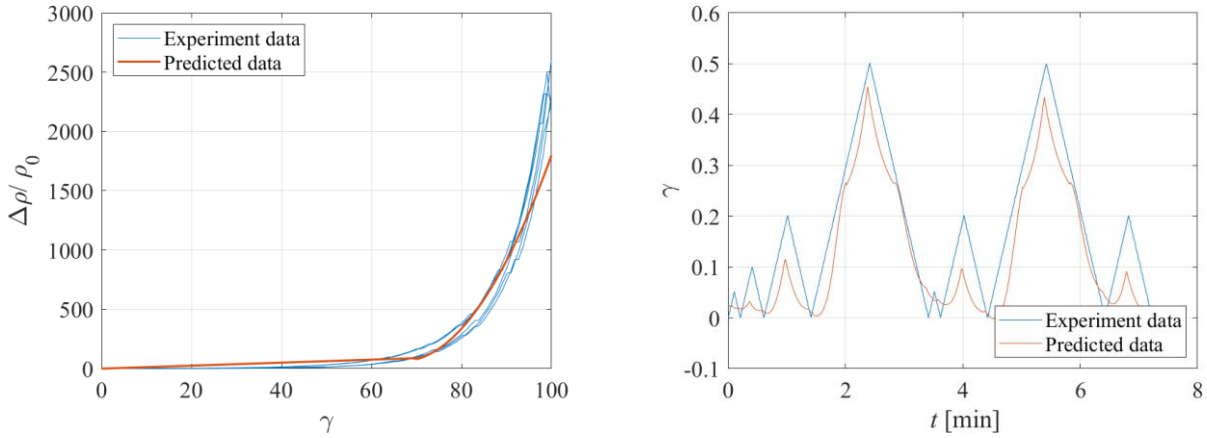

(a) (b)

Figure 7.20 Comparison between experiment and predicted data: (a) Variation of resistance versus strain, (b) Strain versus time

7.5.2 Compression tests on rubber filled with Printex 12phr (specimen with l0/d0=0.1)

Cyclic compressive tests were conducted on the cylindrical specimen with a relatively thick rubber layer (l_0= 5 mm), corresponding to an aspect ratio l_0/d_0 = 5/50=0.1. The sample was compressed by

0.5 mm steps ($\Delta\lambda$=0.166) up to the desired compression ratio λ = 0.6. A dwell time of 60s was considered between each further application of compression. Three identical cycles were imposed. Figure 7.21 shows the stress-compression ratio curve obtained for all the cycles. Some minor hysteresis and stress-softening behaviour is observed, with the peak stress at the second cycle equal to about 96% of the peak stress at the first cycle.

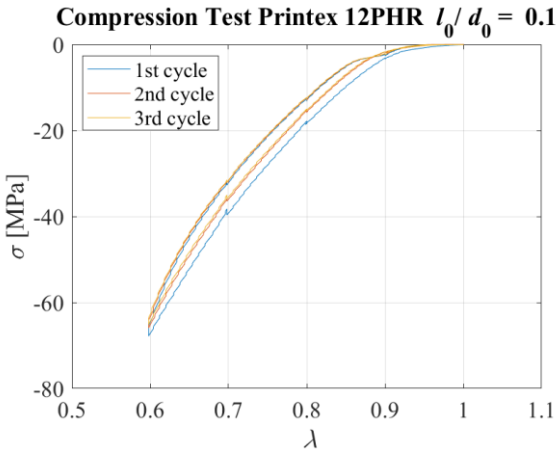

Figure 7.21 Compressive stress-strain curves for three cycles

Figure 7.22 shows the eletrical resistivity as a function of the compression ratio during g the first 3 cycles. The relation between the two quantities is highly nonlinear, with small changes of resistivity for values of λ higher than 0.8. However, a clear trend can be identified and the behaviour is overall quite reversible.

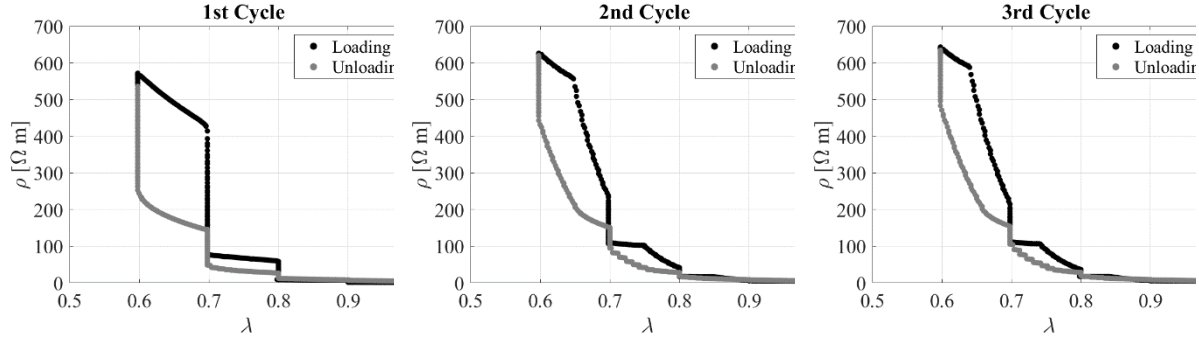

Figure 7.22 Resistivity versus compression ratio during three cycles

Another test was performed on the same sample. It was compressed up to λ = 0.97, then the compression was kept constant for a dwell time reported on Table 7.4 and then the sample was subjected to compression cycles with maximum amplitude of λ_{max} = 0.94 at different loading rates. The displacement pattern corresponding to Test1 is shown in Figure 7.23a as an example. Only the positive part of the triangular wave was applied and the strain rate considered to reach λ=0.97 and during the triangular waves (i.e., from λ=0.97 to λ=0.94) are also reported in Table 7.4. It is noteworthy that the values of

λ=0.97 to λ=0.94 can be assumed to be representative of the compression levels a bridge bearing would be subjected to under the effect of the permanent load, and the permanent load plus the loading of a heavy vehicle passing over the bridge.

Table 7.4 Velocity values and dwell time applied during the tests

	Test 1	**Test 2**	**Test 3**	**Test 4**
$\dot{\lambda}_{1stramp}$**[s^{-1}]**	0.0017	0.0017	0.0075	0.0075
$\dot{\lambda}_{2ndramp}$**[s^{-1}]**	0.0017	0.0017	0.0017	0.01
Dwell time [s]	30	6	6	3

Figure 7.23b shows the nominal stress-compression curve, which is highly nonlinear, although it is characterised by a low hysteresis. The response is slightly affected by the rate of deformation, with higher rates corresponding to a stiffer behaviour. Figure 7.24 shows the resistivity against the compression ratio for Test 3 and Test 4 as an example.

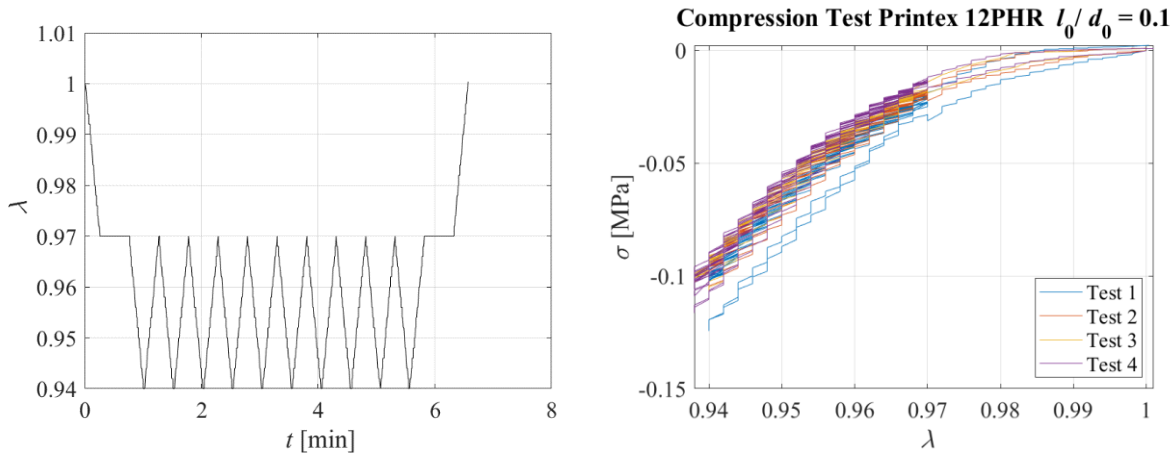

(a) (b)

Figure 7.23(a) Displacement pattern (b) Stress-compression ratio relations for each triangular test

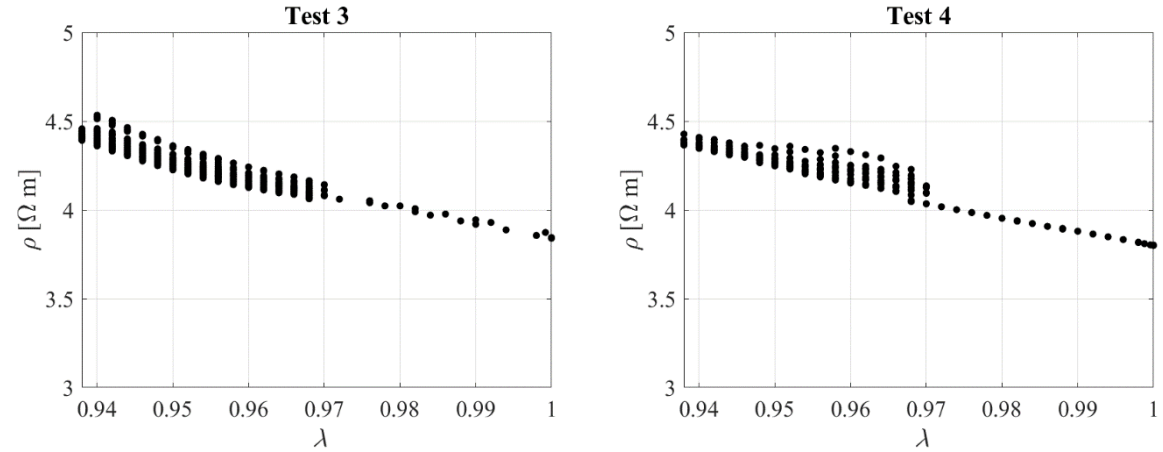

(a) (b)

Figure 7.24 Resistivity against compression ratio: (a) Test 3 and (b) Test 4

An interpolating function is fitted to the observed compression Test 3 data with the aim of establishing a model relating $\Delta\rho/\rho_0$, being ρ_0 = 3.8 Ωm, to the compressive strain $\varepsilon = \lambda - 1$. For this purpose, two functions are used, one linear function with GF = 2.1 valid up to $\varepsilon = -0.04$, and one quadratic function valid beyond this value. Similar results are obtained with Test 4 data. The expressions of the functions are shown in Figure 7.25. The standard deviation of these data point from the linear model is $\sigma_\varepsilon = 0.005$.

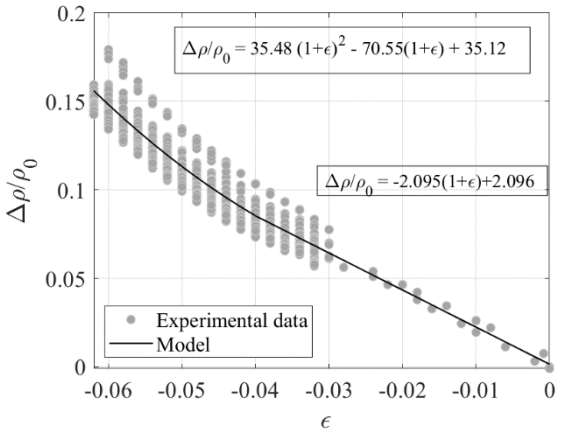

Figure 7.25 Variation of resistivity ratio versus compression strain

A third test has been performed on the same specimen by imposing the random input shown in Figure 7.26a. The obtained histories of stress and electrical resistance are shown in Figure 7.26b. It can be observed that the resistivity increases when the compression increases, and decreases when the compression decreases, showing again the reversible behaviour due to the Printex rubber compound. The relationship obtained from the previous tests to relate the changes of resistivity to the changes of compression (Figure 7.25) can be used to check whether it is possible to infer the changes of strain in the specimen by measuring only the changes of electrical resistivity.

Figure 7.26c shows the measured changes of resistivity vs. the imposed changes of strain. In the same figure, also the model of Figure 7.25 is plotted. Figure 7.26d shows the time history of the experimental and predicted compressive strains. It can be observed that the model predictions are in reasonable accord with the measured values of the resistivity, thus confirming that the Printex-based rubber compound is suitable for developing smart rubber bearings.

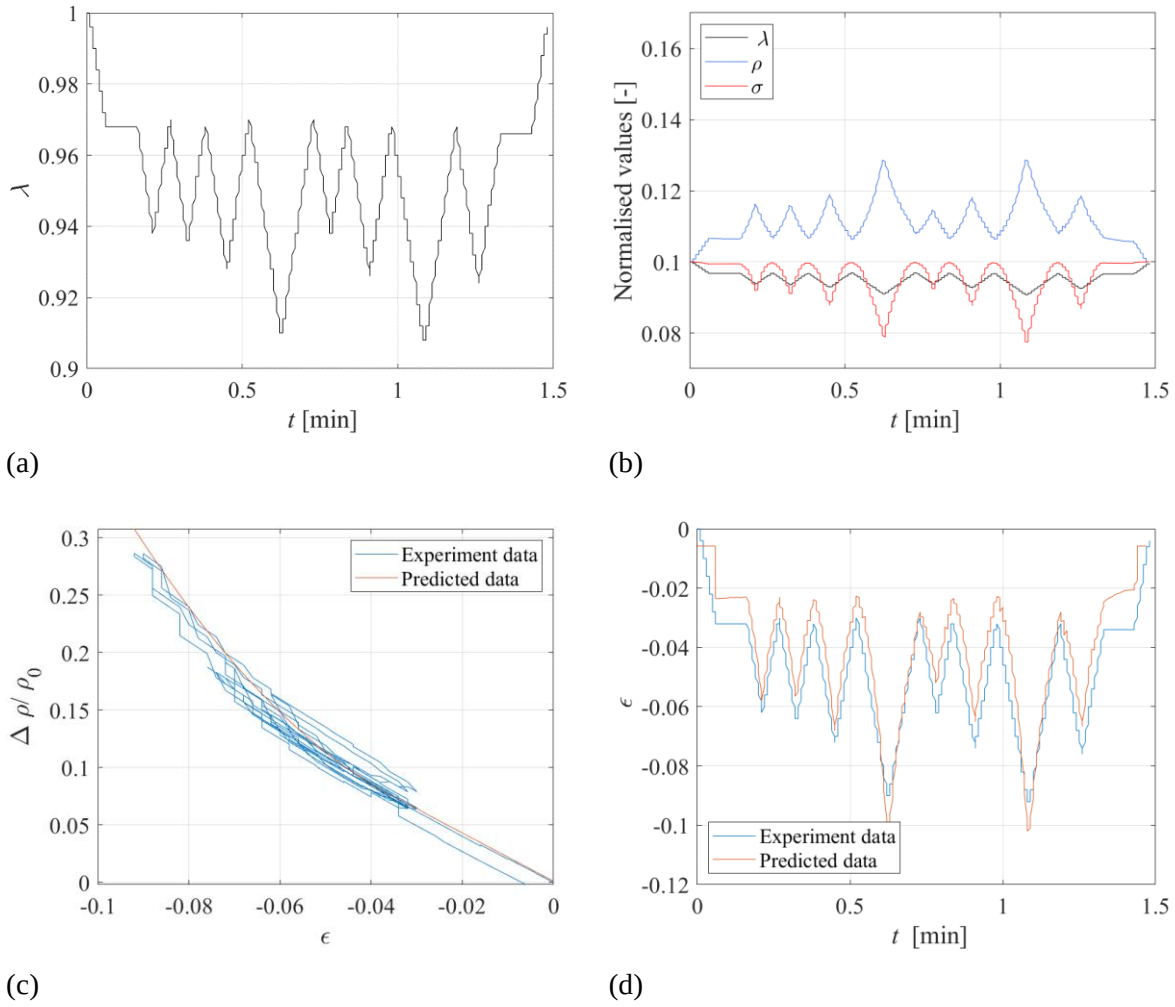

Figure 7.26 (a) Input random, (b) Time history of normalised displacement, stress, and electrical resistance under the displacement input of Figure 7.26a. Comparison between experiment and predicted data (c) Variation of resistivity versus strain and (d)Strain versus time

7.5.3 Compression tests on rubber filled with Printex 12phr (specimen with l0/d0= 0.17)

In order to investigate the influence of the aspect ratio of the rubber layer on the piezo-resistive response of the system, a cylindrical specimen with a more slender rubber layer (l_0= 8.47 mm), compared to the one considered previously (l_0= 5 mm) was manufactured and tested. A measure often employed to characterise the geometry of rubber layers is the shape factor *S*, which is the ratio of the loaded surface area of the rubber layer to the total area free to bulge (Kelly and Konstantinidis, 2011). The *S* values for the two specimens are respectively 2.5 (l_0/d_0= 0.1) and 1.48 (l_0/d_0= 0.17). It is also noteworthy that in the case of bonded discs of rubber, the compressive load induces significant shear strains. In particular, the shear strains are zero in the centre and increase radially with the maximum value being at the edges. Both the maximum and the averaged shear stresses increase with the *S* for a given compression level. Thus, higher shear stresses are expected in the specimen with higher shape factor.

The specimen with S=1.48 was compressed by 0.5 mm steps ($\Delta\lambda$=0.058) up to the desired compression ratio of λ = 0.64. A dwell time of 60 s was considered between each further application of compression. Three identical cycles were imposed. Figure 7.27 shows the plot of the nominal compressive stress vs. the compression ratio obtained for all cycles. In this case, the stress softening is negligible.

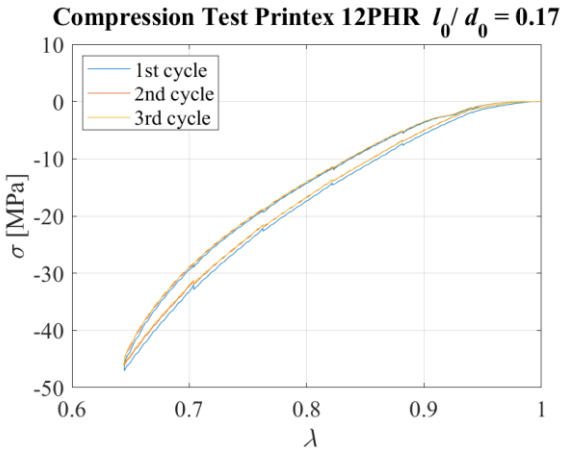

Figure 7.27 Compressive stress-strain curves for three cycles

Figure 7.28 shows the electrical resistivity as a function of the compression ratio during each of the 3 cycles. Also in this case, it can be observed that there is a highly nonlinear behaviour especially for values of the compression ratio lower than λ = 0.8, whereas small changes of resistivity can be observed for higher values.

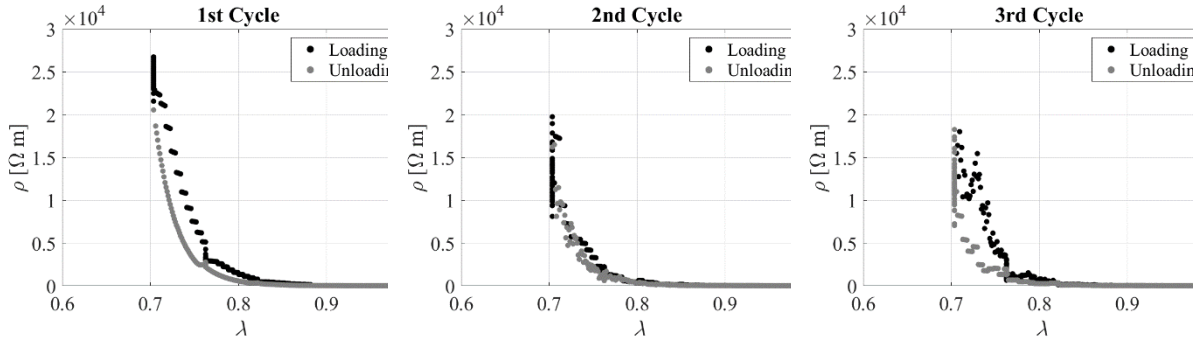

Figure 7.28 Resistivity versus compression ratio during three cycles

Another test was performed on the same sample. It was compressed up to λ = 0.97, then the compression was kept constant for a dwell time reported on Table 7.5 and then the sample was subjected to cycles of deformation with maximum amplitude of λ = 0.94 for different deformation rates as shown in Table 7.5. The displacement pattern applied in Test 1 is shown in Figure 7.29a. Figure 7.29b shows the stress-compression ratio curves whereas Figure 7.30 shows the resistivity vs. the compression ratio obtained for Test 3 and 4.

Table 7.5 Velocity values and dwell time applied during the tests

	Test 1	**Test 2**	**Test 3**	**Test 4**
$\dot{\lambda}_{1stramp}$**[s^{-1}]**	0.0017	0.0017	0.0075	0.0075
$\dot{\lambda}_{2ndramp}$**[s^{-1}]**	0.0017	0.0017	0.0017	0.01
Dwell time [s]	30	6	6	3

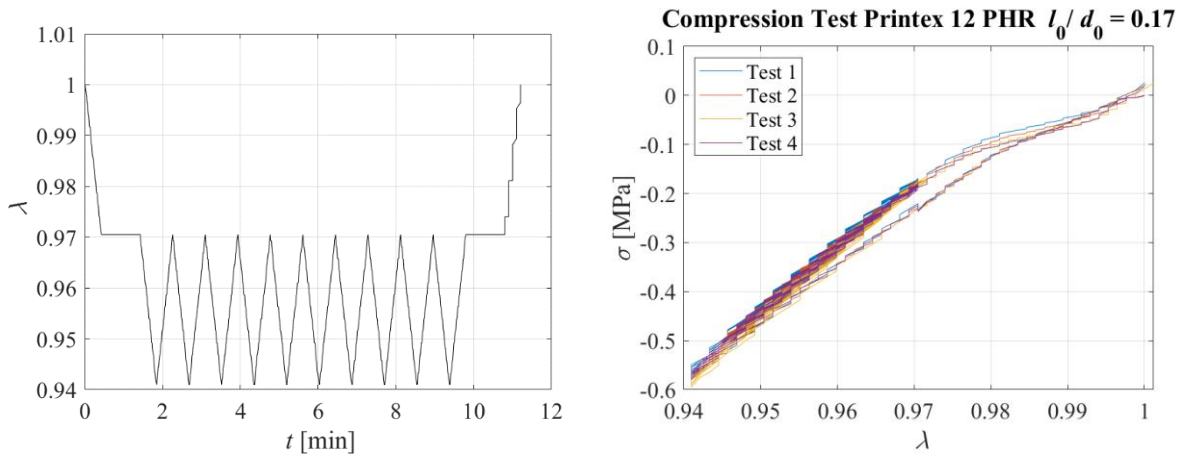

Figure 7.29 (a) Displacement pattern (b) Stress-compression ratio relations for each triangular test

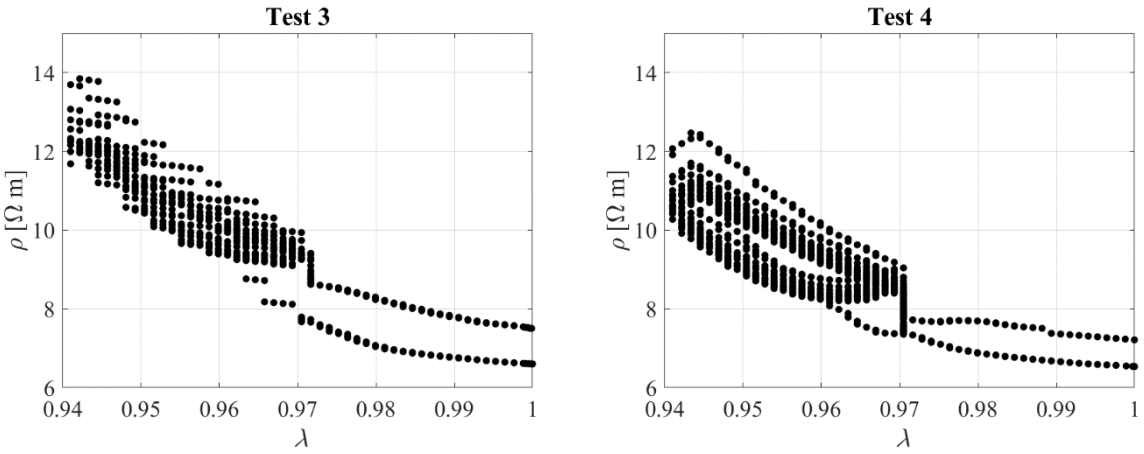

(a) (b)

Figure 7.30 Resistivity against compression ratio: (a) Test 3 and (b) Test 4

Figure 7.31 shows the normalised variation of the resistivity over the initial value at zero strain ρ_0= 6.6 Ωm versus the compression strain $\varepsilon = \lambda - 1$. The observed data are interpolated using a quadratic function. Figure 7.31 shows the data and the model fitted to the data. In order to provide a measure of

the sensing sensitivity and precision, a linear model has also been fitted to the data in the range between λ= 1 and λ= 0.97, resulting in GF=11.53 and σ_ε=0.0085.

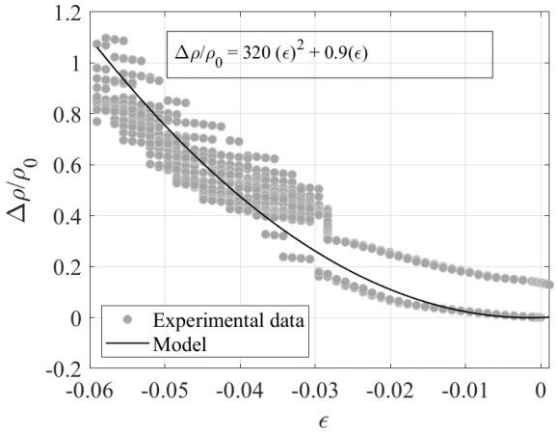

Figure 7.31 Variation of normalised resistivity vs compressive strain.

A third test was performed on the same specimen by imposing the input of Figure 7.32a. Figure 7.32b shows the stress and electrical resistance behaviour due to the applied displacement pattern. It can be observed that the resistivity increases when the compression increases, and decreases when the compression decreases, showing again the reversible behaviour of the compound. Figure 7.32b shows that the strain values predicted using the resistivity measurements and the model of Figure 7.31 are in good agreement with the measured ones, thus confirming that this compound has a good potential to be used to develop smart rubber bearings.

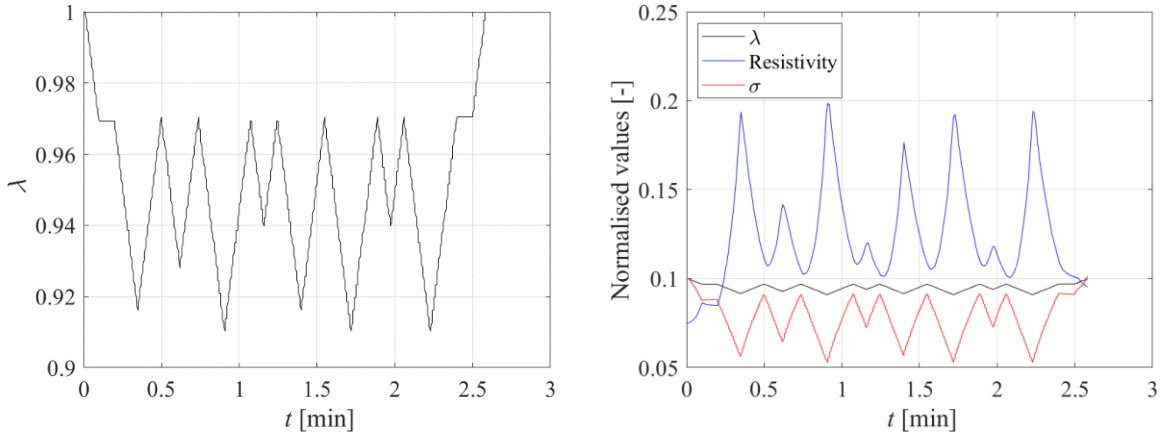

(a) (b)

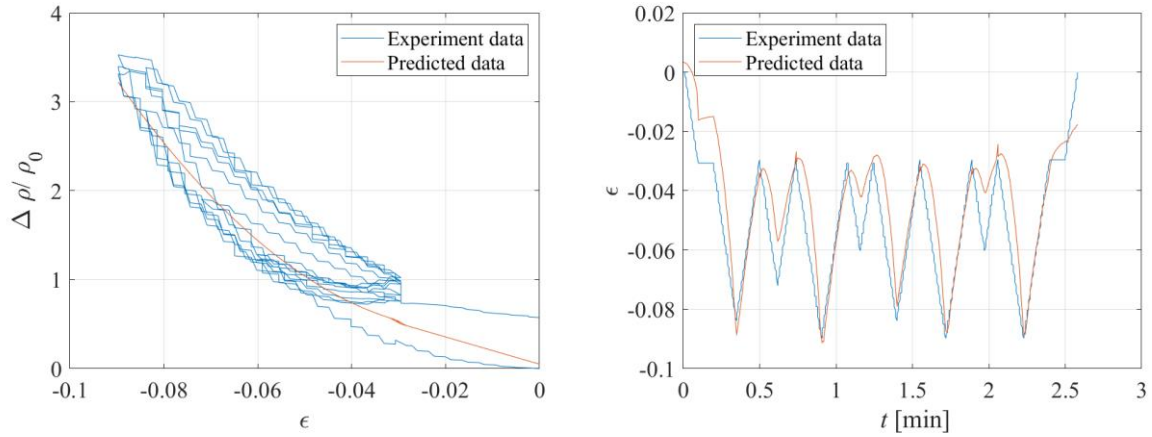

(c) (d)

Figure 7.32 (a) Input random, (b) Time history of normalised displacement, stress, and electrical resistance under the displacement input of Figure 7.32a. Comparison between experiment and predicted data (c) Variation of resistivity versus strain and (d)Strain versus time

7.6 Summary and discussion of results

Figure 7.33 compares the results of the experimental uniaxial tests performed on the specimens made with carbon black-and Printex 15 phr-filled compounds. The resistivity variation with the change of the extension ratio during the loading and the unloading path of the uniaxial test confirms that the Printex-filled compounds has a strong potential for sensing applications, thanks to its reversible behaviour.

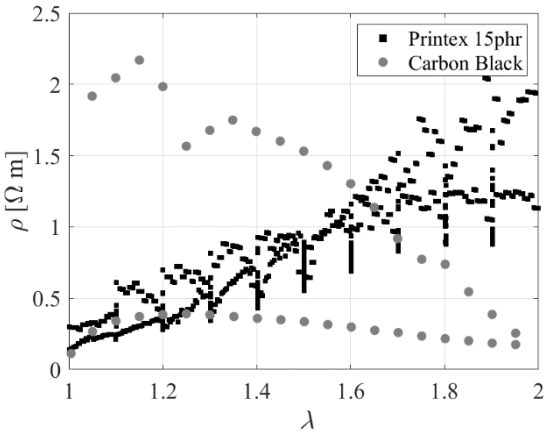

Figure 7.33 Resistivity as a function of the extension ratio for Carbon Black- and Printex 15 phr-filled rubber.

The results presented in Section 7.4 and 7.5 also show that simple linear models can be used to relate the change of resistivity to the changes of strain in the material in the small strain range, i.e. up to λ = 2 for uniaxial tests, γ = 0.7 for DBS tests and λ =0.97 for compression test. Table 7.6 summarizes the gauge factors and the standard deviation in terms of ε for the tensile specimen made with Printex 15 phr and the two compressive specimens made with Printex 12 phr. The sensitivity in compression is

significantly lower than in tension. Moreover, the specimen with higher aspect ratio is characterised by a higher sensitivity of the resistivity to the compression strains. This result can also be visualised by looking at Figure 7.34. A possible explanation of this behaviour can be provided by noting that for a given value of compression, the bulging of a rubber layer is more significant for the case of low shape factors, and that the bulging increases the length of the conductive path (see Figure 7.35). However, other factors may also affect the changes of resistivity, such as the fact that in a bonded rubber layer, the compression causes at local level significant shear strains, which are dependent on the shape factor of the layer.

Table 7.6 Gauge factor and standard deviation of linear models adopted

Specimens	**GF**	σ_ε
Printex 15 phr tensile specimen	9.27	0.16
Printex 12 phr compressive specimen l_0/d_0 = 0.1 (***S*** =2.5)	2.10	0.005
Printex 12 phr compressive specimen l_0/d_0 = 0.17 (***S*** =5.88)	11.5	0.0085

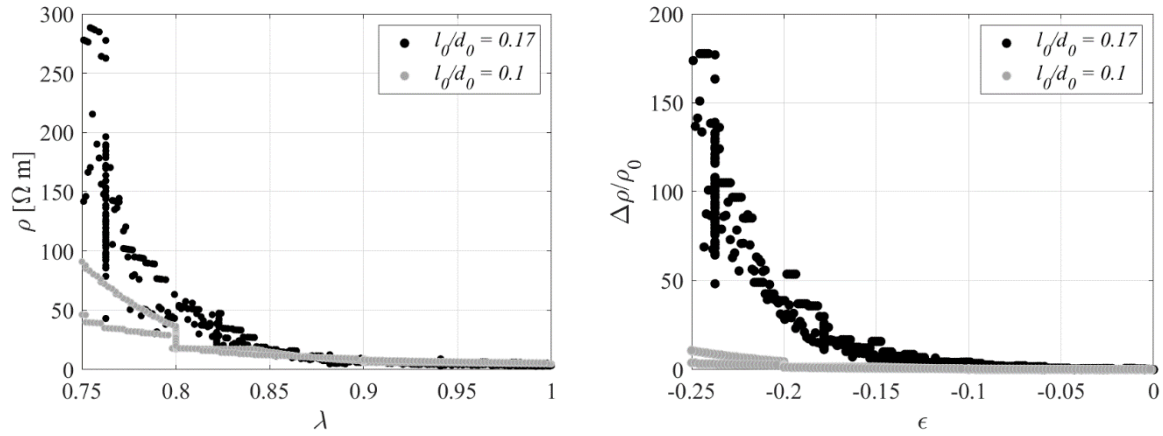

(a) (b)

Figure 7.34 Effect of the shape factor: (a) Resistivity versus compressive strain (b) Normalised resistivity change vs compressive strain.

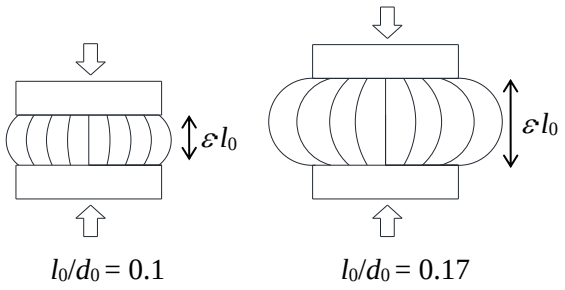

Figure 7.35 Effect of bulging on deformed geometry of the compressive specimens

7.7 Conclusion and future studies

This chapter illustrates the results of an extensive experimental campaign aimed at evaluating the suitability of different elastomeric compounds for the development of smart bridge bearings that can be used for monitoring the condition of the bearing as well as the bridge itself. For this purpose, three different compounds, one incorporating Carbon Black and the others Printex XE2 as filler, have been used to manufacture rubber specimens of different geometry. These specimens have been electromechanically characterized under different loading conditions, namely tensile, compressive and shear.

The study results have confirmed that rubber compounds traditionally employed for laminated rubber bearings, incorporating Carbon Black as filler, do not exhibit an optimal piezo-resistive behaviour, but those filled with Printex XE2 have a significant potential for being used to develop smart rubber bearings. This is mainly thanks to the reversible properties of natural rubber filled with Printex XE2, such that the change of electrical resistivity vs. mechanical strain relationship is almost the same for both the loading and unloading condition.

Based on the test results, simplified models have been developed for relating the change of resistivity to the changes of strain in the material. These models have been used to infer the state of strain in the rubber under a random loading scenario based on electrical resistivity measurements. Moreover, the experimental results of specimens with the Printex XE2 12 phr compound have also shed light on the effect of the aspect ratio or shape factor of the rubber layer on the piezoresistive behaviour. It has been shown that by changing the geometry of the layer, more significant changes of resistivity can be obtained for a given level of applied compression. This could be explained by the fact that the slender specimen bulges more than the stocky one, and thus experiences a more significant increase of the conductive path length. Finite element analyses (FEA) using a coupled electrical-mechanical model of the specimen will be carried out to confirm this. For further investigations, future studies will simulate the motion of the Printex particles distributed within the rubber matrix by FEA when the rubber is subjected to shear deformation and see whether the particles move closer to each other under small shear strains and then move further away when the shear strain gets larger.

Future studies will investigate further the development of smart rubber bearings and the eventual fatigue failure of elastomeric component under cyclic loads. In particular, alternative rubber compounds will be developed, using other volume fractions of Printex, or using alternative fillers such as carbon nanotubes or graphene, in order to reach a more optimal behaviour in terms of mechanical and piezo-resistive proper-ties. For example, further research is needed to increase the gauge factor under small strains, so that the rubber exhibits more significant changes of resistivity for small loadings. This would

unlock the potential to detect also the effect of loadings of lower intensity and not only exceptional loadings or heavy vehicle loadings.

Future experiment tests should include the effect of change in the temperature on the resistivity, assuming the temperature range of interest relevant to the service condition, and more thorough investigations on rate effects. The final material will also be characterised looking at creep rate, fatigue life, and strength properties. Once the optimal rubber compound and the optimal shape factor values is identified, two scaled laminated bearings will be manufactured and used to develop a scaled prototype of a simply supported bridge deck resting on the smart bearings. This will be useful to demonstrate the capabilities of the proposed technology and its use in real applications for bridge monitoring and as weigh in motion system.

8 Conclusion

Rubber bearings and devices have been employed for more than 70 years in the civil construction sector and have been the object of extensive experimental and numerical research. However, many aspects of the mechanical behaviour of rubber blocks and bearings have not been fully investigated yet.

The main aim of this thesis was to examine the mechanical behaviour of low shape factor (LSF) elastomeric bearings made of thick rubber layers and the seismic performance of structures equipped with them, and to investigate the possibility of developing smart bearings by exploiting the piezoresistive behaviour of filled rubber. The proposed aim has been achieved through a combination of experimental data from Cilento et al. (2017) carried at the Tun Abdul Razak Research Centre and University of Naples Federico II, experimental tests conducted at the University of Strathclyde, and numerical analyses employing models of varying degrees of complexity.

8.1 Key findings

Summarised below are the investigations undertaken and the key findings:

- In **Chapter 4**, the behaviour of bonded rectangular blocks with LSF under vertical and horizontal loading was investigated through experimental, numerical, and theoretical methods. It has been shown that the shape factor controls the contribution of the shear and bending deformations to the horizontal deflection, with the block with the highest shape factor deforming mainly in shear and the one with the lowest shape factor block deforming mainly under bending. The Ogden hyperelastic material model was found to provide more accurate results than the neo-Hookean hyperelastic model when simulating the behaviour of the blocks, particularly for high vertical compressions. The numerical analyses have also provided useful insight into the internal distribution of stresses and strains within the block. It was in fact observed the formation of a compression strut and the concentration of tensile stresses and strains at the corners of the block when subjected to horizontal displacements. The theories of Muhr and Lindley were found to provide an accurate description of the compressive behaviour of the blocks. With regards to the response of the compressed blocks under horizontal loading, the theory available in the literature were found to be not sufficiently accurate. Therefore, some improvements were made to the theory of Muhr, in order to better describe the effects of the bulging of the compressed blocks on the shear and flexural response. This allowed to achieve a better fit to experimental and numerical results.
- In **Chapter 5**, an advanced three-dimensional numerical model was developed in Abaqus for describing the mechanical behaviour of LSF elastomeric bearings and of structures mounted

with them. The model was validated against the results of experimental tests carried out on LSF laminated bearings. The numerical model provided valuable information on the stress and strain in the rubber bearings under compressive and shear loading. The Yeoh and Ogden hyperelastic material models were found to be more suitable than the Neo Hooke model for accurately describing the complex nonlinear shear response of LSF bearings under earthquake inputs. A simplified Rayleigh damping model was found to be sufficient for describing the dissipation capabilities of the low-damping compound. It was shown that the theories developed for high shape factor bearings cannot be used for describing the horizontal behaviour of LSF bearings and for estimating the critical load. With the proposed model, a quite accurate simulation of the shaking table test on a structural prototype mounted on the LSF bearings was obtained. The analyses have shown that the horizontal force-displacement relationship of the bearings is linear up to 30% shear deformation, but for higher values, a rapid reduction of tangent stiffness is observed due to the variation of axial loading as well as reduction of shear modulus of the rubber for increasing shear strain amplitudes. These results have been useful to develop the analytical model for LSF bearings in Chapter 6.

- The first part of **Chapter 6** investigated the accuracy of various theories available in the literature for describing the mechanical behaviour of laminated elastomeric bearings with LSF. The theory proposed by Muhr, accounting for the change of height and area of the rubber layers under compression, provided the best fit to the experimental results of compression and shear tests carried out on laminated bearings. The theory was further extended to account for the reduction of horizontal and vertical stiffness with the increase of the horizontal displacement, and it was used to develop a simplified analytical model for evaluating the dynamic behaviour and seismic response of structures mounted on LSF bearings. The proposed model, validated by comparisons with experimental shaking table test results, has been used in further parametric analyses to show that bearings with low shape factor could perform better than bearings with high shape factor, without inducing significant rocking motion in isolated structures.
- **Chapter 7** examined the potential of different elastomeric compounds for the development of smart bridge bearings for monitoring the condition of the bearings themselves and of bridges mounted on them. Three different compounds, one incorporating Carbon Black and the others incorporating Printex XE2 as filler, were used to manufacture rubber specimens. The specimens were tested under different loading conditions, namely tensile, compressive and shear, in order to mechanically characterize the rubber compounds and to determine their piezoresistive properties. The research results indicated the potential of Printex XE2 for the development of smart bridge bearings. Simplified models were developed for relating the change of resistivity to the change of strain in the material. These models were found to be suitable for inferring the state of strain in the rubber under random loadings based on electrical resistivity measurement.

The aspect ratio (shape factor) of the rubber layer was found to influence significantly the piezoresistive behaviour of bearings under compression. It was observed that more significant changes of resistivity can be obtained for a given level of applied compression for more slender layers (i.e., lower shape factors).

8.2 Future research

Future studies and additional investigations that need to be carried out are outlined below:

- The model developed by Muhr for describing the behaviour of LSF blocks and bearings, extended and improved in this Thesis (Chapter 5 and 6), is valid only for low-damping rubber. It needs to be further extended in order to describe the behaviour of high damping rubber compounds. Experimental tests were already carried out on LSF bearings made with high damping rubber, and could be used for validating the theory.
- The numerical modelling strategy for the LSF laminated bearings made with low-damping rubber developed and validated in Chapter 5 needs also to be extended to describe the mechanical behaviour of bearings made with high-damping rubber. This entails a more complex description of the hysteretic behaviour of rubber, using constitutive models that are already embedded in Abaqus (e.g. the one developed by Bergstrom and Boyce) or more complex models.
- The investigation on the dynamic behaviour and seismic performance of structures mounted on LSF bearings should be extended by considering more complex and realistic structural prototypes than the one tested and simulated in this Thesis. The analyses will also include the vertical component of the seismic input, which was not considered in the present study.
- The performance of LSF bearings for vibration isolation is also an aspect that should be investigated.
- Future research will also include the evaluation of rubber compounds using different volume fractions of Printex than those considered in this study, or alternative fillers with conductive behaviour such as carbon nanotubes or graphene. Further experimental tests should be carried out to characterise the creep rate, fatigue life, strength properties of the compounds, and the effects of temperature on the resistivity. In the near future, scaled laminated bearings will be manufactured using the compound incorporating Printex XE2 and tested at University of Strathclyde. An interrogation system will be developed to monitor the changes of resistivity in the bearings under different loading conditions. Moreover, numerical analyses considering a coupled electrical-mechanical model will be developed to describe the piezo-resistive behaviour of the rubber specimens and laminated bearings.

References

Agrawal, A. K., Subramaniam, K. and Pan, Y. (2005) *Development of Smart Bridge Bearings System – a Feasibility Study*. Report number: C-02-02. https://rosap.ntl.bts.gov/view/dot/16158

Ahmadi, H. R., Kingston, J. G. R. and Muhr, A. H. (1992) 'Dynamic Properties of Filled Rubber – Part I : Simple Model, Experimental Data and Simulated Results', *Rubber Chemistry and Technology*, 44(1), pp. 1–18.

Ahmadi, H. R. and Muhr, A. H. (1992) 'Vibration control using rubber components', *International Journal of Materials and Product Technology*. Inderscience Publishers, 7(1), pp. 65–88. doi: 10.1504/IJMPT.1992.036500.

Ahmadi, H. R. and Muhr, A. H. (1997) 'Modelling dynamic properties of filled rubber', *Plastics, Rubber and Composites Processing and Applications*, 26(10), pp. 451–461.

Ahmadi, H.R., Soleimani, S., Konstantinidis, D. and Balomenos, G. P. (2022) 'Nondestructive Assessment of Elastomeric Bridge Bearings Using 3D Digital Image Correlation', *Journal of Structural Engineering*, 148(1), pp. 1–15. doi: 10.1061/(asce)st.1943-541x.0003200.

Aiken, I. D, Kelly, J.M and Clark, P.W.. (1992) 'Experimental studies of mechanical characteristics of three types of seismic isolation bearings'. *Proceedings, 10th World Conference on Earthquake Engineering*, Madrid.

Aiken, I. D. and Kelly, J. M. (1990) Earthquake Simulator Testing And Analytical Studies Of Two Energy-Absorbing Systems For Multistory Structures. Technical Report. University of California Earthquake Engineering Research Central Berkeley

Aiken, I. D., Kelly, J. M. and Tajirian, F. F. (1989). Mechanics of Low Shape Factor Elastomeric Seismic Isolation Bearing, Report No. UCB/EERC-89/13, University of California, Berkeley.

Akbari, R. and Maalek, S. (2009) 'Evaluation of the shear modulus of elastomeric bridge bearings using modal data', *Journal of Testing and Evaluation*, 37(2), pp. 150–159. doi: 10.1520/jte101875.

American Association of State Highway Transportation Officials (2017) 'AASHTO LRFD Bridge Design Specifications', 8(15), p. 74. Available at: https://store.transportation.org/Common/DownloadContentFiles?id=1648.

Aria, M. and Akbari, R. (2013) 'Inspection, condition evaluation and replacement of elastomeric bearings in road bridges', *Structure and Infrastructure Engineering*, 9(9), pp. 918–934. doi: 10.1080/15732479.2011.638171.

Arruda, M. E. and Boyce, E. M. (1993) 'A three-dimensional constitutive model for the large stretch behavior of rubber elastic materials', *Journal of the Mechanics and Physics of Solids*, 41(2), pp. 389–412. doi: 10.1016/0022-5096(93)90013-6.

Basagiannis, C. A. and Williams, M. S. (2017) 'Application of elastomeric dampers to steel moment', in *6 th ECCOMAS Thematic Conference on Computational Methods in Structural Dynamics and Earthquake Engineering*. Rhodes Island, Greece.

Bergstrom, J. S. and Boyce, M.C. (1998) 'Constitutive modeling of the large strain time-dependent behavior of elastomers', *Journal of the Mechanics and Physics of Solids*, 46(5), p. 931. doi: 10.1016/S0022-5096(97)00075-6.

Bergström, J. S. and Boyce, M. C. (1999) 'Mechanical behavior of particle filled elastomers', *Rubber Chemistry and Technology*, 72(4), pp. 633–656. doi: 10.5254/1.3538823.

Blanford, E., Keldrauk, E., Laufer, M., Mieler, M., Wei, J., Stojadinovic, B. and Peterson, P.F. (2010) Advanced seismic base isolation methods for modular reactors. Report UCBTH-09-004. Unversity of California Berkeley. doi: 10.2172/1004114.

Boonstra, B. B. S. T. and Dannenberg, E. M. (1959) 'Swelling Behavior of Rubbers Compounded with Reinforcing Pigments', *Rubber Chemistry and Technology*, 32(3), pp. 825–843. doi: 10.5254/1.3542452.

Brincker, R., Zhang, L. and Andersen, P. (2001) 'Modal identification of output-only systems using frequency domain decomposition', *Smart Materials and Structures*, 10(3), pp. 441–445. doi: 10.1088/0964-1726/10/3/303.

Buckle, I., Nagarajaiah, S. and Ferrell, K. (2002) 'Stability of Elastomeric Isolation Bearings: Experimental Study', *Journal of Structural Engineering*, 2, pp. 3–11.

Busfield, J. J. C., Thomas, A. G. and Yamaguchi, K. (2004a) 'Electrical and mechanical behavior of filled elastomers 1: The effect of Strain', *Journal of Polymer Science, Part B: Polymer Physics*, 42(11 SPEC. ISS.), pp. 2161–2167. doi: 10.1002/polb.20085.

Busfield, J. J. C., Thomas, A. G. and Yamaguchi, K. (2004b) 'Electrical and mechanical behavior of filled elastomers 2: The effect of swelling and temperature', *Journal of Polymer Science, Part B: Polymer Physics*, 42(11 SPEC. ISS.), pp. 2161–2167. doi: 10.1002/polb.20085.

Busfield, J. J. C., Thomas, A. G. and Yamaguchi, K. (2005) 'Electrical and mechanical behavior of filled rubber. III. Dynamic loading and the rate of recovery', *Journal of Polymer Science, Part B: Polymer Physics*, 43(13), pp. 1649–1661. doi: 10.1002/polb.20452.

Calabrese, A., Spizzuoco M., Serino G., Della Corte G., and Maddaloni G. (2015) 'Shaking table investigation of a novel, low-cost, base isolation technology using recycled rubber', *Structural Control and Health Monitoring*, doi: 10.1002/stc.

Candau, N., Laghmach R., Laurent Chazeau, Chenal J.M., Gauthier C., Thierry Biben and Munch E. (2014) 'Strain-Induced Crystallization of Natural Rubber and Cross-Link Densities Heterogeneities', *Macromolecules*. American Chemical Society, 47(16), pp. 5815–5824. doi: 10.1021/ma5006843.

Cardone, D., Flora, A. and Gesualdi, G. (2013) 'Inelastic response of RC frame buildings with seismic isolation', *Earthquake Engineering Structural Dynamics*, (056), pp. 1–6. doi: 10.1002/eqe.

Cardone, D. and Perrone, G. (2012) 'Critical load of slender elastomeric seismic isolators: an experimental perspective', *Engineering Structures*, 40, pp. 198–204.

Carleo, F., Barbieri E.,Whear, R. and Busfield, J. C.. (2018) 'Limitations of viscoelastic constitutive models for carbon-black reinforced rubber in medium dynamic strains and medium strain rates', *Polymers*, 10(9). doi: 10.3390/polym10090988.

Chalhoub M S and Kelly J M (1990). Effect of bulk compressibility on the stiffness of cylindrical base isolation bearings Int. J. Solids Structures Vol. 26, No. 7, pp. 743-760

Chang, C. H. (2002) 'Modeling of laminated rubber bearings using an analytical stiffness matrix', *International Journal of Solids and Structures*, 39(24), pp. 6055–6078. doi: 10.1016/S0020-7683(02)00471-7.

Choi, I. S. and Roland, C. M. (1997) 'Strain-Crystallization of Guayule and Hevea Rubbers', *Rubber Chemistry and Technology*, 70(2), pp. 202–210. doi: 10.5254/1.3538425.

Chopra, A. K. (2013) Dynamics of Structures Theory and Applications to Earthquake Engineering, *Journal of Chemical Information and Modeling*. doi: 10.1017/CBO9781107415324.004.

Cilento, F., Vitale, R., Spizzuoco, M., Serino, G. and Muhr, A. (2017) 'Analysis of the Experimental Behaviour of Low Shape Factor Isolation Rubber Bearings by Shaking Table Investigation'.

Cilento, F.,Vitale, R., Spizzuoco, M., Serino, G. and Muhr, A. (2017) 'Dynamic behaviour in compression and shear of low shape factor rubber blocks', *Ingegneria Sismica*, 36(2), pp. 86–102.

Constantinou, M. C., Kartoum, A. and Kelly, J. M. (1992) 'Analysis of compression of hollow circular elastomeric bearings', *Engineering Structures*, 14(2), pp. 103–111. doi: 10.1016/0141-0296(92)90036-P.

Constantinou, M. C., Soong, T. T. and Dargush, G. F. (1998) 'Passive energy dissipation systems for structural design and retrofit'. Monograph No. 1

Coran, A. (2005). Chapter 7. Vulcanization. Science and Technology of Rubber (Third Edition) 10.1016/B978-012464786-2/50010-9.

Crockett, J. H. A. (1982) 'Early Attempts, Research and Modern Techniques for Insulating Buildings', in *Proceedings of the International Conference on Natural Rubber for Earthquake Protection of Buildings and Vibration Isolation*. Kuala Lumpur, Malaysia, pp. 15–44.

Crowder, A. P. and Becker, T. C. (2017) 'Experimental Investigation of Elastomeric Isolation Bearings with Flexible Supporting Columns', *Journal of Structural Engineering*, 143(7), p. 04017057. doi: 10.1061/(asce)st.1943-541x.0001784.

Cuomo, G. (2014) 'Design, development and experimental validation of multilayer modular laminated natural rubber isolators.'University of Naples Federico II, Naples.

'Dassault Systèmes, Abaqus Analysis User's Manual Version' (2018).

Derham, C. J., Kelly, J. M. and Thomas, A. G. (1985) 'Nonlinear natural rubber bearings for seismic isolation', *Nuclear Engineering and Design*, 84(3), pp. 417–428. doi: https://doi.org/10.1016/0029-5493(85)90258-4.

Derham, C. J., Lake, G. J. and Thomas, A. G. (1969) 'Some factors affecting the service life of natural rubber articles', *Rubber Res Inst Malaya*.

Derham, C. J. and Thomas, A. G. (1977) 'Creep of Rubber under Repeated Stressing', *Rubber Chemistry and Technology*, 50, pp. 397–402.

Derham, C. J. and Thomas, A. G. (1980) 'The design and use of rubber bearings for vibration isolation and seismic protection of structures', *Engineering Structures*, 2(3), pp. 171–175. doi: 10.1016/0141-0296(80)90019-X.

Derham, C. J. and Waller, R. A. (1975) 'Luxury without Rumble', *The Consulting Engineer*, 39(7), pp. 49–53.

Dhir, P. K., Tubaldi, E., Orfeo, A. and Ahmadi, H. (2022) 'Cyclic shear behaviour of masonry triplets with rubber joints', *Construction and Building Materials*. Elsevier Ltd, 351(May), p. 128356. doi: 10.1016/j.conbuildmat.2022.128356.

Ezquerra, T. A., Baltá, C. F. J. and Plans, J. (1986) 'On tunneling effects in metal-deposited polyethylene-carbon black and polycarbonate-carbon black systems', *Journal of Materials Research*, 1(3), pp. 510–514. doi: 10.1557/JMR.1986.0510.

Fan, L. J., Muhr, A.H., Parson, B. and Thomas, A.G. (1992) 'Shear load-deflaction behaviour of compressed Rubber blocks'. *Rubbercon*, Brighton,

Ferry, J. D. (1970) *Viscoelastic properties of polymers*. 2nd ed., *Wiley-Interscience*. New York, N.Y.

Fletcher, W. P. and Gent, A. N. (1954) 'Nonlinearity in the Dynamic Properties of Vulcanized Rubber Compounds', *Rubber Chemistry and Technology*, 27(1), pp. 209–222. doi: 10.5254/1.3543472.

Fred, M. (1979) 'Weigh-in-Motion System Using Instrumented Bridges', *Transportation Engineering Journal of ASCE*. American Society of Civil Engineers, 105(3), pp. 233–249. doi: 10.1061/TPEJAN.0000783.

Freire, L. M. R., de Brito, J. and Correia, J. R. (2015) 'Inspection Survey of Support Bearings in Road Bridges', *Journal of Performance of Constructed Facilities*, 29(4), pp. 1–11. doi: 10.1061/(asce)cf.1943-5509.0000569.

Gent, A. N. (1962a) 'Relaxation processes in vulcanized rubber. I. Relation among stress relaxation, creep, recovery, and hysteresis', *Journal of Applied Polymer Science*. John Wiley & Sons, Ltd, 6(22), pp. 433–441. doi: https://doi.org/10.1002/app.1962.070062207.

Gent, A. N. (1962b) 'Relaxation processes in vulcanized rubber. II. Secondary relaxation due to network breakdown', *Journal of Applied Polymer Science*. John Wiley & Sons, Ltd, 6(22), pp. 442–448. doi: https://doi.org/10.1002/app.1962.070062208.

Gent, A. N. (1965) 'Elastic Stability of Rubber Compression Springs', *Rubber Chemistry and Technology*, 38(2), pp. 415–430. doi: 10.5254/1.3535662.

Gent, A. N. (2012) *Preface - Engineering with Rubber: How to Design Rubber Components*. Third Edit, *Engineering with Rubber How to Design Rubber Components*. Third Edit. Carl Hanser Verlag GmbH & Co. KG. doi: 10.3139/9783446428713.fm.

Gent, A. N. and Lindley, P. B. (1959) 'The Compression of bonded rubber blocks', *Rubber Chemistry and Technology*, 173(1), pp. 111–122. doi: 10.5254/1.3547682.

Gent, A. N. and Meinecke, E. A. (1970) 'Compression, bending, and shear of bonded rubber blocks', *Polymer Engineering & Science*, 10(1), pp. 48–53. doi: 10.1002/pen.760100110.

Gent, A. N., Suh, J. B. and Kelly, S. G. (2007) 'Mechanics of rubber shear springs', *International Journal of Non-Linear Mechanics*, 42(2), pp. 241–249. doi: 10.1016/j.ijnonlinmec.2006.11.006.

Ghoreishy, M. H. R., Firouzbakht, M. and Naderi, G. (2014) 'Parameter determination and experimental verification of Bergström-Boyce hysteresis model for rubber compounds reinforced by carbon black blends', *Materials and Design*. Elsevier Ltd, 53, pp. 457–465. doi: 10.1016/j.matdes.2013.07.040.

Giannone, P., Graziani, S. and Umana, E. (2015) 'Investigation of carbon black loaded natural rubber piezoresistivity', *Conference Record - IEEE Instrumentation and Measurement Technology*

Conference, 2015-July, pp. 1477–1481. doi: 10.1109/I2MTC.2015.7151495.

Goodchild, I. R., Muhr, A. H. and Thomas, A. G. (2018) 'The lateral stiffness and damping of a stretched rubber beam', *Plastics, Rubber and Composites*. Taylor & Francis, 47(4), pp. 176–186. doi: 10.1080/14658011.2018.1459065.

Gough, J. (2000) *Stress-Strain Behaviour of Rubber*. Queen Mary and Westfield College University of London.

Gough, J., Gregory, M. J. and Muhr, A. H. (1999) 'Determination of constitutive equations for vulcanized rubber', *Finite Element Analysis ofElastomers. London: Professional Engineering Publishing*, In D. Boas, pp. 5–26.

Gough, J. and Muhr, A. H. (2005) 'Initiation of failure of rubber close to bondlines', *Angewandte Chemie International Edition*, 6(11), pp. 951–952.

Grant, D. N., Fenves, G. L. and Whittaker, A. S. (2004) 'Bidirectional modelling of high-damping rubber bearings', *Journal of Earthquake Engineering*, 8, pp. 161–185. doi: 10.1080/13632460409350524.

Grant, D. N., Fenves, G. L. and Whittaker, A. S. (2004) 'Bidirectional Modelling Of High-Damping Rubber Bearings', *Journal of Earthquake Engineering*. Taylor & Francis, 8(sup001), pp. 161–185. doi: 10.1080/13632460409350524.

Gregory, I. H. and Muhr, A. H. (1999) 'Stiffness and Fracture analysis of bonded rubber blocks in simple shear' in: D. Boast, V.A. Coveny (Eds.), Finite Element Analysis of Elastomers, Professional Engineering Publications, Bury St. Edmunds, UK, 1999, pp. 265–274

Gregory, M. J. (1979) 'The Stress-Strain behaviour of Filled Rubber at moderate strain', *Plast Rubber Mater Appl*, 8.

Grootenhuis, P. (1982) 'Vibration isolation of buildings—some basic principles', in *Proceedings of the International Conference on Natural Rubber for Earthquake Protection of Buildings and Vibration Isolation*. Kuala Lumpur, Malaysia, pp. 1–14.

Gu, Z., Lei, Y., Qian, W., Xiang, Z., Hao, F. and Wang, Y. (2021) 'An experimental study on the mechanical properties of a high damping rubber bearing with low shape factor', *Applied Sciences (Switzerland)*, 11(21). doi: 10.3390/app112110059.

Han, X. and Warn, G. P. (2015) 'Mechanistic Model for Simulating Critical Behavior in Elastomeric Bearings', *Journal of Structural Engineering*, 141(5), p. 04014140. doi: 10.1061/(asce)st.1943-541x.0001084.

Haringx, J.A. (1948) 'On highly compressible helical springs and rubber rods, and their application for vibration-free mountings',I, *Phillips Research Report*, 4, pp. 49–80.

Haringx, J.A. (1949) 'Elastic Stability of Helical Springs At a Compression Larger Than Original Length', *Appl. Sci. Res.*, 1, pp. 417–434.

Harwood, J. A. C. and Schallamach, A. (1967) 'Dynamic behavior of natural rubber during large extensions', *Journal of Applied Polymer Science*. John Wiley & Sons, Ltd, 11(10), pp. 1835–1850. doi: https://doi.org/10.1002/app.1967.070111002.

Henkel Technical Data (2022) *Loctite Technical Data Sheet*.

Hillmer, K.-H. and Scheele, W. (1970) 'Degradation of Highly Elastic Polymers. VI. The Intermittent Chemo-Stress Relaxation of Crosslinked 1,5-Polyenes', *Rubber Chemistry and Technology*, 43(4), pp. 788–798. doi: 10.5254/1.3547289.

Hirst, A. J. (1961) 'The Applied Science of Rubber', in. London: Edward Arnold, pp. 587–708.

Horgan, C. O. and Murphy, J. G. (2010) 'Simple Shearing of Incompressible and Slightly Compressible Isotropic Nonlinearly Elastic Materials', *Journal of Elasticity*, 98(2), pp. 205–221. doi: 10.1007/s10659-009-9225-1.

Horton, J. M., Tupholme, G. E. and Gover, M. J. C. (2002) 'Axial loading of bonded rubber blocks', *Journal of Applied Mechanics, Transactions ASME*, 69(6), pp. 836–843. doi: 10.1115/1.1507769.

Howgate, P. G. (1979) 'Shape Factor for Rubbers in shear and compression', in. Hepburn, C. and Reynolds, R.J.W., Applied Science Publishers Ltd.

IAEA (2020) 'Seismic Isolation Systems for Nuclear Installations', (1731), pp. 2016–2021.

Imbimbo, M. and Kelly, J. M. (1997) 'Stability of isolators at large horizontal displacements', *Earthquake Spectra*, pp. 415–430. doi: 10.1193/1.1585955.

Imbimbo, M. and De Luca, A. (1998) 'F.E. stress analysis of rubber bearings under axial loads', *Computers and Structures*, 68(1–3), pp. 31–39. doi: 10.1016/S0045-7949(98)00038-8.

Jha, V., Thomas, A.G. and Busfield, J.J. (2010) 'Reversible Electrical Behavior with Strain for a Carbon Black-Filled Rubber', *Journal of Applied Polymer Science*, 116(5), pp. 2658–2667. doi: 10.1002/app.

Kalfas, K. N., Mitoulis, S. A. and Katakalos, K. (2017) 'Numerical study on the response of steel-laminated elastomeric bearings subjected to variable axial loads and development of local tensile stresses', *Engineering Structures*. Elsevier Ltd, 134, pp. 346–357. doi: 10.1016/j.engstruct.2016.12.015.

Kelly, J.M. (1999) 'Analysis of Fiber-Reinforced Elastomeric Isolators', *Journal of Seismology and Earthquake Engineering*, 2(1), pp. 19–34.

Kelly, J. M. (1988) 'Base Isolation in Japan', UCB/EERC-88/20. Report. Unviersity of California, Berkeley.

Kelly, J. M. (1993) *Earthquake-Resistant Design with Rubber*, 2nd Edition, Springer London, doi: 10.1007/978-1-4471-3359-9.

Kelly, J. M. (1997) 'Behavior of Multilayered Bearings Under Compression and Bending BT - Earthquake-Resistant Design with Rubber', in Kelly, J. M. (ed.). London: Springer London, pp. 131–159. doi: 10.1007/978-1-4471-0971-6_7.

Kelly, J. M. and Van Engelen, N. C. (2016) 'Fiber-reinforced elastomeric bearings for vibration isolation', *Journal of Vibration and Acoustics, Transactions of the ASME*, 138(1), pp. 1–6. doi: 10.1115/1.4031755.

Kelly, J. M. and Konstantinidis, D. A. (2011) *Mechanics of Rubber Bearings for Seismic and Vibration Isolation, Mechanics of Rubber Bearings for Seismic and Vibration Isolation*. doi: 10.1002/9781119971870.

Kelly, J.M. and Lee, J. J. L. (2018) 'Vertical Flexibility in Isolation Systems', *Civil Engineering Research Journal*, 4(1), pp. 1–11. doi: 10.19080/cerj.2018.04.555629.

Keys, W. C. (1937) 'Rubber springs', *Mechanical Engineering*, 59(5), pp. 345–349.

Kikuchi, M. and Aiken, I. D. (1997) 'An analytical hysteresis model for elastomeric seismic isolation bearings', *Earthquake Engineering and Structural Dynamics*, 26(2), pp. 215–231. doi: 10.1002/(SICI)1096-9845(199702)26:2<215::AID-EQE640>3.0.CO;2-9.

Kikuchi, M., Nakamura, T. and Aiken, I. D. (2010) 'Three-dimensional analysis for square seismic isolation bearings under large shear deformations and high axial loads', *Earthquake Engineering & Structural Dynamics*. John Wiley & Sons, Ltd, 39(13), pp. 1513–1531. doi: https://doi.org/10.1002/eqe.1042.

Kim, J., Park, Y., Choi, I., Kang, D. (2002) 'Development of smart elastomeric bearing equipped with PVDF polymer film for monitoring vertical load through the support', *1st IMEKO TC20 Conference on Civil Engineering Metrology 2002 - Joint International Conference on Force, Mass, Torque, Hardness and Civil Engineering Metrology in the Age of Globalization*, pp. 15–19.

Kimmich, E. G. (1940) 'Rubber in compression', *India Rubber World*, 103(3), pp. 45–50.

Kingston, J. G. R. and Muhr, A. H. (2011) 'Effect of scragging on parameters in viscoplastic model for

filled rubber', *Plastics, Rubber and Composites*. Taylor & Francis, 40(4), pp. 161–168. doi: 10.1179/1743289811Y.0000000018.

Koh, C. G. and Kelly, J. M. (1986) 'Effects of axial load on elastomeric bearings', *Rep. UCB/EERC-86*, 12. University of California, Berkeley.

Koh, C. G. and Kelly, J. M. (1988) 'A simple mechanical model for elastomeric bearings used in base isolation', *International Journal of Mechanical Sciences*, 30(12), pp. 933–943. doi: 10.1016/0020-7403(88)90075-6.

Koh, C. G. and Kelly, James M. (1989) 'Compression stiffness of bonded square layers of nearly incompressible material', *Engineering Structures*, 11(1), pp. 9–15. doi: 10.1016/0141-0296(89)90027-8.

Koh, C. G. and Kelly, James M (1989) 'Modelling of seismic isolation bearings including shear deformation and stability effects', *Applied Mechanics Reviews*, 42(11), pp. 113–120.

Koh, C. G. and Lim, H. L. (2001) 'Analytical solution for compression stiffness of bonded rectangular layers', *International Journal of Solids and Structures*, pp. 445–455. doi: 10.1016/S0020-7683(00)00057-3.

Kosten, C. W. (1942). Over de elastische eigenschappen van gevulcaniseerde rubber. (On the elastic properties of vulcanized rubber)," thesis presented to Delft University, Delft, Netherlands, in partial fulfillment of the requirements for the degree of Doctor of Philosophy (in Dutch)

Kulak, R., Coveney, V. A. and Jamil, S. (1998) 'Recovery characteristics of high damping elastomers used in seismic isolation bearings', 379, pp. 79–83.

Kumar, M. and Whittaker, A. (2018) 'Cross-platform implementation, verification and validation of advanced mathematical models of elastomeric seismic isolation bearings', *Engineering Structures*, 175, pp. 926–943. doi: 10.1016/j.engstruct.2018.08.047.

Kumar, M., Whittaker, A. S. and Constantinou, M. C. (2012) 'An advanced numerical model of elastomeric seismic isolation bearings Manish', *Earthquake Engineering & Structural Dynamics*, 41(11), pp. 1549–1568. doi: 10.1002/eqe.

Lake, G. J. and Lindley, P. B. (1965) 'The mechanical fatigue limit for rubber', *Journal of Applied Polymer Science*. John Wiley & Sons, Ltd, 9(4), pp. 1233–1251. doi: https://doi.org/10.1002/app.1965.070090405.

Lanzo, A. D. (2004) 'On elastic beam models for stability analysis of multilayered rubber bearings', *International Journal of Solids and Structures*, 41(20), pp. 5733–5757. doi:

10.1016/j.ijsolstr.2004.04.024.

Lee, D. J. and Lee, D. J. (1995) *Bridge Bearings and Expansion Joints (2nd ed.)*. London: CRC Press. Available at: https://doi.org/10.1201/9781482266993.

Li, S., Ning, Q. and Chen, H. (2012) 'Rail elevated bridge bearing displacement monitoring based on FBG sensor', *Applied Mechanics and Materials*, 178–181, pp. 2034–2037. doi: 10.4028/www.scientific.net/AMM.178-181.2034.

Lindley, P. B. (1966). Load-compression relationships of rubber units. The Journal of Strain Analysis for Engineering Design. 1, pp. 190-195. doi:10.1243/03093247V013190

Lindley, P. B. (1981) 'Natural Rubber Structural Bearings', *ACI Symposium Publication*, 70. doi: 10.14359/17418.

V. M. Litvinov and P. A. M. Steeman. EPDM−Carbon Black Interactions and the Reinforcement Mechanisms, As Studied by Low-Resolution H NMR. *Macromolecules* **1999** *32* (25), 8476-8490 DOI: 10.1021/ma9910080

Liu, Q. *et al.* (2016) 'An intelligent monitoring method and its experiment for bridge bearing', (Iccte), pp. 633–638. doi: 10.2991/iccte-16.2016.106.

Loos, K., Park, Y., Choi, I. and Kang, D. (2021) 'Strain-induced crystallisation in natural rubber: a thermodynamically consistent model of the material behaviour using a serial connection of phases', *Continuum Mechanics and Thermodynamics*, 33(4), pp. 1107–1140. doi: 10.1007/s00161-020-00950-9.

Lord Technical Data *LORD TECHNICAL DATA ON CHEMOSIL 211 Primer and/or Bonding Agent*. Available at: www.lord.com.

Losanno, D., Madeira-Sierra, I. E., Spizzuoco, M., Marulanda, J. and Thomson, P. (2019) 'Experimental assessment and analytical modeling of novel fiber-reinforced isolators in unbounded configuration', *Composite Structures*. Elsevier, 212(December 2018), pp. 66–82. doi: 10.1016/j.compstruct.2019.01.026.

Losanno, D., Madeira-Sierra, I. E., Spizzuoco, M., Marulanda, J. and Thomson, P. (2020) 'Experimental performance of unbonded polyester and carbon fiber reinforced elastomeric isolators under bidirectional seismic excitation', *Engineering Structures*. Elsevier, 209(November 2019), p. 110003. doi: 10.1016/j.engstruct.2019.110003.

Losanno, D., Calabrese, A., Madeira-Sierra, I. E., Spizzuoco, M., Marulanda, J., Thomson, P. and Serino, G. (2020) 'Recycled versus Natural-Rubber Fiber-Reinforced Bearings for Base Isolation:

Review of the Experimental Findings', *Journal of Earthquake Engineering*. Taylor & Francis, 00(00), pp. 1–20. doi: 10.1080/13632469.2020.1748764.

Losanno, D., De Domenico, D. and Madera-Sierra, I. E. (2022) 'Experimental testing of full-scale fiber reinforced elastomeric isolators (FREIs) in unbounded configuration', *Engineering Structures*. Elsevier Ltd, 260(April), p. 114234. doi: 10.1016/j.engstruct.2022.114234.

Losanno, D., Spizzuoco, M. and Calabrese, A. (2019) 'Bidirectional shaking-table tests of unbonded recycled-rubber fiber-reinforced bearings (RR-FRBs)', *Structural Control and Health Monitoring*, 26(9). doi: 10.1002/stc.2386.

Magliulo, G., Petrone, C., Capozzi, V., Maddaloni, G., Lopez, P. and Mandredi, G. (2014) 'Seismic performance evaluation of plasterboard partitions via shake table tests', *Bulletin of Earthquake Engineering*, 12(4), pp. 1657–1677. doi: 10.1007/s10518-013-9567-8.

'MATLAB' (2021). version 7.10.0 (R2021b). Natick, Massachusetts: The MathWorks Inc.

McAlorum, J., Perry, M., Ward, A.C. and Vlachakis, C.. (2021) 'ConcrEITS: An Electrical Impedance Interrogator for Concrete Damage Detection Using Self-Sensing Repairs.', *Sensors (Basel, Switzerland)*. Switzerland, 21(21). doi: 10.3390/s21217081.

McKenna, G. B. and Zapas, L. J. (1983) 'Experiments on the small-strain behaviour of crosslinked natural rubber: 1. Torsion', *Polymer*, 24(11), pp. 1495–1501. doi: https://doi.org/10.1016/0032-3861(83)90237-9.

Medalia, A. I. (1986) 'Electrical Conduction in Carbon Black Composites', *Rubber Chemistry and Technology*, 59(3), pp. 432–454. doi: 10.5254/1.3538209.

Medalia, A. I. and Rivin, D. (1982) 'Particulate carbon and other components of soot and carbon black', *Carbon*, 20(6), pp. 481–492. doi: https://doi.org/10.1016/0008-6223(82)90084-7.

Mistry, S. J. and Govindjee, S. (2014) 'A micro-mechanically based continuum model for strain-induced crystallization in natural rubber', *International Journal of Solids and Structures*, 51(2), pp. 530–539. doi: https://doi.org/10.1016/j.ijsolstr.2013.10.027.

Montuori, G. M., Mele, E., Marrazzo, G., Brandonisio, G. and De Luca, A. (2016) 'Stability issues and pressure–shear interaction in elastomeric bearings: the primary role of the secondary shape factor', *Bulletin of Earthquake Engineering*. Springer Netherlands, 14(2), pp. 569–597. doi: 10.1007/s10518-015-9819-x.

Mooney, M. A. (1940) 'Theory of Large Elastic Deformation', *Journal of Applied Physics*, 11, pp. 582–592.

Muhr, A.H. (2009) 'Fitting a viscoplastic time-domain model to equivalent viscoelastic materials data', *Constitutive Models for Rubber VI*, (2), pp. 131–136. doi: 10.1201/noe0415563277.ch22.

Muhr, A. H. (2013) 'Effect of thickness of reinforcing plates on rubber-steel laminated bearings', *Encephale*, 53(1), pp. 59–65. Available at: http://dx.doi.org/10.1016/j.encep.2012.03.001.

Muhr, A. H. (2017) 'Lateral stiffness of rubber mounts under finite axial deformation', *Constitutive Models for Rubber X - Proceedings of the 10th European Conference on Constitutive Models for Rubber, ECCMR X 2017*, pp. 153–158. doi: 10.1201/9781315223278-26.

Mullins, L. (1948) 'Effect of Stretching on the Properties of Rubber', *Rubber Chemistry and Technology*, 21(2), pp. 281–300. doi: 10.5254/1.3546914.

Mullins, L. and Tobin, N. R. (1965) 'Stress softening in rubber vulcanizates. Part I. Use of a strain amplification factor to describe the elastic behavior of filler-reinforced vulcanized rubber', *Journal of Applied Polymer Science*. John Wiley & Sons, Ltd, 9(9), pp. 2993–3009. doi: https://doi.org/10.1002/app.1965.070090906.

Nagarajaiah, S. and Ferrell, K. (1999) 'Stability Of Elastomeric Seismic Isolation Bearings', *Journal of Structural Engineering*,125(September), pp. 946–954.

Nagarajaiah, S., Ferrell, K. and Buckle, I. (1999) 'Stability of elastomeric seismic isolation bearings', *Structures Congress - Proceedings*, 2(September 1999), pp. 1138–1142. doi: 10.1061/(ASCE)0733-9445(1999)125.

Nan, C.-W., Shen, Y. and Ma, J. (2010) 'Physical Properties of Composites Near Percolation', *Annual Review of Materials Research*. Annual Reviews, 40(1), pp. 131–151. doi: 10.1146/annurev-matsci-070909-104529.

Nims, D.K.; Subramaniam, K.; Parvin, A. and Aktan, A.E. (1996) 'The Potential for the Use of Elastomeric Bearings in an Intelligent Bridge System', in *Transportation Research Board 75th Annual Meeting*. Washington, DC.

Nims, D.K. (2000) *Instrumented Elastomeric Bridge Bearings*; ODOT Project No. 14647(0), Final Report; University of Toledo: Toledo, OH, USA.

OBrien, E. J., Enright, B. and Getachew, A. (2010) 'Importance of the Tail in Truck Weight Modeling for Bridge Assessment', *Journal of Bridge Engineering*, 15(2), pp. 210–213. doi: 10.1061/(asce)be.1943-5592.0000043.

Ogden, R. . (1984) 'Dover Civil and Mechanical Engineering R. W. Ogden - Non-Linear Elastic Deformations'.

Ogden, R. W. (1976) 'Volume changes associated with the deformation of rubber-like solids', *Journal of the Mechanics and Physics of Solids*, 24(6), pp. 323–338. doi: 10.1016/0022-5096(76)90007-7.

Ohsaki, M., Miyamura, T., Kohiyama, M., Yamashita, T., Yamamoto, M. and Nakamura, N. (2015) 'Finite-element analysis of laminated rubber bearing of building frame under seismic excitation', *Earthquake Engineering and Structural Dynamics*, 44(11), pp. 1881–1898. doi: 10.1002/eqe.2570.

Okamura, S., Kamishima, Y, Negishi, K., Sakamoto, Y., Kitamura, S. and Kotake, S. (2011) 'Seismic isolation design for JSFR', *Journal of Nuclear Science and Technology*, 48(4), pp. 688–692. doi: 10.1080/18811248.2011.9711750.

Orfeo, A.,Tubaldi, E., Muhr, A.H. and Losanno, D. (2022) 'Mechanical behaviour of rubber bearings with low shape factor', *Engineering Structures*. Elsevier Ltd, 266(February), p. 114532. doi: 10.1016/j.engstruct.2022.114532.

Van Overschee, P. and De Moor, B. (2008) *Subspace Identification For Linear Systems*, *Kluwer Academic Publishers*. doi: 10.1109/IEMBS.2008.4650193.

Payne, A R (1962) 'Effect of compression on the shear modulus of rubber', *I&EC Product Research and Development*, 1(2), pp. 86–88. doi: 10.1021/i360002a005.

Payne, A. R. (1962) 'The Dynamic Properties of Carbon Black-Loaded', *Nature (London)*, VI(19), pp. 57–63.

Payne, A. R. and Whittaker, R. E. (1970) 'Dynamic properties of materials', *Rheologica Acta*, 9(1), pp. 91–96. doi: 10.1007/BF01984598.

Pond, T. J. and Thomas, A. G. (1993) 'The Mechanics of Laminated Rubber Bearings', *Journal of Rubber Research*, 8(4), pp. 260–274.

Porter, L. S. and Meinecke, E. A. (1980) 'Influence of Compression upon the Shear Properties of Bonded Rubber Blocks', *Rubber Chemistry and Technology*, 53(5), pp. 1133–1144. doi: 10.5254/1.3535084.

Ragni, L., Tubaldi, E., Dall'Asta, A., Ahmadi, H., Muhr, A.H. (2018) 'Biaxial shear behaviour of HDNR with Mullins effect and deformation-induced anisotropy', *Engineering Structures*, 154, pp. 78–92. doi: 10.1016/j.engstruct.2017.10.060.

Ragni, L., Cardone, D., Conte, N, Dall'Asta, A., Di Cesare, A., Flora, A., Leccese, G., Micozzi, F. and Ponzo, F. (2018) 'Modelling and Seismic Response Analysis of Italian Code-Conforming Base-Isolated Buildings', *Journal of Earthquake Engineering*, 22, pp. 1–33. doi: 10.1080/13632469.2018.1527263.

Raithel, A. and Serino, G. (1993) 'Stabilità e comportamento post-critico degli isolatori elastomerici

armati', in *6° Convegno Nazionale L'Ingegneria Sismica in Italia*. Perugia.

Rastgoo Moghadam, S. and Konstantinidis, D. (2021) 'Experimental and Analytical Studies on the Horizontal Behavior of Elastomeric Bearings under Support Rotation', *Journal of Structural Engineering*, 147(4), pp. 1–11. doi: 10.1061/(asce)st.1943-541x.0002962.

Ren, X., Lu, W., Zhu, Y.,He, Y. and Li, T. (2020) 'Compressive behavior of low shape factor lead-rubber bearings: Full-scale testing and numerical modeling', *Engineering Structures*, 209(December 2019). doi: 10.1016/j.engstruct.2019.110030.

Rivlin, R.S. (1971) 'Large Elastic Deformations', *Physics Today*, 24(12), p. 57. doi: 10.1063/1.3022479.

Rivlin, R. S. (1948) 'Large elastic deformations of isotropic materials IV. Further developments of the general theory',

Rivlin, R. S. and Thomas, A. G. (1953) 'Rupture of rubber. I. Characteristic energy for tearing', *Journal of Polymer Science*, 10, pp. 291–318.

Roeder, C. W., Stanton, J. F. and Taylor, A. W. (1987) Performance of Elastomeric Bearings., *National Cooperative Highway Research Program Report*.

Roeder, J. F. S. and C. W. (1991) 'Design of Laminated Elastomeric Bridge Bearings', *Transportation research record*, 1290, pp. 199–206.

Sae-oui, P. Thepsuwan, U., Thaptong, P. and Sirisinha, C. (2014) 'Comparison of Reinforcing Efficiency of Carbon Black, Conductive Carbon Black, and Carbon Nanotube in Natural Rubber', *Advances in Polymer Technology*, 33. doi: 10.1002/adv.21422.

Saidou, A., Gauron, O., Busson, A. and Paultre, P. (2021) 'High-order finite element model of bridge rubber bearings for the prediction of buckling and shear failure', *Engineering Structures*. Elsevier Ltd, 240(April), p. 112314. doi: 10.1016/j.engstruct.2021.112314.

Sanchez, J., Masroor, A., Mosqueda, G. and Ryan, K. (2013) 'Static and Dynamic Stability of Elastomeric Bearings for Seismic Protection of Structures', *Journal of Structural Engineering*, 139(7), pp. 1149–1159. doi: 10.1061/(asce)st.1943-541x.0000660.

Schapery, R. A. (2018a) 'Elastomeric bearing sizing analysis Part 1: Spherical bearing', *International Journal of Solids and Structures*. Elsevier Ltd, 152–153, pp. 118–139. doi: 10.1016/j.ijsolstr.2018.03.010.

Schapery, R. A. (2018b) 'Elastomeric bearing sizing analysis Part 2: Flat and cylindrical bearings', *International Journal of Solids and Structures*. Elsevier Ltd, 152–153, pp. 140–150. doi:

10.1016/j.ijsolstr.2018.07.007.

Schapery, R. A. (2018c) 'Shim analysis for spherical elastomeric bearings', *International Journal of Solids and Structures*. Elsevier Ltd, 144–145, pp. 276–288. doi: 10.1016/j.ijsolstr.2018.05.013.

Schapery, R. A. and Skala, D. P. (1976) 'Elastic stability of laminated elastomeric columns', *International Journal of Solids and Structures*. Pergamon Press, 12(6), pp. 401–417. doi: 10.1016/0020-7683(76)90018-4.

Siegenthaler, R. (1970) *Earthquake Proof Building Supporting Structure with Shock Absorbing Damping Elements*. Schweizerische Bauzeitung.

Simo, J. C. (1987) 'On a fully three-dimensional finite-strain viscoelastic damage model: Formulation and computational aspects', *Computer Methods in Applied Mechanics and Engineering*, 60(2), pp. 153–173. doi: https://doi.org/10.1016/0045-7825(87)90107-1.

Sircar, A. K. and Lamond, T. G. (1978) 'Effect of Carbon Black Particle Size Distribution on Electrical Conductivity', *Rubber Chemistry and Technology*, 51, pp. 126–132.

Stanton, J. F., Scroggins, G., Taylor, A. W., & Roeder, C. W.. (1990) 'Stability of Laminated Elastomeric Bearings', 116(6), pp. 1351–1371.

Stanton, J. F. and Roeder, C. W. (1982) *Elastomeric bearings design, construction, and materials*. Edited by D. C. TRANSPORTATION RESEARCH BOARD NATIONAL RESEARCH COUNCIL WASHINGTON.

Stauffer, D. (1979) 'Scaling theory of percolation clusters', *Physics Reports*, 54(1), pp. 1–74. doi: 10.1016/0370-1573(79)90060-7.

Stauffer, D. and Bunde, A. (1987) *Introduction to Percolation Theory*, *Physics Today*. doi: 10.1063/1.2820231.

Subramaniam, K. (1995) *Feasibility of Using Instrumented Elastomeric Bearings for Bridge Monitoring and Condition Assessment*. University of Toledo.

Symans, M. D. (2004) 'SEISMIC PROTECTIVE SYSTEMS : SEISMIC ISOLATION', in, pp. 1–87.

Tajirian, F. F., Kelly, J. M., Aiken, I. D., and Veljovich, W., "Elastomeric Bearings for Three-Dimensional Seismic Isolation", Proceedings, 1990 ASME PVP Conference, ASME PVP-200, Nashville, Tennessee, June, 1990.

Talbot, J. P. and Hunt, H. E. M. (2003) 'Isolation of buildings from rail-tunnel vibration: A review', *Building Acoustics*, 10(3), pp. 177–192. doi: 10.1260/135101003322661998.

Thomas, A. G. (1982) 'The Design of Laminated Bearings I', *Proceeding of the Conference on NR for Earthquake Protection of Buildings*, pp. 229–246.

Thomas AG (1982) 'The design of laminated bearings', in Proceedings of the Conference on NR for Earthquake Protection of Buildings (ed.), pp. 229–246.

Thompson, A. *et al.* (2000) *Property modification factors for elastomeric bearings*.

Thuyet, V. N., Deb, S. K. and Dutta, A. (2018) 'Mitigation of Seismic Vulnerability of Prototype Low-Rise Masonry Building Using U-FREIs', *Journal of Performance of Constructed Facilities*, 32(2), p. 04017136. doi: 10.1061/(asce)cf.1943-5509.0001136.

Timoshenko, S. P. (1921) 'LXVI. On the correction for shear of the differential equation for transverse vibrations of prismatic bars', *The London, Edinburgh, and Dublin Philosophical Magazine and Journal of Science*, 41(245), pp. 744–746. doi: 10.1080/14786442108636264.

Toopchi-Nezhad, H., Tait, M. J. and Drysdale, R. G. (2009) 'Shake table study on an ordinary low-rise building seismically isolated with SU-FREIs (stable unbonded-fiber reinforced elastomeric isolators)', *Earthquake Engineering & Structural Dynamics*. John Wiley & Sons, Ltd, 38(11), pp. 1335–1357. doi: https://doi.org/10.1002/eqe.923.

Topkaya, C. and Yura, J. A. (2002) 'Test Method for Determining the Shear Modulus of Elastomeric Bearings', *Journal of Structural Engineering*, 128(6), pp. 797–805. doi: 10.1061/(asce)0733-9445(2002)128:6(797).

Tosaka, M., Murakami, S., Poompradub, S., Kohjiya, S., Ikeda, Y., Toki, S., Sics, I. and Hsiao, B. (2004) 'Orientation and Crystallization of Natural Rubber Network As Revealed by WAXD Using Synchrotron Radiation', *Macromolecules*, 37, pp. 3299–3309. doi: 10.1021/ma0355608.

Treloar, L. R. . (1949) 'The physics of rubber elasticity', *Journal of Polymer Science*.

Treloar, L. R. . (1975) *The Physics of Rubber Elasticity*. Third Edit. Oxford Classic Texts in the Physical Sciences.

Tsai, H. C. and Lee, C. C. (1998) 'Compressive stiffness of elastic layers bonded between rigid plates', *International Journal of Solids and Structures*, 35(23), pp. 3053–3069. doi: 10.1016/S0020-7683(97)00355-7.

Tschoegl, N. W. (1989) *The Phenomenological Theory of Linear Viscoelastic Behavior*. Springer-Verlag Berlin Heidelberg New York London Paris Tokyo.

Tubaldi, E., Mitoulis, S. A., Ahmadi, H., Muhr, A.H. (2016) 'A parametric study on the axial behaviour of elastomeric isolators in multi-span bridges subjected to horizontal seismic excitations', *Bulletin of*

Earthquake Engineering. Springer Netherlands, 14(4), pp. 1285–1310. doi: 10.1007/s10518-016-9876-9.

Tubaldi, E., Ragni, L.,Dall'Asta, A.,Ahmadi, H., Muhr, A.H. (2017) 'Stress softening behaviour of HDNR bearings: modelling and influence on the seismic response of isolated structures Enrico', *Earthquake Engineering & Structural Dynamics*, 41(11), pp. 1549–1568. doi: 10.1002/eqe.

Tubaldi, E., Mitoulis, S. A. and Ahmadi, H. (2018) 'Comparison of different models for high damping rubber bearings in seismically isolated bridges', *Soil Dynamics and Earthquake Engineering*. Elsevier Ltd, 104(May 2017), pp. 329–345. doi: 10.1016/j.soildyn.2017.09.017.

Verhelst, W. F., Wolthuis, K. G., Voet, A., Ehrburger, P. and Donnet, J. B. (1977) 'The role of morphology and structure of carbon blacks in the electrical conductance of vulcanizates', *Rubber Chemistry and Technology*, 50(4), pp. 735–746.

Wang, C. M. (1995) 'Timoshenko beam-bending solutions in terms of euler-bernoulli solutions', J*ournal of Engineering Mechanics*,pp. 763–765.

Wang, T. and Wang, F. (2012) 'Three-dimensional base-isolation system using thick rubber bearings', *Active and Passive Smart Structures and Integrated Systems 2012*, 8341. doi: 10.1117/12.916965.

Warn, G. P. (2014) 'Vertical Stiffness of Elastomeric and Lead–Rubber Seismic Isolation Bearings', 9445(July 2007). doi: 10.1061/(ASCE)0733-9445(2007)133.

Warn, G. P. and Ryan, K. L. (2012) 'A Review of Seismic Isolation for Buildings: Historical Development and Research Needs', *Buildings*, pp. 300–325. doi: 10.3390/buildings2030300.

Warn, G. P. and Vu, B. (2012) 'Exploring the low shape factor concept to achieve threedimensional seismic isolation', *20th Analysis and Computation Specialty Conference - Proceedings of the Conference*, (1), pp. 1–11. doi: 10.1061/9780784412374.001.

Warn, G. P. and Weisman, J. (2011) 'Parametric finite element investigation of the critical load capacity of elastomeric strip bearings', *Engineering Structures*. Elsevier Ltd, 33(12), pp. 3509–3515. doi: 10.1016/j.engstruct.2011.07.013.

Warn, G. P., Whittaker, A. S. and Constantinou, M. C. (2007) 'Vertical Stiffness of Elastomeric and Lead–Rubber Seismic Isolation Bearings', *Journal of Structural Engineering*, 133(9), pp. 1227–1236. doi: 10.1061/(asce)0733-9445(2007)133:9(1227).

Warnaka, G. E. (1963) 'Dynamic Strain Effects in Elastomers', *Rubber Chemistry and Technology*, 36(2), pp. 407–421. doi: 10.5254/1.3539568.

Yabana, S. and Matsuda, A. (2000) 'Mechanical properties of laminated rubber bearings for three-

dimensional seismic isolation', *12Wcee*, pp. 1–8.

Yamamoto, S., Kikuchi, M., Ueda, M. and Aiken, I. D. (2008) 'Analytical Modeling of Elastomeric Isolation Bearings Under Severe Axial Load and Shear Deformations', *The 14 thWorld Conference on Earthquake Engineering*, p. 8.

Yang, W., Sun, X., Wang, M. and Liu, P. (2017) 'Vertical stiffness degradation of laminated rubber bearings under lateral deformation', *Construction and Building Materials*. Elsevier Ltd, 152, pp. 310–318. doi: 10.1016/j.conbuildmat.2017.07.004.

Yenidogan, C. (2021) 'Earthquake-Resilient Design of Seismically Isolated Buildings: A Review of Technology', *Vibration*, 4(3), pp. 602–647. doi: 10.3390/vibration4030035.

Yeoh, O. H. (1985) 'The Compression Modulus of tall rubber cylinders', *Journal of Rubber Research Institute of Malaysia/*, 33(3), pp. 109–114.

Yeoh, O. H. (1990) 'Characterization of Elastic Properties of Carbon-Black-Filled Rubber Vulcanizates', *Rubber Chemistry and Technology*, 63(5), pp. 792–805. doi: 10.5254/1.3538289.

Yeoh, O. H. (1993) 'Some Forms of the Strain Energy Function for Rubber', *Rubber Chemistry and Technology*, 66, pp. 754–771.

Yeoh, O. H. and Fleming, P. D. (1997) 'A new attempt to reconcile the statistical and phenomenological theories of rubber elasticity', *Journal of Polymer Science Part B: Polymer Physics*, 35(12).

Zhang, Z., Liu, X. and Peng, Y. (2019) 'Improved nonlinear rotational constitutive law for predicting critical loads in elastomeric isolation bearings', *Construction and Building Materials*. Elsevier Ltd, 211, pp. 150–158. doi: 10.1016/j.conbuildmat.2019.03.241.

Zhou, Y., Zhang, Z. and Vassiliou, M. F. (2022) 'Investigation on vertical stiffness reduction of thick rubber bearings under lateral displacement', *Construction and Building Materials*. Elsevier Ltd, 360(November), p. 129563. doi: 10.1016/j.conbuildmat.2022.129563.

Zhou, Z., Wong, J. and Mahin, S. (2016) 'Potentiality of Using Vertical and Three-Dimensional Isolation Systems in Nuclear Structures', *Nuclear Engineering and Technology*. Elsevier B.V, 48(5), pp. 1237–1251. doi: 10.1016/j.net.2016.03.005.